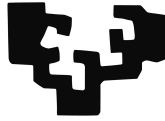eman ta zabal zazu

Universidad del País Vasco Euskal Herriko Unibertsitatea

Department of Theoretical Physics and History of Science
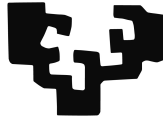
Physical Cosmology with Complete Samples of Massive Clusters of Galaxies

Pablo Jimeno Romero

Ph.D. THESIS
Leioa 2017

eman ta zabal zazu

Universidad   Euskal Herriko
del País Vasco   Unibertsitatea

Department of Theoretical Physics and History of Science

Physical Cosmology with Complete Samples of Massive Clusters of Galaxies

Supervisors:
Dr. Tom Broadhurst
Dr. Ruth Lazkoz Sáez

Submitted by Pablo Jimeno Romero
for the degree of Doctor of Physics

A las tres mujeres de mi vida.

¿No he tenido que entrar en contacto con el mundo? ¿No he tenido que aprender lo que es el vacío y enseñar el vacío? Cuando me parecía hablar razonablemente, la contradicción resonaba con redoblada fuerza; por eso, ante tanta contradicción, tuve que huir hacia la soledad, hacia lo no transitado, y para no estar completamente solo tuve que entregarme al diablo.

Goethe
Fausto

Acknowledgements / Agradecimientos

First of all, of course, I would like to thank my supervisors Tom Broadhurst and Ruth Lazkoz for the opportunity they gave me to work with them on one of the most amazing topics one can work on. I have learned a lot from them during these years, and I have always felt the faith they had in me. I hope they are proud of me and my work, summarised in part in this thesis.

I am also grateful to the people from the Department of Theoretical Physics and History of Science that have ever helped me or taught me something: Alex Feinstein, Iñaki Garay, Ivan De Martino, J. J. Blanco Pillado, Jesus Ibañez, José M. Senovilla, Montserrat Barrio, Raül Vera and Vincenzo Salzano. Among all these people, there are two that I would like to thank specially for their support and assistance, which are Iñigo L. Egusquiza and Jon Urrestilla, who were there when I most needed someone by my side. I really appreciated it.

I thank people and collaborators from other universities, including Jean Coupon, Jeremy Lim, José María (a.k.a. Chema) Diego, Keiichi Umetsu, Nick Kaiser, Ofer Lahav, Sandor Molnar and Shaun Cole, for giving me the chance to discover new ways to make and understand science.

***

Aunque seguro que me dejo a alguien, doy las gracias a Ariadna, Borja, Carlos, Charlotte, Diego, Enrique, Fran, Gael, Giuseppe, Iker, Iñigo, Iraultza, Irene, João, Jon, Julen, Kepa, Lluc, Maria, Mariam, Mattin, Mikel, Naiara, Nastassja, Olatz, Paul, Peio, Raul, Santi, Unai, Uri, Urtzi y a Xiao-Hang, por crear el mejor entorno que uno puede imaginar tener en una universidad; ojalá fuera siempre así y no tuviera que decirles nunca adiós. Espero que sigamos en contacto durante muchos años, en especial con Iagoba, que siempre me enseña cosas de programar y de vivir, y con mis eternos compañeros de despacho Asier y Joanes, a los que quiero ya como a hermanos y que tanto me han ayudado desde que empecé el doctorado.

También me gustaría mencionar en estos agradecimientos a Gerardo, camarada guerrero de la ciencia que siempre ha sido un ejemplo para mí; a Oihane, por haberme recordado lo afortunado que soy por tener este trabajo; y al resto de mis amigos de Bilbao y de Madrid, a los que agradezco el haberme aguantado a mí y a mis chorradas durante todos estos años. Lo peor espero que esté por llegar.

No me olvido ni de Laura ni de Xandra, las dos personas que más me han apoyado durante estos años de tesis, y a las que menos he sabido agradecérselo. Espero con todo mi corazón poder compensarlo algún día, ya que para bien o para mal lo significan todo para mí.

Y como no podía ser de otra manera, finalmente doy las gracias a mi madre, cuyo amor y cariño incondicional han sido para mí siempre un remanso de paz; a mi padre, por haber despertado en mí la curiosidad que me ha llevado a escribir esta tesis; y a Alba, Angel, Carmen, Marcos, Marta, Pepi, y al resto de mi familia, tanto la de acá como la de allá, por todo. Sé que no soy una persona fácil de tratar; que me sigan queriendo a pesar de ello es algo que nunca apreciaré lo suficiente.

Resumen

El objetivo de esta tesis ha sido usar grandes conjuntos de cúmulos de galaxias, obtenidos de distintos catálogos fotométricos construidos a partir de datos del programa *Sloan Digital Sky Survey* (SDSS), para realizar medidas precisas de diferentes efectos que emergen de los fuertes potenciales gravitatorios que generan, y obtener relaciones que permitan asociar la masa total de dichos cúmulos con los distintos observables asociados a éstos.

Los cúmulos de galaxias son generalmente descritos como las "estructuras ligadas gravitacional-mente más masivas del Universo", y aparecen en los picos de densidad de la distribución de materia del Universo. Esta distribución tiene su origen en las microscópicas perturbaciones de densidad que se produjeron en los primeros instantes después del *Big Bang*, y que fueron posteriormente amplificadas por acción de la fuerza gravitatoria, formando lo que se conoce hoy en día como estructura a gran escala del Universo.

El estudio de la dínamica y evolución de este proceso aporta valiosísima información sobre la composición e historia del Universo, y permite ajustar y contrastar distintos modelos cosmológicos. El modelo actualmente más aceptado, conocido como modelo cosmológico estándar o modelo ΛCDM, es capaz de describir las medidas realizadas de este crecimiento de estructuras, así como las observaciones de los "ecos" del *Big Bang* provenientes del fondo cósmico de microondas, resonancias de una era pasada en la que el Universo era extremadamente caliente y denso. Según este modelo, únicamente el 5% del contenido del Universo nos sería conocido, incluyendo las estrellas, las galaxias, y los demás sistemas astrofísicos que podemos observar. El restante 95% correspondería a *materia oscura* y a *energía oscura*, capaces de explicar distintos fenónemos observados en las últimas décadas, pero cuya naturaleza nos es todavía desconocida.

Entre dichos fenómenos se encuentra la actual expansión acelerada del Universo, observada a finales de los años 90 y que representa uno de los descubrimientos más importantes y profundos de la cosmología reciente, y probablemente el mayor misterio de la física actual. Esta expansión puede explicarse apelando a una constante cosmológica Λ originada a partir de la energía del vacío, a la ya mencionada energía oscura, de exóticas propiedas físicas, o a modificaciones de la teoría gravitatoria de la Relatividad General de Albert Einstein, que podría no ser capaz de describir correctamente el comportamiento del espacio-tiempo a grandes distancias. Esta aceleración podría ser la clave que condujese a la comprensión del comportamiento de la gravedad a escalas cosmológicas, revelar la existencia de dimensiones extra, o aportar luz sobre una hipotética teoría cuántica de la gravedad.

En cuanto a la materia oscura, fueron los cúmulos de galaxias los que aportaron las primeras evidencias de su existencia cuando Fritz Zwicky, ya en 1933, dedujo la presencia de materia "invisible" en el cúmulo Coma para poder explicar las altas velocidades de las galaxias que habitan en éste. Casi 50 años más tarde, anomalías encontradas en las curvas de rotación de galaxias, y el inesperado descubrimiento de potentes lentes gravitatorias, confirmaron la necesidad de la

existencia de dicha materia oscura.

Los halos de materia en los que los cúmulos se forman pueden llegar a contener la masa equivalente a más de mil billones de soles. Esta masa está distribuida principalmente en forma de materia oscura, gas y galaxias, representando estas últimas únicamente alrededor del 1% de la masa total del cúmulo, y sólo el 10% de la materia ordinaria.

Una de las ventajas de la naturaleza multi-componente de los cúmulos es que permite estimar su masa de manera independiente a partir de cantidades observables en distintos rangos del espectro electromagnético. Entre estas cantidades se encuentra la llamada *riqueza*, que es simplemente una medida de la cantidad de galaxias contenidas en el cúmulo, y que parece guardar una estrecha relación con la masa total. Al mismo tiempo, la radiación Bremsstrahlung en rayos X proveniente del caliente plasma intracúmulo permite estimar su temperatura y la profundidad del pozo gravitatorio, proporcional a la masa del halo de materia oscura que lo genera. También asociado a la presencia de gas en el cúmulo, la distorsión producida por la interaccion de la radiación del fondo cósmico de microondas con los electrones altamente energéticos del plasma intracúmulo, el llamado efecto Sunyaev-Zel'dovich, proporciona otra estimación de la masa total del cúmulo. Finalmente, y aunque no constituye un observable directo, el efecto de lente gravitacional, que curva la luz proveniente de galaxias lejanas distorsionando así su forma y tamaño, permite realizar estimaciones precisas de la materia contenida en el cúmulo, independiente de su naturaleza o estado dinámico.

Los cúmulos de galaxias fueron los primeros en apuntar ya en los años 80 en la dirección del modelo cosmológico actualmente aceptado. La existencia de masivos cúmulos de galaxias en épocas tempranas del Universo ya indicaba la necesidad de una densidad de materia subcrítica. Así mismo, medidas de su abundancia y distribución relativa confirmaban el modelo de formación de estructuras a partir de fluctuaciones primordiales de naturaleza Gaussiana. Entre las distintas aplicaciones cosmológicas de los cúmulos, también se encuentra su capacidad para discriminar entre distintas teorías gravitatorias que se comportarían de manera equivalente a escalas cosmológicas, pero que podrían mostrar diferencias en la manera en la que éstos se agrupan y colapsan.

En cualquier caso, para realizar cualquier tipo de analisis cosmológico basado en la estadística de cúmulos de galaxias, grandes muestras de éstos han de ser construidas a partir de los datos observacionales aportados por los ambiciosos programas de cartografiado del Universo, generalmente usando algoritmos de busqueda en el rango óptico, o seleccionándolos a partir de su señal en rayos X o través del efecto Sunyaev-Zel'dovich. También son necesarias relaciones que permitan inferir su masa a partir de las cantidades observables anteriormente mencionadas, además de simulaciones cosmológicas lo suficientemente grandes como para ser comparadas con los enormes volúmenes hoy en día considerados.

El trabajo de esta tesis se enfoca hacia esta tarea, estudiando distintos fenómenos gravitatorios que sólo pueden ser observados gracias al uso combinado de un gran número de cúmulos de galaxias, y que nos permitirán validar la pureza y completitud de distintos catálogos construidos a partir de datos del SDSS, el más extenso de estos programas de cartografiado. También ajustaremos una relación entre la riqueza y la masa de los cúmulos a partir del estudio de la distribución y abundancia de éstos en volúmenes observacionalmente completos, así como a través de la intensidad del efecto Sunyaev-Zel'dovich observado en los mapas producidos por el satélite espacial *Planck*.

En el capítulo 1 presentamos algunos de los conceptos básicos de la cosmología moderna, empezando por la definición del concepto de la métrica de un espacio-tiempo. Después discutimos cómo usar las ecuaciones de la Relatividad General para definir un marco en el que describir la

evolución de un Universo en expansión a través de sus distintas épocas, marcadas por las densidades relativas de las distintas componentes contenidas en éste. También describiremos brevemente cómo calcular ciertas distancias cosmológicas de interés, así como el modelo cosmológico actualmente aceptado.

En este mismo capítulo introducimos además la teoría que describe el crecimiento de perturbaciones que acaban dando lugar a la estructura a gran escala que se observa hoy en el Universo, así como las distintas herramientas estadísticas que permiten el análisis de dichas estructuras con el fin de obtener información sobre distintos parámetros cosmológicos o sobre teorías gravitatorias.

En el capítulo 2 analizamos algunos de los fenómenos que tienen su origen en la curvatura del espacio-tiempo generada por la abundante masa contenida en los cúmulos de galaxias, entre los que se encuentra el *redshift* (corrimiento al rojo) gravitatorio de la luz proveniente de las galaxias contenidas en el cúmulo, y la amplificación de la luz proveniente de galaxias lejanas producida por el efecto de lente gravitacional. Después de repasar brevemente cómo relacionar la masa de un cúmulo con su riqueza, describimos las ecuaciones que permiten cuantificar la amplitud del efecto Sunyaev-Zel'dovich a partir de las propiedades del cúmulo que lo genera.

En el capítulo 3 detallamos las características del programa de observación SDSS, en el que basamos gran parte del trabajo realizado en esta tesis. Enumeramos así mismo los dos catálogos de galaxias, *Legacy* y *BOSS*, y los tres catálogos de cúmulos de galaxias, *GMBCG*, *WHL12* y *redMaPPer*, con los que vamos a trabajar y que han sido generados a partir de datos de dicho programa.

En el capítulo 4 usamos conjuntos de cúmulos obtenidos a partir de los tres catálogos antes mencionados para realizar medidas del efecto de redshift gravitatorio. Para ello seleccionamos todos aquellos cúmulos con redshifts comprendidos entre $0.1 \leqslant z \leqslant 0.4$, y, a partir de las posiciones espectroscópicas disponibles de galaxias satélite, construimos un espacio de fases en el que detectar de manera estadística las distorsiones generadas por este efecto, que previamente hemos modelado considerando otro tipo de distorsiones introducidas por efectos relativistas asociados al movimiento de las galaxias. En el caso de los catálogos GMBCG y redMaPPer encontramos una señal consistente con el modelo propuesto, mientras que en el caso del catálogo WHL12 la señal obtenida se desvía completamente del modelo. Si repetimos el mismo análisis dividiendo los conjuntos de cúmulos antes considerados en distintos subconjuntos de masas crecientes, encontramos que la señal anómala proviene de cúmulos poco masivos, lo que podría deberse a la presencia de grupos de galaxias que habrían sido identificados erroneamente como cúmulos por el algoritmo de busqueda debido a efectos de proyección. Por otro lado, con el catálogo redMaPPer encontramos una clara dependencia de la señal con la masa, a pesar de ser el que menos cúmulos contiene.

En este capítulo también medimos la amplificación producida en las galaxias del programa BOSS por el efecto de lente gravitatoria, encontrando que los tres catálogos producen señales de acuerdo con el modelo propuesto, y siendo de nuevo el catálogo redMaPPer el que más clara dependencia de la señal con la masa muestra. De este análisis concluimos que el catálogo redMaPPer es el más fiable de los tres que han sido analizados. El trabajo presentado en este capítulo está basado en el siguiente artículo:

- **Comparing gravitational redshifts of SDSS galaxy clusters with the magnified redshift enhancement of background BOSS galaxies**
  P. Jimeno, T. Broadhurst, J. Coupon, K. Umetsu, R. Lazkoz, *MNRAS, 448, 1999 (2015). arXiv:1410.6050.*

En el capítulo 5, incluyendo los datos de las más recientes observaciones de galaxias realizadas por el SDSS, construimos a partir del catálogo redMaPPer un conjunto de cúmulos con una completitud espectral mayor del 97% en la región $z \leqslant 0.325$, que usamos para realizar una de las medidas más precisas hasta la fecha de la distribución y agrupación relativa de los cúmulos de galaxias. Para ello modificamos los estimadores estadísticos normalmente utilizados para tener en cuenta las propiedades probabilistas del algoritmo de busqueda de cúmulos del catálogo redMaPPer, que proporciona las probabilidades de que las galaxias encontradas en el cúmulo sean realmente la galaxia central que indica la localización de la parte más profunda del pozo de potencial gravitatorio. Los resultados obtenidos confirman las teorías actualmente aceptadas de formación de estructura a gran escala, encontrando que los cúmulos de galaxias tienden a encontrarse más agrupados para masas cada vez mayores, como se espera de objetos que viven en los raros picos de densidad de un campo de fluctuaciones de origen Gaussiano. En cuanto a la densidad de cúmulos observada a través de distintas épocas del Universo, encontramos que ésta desciende aproximadamente en un 20% entre los redshifts $z = 0.1$ y $z = 0.3$.

Posteriormente comparamos nuestros resultados con las predicciones aportadas por la simulación cosmológica *MXXL*, una de las mayores realizadas hasta ahora, para encontrar una relación entre la masa y la riqueza de los cúmulos, que es el observable con el que trabajamos. Tras encontrar esta relación con gran precisión, vemos que las medidas de agrupación de cúmulos son mayores en un 20% de lo que cabría esperar de un modelo cosmológico como el considerado, basado en datos del satélite espacial *Planck*. Esta tensión es aliviada considerando un modelo cosmológico previo, con una densidad menor de materia, y una dispersión mayor de la amplitud de las fluctuaciones de densidad. Los resultados obtenidos en este capítulo han sido publicados en:

- **Precise clustering and density evolution of redMaPPer galaxy clusters versus MXXL simulation**
  P. Jimeno, T. Broadhurst, R. Lazkoz, R. Angulo, J.-M. Diego, K. Umetsu, M.-c. Chu, *MNRAS, 466, 2658 (2017). arXiv:1608.05446.*

En el capítulo 6 definimos un nuevo conjunto de cúmulos obtenidos del catálogo redMaPPer en la región $z \leqslant 0.325$, que usamos para estudiar el efecto Sunyaev-Zel'dovich asociado a éstos a partir de los mapas del fondo cósmico de microondas obtenidos en 4 frecuencias distintas por el satélite espacial *Planck*. Esta señal es detectada con una mayor significancia y a distancias mayores que anteriores trabajos, creciendo además de manera coherente con la riqueza media de los subconjuntos de cúmulos propuestos. A través de un análisis Bayesiano basado en un algoritmo *Markov chain Monte Carlo* (MCMC), conseguimos caracterizar los perfiles de presión de subconjuntos de cúmulos de riquezas diferentes a la vez que obtenemos una estimación de la masa media contenida en cada uno de ellos. Encontramos que las masas que derivamos son alrededor de un 24% menores de lo predicho por modelos que obtienen estimaciones de la masa a partir del efecto de lente gravitacional, en principio más fiables. Estos resultados son parecidos a los encontrados por otros trabajos que encuentran una desviación (el llamado *bias*) similar.

Después de corregir esta desviación basándonos en datos de lentes gravitacionales encontrados en la literatura, realizamos otro análisis MCMC para tratar de obtener la relación óptima entre masa y riqueza que pueda describir nuestras masas corregidas. Finalmente, obtenemos la relación existente entre la masa del cúmulo y la intensidad total del efecto Sunyaev-Zel'dovich, mejorando en precisión la obtenida por el equipo de la misión *Planck* a partir de cúmulos seleccionados

individualmente por la intensidad de dicho efecto, lo cual se explica por el mayor rango de masa y por el potencial estadístico de la muestra de cúmulos con la que trabajamos. Este capítulo se basa en el trabajo descrito en el artículo:

- **Planck/SDSS Cluster Mass and Gas Scaling Relations for a Volume-Complete redMaPPer Sample**
  P. Jimeno, J.-M. Diego, T. Broadhurst, I. De Martino, R. Lazkoz, *Enviado a MNRAS arXiv:1706.00395*.

Finalmente, presentamos las conclusiones derivadas del trabajo realizado en esta tesis en el capítulo 7.

Contents

PART I

Introduction

1

Cosmology and Large Scale Structure of the Universe

In this chapter we overview some basic concepts of modern cosmology, starting from the mathematical theoretical framework of differential geometry and the metric of an space-time. Then, we use the equations of Einstein's General Relativity to describe an expanding Universe through the Friedmann-Lemaître-Robertson-Walker metric and the Friedmann equations, and study its evolution as a function of its components. We also discuss how to calculate the different cosmological distances of interest, and then present the ΛCDM model of cosmology, where an spatially flat Universe filled with radiation, baryons, cold dark matter, and some sort of dark energy can explain with great success the majority of the observational results gathered over the last decades.

We then describe the mechanisms of the growth of structures, a process that leads to the creation of the large scale structures that we observe today in the Universe. Considering a simple linear formalism we are able to track the evolution, triggered primarily by gravity, of the primordial density perturbations through the different epochs of the Universe. We then briefly describe cosmological simulations and the Zel'dovich approximation, two of the multiple ways to characterize the non-linearities that appear at late times and at small scales. After presenting the statistical tools required to describe the distribution of matter, namely the power spectrum and the two-point correlation function, we introduce the concept of the linear halo bias that lets us compare the observed distribution of galaxies and clusters with the underlying matter distribution. We briefly explain the origin of the redshift-space distortions generated by peculiar motions of galaxies, and the way to exploit the information they provide to test gravitational theories and constrain cosmological parameters. Finally, we derive an expression for the mass function that describes the abundance of haloes as a function of their mass, and introduce the cluster counts technique as an extra tool to place constrains on cosmological parameters.

1.1 Cosmology

In 1929 Edwin Hubble discovered that distant galaxies were moving away from us in all directions. This motion was faster for galaxies that were further from us than for those who were closer. The velocity of galaxies seemed to follow the linear relation (Fig. 1.1):

$$v = H\,d\,, \tag{1.1}$$

where H is the *Hubble constant*, and d is the distance to the observed galaxy. Although the initial estimation of the Hubble constant of $H \approx 500\,\mathrm{km\,s^{-1}\,Mpc^{-1}}$ was several factors higher than
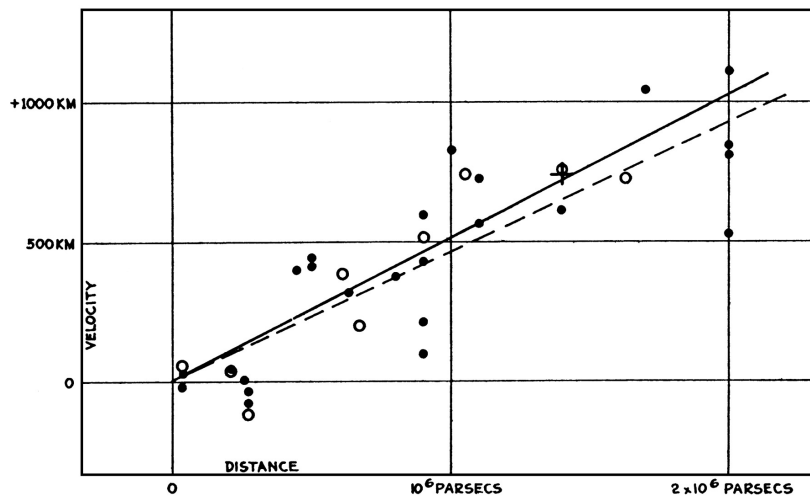
Figure 1.1: *Hubble's original diagram with the receding velocities of galaxies (units should be km s^{-1}) as a function of their distance. The resulting Hubble constant takes a value of $H \approx 500\,\mathrm{km\,s^{-1}\,Mpc^{-1}}$, almost larger by a factor of 10 than current estimates, but it should be noted that the maximum distance measured here is 2 Mpc, three orders of magnitude smaller than the distances considered nowadays.*

current estimates, this empirical result led astronomers to realize that the Universe is not static, but it is expanding and galaxies are moving away from each other in this *Hubble flow* in the same way raisins in a fruit cake move away from each other as the cake grows in the oven.

The discovery of the expansion of the Universe was one among a long list of discoveries in the 20$^{\text{th}}$ century that changed the vision that humankind had of the Universe, and the key observation that inevitably led to the theory of the *Big Bang*. According to this theory, as we go back in time and the cosmic expansion is reversed, the Universe becomes hotter and denser and finally reaches a stage were the density of matter becomes infinite and the space-time turns into a *singularity*. This Big Bang singularity represents, rather than an "explosion", the birth of space-time, which, if the Universe is spatially flat as observations seem to indicate, was already born with an infinite spatial extension. This means that it makes no sense to ask what was there before such singularity, as there is no "before" the Big Bang, or where is the Universe expanding to, as there no "outside" to expand into.

The evidence that the Universe was in the past much hotter than it is now is coming literally from everywhere. Because the speed of light is finite, the further we are looking, the younger the Universe was, and the echo from such early time is coming from all directions in form of the blackbody radiation of the *cosmic microwave background* (CMB), discovered accidentally in 1964 and measured later to high precision with space satellites like COBE, WMAP and *Planck*.

Earlier, the motion of galaxies within clusters required the presence of extra "invisible" or "unseen" matter, which was also needed later to explain both the anomalies on the rotation curves of galaxies, and the strong gravitational lenses unexpectedly found. At the same time, the light emitted by distant supernovas of type Ia indicated that the Universe not only is not slowing its growth due to the gravitational pull of matter, but is going through a phase of accelerated expansion. The presence of *dark matter* and *dark energy* in the Universe seemed to explain these two sets of observations, reducing the part of the Universe that we can directly see to just the $\sim$ 5%.

As the Big Bang standard cosmological model was beginning to take shape, some problems started to arise, like the incapability to explain why the Universe was so flat, or why the CMB was so uniform. These problems were solved by the theory of *inflation*, which states that the Universe went through a phase of incredible cosmic expansion some 10^{-35} seconds after the Big Bang. The quantum fluctuations originated and inflated during this period would explain both the anisotropies observed in the CMB, and its overall spatial homogeneity.

Using the full machinery of differential geometry, the powerful theory of General Relativity, and the Standard Model of Particle Physics, we can now finally understand and explain the majority of the phenomena we see in the skies without the necessity to invoke any god or goddess.

1.1.1 The metric of an space-time

Before being able to describe the behaviour of an expanding Universe, we first need to understand one basic concept of differential geometry, the metric. In our case, the metric will also be needed, among other things, to perform conversions between different coordinate systems, compute distances, and describe the bending of light by gravitational lenses.

One can think of a metric $g_{\mu\nu}$ as a tool to describe the nature of space-time, where:

$$\mathrm{d}s^2 = g_{\mu\nu}\mathrm{d}x^\mu\mathrm{d}x^\nu\,, \tag{1.2}$$

is the infinitesimal distance between two events in space-time, with μ and ν ranging from 0 to $N-1$, where N is the number of dimensions of the space-time with which one is working. From now on, we will consider $N=4$, with the first dimension reserved to the time-like coordinate $(\mathrm{d}x^0 = \mathrm{d}t)$, and the other three to space-like coordinates. One interesting property of this distance is that it is invariant under change of coordinate systems.

The metric $g_{\mu\nu}$ is symmetric, so in a four-dimensional space-time it has four diagonal terms and six off-diagonal terms. In the case of Minkowski flat space-time, the metric is given by:

$$\eta_{\mu\nu} = \begin{bmatrix} -1 & 0 & 0 & 0 \\ 0 & 1 & 0 & 0 \\ 0 & 0 & 1 & 0 \\ 0 & 0 & 0 & 1 \end{bmatrix}. \tag{1.3}$$

In a non-static expanding Universe, any two points in space-time move away from each other as time goes by. In order to describe this expansion we introduce the *scale factor* a, which is nothing else than a measure of how the physical distance between galaxies has been evolving with time, that is, a measure of the relative size of the Universe. If we fix the value of the scale factor to be equal to one today, then at earlier times it had to be smaller than one, and thus galaxies were also closer (the physical distance that separated them was smaller than it is today). In the previous flat metric we could introduce an expansion including this time-dependent scale factor $a(t)$, such that:

$$g_{\mu\nu} = \begin{bmatrix} -1 & 0 & 0 & 0 \\ 0 & a(t) & 0 & 0 \\ 0 & 0 & a(t) & 0 \\ 0 & 0 & 0 & a(t) \end{bmatrix}. \tag{1.4}$$
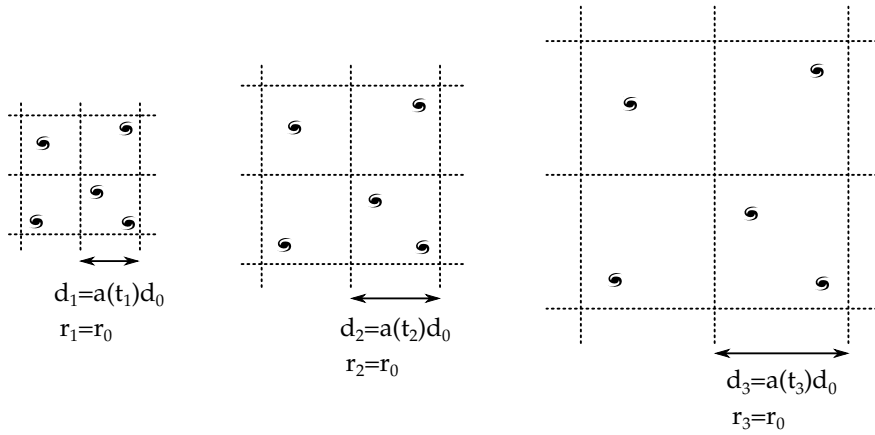
Figure 1.2: *Scheme showing the isotropic expansion of the Universe as time goes forward, with $t_1 < t_2 < t_3$. Physical distances d scale as $a(t)$, with $a(t_1) < a(t_2) < a(t_3)$. Comoving distances r are constant by definition, and if we consider $a(t_0) = 1$, then we can take $r_0 = d_0$.*

In spherical coordinates, the spacetime interval induced by this metric would be:

$$\mathrm{d}s^2 = -\mathrm{d}t^2 + a^2(t)\left[\mathrm{d}r^2 + r^2\mathrm{d}\Omega^2\right] , \tag{1.5}$$

According to this, if today $(t = t_0)$ two points were separated by a distance d_0, and we consider that $a(t_0) = 1$, it means that at some other previous time t these two points would have been separated by a distance $a(t)\,d_0$. Obviously, in an expanding space-time the scale factor a would be smaller at earlier times than it would be today. Finally, it is convenient to define a *comoving distance* between two points as that distance that does not depend on the value of the scale factor, or equivalently, a distance that remains constant between observers moving with the expansion of the Universe. This is shown schematically in Fig. 1.2.

All things considered, this test metric is still not enough to describe the space-time of an expanding Universe, as it has not necessarily be spatially flat.

1.1.2 The equations of General Relativity and the Cosmological Principle

It was the theory of *General Relativity* of Albert Einstein, proposed in 1915, that made modern cosmology possible. The big breakthrough of this theory is that it describes gravity not as a force induced by a gravitational field, but as the consequence of particles being embedded in a four-dimensional space-time curved by its energy and matter content. The Einstein equations read:

$$R_{\mu\nu} - \frac{1}{2}g_{\mu\nu}\,R = \frac{8\pi G}{c^4}T_{\mu\nu} , \tag{1.6}$$

where $R_{\mu\nu}$ is the *Ricci tensor*, $g_{\mu\nu}$ is the metric of the space-time considered, $R = g^{\mu\nu}R_{\mu\nu}$ is the *Ricci scalar*, G is the gravitational constant, c is the speed of light, and $T_{\mu\nu}$ is the energy-momentum tensor. The left hand side of this equations is related to the geometry of the space-time, and the right hand side, to its content. That is, the curvature of space-time tells particles how to move, and the distribution of particles tell the space-time how to curve.

Another keystone of modern cosmology is the *Cosmological Principle* (CP): the assumption that

the Universe is homogeneous and isotropic. According to the CP we are not privileged observers of the Universe, and should see no difference in the properties of the Universe depending on which direction we are looking to. This, of course, is meant in an statistical sense on scales larger than $200\,\mathrm{Mpc}$, where the structures and the distribution of galaxies seem to smooth out and become more homogeneous. This statistical nature is a problem, as there is just one realization of the Universe we can observe, and cosmological observations cannot be repeated and have to be done using finite volume estimators. This is solved assuming the *fair sample* hypothesis [167], which is based on the CP and proposes that separated enough regions of the Universe can be treated as independent realisations of the underlying distribution, so averages over these regions can be treated as averages over some probability ensemble.

The Friedmann-Lemaître-Robertson-Walker metric

Assuming homogeneity and isotropy, that is, the CP, the only solution to Einstein equations is the *Friedmann-Lemaître-Robertson-Walker* (FLRW) metric:

$$\mathrm{d}s^2 = -c^2\,\mathrm{d}t^2 + a^2(t)\left[\frac{\mathrm{d}r^2}{1-Kr^2} + r^2\mathrm{d}\Omega^2\right]\,, \tag{1.7}$$

where $a(t)$ is the scale factor, and K is a constant that describes the geometry of the Universe. This metric is different from that of Eq. 1.5 in that now the Universe can either be spatially flat, closed, or open, depending on the value of K. In a universe with flat Euclidean geometry $(K = 0)$, two particles moving parallel to each other will keep travelling that way if no external force is acting on them. In a closed universe $(K > 0)$, however, two particles that begin moving parallel to each other will converge at the end. A two dimensional example of a closed geometry is that of an sphere, like that of the surface of the Earth: two travellers that begin moving to the north and parallel to each other in the Equator will meet at the end in the North Pole. Finally, in an open universe $(K < 0)$ the paths of these two particles will diverge. A 2-dimensional scheme of these three geometries can be seen in Fig. 1.3.

From the FLRW metric it is clear that in order to understand the history of the Universe we must first understand the dependence of the scale factor a with time, which will be strongly determined by the energy content of the Universe at different epochs. For that purpose, we can define the Hubble function as:

$$H(t) \equiv \frac{\dot{a}(t)}{a(t)}\,, \tag{1.8}$$

where we have introduced the notation $\dot{x} \equiv \mathrm{d}x/\mathrm{d}t$. The Hubble parameter measures how rapidly the scale factor changes, and will be given by the connection between geometry and energy content provided by the equations of General Relativity. Because the value of H_0 is still uncertain, it is usually expressed as:

$$H_0 = 100\,h\,\mathrm{km\,s^{-1}\,Mpc^{-1}}\,, \tag{1.9}$$

where h is a dimensionless quantity, and the subscript "0" means that the quantity is being evaluated at the present time, notation that we will follow from now on when applied to cosmological parameters that evolve with time. As the value of H_0 seems to be close to $70\,\mathrm{km\,s^{-1}\,Mpc^{-1}}$, some authors also consider the dimensionless quantity h_{70}, where $H_0 = 70\,h_{70}\,\mathrm{km\,s^{-1}\,Mpc^{-1}}$, and $h_{70} \approx 1$.
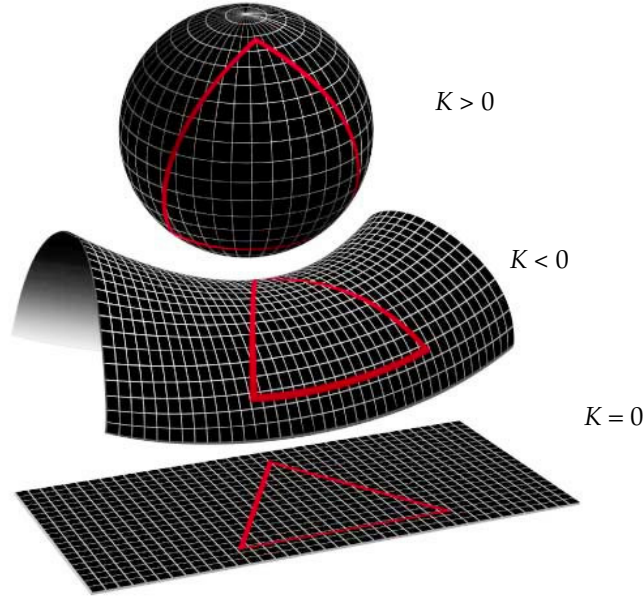
Figure 1.3: *The three different geometries considering a 2-dimensional space, where the curvature is represented using a third spatial dimension. A positive curvature ($K > 0$) leads to a closed geometry, like that of the surface of a sphere, meanwhile a negative curvature ($K < 0$) surface would correspond to a saddle-like structure. Zero curvature ($K = 0$) corresponds to the Euclidean flat space we are used to. Credits: NASA.*

1.1.3 Energy content and evolution of the Universe

In order to progress in our understanding of the Universe, we must now introduce some energy in it through the energy-momentum tensor. For a perfect fluid, this tensor takes the form:

$$T_{\mu\nu} = (p + \rho)u_\mu u_\nu + p\, g_{\mu\nu}\,, \tag{1.10}$$

where p and ρ are the pressure and the energy density of the fluid respectively, u_μ is its 4-momentum, and $g_{\mu\nu}$ is the metric of the space-time. Conservation implies that this energy-momentum tensor satisfies the covariant equation $\nabla^\mu T_{\mu\nu} = 0$, which for an expanding Universe leads to:

$$\dot{\rho} + 3\frac{\dot{a}}{a}\left(\rho + \frac{p}{c^2}\right) = 0\,. \tag{1.11}$$

This equation can be immediately applied to derive the density evolution of different fluids as a function of the scale factor a. Non-relativistic matter, with almost zero pressure, leads to $\rho_m \propto a^{-3}$, meanwhile radiation and relativistic matter like neutrinos, with $p = \rho c^2/3$, implies $\rho_r \propto a^{-4}$. More generally, one can relate the pressure of a barotropic fluid with its energy density trough the equation of state:

$$\omega \equiv \frac{p}{\rho\, c^2}\,. \tag{1.12}$$

According to this, matter and radiation correspond to a fluid with $\omega = 0$ and $\omega = 1/3$, respectively. Introducing Eq. 1.12 into Eq. 1.11, we can see that the energy density evolution of a fluid with a

constant equation of state parameter is given by:

$$\rho \propto a(t)^{-3(1+\omega)} \,. \tag{1.13}$$

From this equation it is clear that a fluid with $\omega = -1$ would have a constant energy density independently of the value of the scale factor, and would provide a negative pressure. There is good evidence nowadays that there does in fact exist an extra component in the Universe with similar properties, the so called *dark energy*. If this dark energy is in the form of a *cosmological constant* (denoted as Λ), it would correspond or would be equivalent to the case just mentioned of a fluid with $\omega = -1$. A more general approach that allows evolution in time of the dark energy equation of state leads to a energy density:

$$\rho_{de} \propto \exp\left[-3 \int^a \frac{\mathrm{d}a'}{a'} \left[1 + \omega(a')\right]\right] \,. \tag{1.14}$$

Friedmann equations

Now that we have an expression for the energy-momentum tensor (Eq.1.10), we can introduce it into the equations of General Relativity (Eq. 1.6) and obtain a set of equations able to describe the dynamics of a universe described by a FLRW metric. These simple first order differential equations are known as the Friedmann equations, and read:

$$\frac{\dot{a}^2}{a^2} = \frac{8\pi G}{3}\rho - \frac{K c^2}{a^2} \,, \tag{1.15}$$

$$\frac{\ddot{a}}{a} = -\frac{4\pi G}{3}\left(\rho + \frac{3p}{c^2}\right) \,. \tag{1.16}$$

In general only the first Friedmann equation, combined with the equations of state of the different components that populate the Universe, is used. In order to rewrite it in terms of the Hubble function, we define the critical density as:

$$\rho_c(t) \equiv \frac{3H^2(t)}{8\pi G} \,. \tag{1.17}$$

Today ($t = t_0$), with the current estimates of the value of H_0, this critical density is estimated to be $\rho_{c,0} = 3H_0^2/(8\pi G) \sim 10^{-17}\,\mathrm{kg\,km^{-3}}$, which corresponds roughly to five hydrogen atoms per cubic metre. We also define the density parameter as:

$$\Omega_x(t) = \frac{\rho_x(t)}{\rho_c(t)} \,, \tag{1.18}$$

where ρ_x can correspond here to the energy density of any component of the Universe, let it be matter, ρ_m, radiation, ρ_r, or a cosmological constant, ρ_Λ.

With these definitions, the first Friedmann equation (Eq. 1.15) is then equivalent to:

$$H^2(t) = H_0^2 \left(\frac{\rho}{\rho_{c,0}}\right) - \frac{K c^2}{a^2} \,. \tag{1.19}$$

Evaluating at $t = t_0$ and taking into account that $\Omega_0 = \rho_0 / \rho_{c,0}$, where ρ_0 here includes the contribution of all the energy components in the Universe ($\rho_0 = \rho_{m,0} + \rho_{r,0} + \rho_{\Lambda,0}$), we obtain that $\Omega_K = 1 - \Omega_0$, where we have defined a "curvature density" as:

$$\Omega_K = -\frac{K\,c^2}{H_0^2} \,.$$
(1.20)

For a flat universe $\Omega_K = 0$, $\Omega = 1$, and $\rho = \rho_c$, implying that the density of the Universe must be equal to the critical density at all times. Finally, taking into account the previously derived density evolution of the matter, radiation and cosmological constant components of the Universe, Eq. 1.19 can we rewritten in its most common form:

$$H^2(t) = H_0^2 \left(\frac{\Omega_{m,0}}{a^3} + \frac{\Omega_{r,0}}{a^4} + \Omega_{\Lambda,0} + \frac{\Omega_K}{a^2} \right) \,.$$
(1.21)

With this formula it is easy to check analytically the behaviour of the Universe in some simple cases.

Spatially flat matter-dominated Universe

Also known as Einstein-de Sitter Universe, in this case $\Omega_{m,0} = 1$ and $\Omega_{r,0} = \Omega_{\Lambda,0} = \Omega_K = 0$. The first Friedmann equation (Eq. 1.21) leads to:

$$\frac{\dot{a}}{a} = H_0 \, \frac{1}{a^{3/2}} \,.$$
(1.22)

Integrating and considering that $a(0) = 0$:

$$a(t) = \left(\frac{3}{2} \, H_0 \, t \right)^{2/3} \,.$$
(1.23)

In this model the expansion is decelerating and the age of the Universe would be equal to $t_0 = 2/(3H_0) \approx 9\,\text{Gyr}$.

Spatially flat radiation-dominated Universe

Now, with $\Omega_{r,0} = 1$ and $\Omega_{m,0} = \Omega_{\Lambda,0} = \Omega_K = 0$, we have that:

$$\frac{\dot{a}}{a} = H_0 \, \frac{1}{a^2} \,.$$
(1.24)

Again, considering $a(0) = 0$:

$$a(t) = (2 \, H_0 \, t)^{1/2} \,.$$
(1.25)

As in the matter-dominated case, the Universe is expanding but this expansion decelerates with time. This would lead to a younger Universe with $t_0 = 1/(2H_0) \approx 6\,\text{Gyr}$.

Spatially flat cosmological constant-dominated Universe

For $\Omega_{\Lambda,0} = 1$ and $\Omega_{m,0} = \Omega_{r,0} = \Omega_K = 0$, the first Friedmann equation simplifies to:

$$\frac{\dot{a}}{a} = H_0 \, . \tag{1.26}$$

This leads to an exponential solution:

$$a(t) = \exp\left[H_0 \, t\right] \, , \tag{1.27}$$

where we cannot set $a(0) = 0$ as this is a Universe with infinite age which keeps accelerating with time.

1.1.4 Distances in cosmology

Now that we have a well defined space-time with a metric and we know how it evolves with time as a function of the components contained in it, we can compute distances. But before proceeding we should introduce the concept of *redshift* z. Because in an expanding Universe all distant galaxies are moving away from us (and from each other), the light that reaches Earth is going to be stretched out with respect to that emitted at the source. The shift of the wavelengths of the photons emitted from the source is equal to:

$$1 + z \equiv \frac{\lambda_{observed}}{\lambda_{source}} = \frac{1}{a(t)} \, , \tag{1.28}$$

where $a(t)$ is the value of the scale factor when the light was emitted, and we have considered that $a(t_0) = 1$. At low redshifts, the usual Doppler formula can be used to estimate the velocity of the receding object, with $v \simeq c \, z$. Combining this first order approximation with the original Hubble relation (Eq. 1.1), we obtain that the distance to an object at redshift z is equal to $d = c \, z / H_0$.

However, to obtain the correct distance to an object at redshift z one needs to integrate along radial trajectories in the FLRW metric, as the light that reaches us now has been travelling across the Universe meanwhile it has been expanding. From Eq. 1.7 we see that the proper distance, that is, the distance that would be measured with rulers at a given time ($\mathrm{d}t = 0$), is given by:

$$D_P = a(t) \int \frac{\mathrm{d}r}{\sqrt{1 - K \, r^2}} \, . \tag{1.29}$$

The comoving distance D_C, defined before as that distance that remains constant with the expansion of the Universe, would then be equal to $D_C = D_P / a(t)$.

As we have a relation between the redshift and the value of the scale factor (Eq. 1.28), we can compute distances in terms of redshifts, which is the quantity that we can actually measure in observations. From now on we will only consider the case of a spatially flat Universe, that is, $K = 0$.

The comoving distance to an object at redshift z, corresponding to a scale factor $a = 1/(1 + z)$, is equal to:

$$D_C(z) = \frac{c}{H_0} \int_0^z \frac{\mathrm{d}z'}{E(z')} \, , \tag{1.30}$$

where $E(z) = H(z)/H_0$. It is important to note that in a flat universe at late times, $\Omega_K = 0$ and $\Omega_{r,0} \approx 0$, so we can express $\Omega_{\Lambda,0}$ in terms of $\Omega_{m,0}$ and simplify calculations taking into account that:

$$E^2(z) = \frac{H^2(z)}{H_0^2} = \left[\Omega_{m,0}(1+z)^3 + (1 - \Omega_{m,0}) \right] . \tag{1.31}$$

Once the comoving distance to an object is known, both the *luminosity distance* and the *angular diameter distance* can be derived from it. The luminosity distance D_L is defined such that the flux observed at Earth from an object at redshift z is equal to:

$$F = \frac{L}{4\pi D_L^2} , \tag{1.32}$$

where L is the intrinsic luminosity of the source. In order to relate the luminosity distance with the comoving distance, one needs to take into account the fact that in an expanding Universe photons loose energy as the scale factor grows, and that although the comoving spherical shell of area $4\pi D_C^2$ does not change with time, the associated physical area does. The luminosity distance is then equal to:

$$D_L = (1+z)\,D_C . \tag{1.33}$$

The angular diameter distance D_A is defined as the distance at which an object of physical size Δl is seen in the sky with an angular extension equal to $\Delta\theta$:

$$D_A = \frac{\Delta l}{\Delta\theta} . \tag{1.34}$$

Because the comoving size of such object is equal to $\Delta l/a$, the angle subtended in the sky would be equal to $\Delta\theta = (\Delta l/a)/D_C$, and the angular diameter distance happens to be related to the comoving distance by:

$$D_A = \frac{D_C}{1+z} . \tag{1.35}$$

One particularity of this quantity is that it does not increase indefinitely with redshift, but starts decreasing after some point and objects at higher redshifts are seen larger in the sky than objects of the same nature located at intermediate redshifts because of the "magnification" lensing effect induced by cosmic expansion.

1.1.5 The ΛCDM model

The lambda cold dark matter (ΛCDM) model, also known as standard or concordance model, is the currently most accepted cosmological model. It became increasingly popular in the late 1990s when two groups observing Type Ia supernovae (SNIa) [170, 189] found that the Universe was going through a phase of accelerated expansion, and hence proved the existence of some sort of dark energy.

Apart from this dark energy resembling a cosmological constant Λ, in this model our Universe is flat, is composed of radiation and matter both in the form of baryons and cold dark matter (CDM), and the underlying gravitational theory is General Relativity. Inflation is usually considered an extension.

According to this model, after an early epoch of radiation domination the Universe expanded and

the energy density of matter and radiation became equal in what is known as the matter-radiation equality era. This epoch of the Universe is important because it shapes the way large scale structure formed, as described later in this chapter. This happens when the universe is approximately 50,000 years old, which corresponds to an scale factor of $a \approx 0.0003$. Then, when matter was already dominating and the Universe was around 350,000 years old, the photons that compose the cosmic microwave background (CMB) were scattered for the last time when they decoupled from matter, and the *dark ages* began and continued until the first stars formed 150 million years later. Finally, when the Universe was 10 billion years old and it had expanded so much that the density of matter was surpassed by the density of dark energy, the dark energy-dominated era commenced, and the Universe began the exponential growth that we observe today, when it is around 13.8 billion years old and the dark energy content is already dominating matter by a factor of ~ 2.5.

Measurements of the CMB from WMAP and *Planck* satellites have confirmed this model with great success, and started what is known as the *precision cosmology era*, with cosmological parameters constrained to the 1% level. In Fig. 1.4 we show the constraints on Ω_m, Ω_m and ω, obtained combining CMB data with SNIa and baryon acoustic oscillations (BAO) data. The state-of-the-art estimation of the cosmological parameters of the ΛCDM model are those provided by Planck Collaboration et al. [179] and shown in Table 1.1.
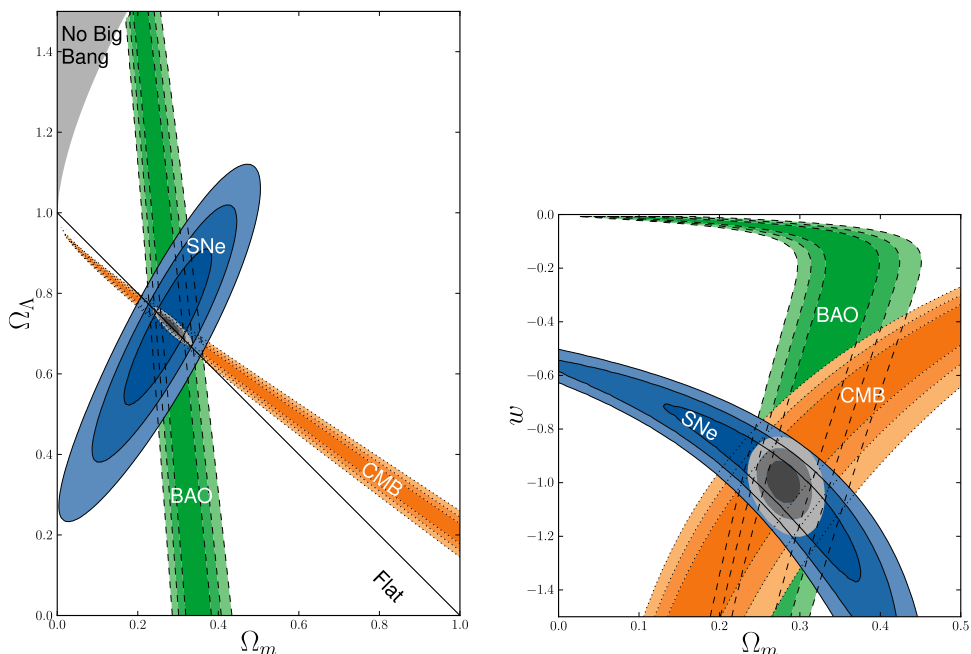
Figure 1.4: *The 1σ, 2σ and 3σ confidence level contours of Ω_m versus Ω_Λ for $\omega = -1$ on the left, and of Ω_m versus ω for a flat universe on the right, obtained combining CMB, SNIa, and BAO data. Figures are taken from Kowalski et al. [115].*

Despite its big success describing observations, this model has one obvious problem: the existence of two "dark" components whose origin is unknown.

The existence of dark matter has been proved in several different ways, including the analysis of galaxy and cluster dynamics, gravitational lensing, the power spectrum of the CMB, and the formation of the large scale structure of the Universe. With several popular candidates including weakly interacting massive particles (WIMPs), axions, and primordial black holes, promising

Table 1.1: *Cosmological parameters for the ΛCDM model as shown in Planck Collaboration et al. [179]. These have been obtained combining CMB data with SNIa and BAO data.*

Parameter	Symbol	Value
Hubble constant today	H_0	$67.74 \pm 0.46 \, \mathrm{km \, s^{-1} \, Mpc^{-1}}$
Dark energy density today	$\Omega_{\Lambda,0}$	0.6911 ± 0.0062
Matter density today	$\Omega_{m,0}$	0.3089 ± 0.0062
Curvature density	Ω_K	< 0.005
Dark energy equation of state parameter	ω	-1.006 ± 0.045
rms of matter fluctuations	σ_8	0.8159 ± 0.0086
Scalar spectral index	n_s	0.9667 ± 0.0040
Redshift of matter-radiation equality	z_{eq}	3371 ± 23
Age of the universe	t_0	$13.799 \pm 0.021 \, \mathrm{Gyr}$

searches to find the nature of the dark matter are now ongoing.

The origin of the dark energy component is also unknown but more elusive, and poses one of the biggest challenges for physics and science today. The cosmological constant Λ as is presented in this concordance model is just an special case of dark energy. Observational constraints, however, seem to favour a value of $\omega \approx -1$, but it is still unknown if this late-time accelerating expansion has its origin in some sort of vacuum energy, quintessence, an unknown behaviour of gravity at large scales, or any other of the thousands of explanations proposed in the last decades. Because there is still not a final theory that provides an equation of state for the dark energy, the effective parametrisation:

$$\omega(a) = \omega_0 + (1-a)\,\omega_a \, , \tag{1.36}$$

is employed to account for any possible scale factor-dependent deviation from $\omega \approx -1$.

Not all hope is lost: the combined analysis of the expansion history of the Universe and the growth of structures may shed some light into this mystery. The existence of dark energy explains at the same time the accelerated expansion of the Universe and the subsequent suppression of the growth of structures, as measured by redshift-space distortions, gravitational weak lensing, or the observed abundances and distribution of clusters as a function of their mass and redshift. However, gravitational theories different from General Relativity could explain the observed cosmic expansion mimicking ΛCDM results, but differ in the way the amplitude of the growth of structures scales with time. Measuring such a deviation would be a big leap forward in the understanding of the physics of dark energy.

1.2 Large scale structure of the Universe

In the last decades we have learned a lot about how matter is distributed in the Universe. Ambitious optical surveys like the Two-Degree Field Galaxy Redshift Survey (2dFGRS) or the Sloan Digital Sky Survey (SDSS) have produced the first 3-dimensional maps of large portions of the observable Universe, like the one shown in Fig. 1.5, and provide nowadays the location of more than a million galaxies. From these maps we have learned that galaxies are not randomly located in the Universe, but tend to be grouped together forming large scale structures like filaments or clusters in what is called the *cosmic web*. These structures seem to be amplified descendants of a primordial quantum
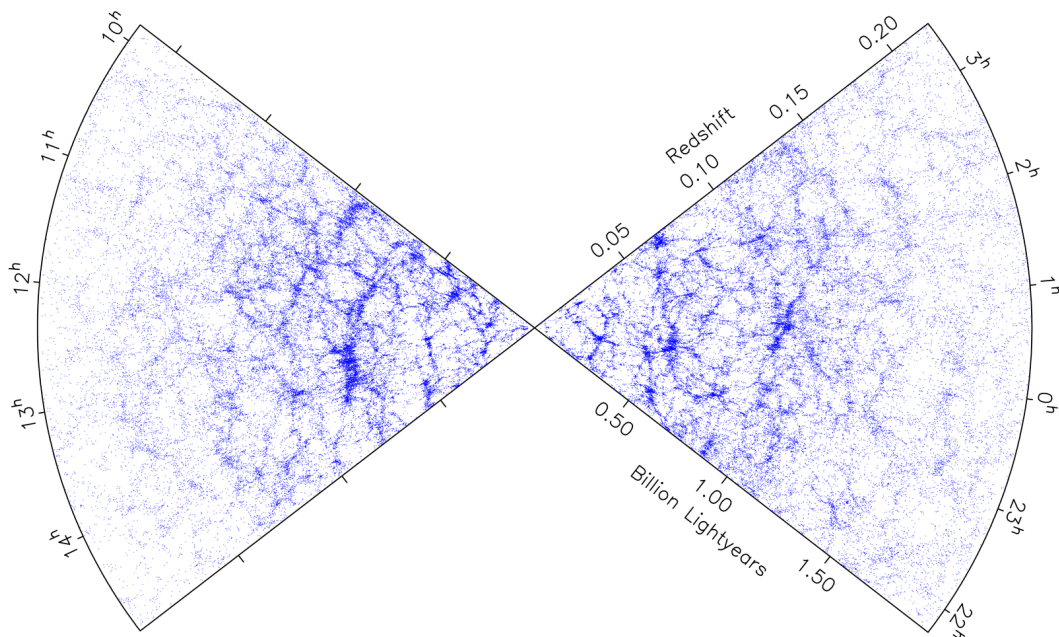
Figure 1.5: *Map of the distribution of galaxies from the completed Two-Degree Field Galaxy Redshift Survey (2dFGRS). Figure is taken from Colless et al. [50].*

density fluctuation field that emerged during inflation in the first 10^{-35} seconds of the history of the Universe, and that was imprinted in the small temperature fluctuations seen in the CMB (shown in Fig. 1.6), when the Universe was very young.

Although the first galaxies have been observed to exist when the Universe was 400 million years old, the matter haloes that host them started forming only 400,000 years after the Big Bang, very shortly after matter and radiation decoupled. In the present paradigm of structure formation driven by dark matter and gravity, galaxy groups and clusters of galaxies are still forming today through a combination of coherent infall and mergers.

The analysis of this growth not only will help understand more about how these structures formed, but may provide some insights on the nature of dark matter and dark energy.

1.2.1 Linear theory of the growth of structures

In order to understand and trace the evolution of density perturbations with time, we will first consider the equations of motion of a cosmological fluid with velocity $\vec{v}(\vec{x}, t)$, pressure $p(\vec{x}, t)$, and mass density $\rho(\vec{x}, t)$ at position $\vec{x}$ and time t. This nonrelativistic Newtonian approach is valid for small amplitude perturbations with length scales smaller than the Hubble horizon $d_H = c/H_0$, where Hubble flow velocities are small and we can work in terms of $\vec{x} = a(t)\, \vec{r}$, where $\vec{r}$ is a comoving coordinate and spatial derivatives are with respect to comoving coordinates. The Euler equation for this fluid is:

$$\frac{\partial \vec{v}}{\partial t} + \left(\vec{v} \cdot \vec{\nabla} \right) \vec{v} = -\frac{\vec{\nabla} p}{\rho} - \nabla \Phi \, , \tag{1.37}$$
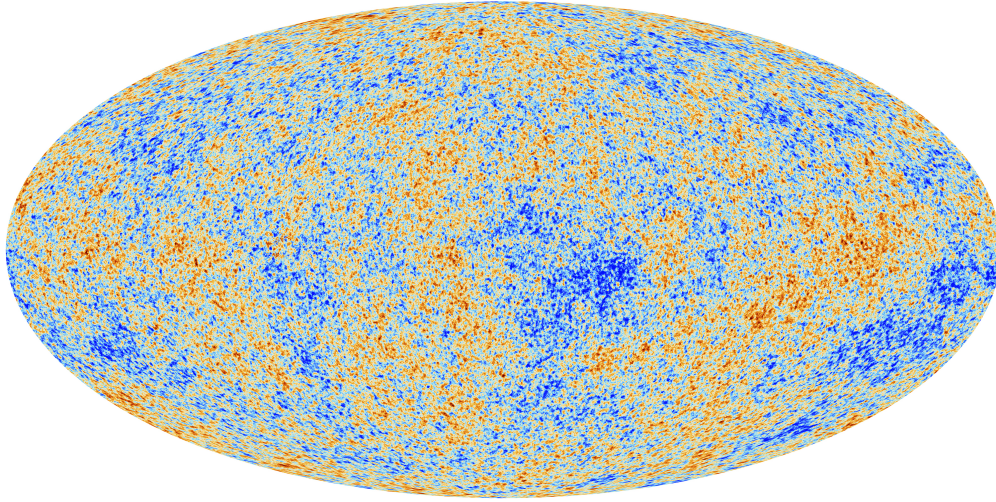
Figure 1.6: *The cosmic microwave background (CMB) as measured by the Planck mission, emitted when the Universe was only $\sim$ 380,000 years old. The average temperature of the radiation that we observe today is $2.73\,\mathrm{K}$, and the fluctuations are only of the order of 10^{-5}. Figure is from the Planck Collaboration.*

where $\vec{\nabla} = \partial/\partial \vec{x}$, and $\Phi(\vec{x}, t)$ is the gravitational potential, which is determined by the Poisson equation:

$$\nabla^2 \Phi = 4\pi G\, \rho\,. \tag{1.38}$$

Finally, we must take into account the continuity equation:

$$\frac{\partial \rho}{\partial t} + \vec{\nabla} \cdot (\rho\, \vec{v}) = 0\,. \tag{1.39}$$

Considering small perturbations $\vec{v} = \vec{v}_0 + \delta \vec{v}$, $p = p_0 + \delta p$, $\rho = \rho_0 + \delta \rho$, and $\Phi = \Phi_0 + \delta \Phi$, and defining $\delta = \delta \rho / \rho_0$, we can obtain a single equation for the growth of density fluctuations with time:

$$\ddot{\delta} + 2\,\frac{\dot{a}}{a}\,\dot{\delta} - (4\pi G\rho_0 + c_s^2\, \nabla^2)\, \delta = 0\,, \tag{1.40}$$

where $c_s^2 = \delta p / \delta \rho$ is the sound speed of the fluid.

Considering now a single Fourier mode $\delta(\vec{x}, t) = \delta_{\vec{k}} \sin(\vec{k} \cdot \vec{r})$ with comoving wavelength $\lambda = 2\pi/k$, Eq. 1.40 turns into:

$$\ddot{\delta} + 2\,\frac{\dot{a}}{a}\,\dot{\delta} - (4\pi G\rho_0 + c_s^2\, \frac{k^2}{a^2})\, \delta = 0\,. \tag{1.41}$$

From this equation we can see that there is a Jeans length $\lambda_J = 2\pi/k_J = c_s\,\sqrt{\pi/(G\,\rho_0)}$ above which gravitational pull exceeds the pressure resistance and perturbations can grow, and below which density fluctuations oscillate as sound waves. In an expanding universe, however, this Jeans length changes with time, so certain range of modes may become allowed to grow as time goes by.

In a flat universe dominated by pressureless matter Eq. 1.40 reduces to:

$$\ddot{\delta} + 2\,\frac{\dot{a}}{a}\,\dot{\delta} - 4\pi G\rho_0\, \delta = 0\,, \tag{1.42}$$

which admits two power law solutions corresponding to a growing mode with $\delta(t) \propto t^{2/3} \propto a(t)$, and a decaying mode with $\delta(t) \propto t^{-1}$.

At late times when $\Omega_m < 1$, the growing mode does not scale as $a(t)$ anymore, and assuming an equation of state for the dark energy of $\omega = -1$, the growing mode evolves as:

$$\delta \propto \frac{\dot{a}}{a} \int_0^a \frac{1}{\dot{a}'^3} \, \mathrm{d}a' \, . \tag{1.43}$$

For a $\Omega_m + \Omega_\Lambda = 1$ cosmology, it can be seen that the present day accelerated expansion of the Universe suppresses the growth of structures.

More generally, it is more convenient to define solutions of Eq. 1.40 in terms of the *linear growth function* $D(a)$ as:

$$\delta(a) = \frac{D_\pm(a)}{D_\pm(a_0)} \, \delta(a_0) \, , \tag{1.44}$$

where the D_+ and D_- notation is used to indicate growing and decaying modes, respectively. $D(a)$ is normalized to unity at present time, so $D(a_0) = 1$. The linear growth function is only dependent on a, but in theories where dark energy is clustered or General Relativity is not the gravity model considered, it may be scale-dependent.

1.2.2 The matter power spectrum

We assumed in our FLRW model that the Universe needs to be homogeneous at very large scales, and this seems to be the case when we consider regions of size of the order of a few hundred Mpc.

However, some sort of initial small scale fluctuations had to be present in order to form through gravitational amplification the large scale structures like clusters that we observe today. We can quantify these fluctuations through the density contrast:

$$\delta(\vec{x}) \equiv \frac{\rho(\vec{x}) - \rho_0}{\rho_0} \, , \tag{1.45}$$

where $\rho(x)$ is the local density at $\vec{x}$ and ρ_0 is the mean background density. The Fourier transform of these density fluctuations is:

$$\delta(\vec{k}) = \frac{1}{(2\pi)^{3/2}} \int \mathrm{d}^3x \, \delta(\vec{x}) \, e^{i\vec{k}\cdot\vec{x}} \, . \tag{1.46}$$

The *power spectrum* $P(k)$ of the density fluctuations can be computed as:

$$\langle \delta(\vec{k})\delta(\vec{k}') \rangle = (2\pi)^3 \, \delta^{(3)}(\vec{k} - \vec{k}') \, P(\vec{k}), \tag{1.47}$$

where $\delta^{(3)}(\vec{k}-\vec{k}')$ is the delta function required by isotropy, meaning that $P(\vec{k}) = P(k)$. Sometimes, the power spectrum is also expressed in terms of the dimensionless function $\Delta^2(k) \equiv k^3 \, P(k)/(2\pi^2)$.

The analogous power spectrum quantity in real space is the two-point correlation function $\xi(r)$:

$$\langle \delta(\vec{x})\delta(\vec{x}') \rangle = \xi(|\vec{x} - \vec{x}'|) = \xi(r) \, , \tag{1.48}$$

which is at the same time the Fourier transform of the power spectrum:

$$\xi(r) = \frac{1}{(2\pi)^{3/2}} \int d^3k \, P(k) \, e^{ikr} \,. \tag{1.49}$$

Again, we have assumed that the two-point correlation function is isotropic, so $\xi(\vec{r}) = \xi(r)$.

Because the growth of individual k modes, if these are small and linear theory applies, is independent and determined by the initial conditions of the early Universe, the decomposition of the density field into several Fourier modes will is indeed very useful. Apart from that, the two-point correlation function and the power spectrum provide a complete statistical characterisation of the stochastic distribution of fluctuations in a Gaussian random field.

The power spectrum encodes the information of the distribution of amplitudes of different Fourier components of the density field, $P(k) \sim |\delta(\vec{k})|^2$, but does not contain phase information. This means that different density distributions may have the same power spectrum, and hence the same two-point correlation function. Equivalently, we could say that our Universe is a realization of an stochastic density Gaussian random field drawn from $P(k)$.

One important quantity that can be computed from the linear power spectrum is the variance of mass fluctuations smoothed with a sphere of radius R:

$$\sigma^2(R, a) = \frac{1}{2\pi^2} \int P(k, a) \, W^2(kR) \, k^2 \, dk \,, \tag{1.50}$$

where $W(kR) = [3/(k^3 R^3)][\sin(kR) - kR\cos(kR)]$ is the Fourier transform of the spherical top-hat window function of radius R, so that $P(k)\,W^2(kR)$ is the power spectrum of the smoothed density field. From Eq. 1.52 we also see that $\sigma(R, a) = \sigma(R, a = 1)\,D(a)/D(a = 1)$. It is when $\sigma(R, a) \sim 1$ that the amplitude of fluctuations approaches unity and the linear approximation is not valid anymore. This quantity today is usually evaluated considering $R = 8\,h^{-1}\,\mathrm{Mpc}$, as $\sigma_8 \equiv \sigma(R = 8\,h^{-1}\,\mathrm{Mpc}, a = 1) \approx 1$ for galaxies.

Primordial density fluctuations and transfer function

Although the origin of cosmological perturbations is still an open question, many inflationary models predict primordial density fluctuations generated by Gaussian microscopic quantum fluctuations in a scalar field that were converted during inflation into macroscopic seeds for structure formation. These models provide a power law primordial power spectrum such as:

$$P_{\mathrm{prim}}(k) = A_s \left(\frac{k}{k_0}\right)^{n_s} \,, \tag{1.51}$$

where A_s and n_s are the amplitude and the spectral index, respectively, and k_0 is a pivot scale. A value of $n_s = 1$ would correspond to an scale-invariant "flat" power spectrum, meanwhile $n_s = 0$ would imply a "white-noise" power spectrum, that is, with no correlations at all. Observations of the CMB seem to indicate a value of n_s very close to 1.

After the end of inflation, the primordial power spectrum of matter grows according to:

$$P_{\mathrm{m}}(k, a) = P_{\mathrm{prim}}(k) \left(\frac{D(a)}{D(a_0)}\right)^2 T^2(k) \,, \tag{1.52}$$
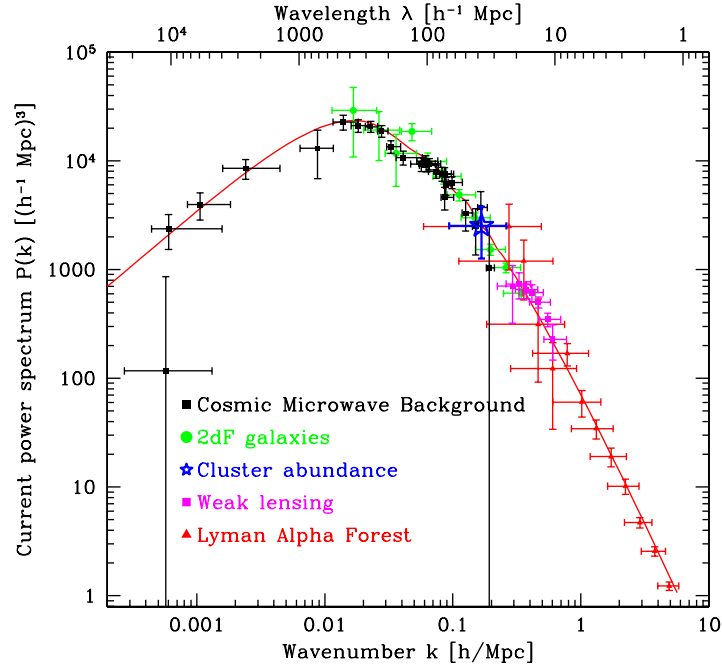
Figure 1.7: *Measurements of the matter power spectrum $P(k)$ obtained considering data from the cosmic microwave background, weak lensing, cluster abundances, Lyman α forest and galaxy clustering. The red solid line represents the prediction from the concordance ΛCDM cosmological model. Figure is from Tegmark and Zaldarriaga [235].*

where $T(k)$ is the *transfer function*, and $D(a)$ is the density perturbation linear growth function (Eq. 1.44). The transfer function $T(k)$ describes the evolution of perturbations before recombination at $z \sim 1100$, that is, through the epochs of horizon crossing and the radiation to matter transition epoch, and does only depend on the value of the wavenumber. The calculation of $T(k)$ is complicated and is usually performed solving the equations numerically with codes such as CAMB [125]. It needs to trace the evolution of the density fluctuations of baryons, photons, dark matter and neutrinos, as well as the evolution of gravitational potentials and other metric perturbations. Of course, it has to take into account the different interactions between these species, as well as the effects of the free streaming of neutrinos, photons and collisionless hot dark matter (if present), which may damp perturbations at different scales. All these processes change the initial shape of the primordial power spectrum and the one that we measure today is related to it through the transfer function via $P(k) = P_{\text{prim}}(k)\,T^2(k)$. The transfer function is uniquely determined by the abundances of the different elements in the Universe. For example, a universe with hot dark matter (HDM) would erase structures on the small scales due to the free streaming of the particles that compose the dark matter, so in this "top-down" scenario clusters would form first and then fragment into galaxies. Meanwhile, in the cold dark matter (CDM) case, small structures would form first and then collapse to form larger ones in this "bottom-up" model.

The power spectrum as is seen today is shown in Fig. 1.7. As we can see, the ΛCDM power spectrum behaves as $P(k) \sim k^1$ for small k, and as $P(k) \sim k^{-3}$ for large k. Even though how $T(k)$ is obtained is rather difficult to understand, this behaviour can be easily explained remembering

that the spectral index of primordial scalar perturbations n_s is close to unity.

After inflation, there are fluctuations which have superhorizon scales with wavenumbers $k < k_h$ and are causally disconnected, and fluctuations with subhorizon scales with $k > k_h$, where k_h is the associated wavenumber of the causal horizon and evolves as $k_h \propto t^{-1}$ (the radius of the horizon grows as $d_h \propto c\,t$). At some point, all superhorizon fluctuations will pass through the horizon and become subhorizon. The difference lies in whether this happens in the radiation or the matter era. Superhorizon fluctuations grow as t in the radiation domination era, and as $t^{2/3}$ in a matter dominated universe. Subhorizon modes, however, remain constant ("frozen") in the radiation era because of the large radiative pressure, and then grow as $t^{2/3}$ after matter–radiation equality. If a fluctuation enters the horizon in the matter era, it means that it has been growing as t in the radiation era and then it has continued to grow as $t^{2/3}$. This means that modes with small wavelengths that entered the horizon in the radiation domination era will have their growth suppressed with respect to larger modes that entered the horizon later during matter domination by a factor $\delta_{\mathrm{subh}}/\delta_{\mathrm{superh}} = (a_{\mathrm{enter}}/a_{\mathrm{eq}})^2$. This can be expressed in the transfer function as:

$$k \ll k_h \Rightarrow T(k) \sim 1\,, \tag{1.53}$$

$$k \gg k_h \Rightarrow T(k) \sim \left(\frac{k}{k_h}\right)^{-2}\,, \tag{1.54}$$

where k_{eq} is the comoving wavenumber of the horizon in the matter–radiation equality epoch. As we saw before, the primordial power spectrum after inflation can be described by a power law $P_{\mathrm{prim}} \propto k^{n_s}$, meaning that the evolved or "processed" power spectrum $P(k) \propto P_{\mathrm{prim}}\,T(k)^2$ goes as $P(k) \propto k^{n_s}$ for modes with $k < k_{eq}$, and $P(k) \propto k^{n_s-4}$ for modes with $k > k_{eq}$. The scale k_{eq} coincides with the maximum of the power spectrum as that is the comoving scale that entered the horizon in the matter–radiation equality, and corresponds to $k_{eq}^{-1} \simeq 16(\Omega_m\,h^{-1})\,h^{-1}\,\mathrm{Mpc}$.

1.2.3 Non-linear evolution

All the previous considerations regarding the evolution of density perturbations work well at high redshifts and large scales, and reproduce with good accuracy the CMB power spectrum. However, at late times and on small scales when $\delta \geq 1$, the linear theory breaks down, fluctuations on different scales do not evolve independently anymore, and non-linearities need to be accounted for.

In the quasi-linear regime, approximately from 50 to 10 Mpc, $\delta < 1$ holds, but modes with different wavelengths start to couple and working in Fourier space becomes difficult. Higher-order perturbative theories try to describe the growth of structures beyond the linear regime, and analytical models like spherical or ellipsoidal collapse offer some insights into the formation of haloes and on the timing of collapse.

Numerical simulations

On scales smaller than 10 Mpc growth is completely non-linear and it is mandatory to use numerical N-body cosmological simulations to trace the formation and resolve the structure of dark matter haloes at these scales. In Fig. 1.8 the formation of a dark matter halo in the Millennium-II Simulation [37] is shown at different redshifts and different scales, showing the complexity of the collapsed structure and the strong non-linearity.
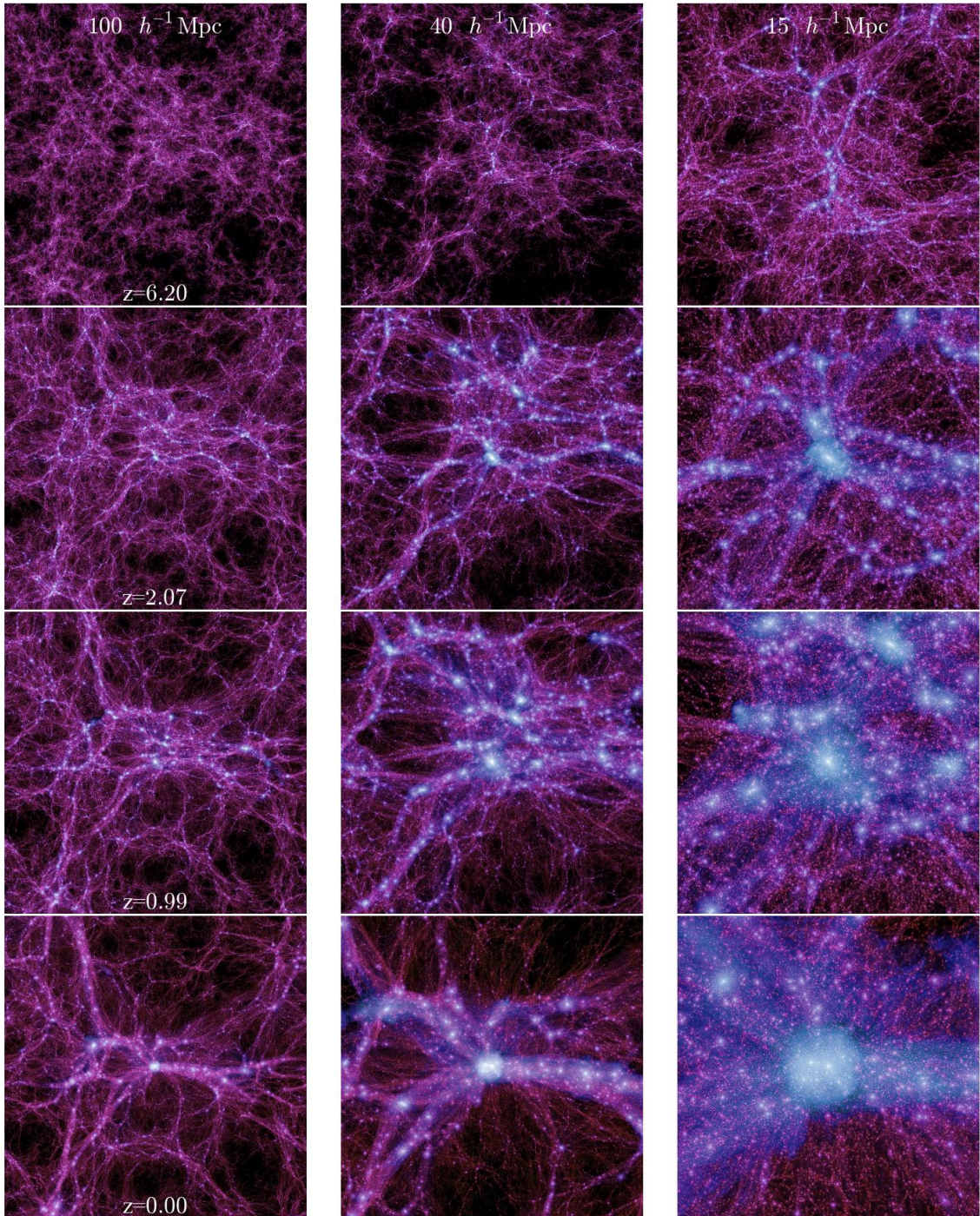
Figure 1.8: *2D slices at different redshifts (from top to bottom: $z = 6.20, 2.07, 0.99, 0.00$) and different comoving scales (from left to right: 100, 40 and 15 $h^{-1}\,\mathrm{Mpc}$) of one of the haloes formed in the Millennium-II Simulation [37]. As can be seen, real collapse is far from being spherical, and N-body simulations are needed to describe complex phenomena like accretion of mass along filaments and the presence of smaller collapsed haloes within larger collapsing structures. Figure is from Boylan-Kolchin et al. [37].*

Also, in this non-linear regime baryonic physics becomes important as hydrodynamical effects like shocks, radiative cooling of gas, active galactic nuclei (AGN) feedback, star formation and other astrophysical processes alter the formation of some structures and the distribution of galaxies may not trace that of dark matter. Thus, to understand how galaxies and clusters are formed within dark matter haloes, the more complicated to perform hydrodynamical simulations are needed too.

The Zel'dovich approximation

One of the approaches to model non-linearities analytically is the Zel'dovich approximation [268], and although it is not able to describe small scale non-linearities with the precision of numerical simulations, it still provides a good approximation of the power spectrum at large scales, and can be used to revert non-linear growth and "reconstruct" evolved density fields. It is also used to prepare the quasi-linear conditions from which numerical simulations are started.

In this model, the density field is described through a kinematical approach where each fluid element is located at an early (Lagrangian) position $\vec{q}$, equivalent to its comoving position at $t_0 = 0$, and then displaced to its (Eulerian) position $\vec{x}$ at time t, such that:

$$\vec{x}(t) = \vec{q} + \Psi(\vec{q}, t) \,, \tag{1.55}$$

where Ψ is the displacement vector field which is evaluated at time t considering the initial position of the fluid element, and can be decomposed as:

$$\Psi(\vec{q}, t) = D_+(t) \, \Psi^0(\vec{q}) \,, \tag{1.56}$$

where $D_+(t)$ is the growing mode specified by the cosmological parameters, and $\Psi^0(\vec{q})$ is the time-independent displacement field. This implies that particles are assumed to keep moving in the initial direction they started moving when they were at $\vec{q}$. The Zel'dovich approximation assumes that this irrotational initial displacement field emerges from a potential which is proportional to the primordial potential field $\Phi(\vec{q})$ through:

$$\Psi^0(\vec{q}) = -\nabla_{\vec{q}} \Phi(\vec{q}) \,, \tag{1.57}$$

and that the deformation of each fluid element induced by this displacement is given by the deformation tensor:

$$\Psi^0_{i,j} \equiv \frac{\partial \Psi^0_i}{\partial q_j} \,. \tag{1.58}$$

From mass conservation we have that $\rho(\vec{x}, t) \, \mathrm{d}\vec{x} = \rho_0 \, \mathrm{d}\vec{q}$, so the density field as a function of the Lagrangian coordinate $\vec{q}$ is related through the Jacobian:

$$\rho(\vec{q}, t) = \rho_0 \left| \frac{\partial \vec{x}}{\partial \vec{q}} \right| \,. \tag{1.59}$$

If a basis for $\vec{q}$ is chosen such that the deformation tensor $\Psi^0_{i,j}$ is diagonal, then:

$$\rho(\vec{q}, t) = \frac{\rho_0}{\left[1 - D_+(t)\Psi^0_{1,1} \right] \left[1 - D_+(t)\Psi^0_{2,2} \right] \left[1 - D_+(t)\Psi^0_{3,3} \right]} \,. \tag{1.60}$$

When any of the eigenvalues of the deformation tensor reaches $\Psi^0_{i,i} = D_+^{-1}(t)$ the first singularity

in Eq. 1.60 appears and the structure collapses along one of the principal axes (the one with the largest eigenvalue), forming a sheet-like structure. Other structures like filaments form when the collapse occurs along two of these axis at the same time.

In Lagrangian perturbation theory one can find a perturbative expression for the displacement field, where the first order solution corresponds to the Zel'dovich approximation. However, the Zel'dovich approximation may be further improved in the future.

1.2.4 The two-point correlation function

The meaning of the two-point correlation function can be understood as follows. If the distribution of galaxies around a target galaxy is given by a Poisson random distribution, then the probability of finding another galaxy around this target galaxy at any distance is going to be given simply by $\Delta P = n \, \Delta V$, where n is the mean number density of galaxies. If the galaxies are not randomly distributed but are clustered instead, then the probability of finding another galaxy at a radial distance r will be given by:

$$\Delta P = n \left[1 + \xi(r) \right] \Delta V \,, \tag{1.61}$$

where $\xi(r)$ is the two-point correlation function (Eq. 1.48). This means that the two-point correlation function can be simply estimated counting the number of galaxy pairs that are found at a certain distance r in the galaxy sample considered, and then comparing those counts with those expected from a random Poisson distribution. If on average there are more galaxies at a distance r than expected from a random distribution, then $\xi(r) > 0$. If there are less, then $-1 < \xi(r) < 0$ and the sample is anticorrelated at that distance. Of course, a random sample would yield $\xi(r) = 0$, and any sample should converge to $\xi(r \to \infty) = 0$.

If the correlation function is being measured using a sample of galaxies constructed from a survey, one has to take into account that galaxies near the edges of the survey volume have fewer objects around them than they should. The expected random counts cannot be modelled analytically but need to be measured instead from a random mock catalogue that follows the same geometry and redshift distribution of the data sample, or else the estimation of the correlation function will be biased. Thus, an approach one could consider would be that by Peebles [168], where one computes ΔP counting the number of pairs of galaxies found at a distance r and within a shell of width Δr, and then divides by the total number of pairs at any distance. Then, $n \, \Delta V$, the probability of having another object at a certain distance considering an stochastic distribution with mean density n, is computed in the same way but from a random sample. Considering Eq. 1.61, the correlation function can be estimated as the ratio:

$$\xi(r) = \frac{dd(r)}{rr(r)} - 1 \,, \tag{1.62}$$

where:

$$dd(r) = \frac{DD(r)}{N_d \left(N_d - 1 \right)/2} \,, \tag{1.63}$$

and:

$$rr(r) = \frac{RR(r)}{N_r \left(N_r - 1 \right)/2} \,, \tag{1.64}$$

are the normalized data-data and random-random pair counts at a comoving distance r, with DD and RR the total counts, and N_d and N_r the number of data and random objects considered,

respectively. The random sample does not need to have the same number of objects. In fact, in order to reduce the variance in the RR counts at a given distance r, the random catalogue should be much larger than the real one.

There are more sophisticated ways to compute the two-point correlation function that are claimed to have better statistical properties and to be free from the bias induced by the survey geometry, like the Landy-Szalay estimator [121]:

$$\xi(r) = \frac{dd(r) - 2dr(r) + rr(r)}{rr(r)}, \tag{1.65}$$

or the Hamilton estimator [87]:

$$\xi(r) = \frac{dd(r) \times rr(r)}{dr^2(r)} - 1, \tag{1.66}$$

where dr is the normalized number of data-random pair counts DR at a distance r:

$$dr(r) = \frac{DR(r)}{N_d\, N_r}, \tag{1.67}$$

which is computed cross correlating the real and the random mock catalogues. The Landy-Szalay estimator has been shown to have no bias and minimum variance, and is the most widely used.

For galaxies and within a distance of $10\,h^{-1}\,\mathrm{Mpc}$, the two-point correlation function seems to be very well described by a power law:

$$\xi(r) = \left(\frac{r}{r_0}\right)^\gamma, \tag{1.68}$$

where r_0 is the *correlation length* and γ is found to be around $\gamma \sim 1.8$.

1.2.5 Halo bias

In a ΛCDM universe where almost all the gravitating matter is invisible to us, the correlation function measured with luminous galaxies may not necessarily correspond to the correlation function of matter. In fact, it is now well known that some kind of galaxies have different clustering properties than others. This is where we introduce the concept of the *halo bias function* b, which relates the two-point correlation function measured considering one or two kind of objects, $\xi_{o_1 o_2}$, with the underlying matter distribution, ξ_m, such that:

$$\xi_{o_1 o_2}(r) = b_1\, b_2\, \xi_m(r), \tag{1.69}$$

where b_1 and b_2 are the bias values that correspond to the objects considered. One could for example measure the correlation function between luminous red galaxies (LRG) and relate it with the correlation function of matter through $\xi_{\mathrm{LRG}} = b_{\mathrm{LRG}}^2\, \xi_m$, or measure the cluster–galaxy cross-correlation function, with $\xi_{cg} = b_c\, b_g\, \xi_m$, considering the different values of the bias for clusters and galaxies, b_c and b_g. Equivalently, the matter power spectrum is related to the power spectrum for one or two different kind of objects through:

$$P_{o_1 o_2}(k) = b_1\, b_2\, P_m(k). \tag{1.70}$$
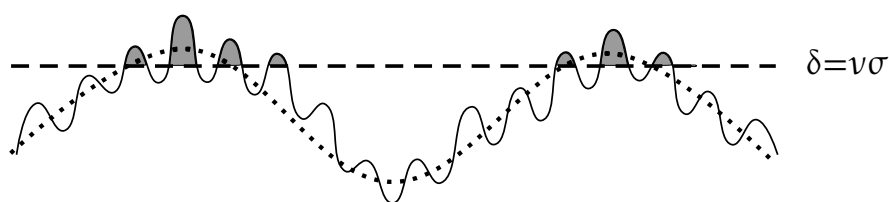
$$\delta = \nu\sigma$$

Figure 1.9: *In this figure the matter density field (solid line) is given by the combination of a long (dotted line) and shorter wavelengths modes. Only those local overdensities above the threshold limit of $\nu\sigma$ (dashed line) will form clusters (grey shaded regions), which will be much more clustered than the underlying matter distribution and hence will provide a biased estimation of the matter correlation function.*

A simple way to understand the bias for galaxies is to take into account that because baryons must cool enough as to form stars and galaxies, they must first radiate through thermal Bremsstrahlung or line emission. This is more efficiently done in deep potential wells, like those formed by very massive collapsed dark matter haloes. Thus, galaxies would only form in regions where the density is above a certain threshold and such haloes can form. At the same time, active galactic nuclei (AGN) feedback could suppress star formation in lower mass haloes, biasing even more the distribution of galaxies with respect to matter.

On larger scales, if both galaxies and clusters emerged due to amplification of primordial density fluctuations, both of them should trace the clustering of matter in the same way, which is not the case. One of the proofs of the existence of the bias was the realization that the cluster-cluster correlation function was several times larger than the galaxy-galaxy correlation function.

The statistics of rare peaks in Gaussian random fields developed by Kaiser [102] explained this discrepancy. It was the rarity of clusters, several orders of magnitude less abundant than galaxies, what explained it, as they could only form at the highest peaks of the dark matter density field. This can be schematically be seen in Fig.1.9. Long wavelength modes enhance in localised overdense regions the presence of these objects with respect to the mean, and thus their clustering. That is, rare high-σ peaks of the density field tend to occur near other high-σ peaks.

In the context of a Gaussian density perturbation field, the value of the bias function $b(M, a)$ is independent of k, but depends on both the epoch of the Universe and on the mass of the dark matter halo where the astrophysical object lives, as it is the coefficient between the overdensity of haloes of certain mass and the overdensity of matter in a certain region. In the Press-Schechter formalism of spherical collapse [183], density fluctuations collapse when $\delta > \delta_c$, where $\delta_c = 1.68$ is the critical value above which collapse happens. The overdensity of haloes δ_h is related to the overdensity of mass δ_m through:

$$\delta_h = \left(1 + \frac{\nu^2 - 1}{\delta_c}\right)\delta_m \,, \tag{1.71}$$

where $\nu = \delta_c/\sigma(M)$ is the normalized peak height, and $\sigma(M)$ is the rms variance of matter fluctuations on a scale M. $\sigma(M)$ is related to the more familiar $\sigma(R)$ (Eq. 1.50) considering that M is the matter contained in an sphere of radius R in a background with average matter density ρ. From Eq. 1.71 we can see that the bias is equal to:

$$b = 1 + \frac{\nu^2 - 1}{\delta_c} \,. \tag{1.72}$$

It can be seen that the value of the bias increases with mass, so massive haloes are predicted to cluster more strongly than the underlying mass density field, with:

$$\xi_h = b^2(M_h, z)\, \xi_m \,, \tag{1.73}$$

where M_h is the mass of the halo with which the two-point correlation function is being evaluated. Equivalently, low mass haloes may be antibiased, with $b < 1$.

The spherical collapse model is just the simplest way to understand the nature of the statistical bias, but the dependence of its value with halo mass depends explicitly on the functional form of the mass function, that is, the density distribution of haloes in the Universe as a function of their mass.

1.2.6 Redshift-space correlation function and distortions

In practice, radial distances to distant objects are estimated from their redshifts, an approach that does not necessarily always provide the real value. Because the Universe is expanding and galaxies are receding from us due to the Hubble flow, the light that we receive from them is redshifted, and this redshift can then be associated to a distance through the Hubble law. However, these galaxies might be also moving with a local *peculiar velocity* not related to the expansion of the Universe, but to random motions or to local displacements induced by local gravitational instabilities. This introduces redshift-space distortions (RSD) in the inferred positions of the galaxies due to the Doppler effect, as the observed redshift is now equal to:

$$z_{\mathrm{obs}} = z_{\mathrm{H}} + \frac{v_{los}}{c}\left(1 + z_{\mathrm{H}}\right) \,, \tag{1.74}$$

where z_{H} is the cosmological redshift associated to Hubble's law, and v_{los} is the line-of-sight (los) component of the peculiar velocity.

There are two well known observational signatures of RSD imprinted in the derived distribution of galaxies, and hence in the correlation function. If the peculiar velocities of galaxies have their origin in the large random motions of virialized objects inside a dark matter halo, then at small scales ($\lesssim 1\,\mathrm{Mpc}$) an apparent stretching of galaxies along the line-of-sight is seen, pointing to the observer. This effect, known as *fingers of God*, is enhanced specially for galaxies that form part of groups and clusters, and can be used to estimate the velocity dispersion within such virialized systems. If, on the contrary, the motion comes from the coherent infall of galaxies originated by gravitational collapse, then the redshift-space correlation function is instead contracted with respect to the real-space correlation function in what is known as the *flattening effect*. These two effects can be schematically seen in Fig. 1.10.

The flattening effect is also known as *Kaiser effect*, as the first profound analysis of the subject was performed by him [104]. Although this distortion may seem like an inconvenience to measure the real-space correlation function, it provides invaluable information on the dynamics of gravitational collapse, and can hence be used to constrain cosmological parameters and gravitational models. If a galaxy is located at a comoving position $\vec{r}$, then its redshift-space position $\vec{s}$ will be given by:

$$\vec{s} = \vec{r} + \frac{\vec{v} \cdot \vec{r}}{|\vec{r}|} \,, \tag{1.75}$$

where the comoving quantity $\vec{v}$ is related to the physical peculiar velocity $\vec{u}$ of the galaxy through
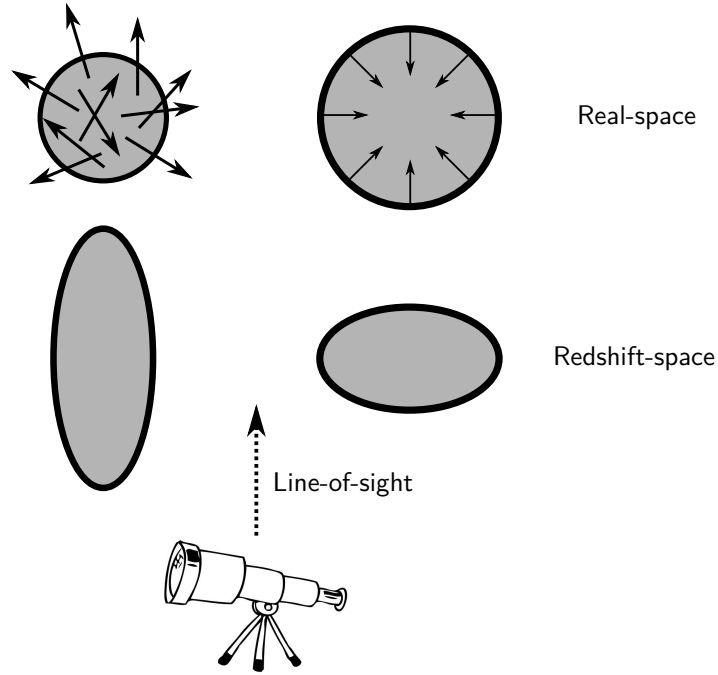
Figure 1.10: *Scheme showing the different redshift-space distortions produced by peculiar velocities of galaxies. Left: at small scales, large random motions of galaxies within groups or clusters result in the apparent smearing of their position along the line-of-sight, generating the structures known as fingers of God. Right: on larger scales, coherent infall velocities of galaxies due to clustering cause the apparent flattening of structures along the line-of-sight.*

$\vec{v} \equiv \vec{u}/(a\,H)$. Kaiser pointed out that in Fourier space and in the linear approximation, each overdensity mode in real-space δ^r can be related to its counterpart in redshift-space δ^s with:

$$\delta^s(\vec{k}) = \left(1 + \beta\,\mu^2\right)\delta^r(\vec{k})\,,\tag{1.76}$$

where μ is the cosine of the angle between $\vec{k}$ and the line-of-sight, and β is the quantity that solves the continuity equation:

$$\vec{\nabla} \cdot \vec{v} + \beta\,\delta = 0\,,\tag{1.77}$$

and thus proportional to the velocity of growth of structures. Considering galaxies a biased estimator of the underlying mass distribution such that $\delta_g = b\,\delta_m$, with b the bias, and considering also Eqs. 1.39 and 1.44 from the linear theory of growth of perturbations, we can see that:

$$\beta = \frac{f(a)}{b} \equiv \frac{1}{b}\frac{\mathrm{d}\ln D(a)}{\mathrm{d}\ln a}\,,\tag{1.78}$$

where f is defined as the *growth rate*, and can be written as:

$$f(a) \simeq \Omega_m(a)^\gamma\,,\tag{1.79}$$

where γ is the *growth index*. For a cosmology where General Relativity is the gravitational theory and there is a dark energy with an equation of state $\omega \simeq -1$, it takes the value of $\gamma \approx 0.545$. As γ depends on the gravitational theory considered, the estimation of $f(a)$ is a powerful tool to test and constrain modified theories of gravity.

Multipolar expansion of the two-point correlation function

From Eq. 1.76, it follows that if $P_m^r(k)$ is the real-space matter power spectrum, the observed redshift-space galaxy power spectrum can be modelled as:

$$P_g^s(k, \mu) = b^2 \left(1 + \beta \, \mu^2\right)^2 P_m^r(k) \,. \tag{1.80}$$

This result was translated by Hamilton [86] in terms of the redshift-space correlation function as:

$$\xi(s, \mu) = \xi_0(s) L_0(\mu) + \xi_2(s) L_2(\mu) + \xi_4(s) L_4(\mu) \,, \tag{1.81}$$

where ξ_0, ξ_2 and ξ_4 are the monopole, the quadrupole, and the octopole of the correlation function. The $L_\ell(\mu)$ are the ℓth Legendre polynomials, with $L_0(\mu) = 1$, $L_2(\mu) = (3\mu^2 - 1)/2$ and $L_4(\mu) = (35\mu^4 - 30\mu^2 + 3)/8$. The monopole includes the correlation information of pure radial redshift-space distances between pairs, and does not consider the angle of the pair with the line-of-sight. The quadrupole, however, takes into account the information of the distribution of pairs along the different observation directions. The octopole is very complicated to measure in practice, and is not usually included in analyses.

The monopole and the quadrupole of the polynomial expansion can be given in terms of the real-space correlation function as:

$$\xi_0(s) = \left(1 + \frac{2\beta}{3} + \frac{\beta^2}{5}\right) \xi(r) \,, \tag{1.82}$$

$$\xi_2(s) = \left(\frac{4\beta}{3} + \frac{4\beta^2}{7}\right) \left[\xi(r) - \overline{\xi}(r)\right] \,, \tag{1.83}$$

with:

$$\overline{\xi}(r) = \frac{3}{r^3} \int_0^r \xi(r') \, r'^2 \, \mathrm{d}r' \,. \tag{1.84}$$

The quadrupole-to-monopole ratio, or normalized quadrupole, is defined as:

$$Q(s) = \frac{\xi_2(s)}{\xi_0(s) - (3/s^2) \int_0^s \xi_0(s') \, s'^2 \, \mathrm{d}s'} \,. \tag{1.85}$$

At small scales its value depends strongly on the random motion of virialized galaxies, but in the Kaiser approximation and at large scales it is directly related to β by:

$$Q = \frac{(4/3)\beta + (4/7)\beta^2}{1 + (2/3)\beta + (1/5)\beta^2} \,. \tag{1.86}$$

In order to extract information from these RSD and obtain an estimation of the amplitudes of the multipoles of the correlation function, what one does is to measure the correlation function in two dimensions decomposing the redshift-space separation $\vec{s}$ into its parallel and perpendicular components, such that:

$$s_{los} = \frac{\vec{s} \cdot \vec{l}}{|\vec{l}|} \,, \tag{1.87}$$

$$s_\perp = \sqrt{\vec{s}\cdot\vec{s} - s_{los}^2}\,, \tag{1.88}$$

where, if $\vec{s}_1$ and $\vec{s}_2$ are the redshift-space positions of the two galaxies considered, then $\vec{s} = \vec{s}_1 - \vec{s}_2$ is the redshift-space separation vector of the pair, and $\vec{l} = (\vec{s}_1 + \vec{s}_2)/2$ is the observer's line-of-sight. Considering the Landy-Szalay estimator (Eq. 1.65), the 2-dimensional correlation function can be computed as:

$$\xi(s_{los}, s_\perp) = \frac{dd(s_{los}, s_\perp) - 2dr(s_{los}, s_\perp) + rr(s_{los}, s_\perp)}{rr(s_{los}, s_\perp)}\,, \tag{1.89}$$

where dd, dr and rr are now the normalized number of pairs found in the data-data, data-random and random-random samples considered. The different multipoles of $\xi(s)$ are obtained from:

$$\xi_\ell(s) = \left(\frac{2\ell + 1}{2}\right) \int_{-1}^{+1} \xi(s_{los}, s_\perp)\, L_\ell(\mu)\, \mathrm{d}\mu\,, \tag{1.90}$$

where $L_\ell(\mu)$ is the ℓth Legendre polynomial, and here $\mu = s_{los}/s$ is the cosine of the angle to the line-of-sight.

Finally, in order to include the non-linear RSD effects introduced by the random peculiar motions of galaxies, the final redshift-space correlation function can be described like a convolution of the linear redshift-space correlation function $\xi(s_{los}, s_\perp)$ with a function $f(u)$ providing the distribution of random velocities u between pairs, such that:

$$\xi(s_{los}, s_\perp) = \int_{-\infty}^{+\infty} \xi(s_{los} - u/(a\,H), s_\perp)\, f(u)\, \mathrm{d}u\,. \tag{1.91}$$

The usually adopted velocity distribution is:

$$f(u) = \frac{1}{\sqrt{2}\,\sigma_u} \exp\left[-\frac{\sqrt{2}\,|u|}{\sigma_u}\right]\,, \tag{1.92}$$

where σ_u is the scale-independent pairwise velocity dispersion. In this case, $f(u)$ is a functional form that is found to describe the data accurately, but other distributions like a Gaussian or a combination of Gaussians could be considered.

Projected two-point correlation function

Because RSD only affect the line-of-sight component of the 2-dimensional correlation function, one can recover the projected real-space correlation function $\Xi(r_\perp)$ integrating $\xi(s_{los}, s_\perp)$ along the line of sight:

$$\Xi(r_\perp) = 2 \int_0^\infty \xi(s_{los}, s_\perp)\, \mathrm{d}s_{los}\,. \tag{1.93}$$

Assuming a power law form for the real-space correlation function (Eq. 1.68), one can model analytically the expected values of $\Xi(r_\perp)$ projecting the real-space correlation function:

$$\Xi(r_\perp) = 2 \int_{r_\perp}^\infty \xi(r) \left(r^2 - r_\perp^2\right)^{-1/2} dr = \sqrt{\pi}\, \frac{\Gamma\left((\gamma - 1)/2\right)}{\Gamma\left(\gamma/2\right)}\, r_0^\gamma\, r_\perp^{1-\gamma}\,, \tag{1.94}$$

where r_0 and γ are the correlation length and the slope of the power law, and $\Gamma(x)$ is the usual gamma function.

1.2.7 The mass function and cluster abundances

Large astrophysical objects like galaxies and clusters of galaxies tend to emerge in dark matter haloes, that at the same time form in the local maxima of the smoothed matter density field.

As we saw in Sect. 1.2.5, in the Press-Schechter spherical collapse model, density perturbations collapse after the critical threshold of $\delta_c = 1.68$ is reached. In this scenario and assuming Gaussian random perturbations, the probability for the smoothed density perturbation field to exceed δ_c at a given z and form a halo is given by:

$$P_h(M,z) = \frac{1}{\sqrt{2\pi\sigma^2(M,z)}} \int_{\delta_c}^{\infty} \exp\left[-\frac{\delta^2}{2\sigma^2(M,z)}\right] \mathrm{d}\delta = \frac{1}{2}\mathrm{erfc}\left[\frac{\delta_c}{\sqrt{2\sigma^2(M,z)}}\right], \qquad (1.95)$$

where erfc is the complementary error function, and $\sigma(M,z)$ is the rms variance of matter fluctuations on a scale M. This expression provides the fraction of volume that is converted in objects of mass above M, and differentiating it we can find the same fraction but for objects with masses in the $[M, M + \mathrm{d}M]$ mass range:

$$\mathrm{d}P_h(M,z) = \left(\frac{\partial P_h(M,z)}{\partial M}\right)\mathrm{d}M. \qquad (1.96)$$

Finally, dividing this expression by the volume that each of these objects occupies ($V(M) = M/\rho_m$, with ρ_m the mean matter density), we can obtain the *mass function* $n(M,z)$, which gives the number density of collapsed haloes found at redshift z and with masses in the range $[M, M+\mathrm{d}M]$. It is expressed in terms of the comoving number density of collapsed objects per unit mass $\mathrm{d}M$, and its functional form can be expressed analytically as:

$$\frac{\mathrm{d}n(M,z)}{\mathrm{d}M} = \frac{1}{V(M)}\frac{\mathrm{d}P_h(M,z)}{\mathrm{d}M} = f(\sigma(M,z))\frac{\rho_m}{M}\frac{\mathrm{d}\ln\sigma(M,z)^{-1}}{\mathrm{d}M}, \qquad (1.97)$$

where $f(\sigma)$ is a model-dependent function that corresponds to the fraction of mass in collapsed objects. In this case, it is equal to:

$$f(\sigma(M,z)) = \frac{1}{\sqrt{2\pi\sigma^2(M,z)}}\exp\left[-\frac{\delta_c^2}{2\sigma^2(M,z)}\right]. \qquad (1.98)$$

Because σ evolves like $\sigma(a) = D(a)\sigma_0$, different epochs will have different spectra of halo masses.

Although the spherical collapse approach can be improved considering ellipsoidal collapse, the most common way nowadays to obtain an expression for the mass function is to measure it directly from numerical simulations. Using several N-body codes and simulations with different ΛCDM cosmological parameters, Tinker et al. [237] calibrated with good results the functional form of the mass function:

$$f(\sigma(M,z)) = A\left[\left(\frac{\sigma(M,z)}{b}\right)^{-a} + 1\right]\exp\left[-\frac{c}{\sigma^2(M,z)}\right], \qquad (1.99)$$

where A sets the amplitude of the mass function, a and b are the slope and the amplitude of the low mass power law, and c controls the shape of the exponential decrease in the high mass end. The parameters A, a, and b include an small dependence with redshift if the precision of the fit wants to be preserved.

Once the mass function is defined, the total number of haloes in the $[M_{\mathrm{min}}, M_{\mathrm{max}}]$ mass range and the $[z_{\mathrm{min}}, z_{\mathrm{max}}]$ redshift region is expected to be:

$$N_h = f_{\mathrm{sky}} \int_{z_{\mathrm{min}}}^{z_{\mathrm{max}}} \frac{\mathrm{d}V}{\mathrm{d}z}\, \mathrm{d}z \int_{M_{\mathrm{min}}}^{M_{\mathrm{max}}} \frac{\mathrm{d}n(M, z)}{\mathrm{d}M}\, \mathrm{d}M \ , \tag{1.100}$$

where f_{sky} is the fraction of the sky considered, and $\mathrm{d}V/\mathrm{d}z$ is the comoving volume element per unit redshift.

Because the variance of matter fluctuations decreases with increasing smoothing scale, that is, higher M correspond to lower σ and thus larger peak heights $\nu = \delta_c/\sigma$, the mass function decreases with increasing masses, and massive haloes are supposed to be less abundant than low mass haloes. Clusters, the most massive gravitationally bound structures in the Universe, form in the densest regions of the dark matter field, usually where two or more filaments intersect, and measuring their abundance as a function of mass and redshift is one of the most straightforward ways to constrain cosmological parameters. This *cluster counts* technique is particularly useful to evaluate Ω_m and σ_8, as the massive end of the mass function where clusters form is exponentially sensitive to the value of σ, which depends on the scale $R \propto [M/(\Omega_m\, \rho_c)]^{1/3}$ that is containing the mass M. The degeneracy between Ω_m and σ_8 can be broken if cluster counts are combined with measurements of the growth rate, that depends primarily on Ω_m.

2

Clusters of Galaxies

Before being able to use clusters of galaxies to constrain cosmological models and gravitational theories, one needs to build a sample of them and understand their physics. Clusters, which are usually defined as the "most massive gravitationally bound structures in the Universe", have a rich phenomenology that permits their extreme physical conditions to be examined in many independent ways. In this Chapter we describe some of these physical effects, which we measure and characterise in the following Chapters. These include the gravitational redshift effect predicted by General Relativity, the redshift enhancement of background galaxies produced by gravitational lensing, and the distortion of the CMB induced by the Sunyaev-Zel'dovich effect.

In practice, the cluster mass range considered in surveys is about one order of magnitude in mass, and needs to be estimated through weak lensing analysis, or traced from indirect *mass proxies*, like the number of galaxies contained in them, or the amplitude of the Sunyaev-Zel'dovich distortion of the CMB. In this Chapter we also describe how to relate masses to these two observables, as one of the purposes of the following Chapters is to constrain these relations.

Before continuing, we briefly describe the halo density profile that we assume, namely the NFW profile, and the concept of the luminosity function, both needed in order to model the observational signatures of the gravitational redshift and the redshift enhancement effects.

2.1 NFW density profile

Dark matter haloes represent the building blocks of the large scale structure of the Universe. Although they have complicated structures, cluster size systems with masses above $10^{14}\,M_\odot$ are found to be dominated by large massive haloes generally in equilibrium [74]. In 1997, Navarro, Frenk & White [152] showed that the cold dark matter haloes generated in a suite of N-body simulations with different cosmological parameters followed an average "universal" density profile which is now called the "NFW profile", and has been found to describe the shape of real dark matter haloes with great precision, regardless of their dynamical state, shape or mass. It is given by:

$$\rho_{\mathsf{NFW}}(r) = \rho_c \, \frac{\delta_s}{(r/r_s)(1 + r/r_s)^2} \, , \tag{2.1}$$

where the mass scale parameter, δ_s, and the scale radius, r_s, are related and depend on the halo mass. The scale radius r_s specifies the behaviour of the slope of the density profile, with $\rho \propto 1/r$ for $r \ll r_s$, $\rho \propto 1/r^2$ when $r \sim r_s$, and $\rho \propto 1/r^3$ for $r \gg r_s$.

However, the quantity that completely determines the shape of the halo is the *concentration parameter*. It is defined as:

$$c_\Delta = \frac{r_\Delta}{r_s} , \qquad (2.2)$$

where r_Δ corresponds to the radial distance from the center of the halo within which the mean density is $\Delta_{c/m}$ times the critical/mean density of the Universe, $\rho_{c/m}$. According to this, the mass enclosed in an sphere of radius r_Δ is equal to:

$$M_\Delta = \int_0^{r_\Delta} \rho_{\mathrm{NFW}}(r) \, r^2 \, \mathrm{d}r = 4\pi \rho_c \, \delta_s \, r_\Delta^3 \, f(r_s/r_\Delta) , \qquad (2.3)$$

where:

$$f(x) = x^3 \left[\ln(1 + 1/x) - (1+x)^{-1} \right] . \qquad (2.4)$$

Taking into account that from the definition of r_Δ the mass of the halo must be equal to:

$$M_\Delta = \frac{4\pi}{3} \, \Delta \, \rho_c \, r_\Delta^3 , \qquad (2.5)$$

the masses provided by different choices of Δ can be related solving for the characteristic scale δ_s, and taking into account Eqs. 2.2, 2.3, and 2.5:

$$\frac{M_{\Delta_X}}{M_{\Delta_Y}} = \frac{r_{\Delta_X}^3}{r_{\Delta_Y}^3} \frac{f(1/c_{\Delta_X})}{f(1/c_{\Delta_Y})} = \frac{\Delta_X \, r_{\Delta_X}^3}{\Delta_Y \, r_{\Delta_Y}^3} . \qquad (2.6)$$

From this equation it is clear that to convert between different definitions of the concentration parameter one only needs to invert Eq. 2.4, so that:

$$\frac{1}{c_{\Delta_X}} = x \left(f_{\Delta_X} = f\left(\frac{1}{c_{\Delta_Y}}\right) \frac{\Delta_X}{\Delta_Y} \right) . \qquad (2.7)$$

The inversion of $f(x)$ can be easily obtained using an iterative process, however, the following formula to do it was provided by Hu and Kravtsov [95], and can be used with great accuracy:

$$x(f) = \left[a_1 \, f^{2p} + \left(\frac{3}{4}\right)^2 \right]^{-1/2} + 2f , \qquad (2.8)$$

where $p = a_2 + a_3 \ln f + a_4 (\ln f)^2$, $a_1 = 0.5116$, $a_2 = -0.4283$, $a_3 = -3.13 \times 10^{-3}$ and $a_4 = -3.52 \times 10^{-5}$.

So, once a value of c_Δ is given for any mass M_Δ, one can straightforwardly perform conversions between different mass definitions following this methodology. To have an estimate of the value of the concentration parameter given a certain mass, throughout this work we use the mass–concentration relations provided by Bhattacharya et al. [29], which were obtained analysing the shape of the haloes found in large ΛCDM numerical simulations, and are favoured by recent cluster lensing observations [53, 141, 159, 246].

2.2 The luminosity function

The *luminosity function* of a sample is defined as the number density of objects per unit luminosity and per unit volume with luminosity L. The 3 parameter function provided by Schechter [207] and commonly used reads:

$$\phi(L)\,\mathrm{d}L = \left(\frac{\phi^*}{L^*}\right)\left(\frac{L}{L^*}\right)^{\alpha}\exp\left[-\frac{L}{L^*}\right]\mathrm{d}L\,, \tag{2.9}$$

where ϕ^* is the normalisation density of the luminosity function, L^* is a characteristic luminosity that may depend on redshift, and α is the power law slope at low L. This function behaves as a power law at faint intrinsic luminosities, and is truncated by the exponential behaviour at bright ones, when $L > L^*$. It is usually expressed in terms of magnitudes taking into account that the magnitude and the luminosity are simply related by:

$$M - M^* = -2.5\,\log\left(\frac{L}{L^*}\right)\,, \tag{2.10}$$

and taking into account that $\phi(M)\,\mathrm{d}M = \phi(L)\,\mathrm{d}(-L)$ must hold, leading to the expression:

$$\phi(M)\,\mathrm{d}M = (0.4\ln 10)\,\phi^*\,10^{0.4(\alpha+1)(M-M^*)}\exp\left[-10^{0.4(M-M^*)}\right]\mathrm{d}M\,, \tag{2.11}$$

where M^* is the corresponding characteristic absolute magnitude.

From the definition of the luminosity function, the number density of galaxies in a sample with a luminosity higher than L is then equal to:

$$n(> L) = \int_L^{\infty}\phi(L)\,\mathrm{d}L = \phi^*\,\Gamma(\alpha + 2,\, L/L^*)\,, \tag{2.12}$$

where Γ is the incomplete gamma function.

2.3 Gravitational effects in clusters

In the weak field regime, the metric of spacetime around an isolated distribution of mass, like that of a galaxy or a cluster, can be locally described by:

$$\mathrm{d}s^2 = -\left(1 + \frac{2\Phi}{c^2}\right)c^2\,\mathrm{d}t^2 + \left(1 - \frac{2\Phi}{c^2}\right)\mathrm{d}\vec{x}^2\,, \tag{2.13}$$

where Φ is the Newtonian gravitational potential, and $\mathrm{d}\vec{x}^2$ is the 3-dimensional line element in a flat Euclidean space. According to General Relativity, photons move along null geodesics defined by the metric, satisfying $\mathrm{d}s^2 = 0$. From this metric, two interesting phenomena related to the behaviour of light can be described.

The effect of *gravitational redshift* is simply a consequence of the reduced frequency of light observed for objects emitting from a lower gravitational potential relative to the observer. Applied to clusters, this new observational signature differs from others in the sense that it provides a novel and unique way to test gravity, as modified gravity could lead to deeper potential wells inside clusters, and thus, an stronger gravitational redshift than predicted by General Relativity

[84, 98]. An statistical effect on the redshifts of member galaxies has been claimed to be detected for optically selected stacked samples of clusters from the SDSS survey [64, 202, 264], for which the brightest cluster galaxy (BCG), in principle located at the deepest part of the potential well, is found to lie systemically offset in velocity space relative to other member galaxies, which are located in an outer region of the potential well.

After the first claimed detection of this redshift deviation by Wojtak et al. [264], it was soon realised that the measured signal would also have a contribution induced by tangential motions [270] and from two other effects related to galaxy kinematics [105], complicating the analysis.

Apart from this gravitational redshift effect, this metric also allows us to describe another interesting gravitational effect induced by the presence of massive objects. As we saw in the previous Chapter, according to General Relativity concentrations of matter curve spacetime, and this curvature determines the trajectories of particles, leading, among other things, to the deflection of photons that travel near these concentrations of matter.

In the case of a photon travelling tangentially to the surface of the Sun, this deflection should be equal to 1.7 arcsec. This was confirmed in 1919 during a total solar eclipse in the famous observation by Dyson, Eddington, & Davidson [66]. This *gravitational lensing* effect is one of the most direct ways to estimate the masses of clusters of galaxies, as it only depends on its projected 2-dimensional mass distribution, and is independent of the nature and the dynamical state of the matter contained in the cluster. This effect provides us with a unique tool to probe the dark matter content of the Universe, its distribution, and therefore the growth of structures.

Gravitational lensing by clusters of galaxies was observed for the first time with the discovery of giant arcs three decades ago [130, 222]. These giant arcs are distorted lensed images of background galaxies produced in the *strong* gravitational lensing regime, which can originate other effects like the splitting into multiple images of a single source object. In fact, the discovery of the twin lensed images of the quasar 0957+561 represents the first observed gravitational lensing phenomena [256]. In the *weak* gravitational lensing regime, the distortion manifests in a more statistical coherent way, changing slightly the appearance of faint background galaxies. Measuring the shear distortion distribution of these galaxies across the sky, one can reconstruct the 2-dimensional mass distribution of the foreground cluster.

In addition to the distortion of shapes, gravitational lensing also magnifies images, and because surface brightness is conserved, changes in the size of these background objects due to magnification leads to an increase in their flux. The magnification bias effect is related to this increased luminosity from background galaxies, which promotes galaxies above the flux limit whilst magnifying the area of sky over which they are detected, leading to greater depth for luminous background galaxies [41]. This effect has the advantage over weak lensing estimated from shear to be free from the large intrinsic and instrumental shape dispersion. It requires on the other hand a clean sample of background galaxies with accurate spectroscopic redshifts, limited to fewer galaxies.

Individual massive clusters now routinely provide a measurement of magnification bias, in terms of the background counts. This effect is a projection over the integrated luminosity function described before in this Chapter, which has been shown to reduce significantly the surface number density of red background galaxies behind individual clusters [39, 239, 243, 245] and similar effects are claimed for background quasars and Lyman break galaxies [79, 93]. The expansion of the sky by magnification is found to dominate over the opposing increase from objects promoted from lower luminosity above the flux limit. The requirement for this is deep imaging [234, 246], so that this effect can be traced with sufficient numbers over several independent radial bins per cluster.
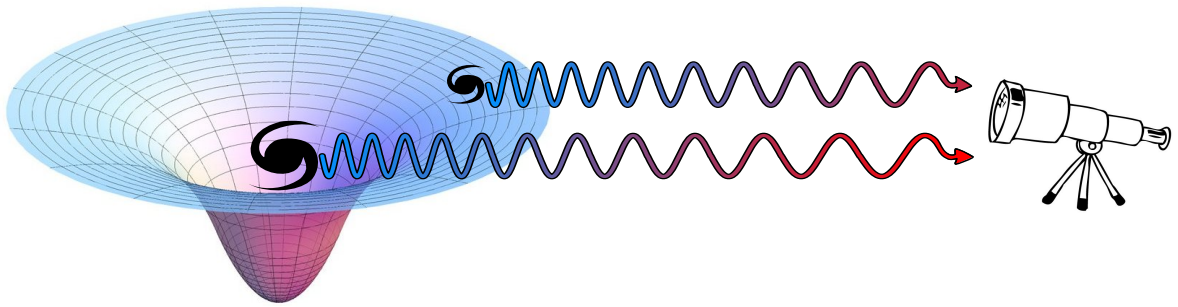
Figure 2.1: *Both the BCG, located in principle in the deepest part of the potential well, and the neighbouring satellite galaxies have their light redshifted due to the gravitational redshift effect. This redshift is stronger for the BCG than for satellite galaxies, so a distant observer finds that the BCG is redshifted with respect to satellite galaxies, or equivalently, that satellite galaxies are blueshifted with respect to the BCG.*

This effect magnification bias effect has proven a practicable way of constraining the mass profiles of individual massive clusters, typically increasing the precision by 30% when added simultaneously to shear measurements within the same data [241].

In this section we review both the gravitational redshift and the magnification bias effects, whose origin is found in the curvature of spacetime.

2.3.1 Gravitational redshift and other internal redshift distortion effects

General relativistic time dilation means light emitted from within a gravitational potential is redshifted relative to a distant observer, and in proportion to the depth of the potential well. This means we may expect the light coming from centrally located BCG galaxies to be relatively more affected than the light emitted by an average cluster member. This effect is schematically shown in Fig. 2.1. From the metric given by Eq. 2.13 this relative gravitational redshift (GR) is found to be equal to:

$$\Delta z_{\mathrm{GR}} = \frac{\Delta \Phi}{c^2} \, , \tag{2.14}$$

where $\Delta \Phi$ is the gravitational potential difference between the cluster galaxy and the cluster BCG. Analytic models [44] predict a gravitational redshift of the order of $c\,\Delta z_{\mathrm{GR}} \sim 10\,\mathrm{km\,s^{-1}}$ for clusters with masses $\sim 10^{14} M_\odot$, and as high as $300\,\mathrm{km\,s^{-1}}$ for clusters with masses $\sim 10^{16} M_\odot$.

Making use of N-body simulations in a ΛCDM universe, Kim and Croft [109] concluded that, assuming a redshift accuracy of $30\,\mathrm{km\,s^{-1}}$, over 5,000 clusters with masses above $\sim 5 \times 10^{13} M_\odot$ were needed in order to measure the gravitational redshift effect at the 2σ level. An important result of their study is that, above masses $\sim 10^{14} M_\odot$, the gravitational redshift signal is proportional to the cluster velocity dispersion, and hence, the number of clusters actually needed to detect the gravitational redshift signal does not depend on the mass of the clusters used. This is because the dispersion in the velocity difference between the BCG and the rest of the galaxies is found to increase with cluster mass in the simulations, adding to the inherent noise. They stress that a convincing detection would require sufficient data so that independent mass bins can be compared to examine the signature of gravitational redshift as a function of cluster mass.

Shortly after the first detection claim of this effect by Wojtak et al. [264], Zhao et al. [270]

pointed out a potentially significant additional new blueshift deviation effect related to the special relativistic transverse Doppler effect (TD) generated by random motions of the galaxies moving within the cluster potential. This additional shift is equal to:

$$\Delta z_{\mathrm{TD}} = \frac{\langle |\vec{v}_{gal}|^2 \rangle - |\vec{v}_{BCG}|^2}{2\,c^2} , \qquad (2.15)$$

opposite in sign to the gravitational redshift, and of the same order of magnitude for clusters in virial equilibrium. In fact, for an spherical cluster in equilibrium, this yields $c\,\Delta z_{\mathrm{TD}} = (3\sigma_{obs}^2 - 3\sigma_{BCG}^2)/2c$, where σ_{obs} is the observed line-of-sight velocity dispersion of the galaxies around the BCG, and σ_{BCG} is the velocity dispersion associated to BCGs, which is usually taken to be $\sigma_{BCG} \sim \sigma_{obs}/3$.

More recently, Kaiser [105] has raised other significant corrections. As we are observing galaxies in our past light cone (LC), and due to the time it takes light to travel through the cluster, we will see on average more galaxies moving away from us than toward us. This effect is compared by Kaiser to the one that "causes a runner on a trail to meet more hikers coming toward her than going in the same direction". This results in another shift of the distribution of galaxies around the BCGs equal to:

$$\Delta z_{\mathrm{LC}} = \frac{\langle |\vec{v}_{los,\,gal}|^2 \rangle - |\vec{v}_{los,\,BCG}|^2}{c^2} , \qquad (2.16)$$

which has the same sign as the TD effect, and is of the same order of magnitude.

In addition to that, according to Kaiser [105] we also have to deal with the fact that we are working with a magnitude-limited sample of galaxies: although the cluster catalogues that are obtained using photometric data are volume-complete up to a certain redshift, the sample of galaxies with measured spectroscopic redshifts is usually magnitude-limited. Proper motion, changing the surface brightness (SB) and therefore the apparent luminosity of galaxies due to the relativistic beaming effect, will bias the distribution of galaxies within clusters that are selected for spectroscopic surveys. For low velocities, the proportional change in the fluence is equal to $3\,v_{los}/c$, but if we consider the change in frequency and the effect that this introduces on the measurement, the change in the apparent luminosity l of the galaxy is equal to:

$$\frac{\Delta l}{l} = (3 + \alpha(z))\,\frac{v_{los}}{c}, \qquad (2.17)$$

where $\alpha(z)$ is the effective spectral index that takes into account the change in frequency and the resulting response of the photon count detector to this change. Considering a broad-band filter with an spectral transmission curve $R(\lambda)$, the spectral index for a galaxy at redshift z with an spectral energy distribution (SED) with a flux density $f(\lambda)$ can be computed as:

$$\alpha(z) = -\frac{\mathrm{d}\ln\left(\int R(\lambda/(1+z))\,\lambda\,f(\lambda)\,\mathrm{d}\lambda\right)}{\mathrm{d}\ln(1+z)} . \qquad (2.18)$$

The modulation on the number of observable galaxies is thus obtained multiplying $\Delta l/l$ by the logarithmic derivative of the comoving density of observable objects n_{obs} above the luminosity limit $L_{lim}(z)$, $\mathrm{d}\ln n_{obs}[> L_{lim}(z)]/\mathrm{d}\ln L$, which depends on the redshift distribution and the luminosity function associated to the galaxy survey considered. This density modulation introduces a change on the observed redshift distribution of galaxies equal to:

$$\Delta z_{\mathrm{SB}} = -\left\langle (3 + \alpha(z))\,\frac{\mathrm{d}\ln n_{\mathrm{obs}}[> L_{\mathrm{lim}}(z)]}{\mathrm{d}\ln L} \right\rangle \frac{\langle |\vec{v}_{los}|^2 \rangle}{c^2} . \qquad (2.19)$$

In opposition to the transverse Doppler and past light-cone kinematical effects, this new shift introduces a net blueshift, which is also of the same order of magnitude, so it partly cancels these other two contributions.

All this considered, the total redshift velocity difference v_{los} between a galaxy and the central BCG is given by:

$$v_{los} = H\left(d_{gal} - d_{BCG}\right) + v_{pec,los} + c\,\Delta z\,, \tag{2.20}$$

where d is the distance between the observer and the object in Mpc, $v_{pec,los}$ is the line-of-sight component of the peculiar motion of the galaxy, responsible for the fingers of God and the flattening RSD effects (see Sec. 1.2.6), and Δz is the term arising from the combination of the previously mentioned distortions. To avoid confusion we will subsequently refer to the combination of these four effects as an "internal redshift distortion", which induces a new asymmetry on the cluster-galaxy cross-correlation function [35, 55], different from the well known RSD asymmetry, as it depends not only on the absolute value of the line-of-sight separation from the center of the cluster, but also on its sign.

2.3.2 Magnification bias and redshift enhancement

In the case of the simple metric given by Eq. 2.13, the way light from background sources is deflected by a concentration of matter, i.e., a lens, can be described as a first approximation in a simple geometrical way.

In the "thin lens" case, when the thickness of the lens is much smaller than the distances between the observer and the lens, and between the lens and the source, the lens equation that describes the trajectories of photons is:

$$\vec{\eta} = \frac{D_s}{D_l}\vec{\xi} - D_{ls}\,\vec{\hat{\alpha}}(\vec{\xi})\,, \tag{2.21}$$

where η is the distance between the source and the lens if the latter were projected on the source plane, ξ is the impact parameter of the deflected light ray with the lens, $\hat{\alpha}$ is the deflection angle, and D_s, D_l and D_{ls} refer to the observer-source, observer-lens and lens-source angular diameter distances, respectively. This is schematically shown in Fig. 2.2. This "thin lens" approximation is reasonable in our case, as clusters have sizes of the order of a few Mpc, and the distances between us, the clusters and the background objects are in general of the order of hundreds of Mpc.

The lens equation can be rewritten in terms of angular quantities, considering $\vec{\eta} = D_s\vec{\beta}$ and $\vec{\xi} = D_l\,\vec{\theta}$:

$$\vec{\beta} = \vec{\theta} - \frac{D_{ls}}{D_s}\,\vec{\hat{\alpha}}(D_l\,\vec{\theta}) \equiv \vec{\theta} - \vec{\alpha}(\vec{\theta})\,, \tag{2.22}$$

where $\vec{\alpha}$ is the scaled deflection angle. This equation provides the position in the sky $\vec{\theta}$ in which the observer sees an object really located at $\vec{\beta}$, and if there is more than one solution of $\vec{\theta}$ for a fixed $\vec{\beta}$, then the lens produces more than one image of the background object. In order to study whether this happens or not in a lens, it is useful to define the *convergence* κ as:

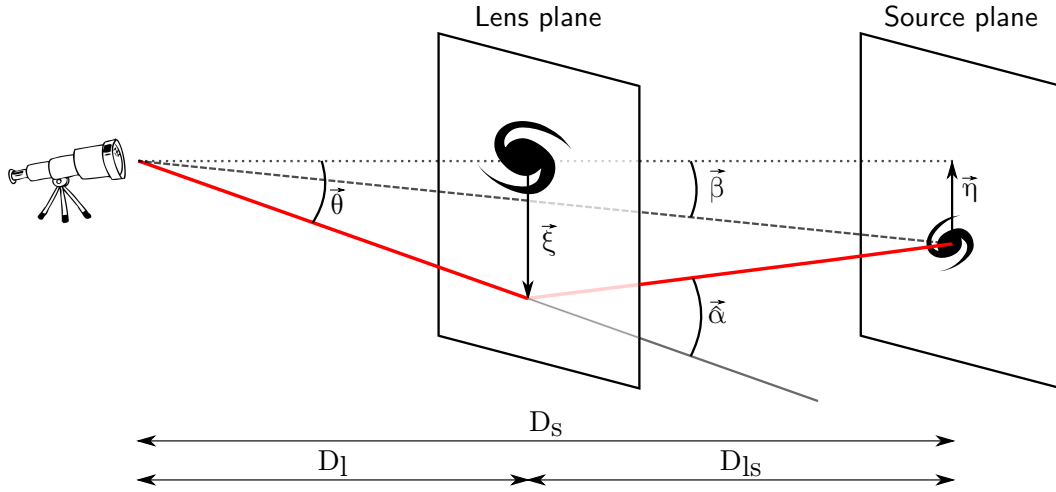$$\kappa = \frac{\Sigma}{\Sigma_{crit}}\,, \tag{2.23}$$

Figure 2.2: *Scheme showing the different quantities involved in the lens equation. The deflected ray of light that reaches the observer is marked in red.*

where Σ is the projected mass density of the lens in units of the critical surface density for lensing:

$$\Sigma_{crit} = \frac{c^2}{4\pi G}\frac{D_s}{D_l D_{ls}} \, . \tag{2.24}$$

If in any region of the lens $\Sigma \geq \Sigma_{crit}$, then $\kappa \geq 1$ and the lens, in the "strong" lensing regime, produces more than one image of the objects located (if any) at $\vec{\beta}$.

To describe the distortions generated by gravitational lenses, the 2-dimensional gravitational *deflection potential* Ψ is defined as:

$$\Psi(\vec{\theta}) = \frac{1}{\pi}\int_{A_{lens}} \kappa(\vec{\theta'}) \ln|\vec{\theta} - \vec{\theta'}| \, \mathrm{d}^2\vec{\theta'} \, , \tag{2.25}$$

which satisfies the equivalent 2-dimensional Poisson equation $\nabla^2\Psi(\vec{\theta}) = 2\kappa(\vec{\theta})$. The scaled deflection angle $\vec{\alpha}$ can be written as the gradient of this potential, $\vec{\alpha} = \nabla\Psi$.

Because light from background sources is deflected differentially, the original surface brightness of the source f_s is remapped following $f_{obs}(\vec{\theta}) = f_s(\vec{\beta}(\vec{\theta}))$. In the "weak" lensing regime, when the deflection angle and the size of the source are small, then this equation can be linearised as $f_{obs}(\vec{\theta}) = f_s(\mathcal{A}\,\vec{\theta})$, where $\mathcal{A}$ is the "distortion matrix", equal to the Jacobian of the transformation:

$$\mathcal{A} = \frac{\partial\vec{\beta}}{\partial\vec{\theta}} = \left(\delta_{ij} - \frac{\partial^2\Psi(\vec{\theta})}{\partial\theta_i\partial\theta_j}\right) = \begin{bmatrix} 1 - \kappa - \gamma_1 & -\gamma_2 \\ -\gamma_2 & 1 - \kappa + \gamma_1 \end{bmatrix} , \tag{2.26}$$

where γ_1 and γ_2 correspond to the real and imaginary parts of the *shear* $\gamma = \gamma_1 + i\gamma_2$, with:

$$\gamma_1 = \frac{1}{2}\left(\frac{\partial^2\Psi}{\partial\theta_1^2} - \frac{\partial^2\Psi}{\partial\theta_2^2}\right) , \tag{2.27}$$

$$\gamma_2 = \frac{\partial^2\Psi}{\partial\theta_1\partial\theta_2} \, . \tag{2.28}$$
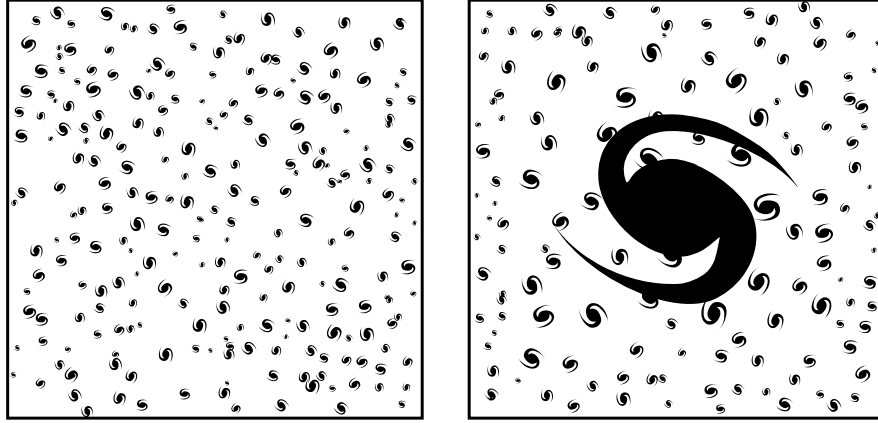
Figure 2.3: *When a massive object like a galaxy or a cluster of galaxies is located in front of an homogeneous distribution of background galaxies, it acts like a gravitational lens magnifying these background sources and expanding the area of the sky behind it. These two competing effects lead to an effective variation on the number density of background sources, known as the magnification bias.*

according to this, images are distorted in shape and size.

In the case we are interested in, lens magnification is caused by a foreground cluster which acts as a gravitational lens with a lensing shear γ and convergence κ. In this case, the *magnification* produced by the lens is equal to:

$$\mu = \frac{1}{\det \mathcal{A}} = \frac{1}{(1-\kappa)^2 - |\gamma|^2} \, , \tag{2.29}$$

which distorts the background region in two ways: i) because gravitational lensing preserves surface brightness, the flux from a source is amplified as the lens increases the solid angle under which such source appears. This implies that the luminosity limit of a survey is increased by a factor L_{lim}/μ in the lens region, resulting in a higher surface density of observed background objects due to the ones which could not had been seen otherwise. ii) The sky area behind the foreground lens is expanded by a factor $1/\mu$, so that the surface density of objects decreases as the effective cross-section behind the clusters becomes smaller. The combination of these two effects and the resulting difference on the number of lensed sourced detected is known as *magnification bias* [41], shown schematically in Fig. 2.3.

Thus, if the observed apparent luminosity of a lensed source is given by $L_{obs} = \mu L_0$, the observed number of objects with luminosities bigger than L_{lim} at redshift z is given by:

$$n_{obs}[> L_{lim}(z), z] = \frac{1}{\mu} \, n_0[> L_{lim}(z)/\mu, z] \, , \tag{2.30}$$

where the $1/\mu$ factor comes from the dilation of the sky solid angle. In the case of faint galaxies, their number counts is observed to closely follow a power law, so if $n_0[> L(z)] \propto L(z)^{-\beta}$, then the previous equation simplifies to:

$$n_{obs}(z) = \mu^{\beta(z,L)-1} \, n_0(z) \, , \tag{2.31}$$

where β is the logarithmic slope of the luminosity function ϕ evaluated at L:

$$\beta(z, L) = - \left. \frac{\mathrm{d} \ln \phi(z, L')}{\mathrm{d} \ln L'} \right|_{L} .$$ (2.32)

Taking into account that the number density of observed objects $n_{obs}(z)$ depends on redshift, the average redshift of the background lensed sources is given by:

$$\langle z_{back} \rangle = \frac{\int n_{obs}(z)\, z\, \mathrm{d}z}{\int n_{obs}(z)\, \mathrm{d}z} ,$$ (2.33)

which, if $\beta(z, L)$ is larger than unity, is higher than the average redshift in the absence of gravitational lenses. We define the redshift enhancement of these background objects δ_z as:

$$\delta_z \equiv \frac{\langle z_{obs} \rangle - \langle z_{\mathrm{total}} \rangle}{\langle z_{\mathrm{total}} \rangle} ,$$ (2.34)

where $\langle z_{obs} \rangle$ is the average redshift of the lensed n_{obs} background objects, and $\langle z_{\mathrm{total}} \rangle$ is the average redshift of the unlensed background objects, as would be seen without a lens.

2.4 The mass–richness relation

The mass–richness relation has been the focus of intense research in the past decade, as an accurate scaling between the mass of a halo and the cluster observables is mandatory to constrain cosmological parameters from cluster counting techniques [192, 238]. If one wants to obtain a calibration which does not rely on matching a certain cosmology, a relation between the mass of the cluster and a mass proxy like the number of galaxies contained in the cluster, the X-ray luminosity L_X, the thermal Sunyaev-Zel'dovich signal Y_{SZ}, or the lensing mass M_{lens}, must be found.

Under the assumption of equilibrium, radial mass profiles have been estimated hydrodynamically from Brehmmstralung X-ray emission profiles. However, usually X-ray data is too low surface brightness to reach the virial radius. The SZ effect provides independent gas related data that may be related to mass by augmenting X-ray data or through scalings that may be established independently [193], but only recently samples of clusters with SZ-based mass estimates have been constructed, usually limited to a few hundred clusters. The velocity dispersion of member galaxies has also traditionally been used for mass estimation, via the Jeans equation [215] or via the "caustic method" [62] which identifies the escape velocity as a sharp caustic transition where data is plentiful. The unknown velocity anisotropy profile required by the Jeans equation can be solved for by combining dynamical and lensing data but only for the best studied clusters [124]. Weak lensing is understood to be one of the cleanest methods to derive cluster mass profiles, requiring no assumptions about the dynamical state of the cluster [106]. However, it requires correction for instrumental effects [107] and high resolution data to overcome the inherently wide dispersion in galaxy shapes. The cleanest mass proxy is arguably provided by the number of member galaxies, the so called *richness*, implicit in the assumption that the dominant cluster dark matter is collisionless like galaxies.

Because these cluster observables are intrinsically noisy, for each mass–observable relation there is a scatter $\sigma_{M|obs}$ associated to the distribution of the random values of such observable given a

true mass. The uncertainty in the value of this scatter alters the effectiveness of any cosmological analysis as much as the uncertainty in the mean mass–observable relation.

The scaling between mass and the optical richness λ in clusters, which is found to be closely proportional [18, 82], is described by the standard power law cluster mass–richness mean relation:

$$\langle M|\lambda \rangle = M_0 \left(\frac{\lambda}{\lambda_0}\right)^{\alpha_{M|\lambda}} , \tag{2.35}$$

where M_0 is a reference mass at a given value of the richness $\lambda = \lambda_0$, and $\alpha_{M|\lambda}$ is the slope of the mass–richness relation.

In order to compute the mean mass of a cluster subsample, one first needs to consider the probability $P(M|\lambda^{\mathrm{obs}})$ of having a given value of the mass M for a cluster with an observed richness λ^{obs}, which is itself a random variable:

$$P(M|\lambda^{\mathrm{obs}}) = \int P(M|\lambda)\,P(\lambda|\lambda^{\mathrm{obs}})\,\mathrm{d}\lambda , \tag{2.36}$$

where $P(M|\lambda)$ is a delta function (as the relation between mass and expected richness λ is given by Eq. 2.35) and $P(\lambda|\lambda^{\mathrm{obs}})$ is described by a log-normal distribution [129], following the usual approach:

$$P(\lambda|\lambda^{\mathrm{obs}}) = \frac{1}{\sqrt{2\pi\sigma^2_{\ln\lambda|\lambda^{\mathrm{obs}}}}} \exp[-x^2(\lambda)] , \tag{2.37}$$

with:

$$x(\lambda) = \frac{\ln\lambda - \ln\lambda^{\mathrm{obs}}}{\sqrt{2\sigma^2_{\ln\lambda|\lambda^{\mathrm{obs}}}}} . \tag{2.38}$$

Here $\sigma_{\ln\lambda|\lambda^{\mathrm{obs}}}$ is the fractional scatter on the halo richness at fixed observed richness, and is usually assumed to be constant with cluster redshift and richness. Because $P(M|\lambda)$ is a delta function, and considering Eq. 2.35, we also have that $\sigma^2_{\ln\lambda|\lambda^{\mathrm{obs}}} = \sigma^2_{\ln M|\lambda^{\mathrm{obs}}}$.

All this considered, the mean mass $\langle M \rangle$ of a sample of clusters binned in richness, with $\lambda \in [\lambda^{\mathrm{obs}}_i, \lambda^{\mathrm{obs}}_{i+1}]$ and containing N_i clusters, is given by:

$$\langle M \rangle = \frac{1}{N_i} \sum_{j=1}^{N_i} \int M\,P(M|\lambda^{\mathrm{obs}}_j)\,\mathrm{d}M . \tag{2.39}$$

It should be noted that the parametrisation presented in Eq. 2.35 is not unique. The mean mass–richness relation can also be given in terms of the logarithmic mass:

$$\langle \ln M|\lambda \rangle = \ln \tilde{M}_0 + \tilde{\alpha}_{M|\lambda} \left(\frac{\lambda}{\lambda_0}\right) . \tag{2.40}$$

These two different parametrisations are simply related by:

$$\langle \ln M|\lambda \rangle = \ln \langle M|\lambda \rangle - \frac{1}{2}\sigma^2_{\ln M|\lambda^{\mathrm{obs}}}. \tag{2.41}$$

Some authors and due to the recent data coming from deep optical surveys that extend to redshifts as high as $z \approx 1$, introduce a redshift dependence in these mass-richness relations, such
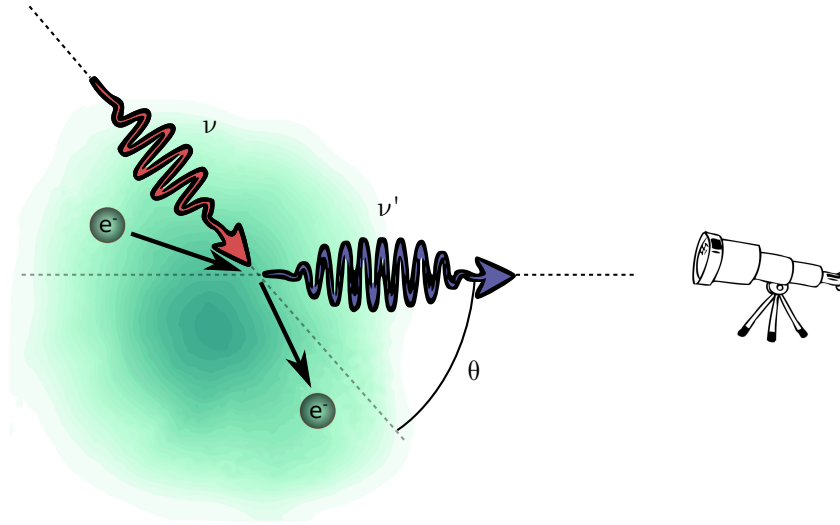
Figure 2.4: *Inverse Compton scattering: a low energy CMB photon with initial frequency ν interacts with a ICM high energy electron and is scattered an angle θ, gaining energy in the process and reaching the observer with a final frequency ν'.*

that Eq. 2.35 is modified to contain an additional redshift term, yielding:

$$\langle M|\lambda \rangle = M_0 \left(\frac{\lambda}{\lambda_0} \right)^{\alpha_{M|\lambda}} \left(\frac{1+z}{1+z_0} \right)^{\beta_{M|\lambda}} , \qquad (2.42)$$

where $\beta_{M|\lambda}$ is the slope of the redshift-dependent term, and z_0 is some arbitrarily chosen pivot redshift. Equivalently, Eq. 2.40 would be expressed as:

$$\langle \ln M|\lambda \rangle = \ln \tilde{M}_0 + \tilde{\alpha}_{M|\lambda} \left(\frac{\lambda}{\lambda_0} \right) + \tilde{\beta}_{M|\lambda} \left(\frac{1+z}{1+z_0} \right) . \qquad (2.43)$$

2.5 Thermal Sunyaev-Zel'dovich effect

The thermal Sunyaev-Zel'dovich (tSZ) effect has its origin in the interaction of the CMB photons with the high energy free electrons found on the hot intracluster medium (ICM). When a photon is scattered by an electron, its frequency change is given by the Compton scattering formula:

$$\frac{\nu'}{\nu} = \frac{1}{1 + [h/(m_e c^2)](1 - \cos\theta)} , \qquad (2.44)$$

where θ is the angle of scattering, and ν and ν' are the initial and final frequencies, as shown in Fig. 2.4. Although the probability of this to happen for a photon that is travelling through a cluster is of the order of the 1%, the net effect results in an small mK change in the spectral energy distribution of CMB photons.

Ignoring relativistic corrections, the tSZ spectral distortion of the CMB along the line-of-sight

to the cluster, expressed in terms of temperature change, is:

$$\frac{\Delta T_{\mathrm{tSZ}}}{T_{\mathrm{CMB}}} = g(x)\, y \,, \tag{2.45}$$

where $x = (h\,\nu)/(k_B\, T_{\mathrm{CMB}})$ is the dimensionless frequency, y is the *Compton parameter*, and

$$g(x) = \left(x\, \frac{e^x + 1}{e^x - 1} - 4 \right) \,. \tag{2.46}$$

This expression is obtained from the distribution of photon frequency shifts caused by inverse Compton scattering with a population of free electrons with concentration n_e and at a given temperature T_e. For a derivation of this equation, we refer the reader to the papers of Rephaeli [187], Sunyaev and Zel'dovich [229], or the more recent work by Birkinshaw [30]. Considering that the scattering optical depth along a light-of-sight is equal to:

$$\tau_e = \sigma_T \int_0^\infty n_e \, \mathrm{d}l \,, \tag{2.47}$$

the Compton parameter y is defined as this optical depth times the fractional energy gain per scattering, such that:

$$y = \frac{\sigma_T}{m_e\, c^2} \int_0^\infty P(l)\, \mathrm{d}l \,, \tag{2.48}$$

where σ_T is the Thomson cross section and $P = k_B\, n_e\, T_e$ is the pressure produced by the free electrons of the ICM.

Integrating over the solid angle of the cluster one obtains the integrated Compton parameter:

$$Y = \int_\Omega y \, \mathrm{d}\Omega = D_A^{-2} \frac{\sigma_T}{m_e\, c^2} \int_0^\infty \mathrm{d}l \int_{A_{\mathrm{clu}}} P(l) \, \mathrm{d}A \,, \tag{2.49}$$

where A_{clu} is the area of the cluster in the plane of the sky, and $D_A(z)$ is the angular diameter distance at redshift z. This quantity is a measure of the total thermal energy of the gas contained in the cluster.

Due to this thermal SZ effect, the change in intensity of the scattered CMB spectrum is given by:

$$\Delta I_{\mathrm{tSZ}}(\nu) = I_0\, h(x)\, g(x)\, y \,, \tag{2.50}$$

where:

$$I_0 = \frac{2h}{c^2} \left(\frac{k_B\, T_{\mathrm{CMB}}}{h} \right)^3 \,, \tag{2.51}$$

$$h(x) = \frac{x^4\, e^x}{(e^x - 1)^2} \,. \tag{2.52}$$

One of the most interesting features of the tSZ effect is that it is redshift-independent, i.e., no matter how far the cluster is, the distortion that it induces in the CMB spectra is the same. The only redshift dependence comes from the diminishing size of the area subtended by the cluster in the sky with increasing redshift, proportional to D_A^{-2}, where D_A is the angular diameter distance. However, as we explained in Sec. 1.1.4, in the ΛCDM model the angular diameter distance starts to decrease after redshift $z \approx 1$, so objects at redshift $z > 1$ may be easier to detect than objects at redshift $z \approx 1$ because they appear larger in the sky.

Considering the actual temperature of the CMB, $T_{\mathrm{CMB}} = 2.73\,\mathrm{K}$, ΔI_{tSZ} cancels at $\nu \approx 217\mathrm{GHz}$, and is negative and positive for smaller and higher frequencies, respectively.

Kinetic Sunyaev Zel'dovich and IR emission from galaxies

Apart from this thermal component, the peculiar motion of the cluster with respect to the CMB frame produces another kind of distortion in the observed temperature fluctuations, known as kinetic SZ (kSZ), much smaller and more difficult to detect. In the non-relativistic limit, the temperature change of the CMB induced by this effect can be approximated as:

$$\frac{\Delta T_{\mathrm{kSZ}}}{T_{\mathrm{CMB}}} = -\tau \, \frac{v_{los}}{c} \, , \tag{2.53}$$

where v_{los} is the line-of-sight component of the peculiar velocity of the cluster. The associated change in intensity is equal to:

$$\Delta I_{\mathrm{kSZ}}(\nu) = -I_0 \, h(x) \, \tau \, \frac{v_{los}}{c} \, . \tag{2.54}$$

Although the amplitude of the kSZ effect is smaller than the amplitude of the tSZ effect for typical cluster velocities and temperatures, it produces its maximum spectral distortion precisely near $\nu \approx 217\,\mathrm{GHz}$, where the tSZ effect cancels. Careful observations around this frequency can provide estimations of cluster radial peculiar velocities.

Finally, in order to disentangle the different CMB spectral distortions generated by clusters, one needs to take into account the emission on the infrared (IR) coming from the dust contained in the luminous galaxies that belong to the cluster, or from our own Galactic dust. This emission can be modelled as a simple emitting blackbody, represented by the Planck function $B(\nu, T_{\mathrm{dust}})$ at rest frequency ν, which depends only on the dust temperature T_{dust} contained in these galaxies. To account for the dust opacity, $B(\nu, T_{\mathrm{dust}})$ is multiplied by the term $(1 - e^{-\tau(\nu)})$, where $\tau(\nu) = (\nu/\nu_0)^{\beta_{\mathrm{dust}}}$ is the optical depth, with ν_0 the frequency at which it is equal to unity, and β_{dust} the spectral emissivity index. In the optically thin case $(1 - e^{-\tau(\nu)}) \sim \nu^{\beta_{\mathrm{dust}}}$, and the expression of the flux density $G \propto \nu^{\beta_{\mathrm{dust}}} B(\nu, T_{\mathrm{dust}})$ of such graybody is:

$$G(\nu) \propto \frac{\nu^{\beta_{\mathrm{dust}}+3}}{e^{h\nu/kT_{\mathrm{dust}}} - 1} \, . \tag{2.55}$$

For typical temperatures of $T_{\mathrm{dust}} \approx 25\,\mathrm{keV}$, this emission becomes strong in the region where the intensity change generated by the tSZ is positive, i.e., at $\nu > 200\text{-}300\,\mathrm{GHz}$.

In Fig. 2.5 and for a typical cluster with $y = 10^{-4}$, $T_e = 5\,\mathrm{keV}$ and $v_{los} = 600\,\mathrm{km\,s^{-1}}$, we plot the different components of the observed change in intensity ΔI of the CMB photons, coming from the tSZ and kSZ effects, and from the dust IR emission. In Fig. 2.6 we show the CMB distortion as seen by the space satellite *Planck* at 6 different effective frequencies, ranging from $100\,\mathrm{GHz}$ to $857\,\mathrm{GHz}$. In Chapter 6 we use data from this satellite to study the tSZ emission from clusters.
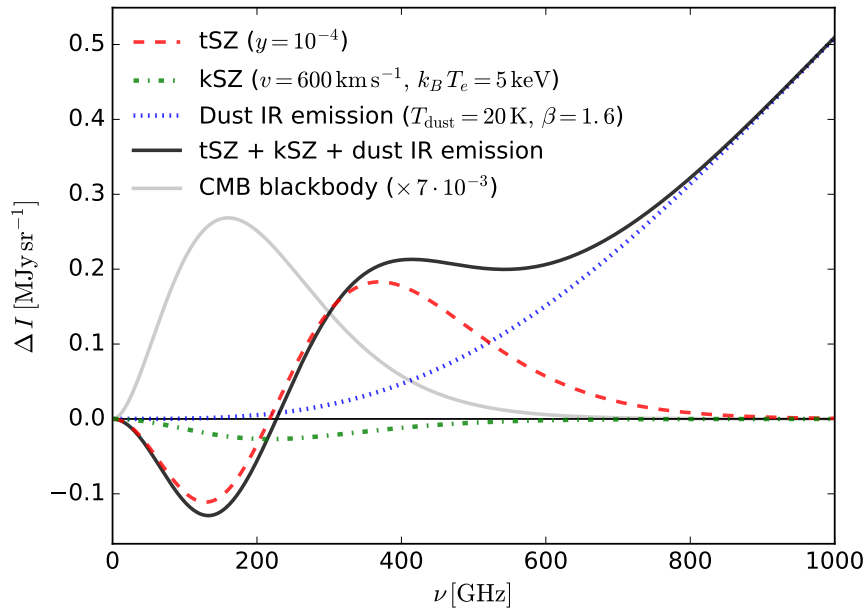
Figure 2.5: *Different components of the CMB intensity distortion (solid black) generated by clusters, including the tSZ effect (dashed red), the kSZ effect (dash-dotted green), and IR emission (dotted blue) coming from dust. For comparison, we also plot the scaled CMB spectral energy distribution (solid gray). For the model we have considered a cluster with $y = 10^{-4}$, $T_e = 5\,\mathrm{keV}$ and $v_{los} = 600\,\mathrm{km\,s^{-1}}$, and dust at a temperature $T_{\mathrm{dust}} = 25\,\mathrm{keV}$ with an spectral emissivity index equal to $\beta_{\mathrm{dust}} = 1.6$.*
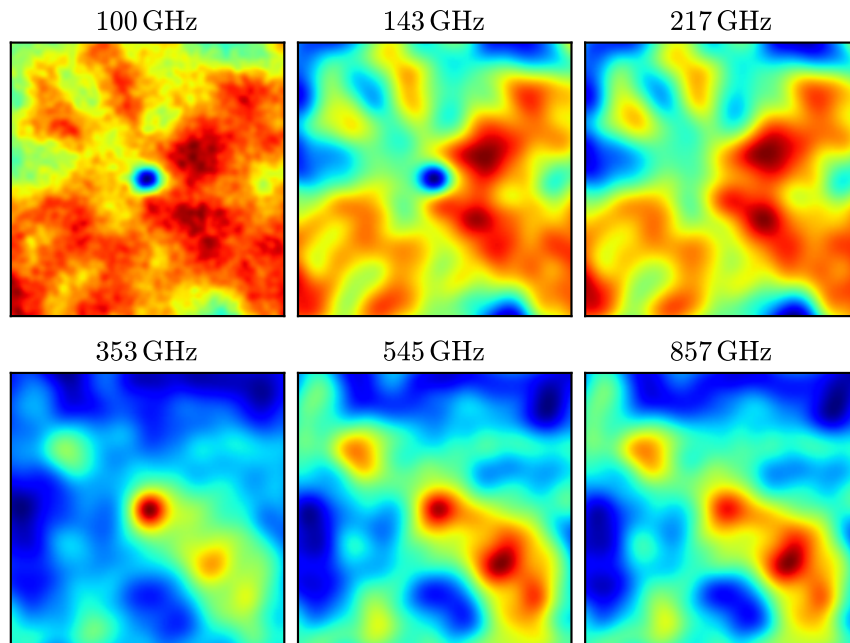

Figure 2.6: *CMB distortion induced by the presence of clusters of galaxies as seen in the 6 $\Delta T/T$ maps produced by the Planck High-Frequency Instrument. The size of the stamps is 2.3 deg × 2.3 deg. In this example, the signal is obtained stacking the maps of a sample of $\sim$ 100 clusters with richness $N > 100$ in the $0.1 < z < 0.5$ redshift range.*

3

SDSS and Cluster Catalogues

In this chapter we review the SDSS data that we use in the following chapters. First, we introduce the characteristics of the survey, the different data releases (DR), and the two main spectroscopic samples that we consider in our analyses, namely, the *Legacy* and the BOSS samples.

We also briefly introduce the concept of cluster catalogue, the different ways in which they can be created from a cluster finder algorithm, and then we describe the three large catalogues that we test in Chapter 4 and that have been constructed from SDSS data, that is, the GMBCG catalogue, the WHL12 catalogue, and the redMaPPer catalogue, with an special emphasis in the latter, as it is the one that we consider in Chapters 5 and 6.

3.1 Sloan Digital Sky Survey

All our observational data comes from the Sloan Digital Sky Survey (SDSS), the most successful photometric and spectroscopic survey to date, conducted on a 2.5-meter wide angle telescope located at Apache Point Observatory [85], which is shown in Fig. 3.1.

Since it began in 2000, the SDSS has mapped the largest portion of the Universe to date, and provides high-precision data that has proved very useful for several kinds of large scale structure analyses. The telescope has scanned more than 14,000 deg^2 of the sky with a mosaic CCD with five colour-bands, *u*, *g*, *r*, *i* and *z* [81], shown in Fig. 3.2. The central wavelengths of these filters are 355.1, 468.6, 616.6, 748.0, and 893.2 nm for the five *u*, *g*, *r*, *i* and *z* filters, respectively.

It has also obtained the spectra of more than 1,600,000 unique objects during the SDSS-I/II *Legacy* programme [266] with the original SDSS spectrograph, that had 640 spectroscopic fibers per plate, and more than 1,500,000 unique spectra with a more advanced 1,000-fiber per plate spectrograph [219] during the SDSS-III [70] BOSS programme, with a wavelength coverage that ranges from 360.0 nm to 1,040.0 nm. In both of these SDSS spectrographs, the light spectrum is split and conducted to "blue" and "red" cameras that process different wavelength ranges. The diameter size of the fibers that are plugged into the plates was updated from the 3 arcsec of the original SDSS spectrograph, to 2 arcsec in the BOSS spectrograph. One of the aluminium plates used to plug the fibers that conduct the light to the spectrograph is shown in Fig. 3.2.

The information obtained in this survey has been made public to the scientific community on a series of different Data Releases (DR), with DR12 [4] being the latest at the time this work was done, which contains, among other information, 14,500 deg^2 of imaging comprising photometric
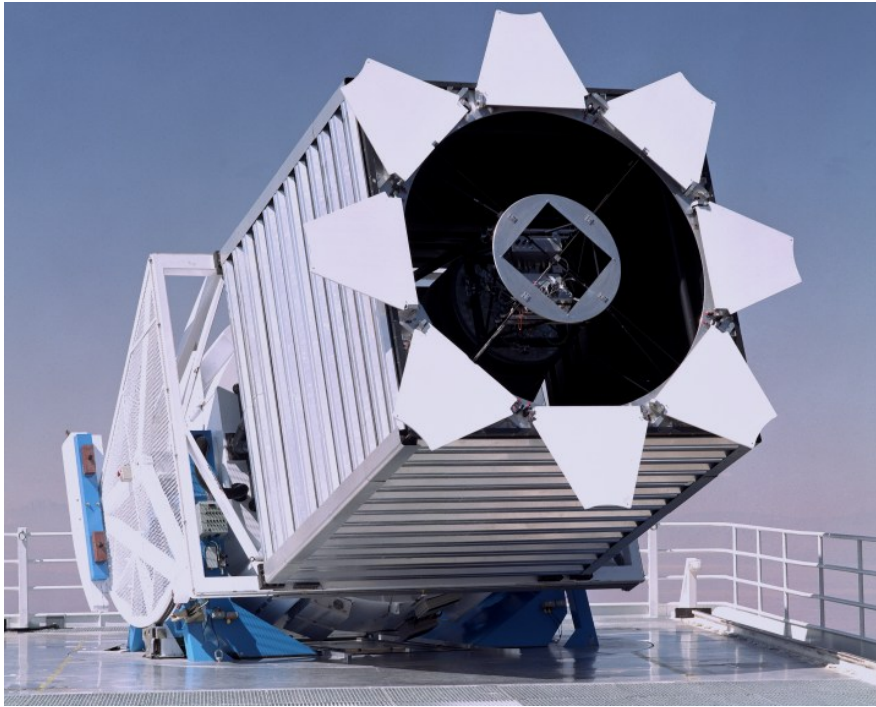
Figure 3.1: *The 2.5 meter f/5 modified Ritchey-Chrétien altitude-azimuth telescope of the SDSS survey. It is located at Apache Point Observatory, New Mexico.*
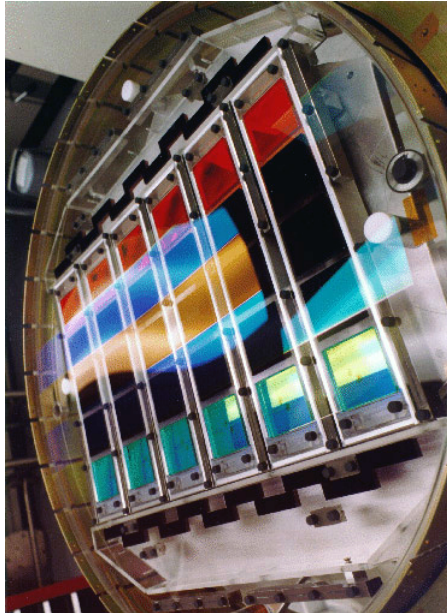
Figure 3.2: *Left: the optical camera of the SDSS-III survey, composed of an array of 30 CCDs with 2048 × 2048 pixels each. The filters correspond to the five colour-bands u, g, r, i and z. Right: One of the plates used in the BOSS survey. The holes in the plate indicate the positions in the sky of the objects whose redshift is measured placing optic fibers that conduct the light to the spectrograph. The equivalent diameter sizes in the sky of the plate and the fibers are 3 degrees and 2 arcsec, respectively.*
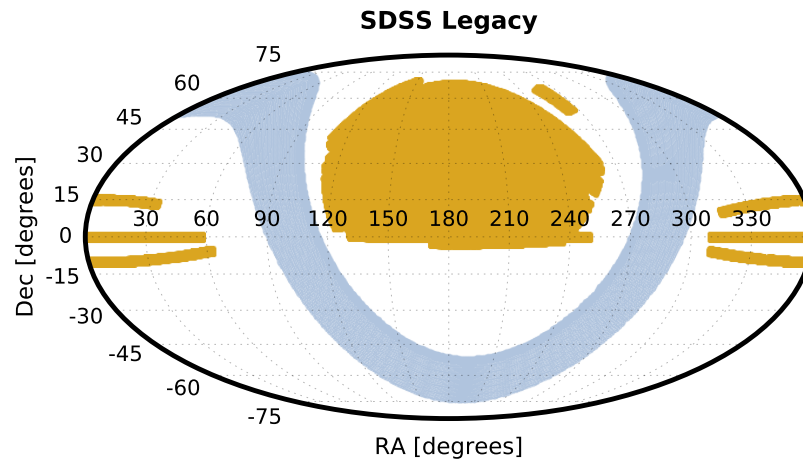
Figure 3.3: *Sky footprint of the 801,945 galaxies with spectroscopic spectra that we use from the Legacy survey, as available in DR10. The grey shaded area represents the galactic plane.*

data of 208,478,448 galaxies, and the optical spectra of 2,401,952 unique galaxies to $z = 0.7$ in ~10,500 deg^2 of the sky.

In Chapter 4 we use the DR10 release, which contains all galaxies with reliable spectroscopic measurements from the *Legacy* programme plus more than 850,000 galaxies from the BOSS programme, and in Chapters 5 and 6 we use the data from the more recent DR12.

3.1.1 The *Legacy* spectroscopic sample

The spectroscopic redshifts of the *Legacy* survey were obtained as part of the SDSS-I and SDSS-II programmes [266], over an observing period of eight years, shared with two additional surveys, the Sloan Extension for Galactic Understanding and Exploration (SEGUE), for stars, and a Supernova survey. The *Legacy* survey, originally designed to investigate the large scale structure of the universe, is composed of:

- the *Main* sample [227], a magnitude-limited sample of galaxies with r-band Petrosian magnitudes $r < 17.7$, and a median redshift of $z \sim 0.1$,

- and the *Luminous Red Galaxies* (LRG) sample [69], an approximately volume-complete sample up to $z \sim 0.4$.

With a total sky coverage of 8,032 deg^2, as shown in Fig. 3.3, the *Legacy* Survey includes over 930,000 unique galaxies with spectroscopic redshift. Of those, we select the most reliable spectra with database flags `ZWARNING` equal to 0 or 16, a "good" or "marginal" `plateQuality`, and `Z_ERR` < 0.0006. Within the redshift range in common with the cluster catalogues listed in Sec. 3.2, we find 801,945 galaxy spectra useful for our purposes.

Although the spectroscopic sample and the sky coverage of the *Legacy* sample have remained unchanged, the imaging and the spectroscopic pipelines have been improved in subsequent SDSS data releases. Thus, here we use the *Legacy* survey spectra of the DR10 release [3]. The redshift distribution of this sample is shown in Fig. 3.4, where it can be seen that most of these galaxies are confined in the $0.00 < z < 0.20$ range, with an extra contribution coming from LRG at higher redshifts that peaks at $z \sim 0.35$.
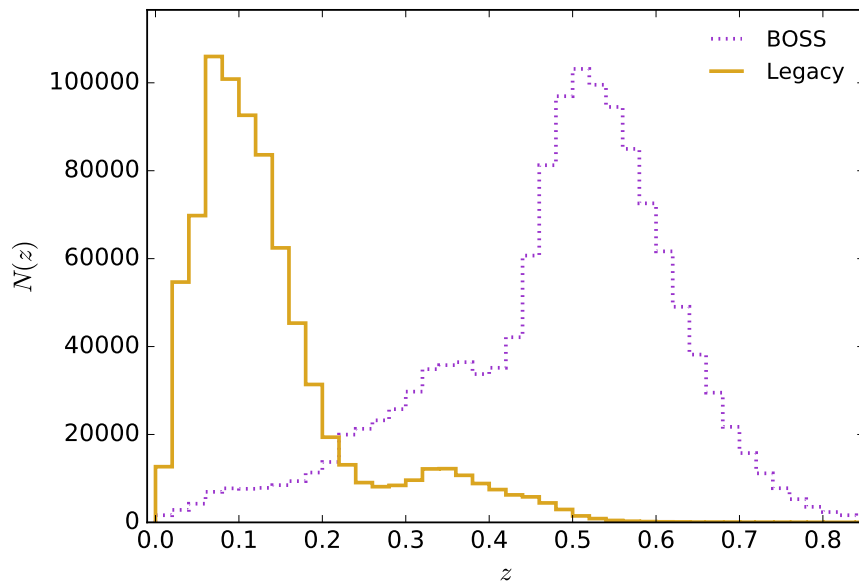
Figure 3.4: *Legacy (solid yellow) and BOSS (dashed purple) galaxy redshift distributions. The Legacy survey is composed of a "Main" sample with median redshift $z \sim 0.1$, and a LRG sample that is volume-complete to $z \sim 0.4$. The BOSS survey contains the spectra of the "LOWZ" sample defined in the $0.15 < z < 0.40$ redshift range, and the large "CMASS" sample, composed of galaxies targeted in the $0.4 < z < 0.8$ redshift region.*

3.1.2 BOSS spectroscopic sample

The Baryon Oscillations Spectroscopic Survey (BOSS, [60]), designed to measure the Baryon Acoustic Oscillations (BAO) scale at $z = 0.3$ and $z = 0.57$ to a 1.0% accuracy, is the largest of the four surveys that comprise the six-year SDSS-III program. It aimed to obtain the spectroscopic redshifts of 1.5 million LRG out to $z = 0.7$, and the Lyman-α absorption lines of 160,000 quasars in the $2.2 < z < 3.0$ range.

Completed on the 14th July 2014, it uniformly targeted and obtained the spectra of galaxies in two redshift ranges: $0.15 < z < 0.40$, which lead to the colour-selected "LOWZ" sample, composed of the brightest and the reddest of the low redshift galaxies; and $0.4 < z < 0.8$, designed to obtain through a series of photometric colour cuts a volume-limited sample of galaxies with approximately constant stellar mass, the so called "CMASS" sample. A total of about 1,500,000 unique galaxy spectra were measured over 10,000 deg^2 of the sky in the Northern and Southern Galactic Caps. The imaging data of these regions, shown in the top part of Fig. 3.5, was made public in the DR8 release.

The DR10 provided the spectra of 859,322 unique galaxies over 6,373 deg^2 in the sky, area displayed in Fig. 3.5. As with the *Legacy* spectra, we select only the most reliable redshifts, imposing the database flags `ZWARNING_NOQSO = 0` or `ZWARNING_NOQSO = 16`, and removing objects with `PLATEQUALITY` set to "bad" or `Z_ERR_NOQSO > 0.0006`. This gives us a sample of 855,097 galaxies. As seen from the redshift distribution in Fig. 3.4, most of BOSS galaxies lie above $z \sim 0.4$.

For the more recent DR12 considered in Chapters 5 and 6, we follow a similar approach, selecting those spectra that satisfy the following quality flag conditions: `ZWARNING_NOQSO = 0`

or `ZWARNING_NOQSO` $= 16$, `PLATEQUALITY` $=$ good, and `Z_ERR_NOQSO` < 0.001. The 9,376 deg^2 footprint of the final sample, which contains the spectra of 1,339,107 galaxies, is shown in Fig. 3.5.

3.2 SDSS cluster catalogues

Since the creation of the first catalogues of clusters of galaxies [1, 274], many efforts have been conducted to create large catalogues of these objects because of their astrophysical and cosmological interest.

Galaxy clusters can be detected in the sky using several observables. These include the X-ray emission from the hot intra-cluster gas, the Sunyaev-Zel'dovich (SZ) distortion of the CMB spectrum produced by the same gas, or the gravitational lensing distortion of background galaxies located behind clusters. The first two methods require the gas to be abundant and hot enough for the cluster to be detected by actual surveys, so usually only very massive clusters are included in catalogues that are based on these emissions. While the data from the new deeper, higher resolution lensing surveys arrives, many tens of thousands of clusters have been painstakingly identified independently by several groups using different cluster finding algorithms in the huge volume observed by the SDSS-I/II and BOSS surveys.

Among some of the recent ones based on SDSS data, we find the maxBCG catalogue by Koester et al. [111], which is based on red-sequence cluster detection techniques and has provided 13,823 clusters with photometric redshifts (hereafter photo-z's) using SDSS DR5 data. Szabo et al. [232], using an adaptive matched filter (AMF) cluster finder [65], presented an optical catalogue of 69,173 clusters in the redshift range $0.045 \leqslant z < 0.780$, based on SDSS DR6 data. This catalogue, differing from others, did not rely on the presence of a luminous central galaxy in order to detect and measure the properties of each cluster, but provided a catalogue with the three brightest galaxies associated to them. Using also DR6 photometric data, Wen et al. [259] found 39,716 clusters of galaxies below redshift $z = 0.6$, identifying as clusters those groups with more than eight $M_r \leqslant -21$ galaxies inside a determined volume. Tempel et al. [236] constructed flux- and volume-limited galaxy groups catalogues from SDSS spectroscopic data using a variable linking length friends-of-friends (FoF) algorithm. The masses of the groups were estimated using the velocity dispersion measurements via the virial theorem, and although 82,458 groups were found, only around 2,000 of them had masses above $10^{14} M_\odot$. The CAMIRA algorithm by Oguri [155], based on colour prediction of red-sequence galaxies in clusters, provided richness and photometric redshift estimates for 71,743 clusters in the $0.1 < z < 0.6$ redshift range using SDSS DR8 photometric data.

Large numbers of clusters with spectroscopic redshift measurements are needed for the analyses described in the following chapters, so here we focus on the three catalogues described below, which offer some of the largest samples of clusters to date.

3.2.1 GMBCG cluster catalogue

We use the optical-based cluster catalogue presented by Hao et al. [89], obtained applying the Gaussian Mixture Brightest Cluster Galaxy (GMBCG) algorithm to SDSS DR7 data. This cluster finding algorithm relies on the galaxy red-sequence pattern and the presence of a Brightest Cluster Galaxy (BCG) as key features of galaxy clusters. The SDSS photometric and redshift catalogues
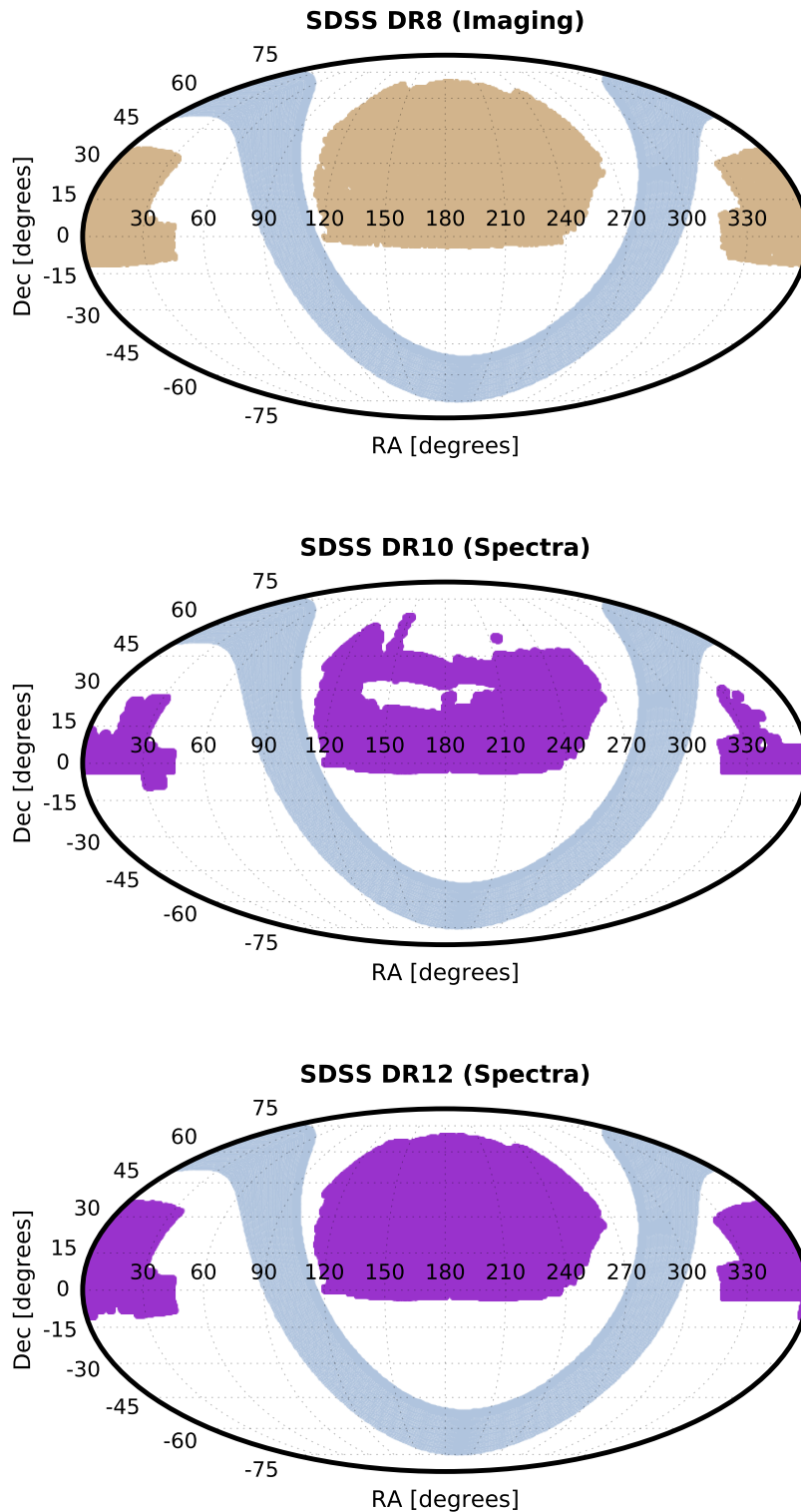
Figure 3.5: Top: *Area of the sky with imaging data, as available in DR8. Although there is extra imaging collected, these are the two contiguous areas we are interested in: in the center of the figure, the Northern Galactic Cap, and centered in* $\mathrm{RA} = 0$*, the Southern Galactic Cap.* Middle: *Sky distribution of the 855,097 BOSS galaxies with spectra that we select from the DR10.* Bottom: *The same as above but for the DR12 release, the final SDSS-III release that completed the BOSS survey, and from which we use the spectra of 1,339,107 galaxies.*
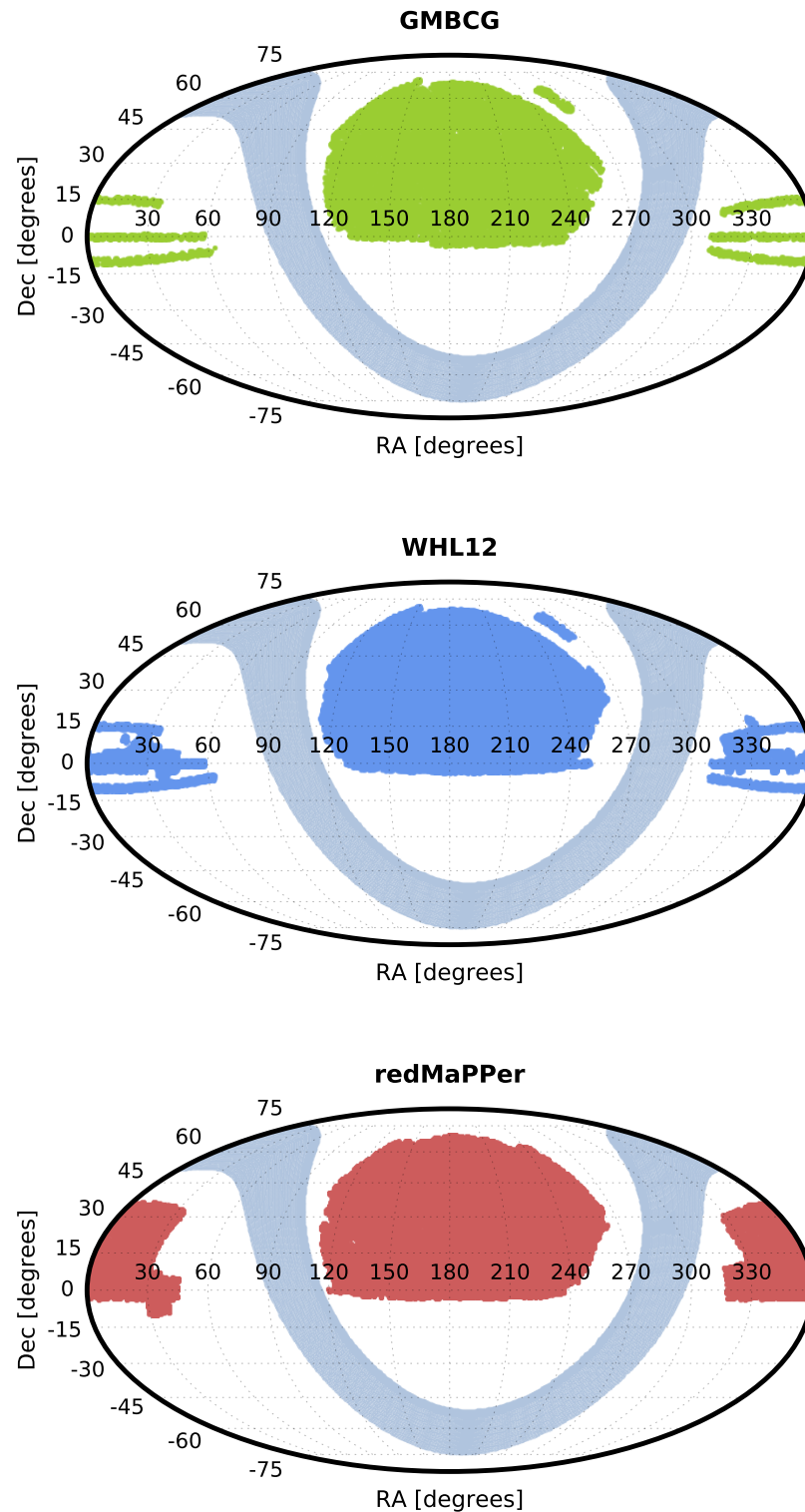
Figure 3.6: Top: *Distribution of the 20,119 GMBCG clusters in the sky with good spectroscopic measurements of their central BCG.* Middle: *Footprint in the sky of the 52,682 clusters contained in the WHL12 catalogue that have an spectroscopic redshift for their BCG.* Bottom: *Sky footprint of the 26,350 clusters contained in the redMaPPer cluster catalogue, as given in the public 5.10 version based on SDSS DR8 photometric data. From these, 16,259 contain the spectroscopic redshift of their most probable CG, number that increases to 19,473 when cross-matched with DR12 data.*
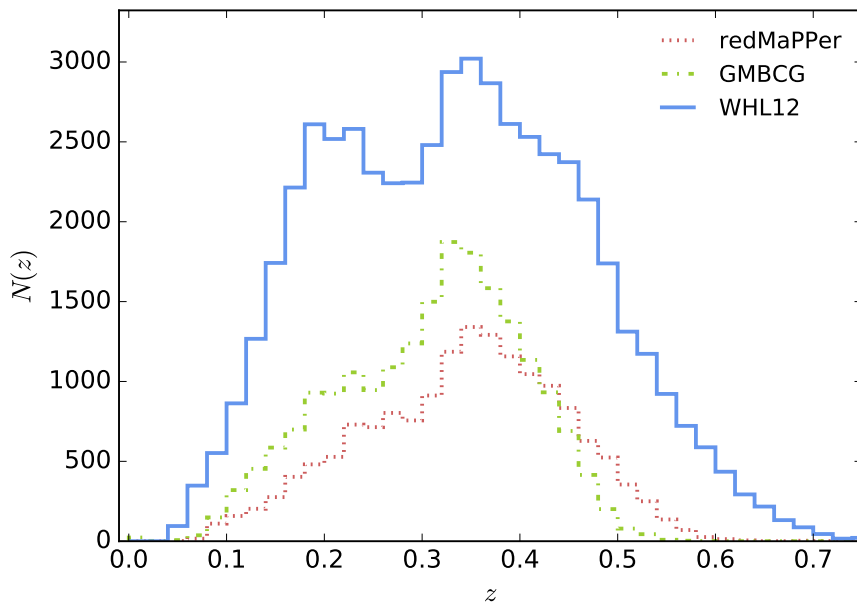
Figure 3.7: *GMBCG (dotted, red), WHL12 (continuous, blue) and redMaPPer (dashed, green) cluster redshift distributions. Only those clusters with an spectroscopic measurement of their central galaxy have been included.*

are used to determine BCG candidates. To estimate the richness N of the cluster, a combination of Gaussian fitters in colour space is used to identify overdensities around a BCG candidate among galaxies brighter than $0.4L^*$, where L^* is the characteristic luminosity of the Schechter luminosity function as given by see Blanton et al. [31], closer than $0.5\,\mathrm{Mpc}$ from the BCG, and within a photo-z range of ± 0.25. Then a circular aperture scaled to the amplitude of the overdensity around the BCG is set to recompute the richness of the cluster. Only clusters with $N \geqslant 8$ are included in the final catalogue, and their sky and spectroscopic redshift distributions are shown in Figs. 3.6 and 3.7.

The resulting sample created from the application of this method comprises 55,424 clusters, and is approximately volume limited up to redshift $z \sim 0.4$, showing high purity and completeness in this range. Of all these clusters, we are interested in just 20,119 of them, which have spectroscopic redshift measurements of their associated BCGs.

In Chapter 4, in order to have an estimation of the mass in terms of the richness values provided by the catalogue, we use the mean mass–richness relation provided by the authors of the maxBCG catalogue [193], which uses the same richness definition as the GMBCG catalogue:

$$\frac{\langle M_{500c}|N\rangle}{10^{14}\,M_\odot} = B_{M|N}\left(\frac{N}{40}\right)^{\alpha_{M|N}},\qquad(3.1)$$

with:

$$B_{M|N} = 0.95 \pm 0.07\,(\mathrm{stat}) \pm 0.10\,(\mathrm{sys})\,,$$

$$\alpha_{M|N} = 1.06 \pm 0.08\,(\mathrm{stat}) \pm 0.08\,(\mathrm{sys})\,,$$

where N accounts for the richness estimation provided by the catalogue, and M_{500c} is the cluster mass contained within the radius r_{500c}, where the mean density of the cluster is 500 times the

critical density of the Universe at the redshift of the cluster.

Finally, we would like to clarify that when the catalogue flag `WeightOK` is set equal to 1 for a cluster, we choose to work with the `GM_Ngals_weighted` richness measurement recommended by the catalogue authors, instead of `GM_Scaled_Ngals`.

3.2.2 WHL12 cluster catalogue

Using photometric redshifts, Wen et al. [260] identified 132,684 clusters from SDSS DR8 below redshift $z \sim 0.8$. This catalogue, which we denote as "WHL12" from now on, is constructed on base of a FoF algorithm that links galaxies closer than $0.5\,\mathrm{Mpc}$ in the transverse direction, and with a photo-z value differing less than $\pm 0.04(1 + z)$. When an overdensity is detected, the galaxy with the maximum number of links to other cluster candidates is taken as a temporary center, and the BCG is identified as the brightest among those galaxies closer than a linking length from this temporary center. Then, the total luminosity of the cluster candidate in the r-band is calculated as the sum of all those members with luminosities brighter than $0.4L^*$, and used to estimate its richness N_{L^*}. A galaxy cluster is included in the catalogue if $N_{L^*} \geqslant 12$.

Because of the magnitude limit of the SDSS photometric data, this catalogue is claimed to be complete up to redshift $z \sim 0.42$ to a 95% level, in the sense that there are almost no missing members among the galaxies contributing to the estimation of the cluster richness. From these 132,684 clusters, 52,682 of them have SDSS DR9 spectroscopic redshifts of the BCGs, and lie within the region of interest for us. As we can see from Fig. 3.7, WHL12 is the catalogue that provides at all redshift ranges the largest sample of clusters with an spectroscopic measurement of their BCG. The sky footprint of this catalogue is shown in Fig. 3.6.

When converting richness into mass in Chapter 4, we use the scaling relation provided by the authors of the catalogue, which reads:

$$\log_{10}\left(\frac{M_{200c}}{10^{14}\,M_\odot}\right) = (-1.49 \pm 0.05) + (1.17 \pm 0.03)\log_{10}(N)\,, \tag{3.2}$$

where N is the cluster richness. This relation was calibrated correlating the available X-ray and weak lensing masses of some of the clusters contained in the catalogue, with the richness that the algorithm had estimated for them.

3.2.3 redMaPPer cluster catalogue

More recently, Rykoff et al. [200] presented the "red-sequence Matched-filter Probabilistic Percolation" (redMaPPer) cluster finding algorithm, prepared to process large amounts of photometric data.

It may be considered an improved multi-colour evolution of the maxBCG [113] and GMBCG [89] cluster finding algorithms, as the red-sequence cluster detection and the richness estimation process were developed using the lessons obtained from those two previous catalogues.

The redMaPPer cluster finder algorithm relies on a self-training procedure that calibrates the red-sequence as a function of redshift from a sample of galaxy clusters with known red spectroscopic galaxies. This red-sequence pattern is then used in the photometric data to find potential clusters and find, through an iterative process, the central galaxies (CGs), the redshift z_λ, and the richness

λ of each cluster. The authors of this catalogue argue that their method outperforms photo-z algorithm finders in the redshift range where this catalogue is defined, although for higher redshifts others may perform better, as the red-sequence clusters are of low contrast.

Among all the other cluster catalogues described in the literature, there are several reasons why we consider redMaPPer to be the most robust and complete cluster catalogue based on SDSS data that has been produced to date. These include:

- High purity, where purity here is not understood as false detections (as it is usually defined in SZ and X-ray cluster samples), but as the fraction of clusters that is not affected by projection effects that may lead to overestimated richness measurements. According to the thorough analysis of Rykoff et al. [200], this purity is higher than the 95%, although a more recent study [217] finds a higher rate of projection effects of the order of $12\% \pm 4\%$. For $\lambda > 30$ and $z < 0.3$, the completeness is claimed to be as high as $\gtrsim 99\%$.

- A conservative low richness cutoff, or detection threshold of $\lambda/S(z) > 20$, that enhances the performance of the resulting cluster catalogue. The "scale factor" $S(z)$ is introduced in order to take into account the limited depth of the sample, so a cluster of richness λ has $\lambda/S(z)$ galaxies above the magnitude limit of the survey, and $S = 1$ at $z < 0.35$, where the DR8 is volume limited. This richness cut corresponds to a mass limit of approximately $M_{200c} \geqslant 1.4 \times 10^{14}\, M_\odot$, or $M_{500c} \geqslant 0.7 \times 10^{14}\, M_\odot$.

- Together with the photometric redshift estimates of each cluster, an SDSS spectroscopic redshift measurement is provided for the CG when available.

- Instead of providing a unique CG candidate for the cluster, the algorithm indicates the centering probability p_cen of the five most probable CGs, together with their position in the cluster.

- Provides supplementary information of the member galaxies that have been considered in the richness estimation, with their membership probability. There is information for 1,736,221 member galaxies, of which 72,642 also contain spectroscopic redshift measurements.

The richness estimator λ, developed for this sample, is based on the previous optical single-colour richness estimator λ_col of Rozo et al. [193] and Rykoff et al. [199], with several improvements to take into account things such as the survey mask, the probability of each galaxy to belong to the cluster, or the contribution of foreground and background galaxies. We refer the reader to Rykoff et al. [200] and Rozo et al. [198] for an in-depth explanation of the algorithm features.

In this catalogue the richness of a cluster is defined as:

$$\lambda = \sum p_i\, \theta_i^L\, \theta_i^R\,, \tag{3.3}$$

where p_i is the probability that each galaxy found near the cluster is actually a cluster member, and θ_i^L and θ_i^R are the luminosity and radius-dependant optimized weights:

$$\theta_i^L = \frac{1}{2}\left[1 + \mathrm{erf}\left(\frac{m_\mathrm{max} - m_i}{\sigma_i}\right)\right]\,, \tag{3.4}$$

$$\theta_i^R = \frac{1}{2}\left[1 + \mathrm{erf}\left(\frac{R(\lambda) - R}{\sigma_R}\right)\right]\,, \tag{3.5}$$

where m_max is the magnitude that corresponds to the $0.2L_*$ luminosity threshold, σ_i is the

photometric error of the galaxy i, $\sigma_R = 0.05\,h^{-1}\,\mathrm{Mpc}$, and $R(\lambda)$ the richness-dependant aperture:

$$R(\lambda) = \left(\frac{\lambda}{100}\right)^{0.2} h^{-1}\,\mathrm{Mpc}\,. \tag{3.6}$$

In Chapter 4, in order to obtain a mass estimate from the richness values included in the catalogue, we will use the mass–richness relation by Rykoff et al. [199]:

$$\ln\left(\frac{M_{200m}}{10^{14}\,h_{70}^{-1}\,M_\odot}\right) = 1.72 + 1.08\ln\left(\frac{\lambda}{60}\right)\,. \tag{3.7}$$

Although the richness estimators λ_{col} and λ differ in many aspects, it is shown that the mean deviation between them is no larger than 10%. It may be noted that this does not provide a rigorous mass calibration, as it is based on abundance matching techniques using the mass function by Tinker et al. [237], and it has not been corrected for selection effects. A more precise mass–richness relation has benn announced to be released in the future by the authors. Meanwhile we will make use of this relation.

This cluster finder algorithm was designed to process future large photometric surveys like DES and LSST, but it has been already run on the SDSS DR8 photometric and SDSS DR9 spectroscopic data in order to check the possible systematics associated to the algorithm itself, and compare its results with other clusters catalogues, like the SZ *Planck* cluster catalogue [197], or the X-CLASS X-ray clusters [203]. These analyses led first to an updated 5.10 public version of the algorithm, described in Rozo et al. [198], and later to a 6.3 version, detailed in Rykoff et al. [201].

The first publicly available DR8 redMaPPer catalogue covered an effective area of 10,400 deg^2, displayed in Fig. 3.6, and contained 25,236 clusters in the $0.08 \leqslant z_{\mathrm{photo}} \leqslant 0.55$ redshift range, of which 13,128 also had spectroscopic measurements of their CG. The redshift distribution of the clusters with spectroscopic measurements in this catalogue is shown in Fig. 3.7, and a sample of optical images of a selection of reMaPPer clusters at different redshift ranges can be seen in Fig. 3.8. The photometric sample was increased to 26,350 clusters in the updated 5.10 version, and decreased to 26,111 in the 6.3 version. Finally, it should be mentioned that this catalogue is claimed to be volume-complete up to $z \lesssim 0.33$.

Figure 3.8: *SDSS optical images of a selection of clusters included in the redMaPPer catalogue, with a value of the richness $\lambda > 80$. From top to bottom, the rows correspond to clusters in the redshift ranges: $z \in [0.1, 0.2)$, $[0.2, 0.3)$, $[0.3, 0.4)$ and $[0.4, 0.55)$. The scale of the images is fixed to 3 arcmin $\times$ 3 arcmin in all cases.*

PART II

Results

4

Gravitational Redshift and Redshift Enhancement in Clusters

The evolution of the mass function of galaxy clusters is sensitively related to cosmology via the dynamically opposing effects of gravity and the cosmological acceleration (Chapter 1, see Huterer et al. [96] for a thorough review). It has been claimed that with only a few hundred massive clusters below redshift $z \sim 0.5$, competitive constraints on the standard cosmological model and a consistency check of the viability of General Relativity on cluster scales can be achieved [5, 134, 184]. In terms of the standard model, the parameters most sensitively constrained are the normalization of the mass function, σ_8, and the cosmological mean matter density, Ω_m. These parameters can, in principle, be constrained using the most massive clusters [90, 255, 257]. Currently the samples of clusters constructed for these purposes are X-ray or Sunyaev-Zel'dovich (SZ) effect selected so that the masses are generally inferred from indirect scalings derived from other samples of clusters at lower redshift related to lensing and/or internal dynamics. Efforts are underway to obtain accurate masses of sizeable samples of massive clusters from deep multi-band lensing observations, such as the CLASH survey [141, 246] and the "Weighing the Giants" project [253]. These samples are a substantial step forward in that lensing based masses can indeed be constructed, but they still rely on X-ray selection, with a significant scatter and the possibility to be affected by serious biases when inferring masses indirectly this way [193]. Ideally the sample selection would be best made by selecting clusters in a volume limited way from densely sampled redshift surveys with masses obtained by weak lensing. Large surveys with the resolution required for weak lensing work are underway: HSC [233], JPAS [27] and planned eBOSS, Large Synoptic Survey Telescope (LSST), EUCLID, Wide-Field Infrared Survey Telescope (WFIRST), and the Dark Energy Survey (DES), but currently no statistical sample of clusters selected this way exists so far.

The relation between richness and mass has been shown to be fraught with systematic uncertainty [193], related perhaps mainly to the complexities of gas physics that may be expected to significantly complicate the conversion of X-ray or SZ luminosities to total cluster mass. Weak lensing mass measurements for subsamples of relaxed clusters can help reduce the scatter in mass-observable scaling relations [253]. Recent cluster weak lensing efforts with deep Subaru observations have achieved an accuracy of sub-10% in the overall cluster mass calibration [246, 253], which is currently limited by relatively small sample sizes.

Using three of the largest cluster catalogues produced to date, namely the GMBCG, the WHL12 and the redMaPPer catalogues described in Chapter 3, we relate the optical richness to statistical measures of mass related observables, in particular we focus here on two independent effects related to the gravitational fields of clusters of galaxies: gravitational redshift and gravitational

magnification, both described in Chapter 2.

Wojtak et al. [264] claimed in 2011 to have measured for the first time the gravitational redshift effect, using the GMBCG cluster catalogue and DR7 data. As for the redshift enhancement effect, a significant first detection of this effect has been also reported recently by Coupon et al. [52] combining SDSS clusters and lensing background galaxies from the BOSS survey. Here we explore these effects further with the new data releases in an enlarged sample of clusters and background galaxies, allowing new correlations to be examined in this context.

In this chapter, after converting richness into mass in Sec. 4.1 using the pertinent mass–richness relations, and fitting an effective mass function to the number density distributions needed for the models, we define in Sec. 4.2 the phase space region in which we study the velocity distribution of galaxies around clusters to identify any possible gravitational redshift or internal motion related effects. For the magnification we examine in Sec. 4.3 the mean redshift of background BOSS galaxies, and report our conclusions in Sec. 4.4.

Throughout this chapter we adopt the cosmological parameters of a fiducial spatially flat WMAP7 ΛCDM cosmology [114] with $H_0 = 72\,\mathrm{km\,s^{-1}\,Mpc}$ and $\Omega_m = 0.26$.

4.1 Data

In order to obtain a decent signal-to-noise ratio, thousands of clusters are needed to statistically investigate their gravitational redshift and lensing properties. For that reason we focus our analysis in the three cluster catalogues described in Chapter 3, the GMBCG (Sec. 3.2.1), the WHL12 (Sec. 3.2.2), and the redMaPPer (Sec. 3.2.3) catalogue, which offer some of the largest samples of clusters with precise spectroscopic redshift measurements of their central galaxies, mandatory in the gravitational redshift analysis. The spectroscopic redshift and sky distributions of these cluster samples are shown in Figs. 3.6 and 3.7.

Throughout this chapter we convert the richness observable into mass using the mass–richness relations appropriate for each case. We do this because we need to model the gravitational redshift and the lensing magnification amplitudes, which result from the contribution of clusters of very different mass ranges. Because we do not intend to constrain any cosmological parameter, for our purposes a rough estimation of the mass function, that is, the number density of cluster as a function of their mass, is enough.

To quantify cluster masses we adopt M_{200m} units, i.e., mass measured with respect to 200 times the mean background density of the Universe. Because the mass–richness relations provided by the authors of the catalogues are given in different units, when needed we use the prescription given by Hu and Kravtsov [95] to convert between different mass definitions, which assumes a Navarro-Frenk-White ([152], hereafter NFW) halo density profile. To obtain the appropriate concentration parameters needed for this conversion, we use the mass–concentration relations provided by Bhattacharya et al. [29]. After converting to M_{200m} the richness values provided by the three catalogues, we fit a Press-Schechter-like mass function to the observed cluster mass-density distributions, shown in Fig. 4.1.

We summarise the cluster samples properties in Table 4.1, where the final number of clusters considered in this study, N_{clusters}, takes into account the strong restrictions described in Sec. 4.2.

As for the galaxy catalogues used in this analysis, we have selected from the *Legacy* spectroscopic
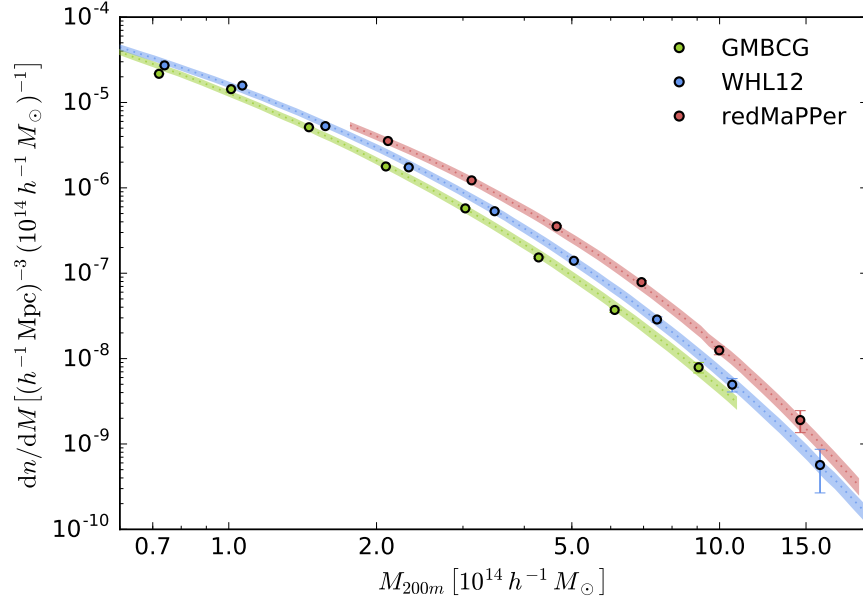
Figure 4.1: *Observed mass distributions of clusters after converting richness into mass using the corresponding mass–richness relations. Here $\mathrm{d}n/\mathrm{d}M$ is the differential number of clusters per unit of comoving volume and unit of mass. In order to model these mass distributions, for each cluster sample we fitted a Press-Schechter-like mass function, shown as the dotted lines, which spans from the least massive cluster contained in each catalogue, to the most massive one. The shaded regions represent 90% confidence range.*

Catalogue	N_{clusters}	$\langle z \rangle$	$\langle M_{200m} \rangle [10^{14}\, h^{-1}\, M_\odot]$
GMBCG	4,278	0.22	1.5
WHL12	12,661	0.19	1.4
redMaPPer	3,372	0.23	3.2

Table 4.1: *Final number of clusters, mean redshift, and mean estimated mass of the samples considered.*

SDSS sample the cluster galaxies needed to construct the phase space distribution of galaxies in which to measure the gravitational redshift effect. For the redshift enhancement measurement, we restrict background galaxies to those contained in the CMASS sample, which are located at $z > 0.43$.

Because the majority of the work presented in this chapter is based on Jimeno et al. [99], the data that we use is collected from DR10. However, at the end we include part of the results shown in Jimeno et al. [100], that make use of the more recent DR12. As we explained in Chapter 3, these two data releases share the same imaging photometric information, and thus there should not be much difference between the cluster catalogues produced from them. However, the increased number of CMASS background galaxies lets us obtain a much more precise measurement of the redshift enhancement effect.

4.2 Gravitational redshift

We now investigate the signal associated to the gravitational redshift and the other components of the internal redshift distortions found in clusters of galaxies. The origin and observational consequences of these effects is explained in detail in Sec. 2.3.1 of Chapter 2.

4.2.1 Model

We compute now the expected internal redshift distortion, Δz, coming from the gravitational redshift (GR), transverse Doppler (TD), past light cone (LC) and surface brightness (SB) effects for GMBCG, WHL12 and redMaPPer catalogues. The internal redshift that one would observe at a projected transverse distance $r_\perp$ from the center of a cluster halo with mass M would be:

$$\Delta z = \Delta z_{\mathrm{GR}} + \Delta z_{\mathrm{TD}} + \Delta z_{\mathrm{LC}} + \Delta z_{\mathrm{SB}} \,. \tag{4.1}$$

First, we compute the redshift distortion induced by the pure gravitational redshift as:

$$\Delta z_{\mathrm{GR}} = \frac{-2}{c^2 \, \Sigma(r_\perp)} \int_{r_\perp}^{\infty} \Delta\Phi(r) \frac{\rho_{\mathrm{NFW}}(r) \, r \, \mathrm{d}r}{\sqrt{r^2 - r_\perp^2}} \,, \tag{4.2}$$

where Σ is the 2-dimensional projected surface density of the 3-dimensional NFW density profile ρ_{NFW} of a cluster halo with mass M, $r_\perp$ is the transverse distance from the center of the halo, and $\Delta\Phi(r)$ is the potential energy difference between r and the center of such halo.

Then, we model the redshift distortions induced by the "kinematic" effects as:

$$\Delta z_{\mathrm{TD}} = \frac{1}{2 \, c^2} \left(\langle |\vec{v}_{\mathrm{gal}}|^2 \rangle - |\vec{v}_{\mathrm{BCG}}|^2 \right) , \tag{4.3}$$

$$\Delta z_{\mathrm{LC}} = \frac{1}{c^2} \left(\langle |\vec{v}_{\mathrm{los\,gal}}|^2 \rangle - |\vec{v}_{\mathrm{los\,BCG}}|^2 \right) , \tag{4.4}$$

where the $\vec{v}_{\mathrm{gal}}$, $\vec{v}_{\mathrm{BCG}}$, $\vec{v}_{\mathrm{los\,gal}}$ and $\vec{v}_{\mathrm{los\,gal}}$ correspond to the velocities and the line-of-sight component of the velocities of the satellite galaxies and the BCGs, and use the prescription given by Zhao

et al. [270] to compute $\langle |\vec{v}_{\mathrm{gal}}|^2 \rangle$ as a function of the potential via the isotropic Jeans equation:

$$\langle |\vec{v}_{\mathrm{gal}}|^2 \rangle = 3\,\sigma_{\mathrm{los}}^2 = 3\,\langle \sqrt{r^2 - r_\perp^2}\,\frac{\partial \Phi(r)}{\partial(\sqrt{r^2 - r_\perp^2})} \rangle . \tag{4.5}$$

Finally, we take into account the SB effect adding the additional redshift deviation:

$$\Delta z_{\mathrm{SB}} = \frac{-\langle |\vec{v}_{\mathrm{los\,gal}}|^2 \rangle}{c^2}\,\langle (3 + \alpha(z))\,\frac{\mathrm{d}\ln n_{\mathrm{obs}}[> L_{\mathrm{lim}}(z)]}{\mathrm{d}\ln L} \rangle . \tag{4.6}$$

The value of $\alpha(z)$, the effective spectral index in SDSS r band, can be taken to be approximately 2 [105] considering the average redshift of the sample and the typical spectral energy distribution (SED) of the galaxies with which we are measuring this effect. To compute $\mathrm{d}\ln n/\mathrm{d}\ln L$, we take $r < 17.77$ as the apparent magnitude limit for our galaxies sample, and use the estimate of the luminosity function in the r-band given by Montero-Dorta and Prada [145] based on DR6 data, whose Schechter best fit parameters (see Eq. 2.11) are $\Phi^* = 0.0093$, $M^* - 5\log_{10} h = -20.71$ and $\alpha = -1.26$. It would be more accurate to use the specific luminosity function associated to galaxies belonging to the clusters considered, but it was shown by Hansen et al. [88] that it does not differ much from the overall survey luminosity function, so we can use it as a good approximation. To calculate the average in Eq. 4.6, we do:

$$\langle \mathrm{d}\ln n/\mathrm{d}\ln L \rangle = \frac{\int_{z_1}^{z_2} (\mathrm{d}\ln n/\mathrm{d}\ln L)\,(\mathrm{d}N/\mathrm{d}z)\,\mathrm{d}z}{\int_{z_1}^{z_2} (\mathrm{d}N/\mathrm{d}z)\,\mathrm{d}z} , \tag{4.7}$$

where $\mathrm{d}N/\mathrm{d}z$ is taken from the *Legacy* galaxy redshift distribution as displayed in Fig. 3.4. The lowest z_1 and highest z_2 redshift limits of integration are chosen according to the cluster sample considered in each case.

Combining all these effects, the expected internal velocity distortion from an stacked sample of clusters is obtained convolving Δz with the distribution of masses contained in the cluster sample:

$$\Delta(r_\perp) = c\,\frac{\int_{M_1}^{M_2} \Delta z\,(r_\perp)\,\Sigma(r_\perp)\,(\mathrm{d}n/\mathrm{d}M)\,\mathrm{d}M}{\int_{M_1}^{M_2} \Sigma(r_\perp)\,(\mathrm{d}n/\mathrm{d}M)\,\mathrm{d}M} , \tag{4.8}$$

where we integrate in the mass range defined by the lowest M_1 and highest M_2 masses considered in each catalogue, and the mass distribution in each case is given by $\mathrm{d}n/\mathrm{d}M$, which is functionally fitted from the observed distribution of clusters, as in Fig. 4.1, but in this case considering only those that were not discarded in the process, that is, with sufficient nearby galaxies with spectroscopic measurements for a meaningful measurement. The model curves predict almost the same internal redshift distortion for both GMBCG and WHL12 cluster samples, as the lowest mass and the mass distribution of clusters are almost identical for both catalogues. The main difference between these two catalogues, i.e., WHL12 ranging to higher masses, does not noticeably change the shape of the model curve as the contribution coming from high mass clusters is highly suppressed by the low values of the mass function at these scales. The redMaPPer model curve, in the other hand, predicts a larger signal amplitude, which is consistent with the fact that redMaPPer minimum richness value is much higher than GMBCG and WHL12 ones, resulting in a higher average cluster mass.

4.2.2 Results

In order to study the spatial distribution of galaxies around clusters, first, we carefully remove from the SDSS *Legacy* and BOSS galaxy catalogues those galaxies identified as the BCGs of the cluster catalogues. Here we take into account the fact that, according to SDSS specifications, two galaxies with spectroscopic measurements are considered the same object if they are closer than 3 arcsec in the *Legacy* survey case, and 2 arcsec in the BOSS survey case. This also helps us identify which of the BCGs have the best spectroscopic measurements, so, in order to reduce the noise introduced by uncertainties in the estimation of the center of the cluster, we only work with those BCGs identified in our "high quality" SDSS galaxy sample, discarding this way BCG redshift measurements obtained from "bad" plates. This leaves us with a total sample of 19,867 BCGs in the GMBCG catalogue, 52,255 in the WHL12 case, and 10,197 in the redMaPPer one.

After the selection of field and central galaxies is done, we compute the projected transverse distance $r_\perp$ and the line-of-sight velocity $v_{los} = c\,(z_{\mathrm{gal}} - z_{\mathrm{BCG}})/(1 + z_{\mathrm{BCG}})$ of all galaxies with respect to the BCGs, and keep those that lie within a separation of $r_\perp < 7\,\mathrm{Mpc}$ and $|v_{los}| < 6{,}000\,\mathrm{km\,s^{-1}}$ from these. Stacking all the obtained pairs into one single phase space diagram, we get the density distributions shown on the left handside of Fig. 4.2. It should be noted that, as we are working mainly in a low redshift region, the impact of the cosmological parameters used to compute distances is not significant.

To remove the contribution of foreground and background galaxies not gravitationally bound to clusters, we adopt an *indirect* approximation, where galaxies not belonging to clusters are not identified individually in each cluster, as in the *direct* method, but taken into account statistically once all the cluster information has been stacked into one single distribution of galaxies. See Wojtak et al. [263] for a detailed study of different direct and indirect foreground and background galaxies removal techniques.

In our case, we apply the following procedure: first, we bin the whole phase space distribution in cells of size $0.04\,\mathrm{Mpc} \times 50\,\mathrm{km\,s^{-1}}$. After that, we take all those bins lying in two "boundary" stripes $4{,}500\,\mathrm{km\,s^{-1}} < |v_{los}| < 6{,}000\,\mathrm{km\,s^{-1}}$, and fit to the values found there a quadratic polynomial that depends on both v_{los} and $r_\perp$. Here we have assumed that all the galaxies in these regions belong either to the pure foreground $(v_{los} < -4{,}500\,\mathrm{km\,s^{-1}})$ or to the pure background $(v_{los} > 4{,}500\,\mathrm{km\,s^{-1}})$ sample. Then, we use this interpolated background model to correct the "inner" phase space region $(|v_{los}| < 4{,}500\,\mathrm{km\,s^{-1}})$ bins. The background-corrected phase space diagrams for the three cluster catalogues can be seen on the right handside of Fig. 4.2.

In Fig. 4.2 we can spot two clearly distinguishable regions: the "inner", dynamically relaxed, region of the cluster at $r_\perp \lesssim 1.5 - 2\,\mathrm{Mpc}$, where iso-density contours are closed, and, at larger radius, the "outer" radial infall region, highly compressed along the line of sight. This characteristic trumpet-shaped phase space distribution, related to the escape velocity, is applied as a "caustic method" [62] to infer cluster mass profiles dynamically, where many redshifts of cluster members can define the caustic location. See Zu and Weinberg [273] and Lam et al. [120] for recent developments on the field.

Following the method described in Wojtak et al. [264], we split the background-corrected phase space diagram into different transverse distance bins, and measure the galaxy velocity distributions within these bins. In order to fit these distributions and detect any possible deviation from
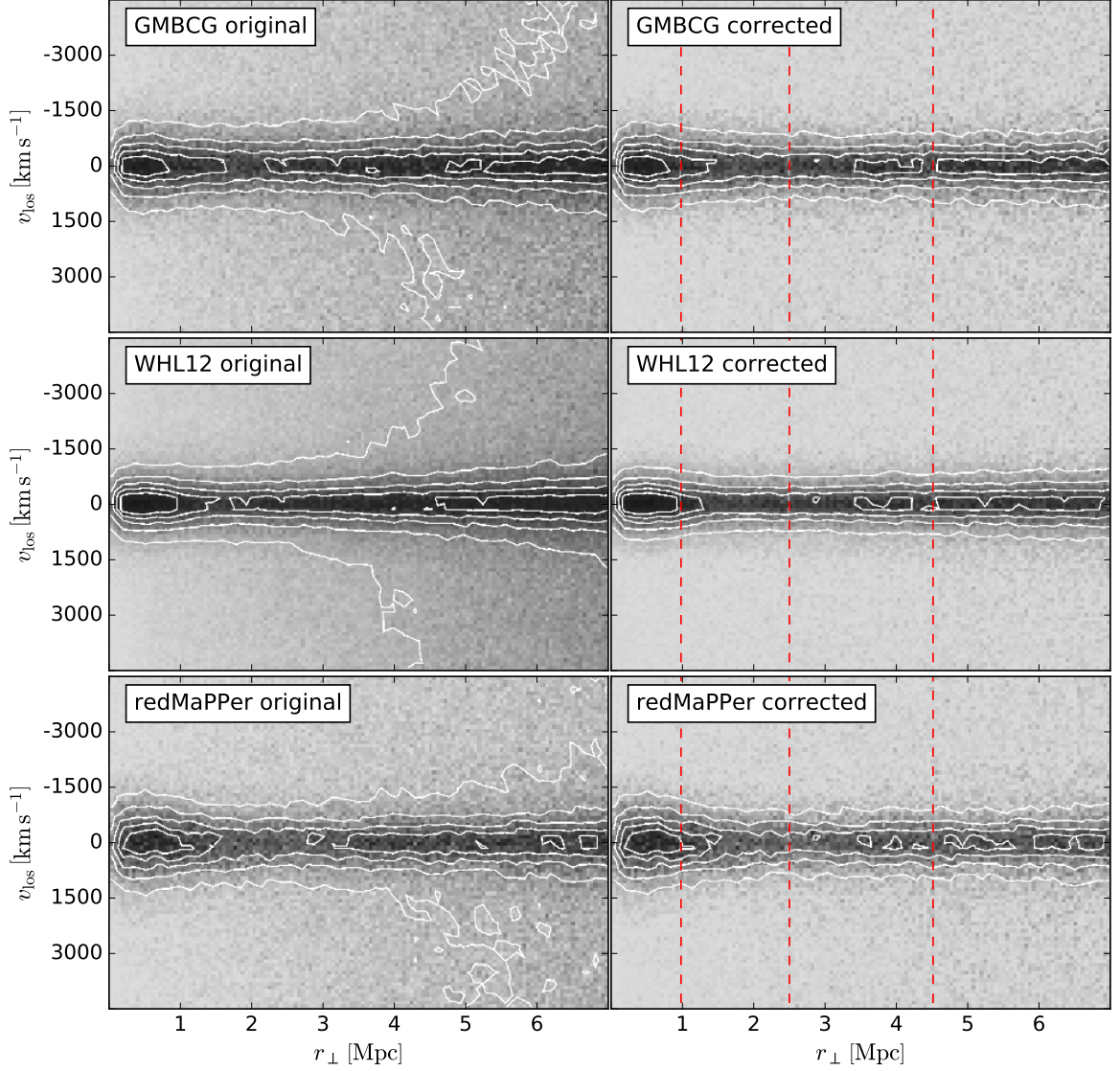
Figure 4.2: *GMBCG (top), WHL12 (middle) and redMaPPer (bottom) phase space diagrams before (left) and after (right) removing statistically the contribution from foreground and background galaxies. White contours represent iso-density regions. The asymmetry between the distribution of galaxies in the positive and negative v_{los} regions can be particularly clearly seen in the redMaPPer case. This difference disappears after the statistical interloper removal. We also plot as red dashed lines the boundaries at 1, 2.5 and $4.5 \, \mathrm{Mpc}$ that determine the 4 radial bins considered. In these diagrams, the position of the BCG is fixed at $r_\perp = 0 \, \mathrm{Mpc}$ and $v_{los} = 0 \, \mathrm{km \, s^{-1}}$ by definition, and the density is determined by the number of galaxies with spectroscopic redshift measurements around them.*
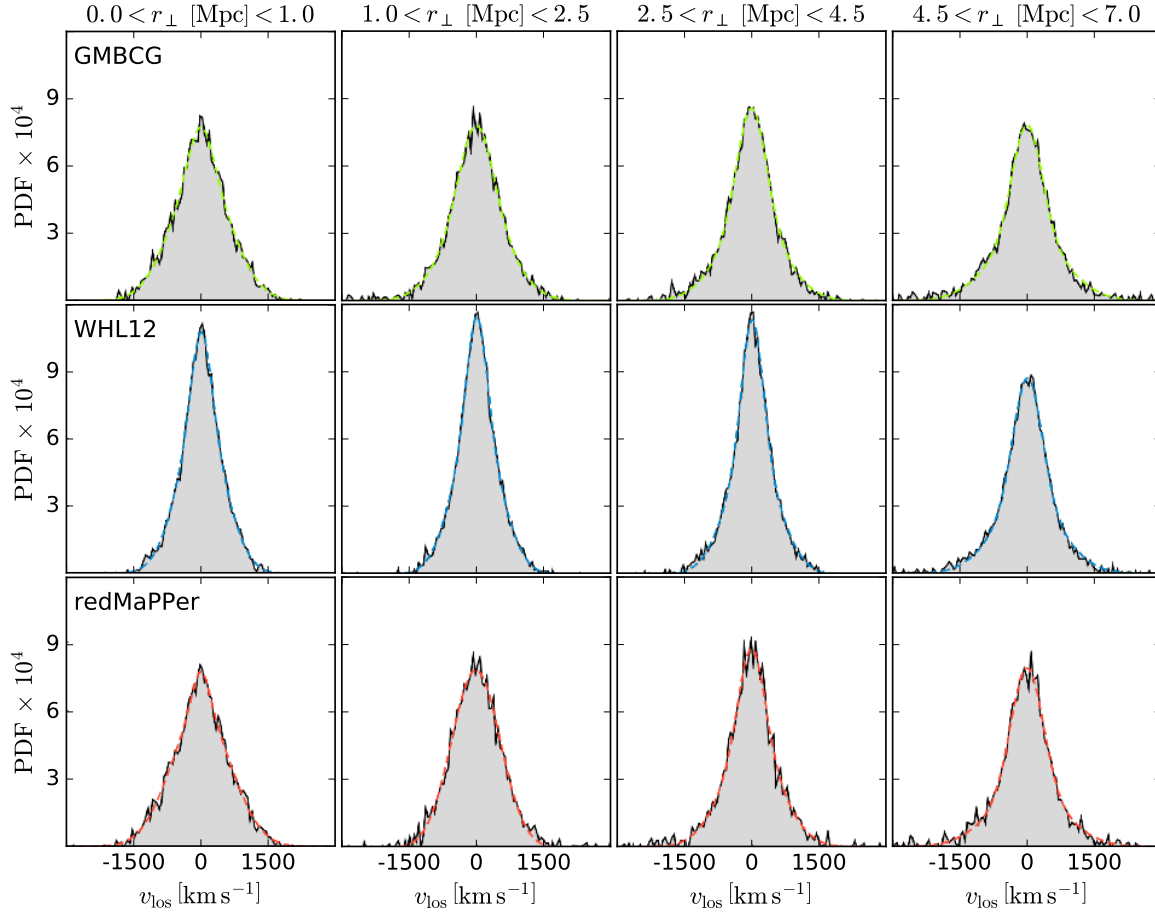
Figure 4.3: *GMBCG (top), WHL12 (middle) and redMaPPer (bottom) velocity distributions for 4 different radial bins, after the background and foreground contribution of galaxies has been removed. In top of these distributions, as dashed curves, the double Gaussian functional fits that provide the values of Δ, the deviation from $\langle v_{los} \rangle = 0$.*

$\langle v_{los} \rangle = 0$, we adopt the double Gaussian functional form:

$$f(v_{los}) = A \exp\left[\frac{(v_{los} - \Delta)^2}{2\,\sigma_A^2}\right] + B \exp\left[\frac{(v_{los} - \Delta)^2}{2\,\sigma_B^2}\right], \tag{4.9}$$

where both Gaussians, each with different amplitude and variance, share the same mean velocity Δ.

We now present the results obtained for each of the catalogues used in our analysis.

GMBCG catalogue

In order to work only with the most reliable data, we decide to use only those clusters with 6 or more galaxies with an spectroscopic redshift measurement in the previously defined "inner" phase space region, $7\,\mathrm{Mpc}$ and $\pm 4{,}500\,\mathrm{km\,s^{-1}}$. We also restrict our sample to those clusters located in the redshift range $0.1 \leqslant z \leqslant 0.4$, where the catalogue is claimed to be complete, and with
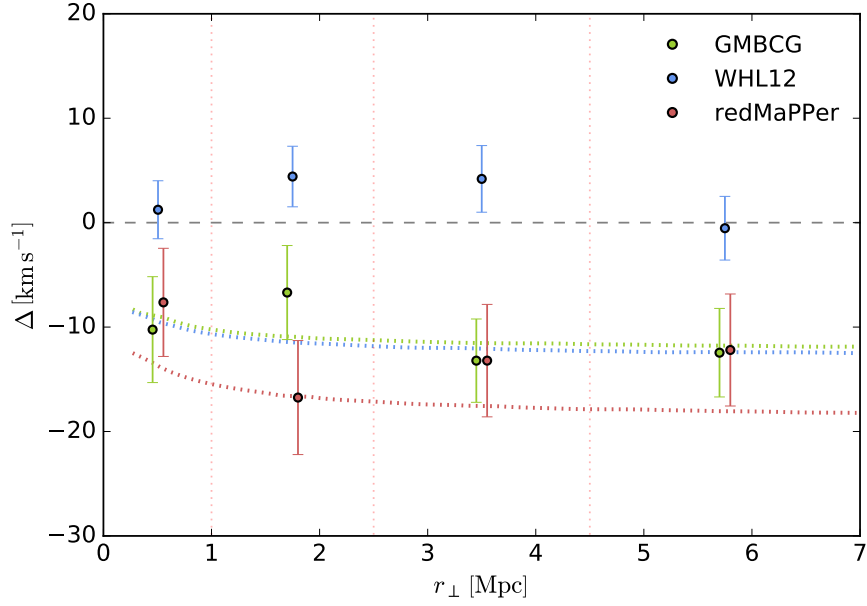
Figure 4.4: *GMBCG (green), WHL12 (blue) and redMaPPer (red) Δ points for 4 different projected radial bins. The $r_\perp$ boundaries of these projected radial bins, marked as dashed red vertical lines, are: 0, 1, 2.5, 4.5 and $7\,\mathrm{Mpc}$. Dotted curves represent predictions from model. GMBCG and WHL12 model curves are almost identical, as the mass distribution of the clusters contained in these catalogues is very similar. On the other hand, redMaPPer clusters are on average much more massive, leading to an expected stronger effect.*

a richness larger than 10, which corresponds to $M_{200m} \sim 0.75 \times 10^{14}\,h^{-1}\,M_\odot$. From the initial 19,867 clusters contained in the spectroscopic catalogue, this leaves us with a sample of 4,278 objects, with mean richness 18 (corresponding to $M_{200m} \sim 1.5 \times 10^{14}\,h^{-1}\,M_\odot$), and mean redshift $z \approx 0.22$.

The velocity distribution and the resulting double Gaussian fits of the 4 radial bins considered are shown in the top part of Fig. 4.3. The corresponding values of Δ obtained from the fits are displayed in Fig. 4.4. These values are negative for all the radial bins, and seem to be consistent with the model proposed, for which the prediction is a nearly flat profile of $\Delta \sim -10\,\mathrm{km\,s^{-1}}$ at radius beyond $r_\perp > 0.5\,\mathrm{Mpc}$ from the central BCG position. Our measurements are compatible with those obtained by Wojtak et al. [264], the difference between them coming from the different radial binning used.

We also divide the data into different mass bins in order to test how the amplitude of the signal changes with cluster mass. As before, we select only those clusters with 6 spectroscopic BCG-galaxy pairs or more. Then, we divide the resulting sample into 3 different mass subsamples. For each of these subsamples we would like to measure the integrated signal up to a certain radius $r_\perp$, but, as we expect cluster size to increase with richness, at a fixed distance galaxies in high richness clusters are located deeper in the gravitational potential than in low richness clusters. In order to make the measurements more comparable, we convert the projected $r_\perp$ radial distances from the BCGs into r_{200c} units, i.e., we rescale the comoving transverse distances of the galaxies that belong to a particular cluster using the r_{200c} estimate of that cluster, obtained assuming a NFW halo density profile, and using the mass–concentration relations provided by Bhattacharya et al. [29], as explained in Sec. 4.1. We then measure, for each of the mass subsamples, the integrated signal of
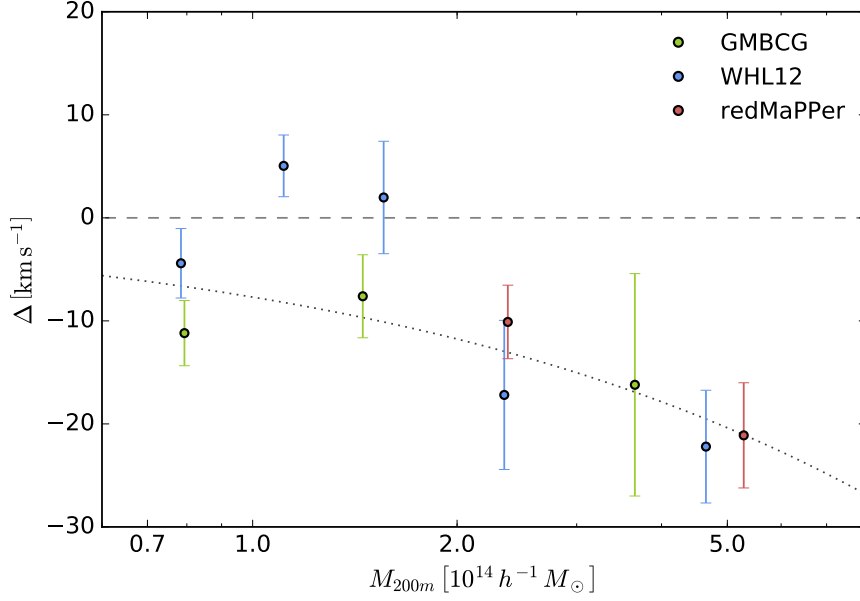
Figure 4.5: *Measurements of the integrated signal of Δ to a distance of $7\,r_{200c}$, for 3 different mass bins in the GMBCG cluster sample (green), 5 bins in the WHL12 one (blue), and 2 in the redMaPPer case (red). Dotted curve represents model prediction.*

Δ up to $7\,r_{200c}$, and the resulting values obtained are displayed in Fig. 4.5. The first and the second mass subsamples, with average masses of $\sim 0.8\times10^{14}\,h^{-1}\,M_{\odot}$ and $1.4\times10^{14}\,h^{-1}\,M_{\odot}$, show values of Δ equal to $-11.2\pm3.2\,\mathrm{km\,s^{-1}}$ and $-7.6\pm4.0\,\mathrm{km\,s^{-1}}$, respectively. The third mass subsample, with a higher average mass of $\sim 3.6\times10^{14}\,h^{-1}\,M_{\odot}$, gives a value of $\Delta = -16.2\pm10.8\,\mathrm{km\,s^{-1}}$. The error in this last measurement is such that it seems inappropriate to claim an observed signal dependence with increasing mass, despite the seemingly detection of a negative internal redshift distortion signal for the three mass subsamples taken together.

WHL12 catalogue

Taking the same conservative approach, we discard all those clusters with less than 6 spectroscopic BCG-galaxy pairs in the phase space defined region. On the other hand, although the WHL12 catalogue is claimed to be complete over a wider redshift range than the GMBCG catalogue, we decide to adopt the same limited range, $0.1 \leqslant z \leqslant 0.4$, in order to reduce the potential for any systematic differences between measurements, making further comparisons easier to interpret. These limitations leave us with a sample of 12,661 clusters, with a mean richness of 23 (corresponding to $M_{200m} \sim 1.4\times10^{14}\,h^{-1}\,M_{\odot}$), and a mean redshift of $z \approx 0.19$. The resulting velocity distribution and fits are displayed in the middle part of Fig. 4.3 for the 4 different radial bins used, and the fitted values of Δ are shown in Fig. 4.4. As we can observe from the figure, the measured signal deviates completely from the model proposed: the first and fourth radial bins, centered at $1\,\mathrm{Mpc}$ and $5.75\,\mathrm{Mpc}$, show values of Δ consistent with zero. Even worse, the second and third radial bins, centered at $1.75\,\mathrm{Mpc}$ and $3.5\,\mathrm{Mpc}$, display positive values of $\Delta \sim +5\,\mathrm{km\,s^{-1}}$.

The number of clusters contained in this catalogue is large enough as to split it into different

mass bins and still have enough number of objects to have a decent signal-to-noise ratio and test the reliability of this detection. In this case we divide those clusters with more than 5 galaxies with spectroscopic redshifts into 5 different mass subsamples. As before, we measure, for each of these mass subsamples, the integrated signal of Δ up to $7\,r_{200c}$, where here we use the estimation of r_{200c} provided by the WHL12 cluster finder algorithm, a more direct indicator of the size and concentration of each cluster. The resulting values obtained are displayed in Fig. 4.5. In this case, the results obtained seem to be more illustrative than in the GMBCG case. The Δ value obtained from the first mass subsample, with an average $M_{200m} \sim 0.8 \times 10^{14}\,h^{-1}\,M_\odot$, seems to be in agreement with the model prediction, but the signal obtained is very weak, compatible with zero at the $\sim 1\sigma$ level. The second and third mass subsamples, with average masses around $1.1 \times 10^{14}\,h^{-1}\,M_\odot$ and $1.6 \times 10^{14}\,h^{-1}\,M_\odot$, show positive values of Δ. However, the fourth and fifth mass subsamples, whose average masses are $2.4 \times 10^{14}\,h^{-1}\,M_\odot$ and $4.6 \times 10^{14}\,h^{-1}\,M_\odot$ respectively, with values of Δ equal to $-17.2 \pm 7.2\,\mathrm{km\,s^{-1}}$ and $-22.2 \pm 5.4\,\mathrm{km\,s^{-1}}$, indicate a trend of a larger negative signal for larger cluster masses, corresponding to what one would expect from the model. We may think of this as a result of the cluster finding algorithm being more efficient in the task of identifying real clusters and their corresponding BCG for halo masses above $M_{200m} \sim 2 \times 10^{14}\,h^{-1}\,M_\odot$, or the noise introduced by substructure and cluster mergers being less important for massive, relaxed clusters. In any case, it is clear that the positive values obtained in the radial global measurement of Δ are explained by the fact that the clusters in the WHL12 catalogue residing in this less massive region dominate over the more massive and "reliable" ones. The difference between GMBCG and WHL12 measurements may reside precisely in the fact that GMBCG algorithm is optimised to identify red-sequence clusters and WHL12 relies only on galaxy friends-of-friends counting for their detection. The former method may contain a higher percentage of concentrated clusters, with a higher degree of virialisation resulting in concordance between the measurement of internal redshift distortion effects and the model for which virialisation is assumed.

redMaPPer catalogue

We also restrict the redMaPPer sample to those clusters in the $0.1 \leqslant z \leqslant 0.4$ redshift range and with 6 or more galaxies with spectroscopic redshift measurements, reducing their number from 10,197 to only 3,372, these having a mean richness of 35 (corresponding to $M_{200m} \sim 3.2 \times 10^{14}\,h^{-1}\,M_\odot$, the double than in the two previously considered catalogues), and a mean redshift of $z \approx 0.23$. The velocity distribution with the corresponding double Gaussian fits and the resulting values of Δ obtained from them are shown in Figs. 4.3 and 4.4 respectively. Although the amplitude of the signal is expected to be higher for this cluster sample, apart from the second radial bin centered at $r_\perp = 1.75\,\mathrm{Mpc}$, with $\Delta = -16.7 \pm 5.5\,\mathrm{km\,s^{-1}}$, all the other radial measurements of Δ do not deviate more than $\pm 2\,\mathrm{km\,s^{-1}}$ from the measurements obtained using the GMBCG catalogue. Even when all the Δ measured points remain negative, there is no clear evidence for a stronger internal redshift signal compared to the one provided by GMBCG catalogue.

Now, as the number of clusters is relatively small, we measure the integrated signal of Δ up to $7\,r_{200c}$ for only two mass subsamples of clusters. In this case, we use, as in the GMBCG case, the r_{200c} estimates obtained assuming a NFW density profile for the clusters considered. The resulting measurements for the two mass bins, $\Delta = -10.1 \pm 3.5\,\mathrm{km\,s^{-1}}$ and $-21.1 \pm 5.1\,\mathrm{km\,s^{-1}}$ at $M_{200m} = 2.4 \times 10^{14}\,h^{-1}\,M_\odot$ and $5.3 \times 10^{14}\,h^{-1}\,M_\odot$, respectively, are displayed in Fig. 4.5. This comparison shows that the measured amplitude of Δ appears to be higher for the high-mass sample than for the low-mass one at 1.8σ significance. It is also reassuring that these measurements

follow closely the model prediction.

4.3 Redshift enhancement

In this section we describe the measurement of the redshift enhancement of background galaxies behind the SDSS clusters due to lens magnification described in Sec. 2.3.2 of Chapter 2. This may help elucidate further the results we have found above for the gravitational redshift. We are interested in seeing to what extent the three cluster samples provide a consistent level of projected mass as determined by a completely independent mass estimate generated by the effect of gravitational lensing.

4.3.1 Model

In order to model the expected redshift enhancement signal produced by an ensemble of clusters, we first calculate the effect of magnification on the unlensed redshift distribution $n_0(z)$ of background sources using Eq. (2.31). To compute the magnification μ as a function of mass and distance from the cluster center, as done throughout the chapter, we adopt the NFW density profile [152] with the mass–concentration relations provided by Bhattacharya et al. [29], described at the beginning of Chapter 2. We employ the projected NFW functionals given by Wright and Brainerd [265], which provide a good description of the projected total matter distribution of cluster-sized haloes out to approximately twice the virial radius, beyond which the two-halo term cannot be ignored [156, 246]. As we shall see, however, this projected NFW model is sufficient to describe the data with the current sensitivity. The model values are computed applying the relevant mass–richness relation to individual clusters and summing over the cluster mass distribution of each cluster sample, as shown in Fig. 4.1.

As for the luminosity function Φ of the source galaxies, from which we compute the logarithmic slope β of Eq. 2.32, we follow Coupon et al. [52, hereafter, CBU13] and use the Schechter parametrisation (Eq. 2.11) of the V-band luminosity function given by Ilbert et al. [97], obtained using VIMOS VLT Deep Survey [122] data, and adopt the redshift evolution from Faber et al. [75]: $M^* = -22.27 - 1.23 \times (z - 0.5)$ and $\alpha = -1.35$. The advantage of using this particular survey, despite its small $1 \deg^2$ survey area, resides in that it is much deeper ($0.2 < z < 2.0$, $i < 24$) than the background galaxy sample we are using ($0.43 \leqslant z \leqslant 0.90$), so that the logarithmic slope of the luminosity function as a function of redshift is very well described in the range of redshift and magnitude we are interested in.

Finally, the limiting luminosity used to evaluate $\mathrm{d}\ln\Phi(z,L')/\mathrm{d}\ln L'$ in Eq. 2.32 is given by:

$$-2.5\log_{10} L(z) = i_{\mathrm{AB}} - 5\log_{10}\frac{d_L(z)}{10\,\mathrm{pc}} - K(z)\,, \tag{4.10}$$

with $i_{\mathrm{AB}} = 19.9$ the limiting magnitude of the BOSS survey, and $K(z)$ the K-correction:

$$K(z) = 2.5\,(1+z) + 2.5\log_{10}\left(\frac{L(\lambda_e)}{L(\lambda_0)}\right)\,, \tag{4.11}$$

where the second term can be neglected as the V-band rest-frame flux falls in the i-band at $z \sim 0.5$.

4.3.2 Results

Observationally, the redshift enhancement δ_z of background galaxies is defined as:

$$\delta_z(r_\perp) \equiv \frac{\langle z(r_\perp) \rangle - \langle z_{\text{total}} \rangle}{\langle z_{\text{total}} \rangle} \,, \tag{4.12}$$

where $\langle z_{\text{total}} \rangle$ is the average redshift of the unlensed N_{back} background BOSS galaxies:

$$\langle z_{\text{total}} \rangle = \frac{1}{N_{\text{back}}} \sum_{i=1}^{N_{\text{back}}} z_i \,, \tag{4.13}$$

and $\langle z(r_\perp) \rangle$ is the average redshift of the lensed $n(r_\perp)$ background galaxies inside a radial bin at a physical transverse distance $r_\perp$ from the cluster BCG:

$$\langle z(r_\perp) \rangle = \frac{1}{n(r_\perp)} \sum_{i=1}^{n(r_\perp)} z_i \,. \tag{4.14}$$

A redshift enhancement signal at a significance level of 4σ was first detected by CBU13, who used five different cluster catalogues and a total of 316,220 background BOSS galaxies from an earlier data release (DR9). Compared to CBU13, here we use around a factor of two increase in the number of background galaxies (855,097 in total), however, we restrict our analysis to those clusters with a BCG spectroscopic redshift to ease the comparison with the gravitational redshift measurements. We note that the increased number of background galaxies somehow compensate the fewer clusters used in the analysis, so that the signal-to-noise ratio is similar to CBU13.

We first measure the redshift enhancement signal $\delta_z(r_\perp)$ as a function of transverse distance $r_\perp$ from the BCG for the full cluster sample, and then the radially integrated redshift enhancement as a function of mass $\delta_z(M_{200m})$. We repeat the measurements for each of the three cluster catalogues described in Chapter 3.

To estimate the errors on our measurements we generate 500 cluster random catalogues with 25,000 objects each, distributed inside the BOSS angular footprint and following the same redshift distribution as the cluster catalogue of interest. Then, using the same radial or mass binning, we measure δ_z in the exact same way as for the real cluster sample, and define the error bars as the standard deviation of the 500 measured signal amplitudes. We also compute the full covariance matrices to account for the re-use of cluster-background galaxy pairs in the stacked signal, when computing the significance. As pointed out in more details by CBU13, here the level of systematic is negligible compared to statistical errors.

Radial redshift enhancement

We measure δ_z in seven logarithmically spaced radial bins in the range $0.04\,\text{Mpc} < r_\perp < 15\,\text{Mpc}$. To compare these results with our gravitational redshift results (see Sec. 4.2.2), we consider only those clusters for which the BCG has a spectroscopic redshift in the range $0.1 \leqslant z \leqslant 0.4$. To ensure a significant gap between the cluster lenses and background galaxies and avoid physically associated pairs, we only use those CMASS galaxies with a spectroscopic redshift larger than $z = 0.45$.
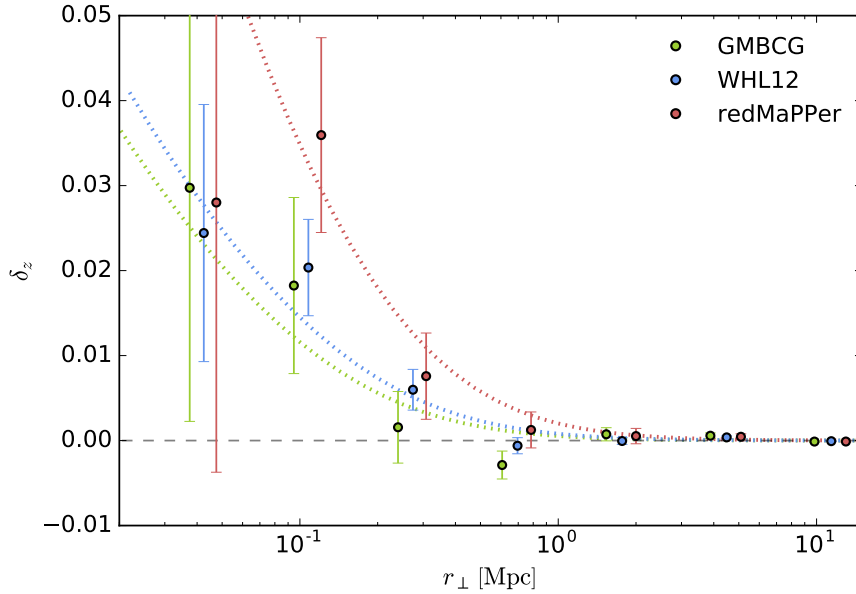
Figure 4.6: *Radial redshift enhancement signals for the GMBCG (green), WHL12 (blue) and redMaPPer (red) cluster catalogues. The dotted curves represent the model predictions for the three different cluster samples. For visual clarity, the symbols for GMBCG and redMaPPer are horizontally shifted by $\mp 10\%$ with respect to WHL12.*

In Fig. 4.6 we show the results obtained for the GMBCG, WHL12, and redMaPPer cluster catalogues. All measurements feature a δ_z value in agreement with the models within statistical errors. We note that the difference between the redMaPPer model and the GMBCG/WHL12 models arises from the rather different mass distributions. As seen in Fig. 4.6, the difference is most significant at a scale of $\sim 0.1 - 0.4\,\mathrm{Mpc}$. The detection significance of the redshift enhancement of background CMASS galaxies behind clusters is calculated to be 2.8σ, 4.7σ and 3.9σ for the GMBCG, WHL12 and redMaPPer cluster catalogues, respectively.

Integrated redshift enhancement

To study the mass dependence of this effect, we measure now the radially integrated redshift enhancement signal in different mass bins. To keep an approximately constant signal-to-noise, we use the same mass binning as in Sec. 4.2 and divide the GMBCG, WHL12 and redMaPPer cluster samples into 3, 5 and 2 mass bins, respectively. We integrate $\delta_z(r)$ radially in the range $0.04\,\mathrm{Mpc} < r < 0.40\,\mathrm{Mpc}$, where the signal-to-noise ratio is found to be highest.

Results are displayed in Fig. 4.7. We report a clear tendency of an increasing value of δ_z with increasing average cluster-sample mass, in qualitative agreement with the model. However we observe a $\sim 1 - 2\sigma$ discrepancy at low mass $(M_{200m} < 1 \times 10^{14}\,h^{-1}\,M_\odot)$ for the GMBCG and WHL12 cluster subsamples, and a $\sim 2 - 3\sigma$ discrepancy for the WHL12 subsample at high mass $(M_{200m} \sim 5 \times 10^{14}\,h^{-1}\,M_\odot)$.
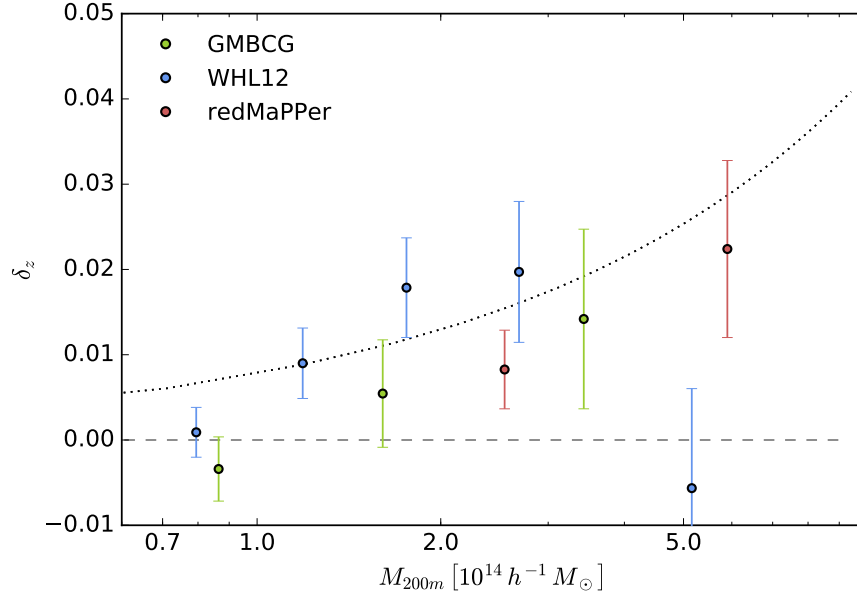
Figure 4.7: *Radially integrated redshift enhancement signal in the range* $0.04\,\mathrm{Mpc} < r < 0.40\,\mathrm{Mpc}$*, in 3 different richness bins in the case of the GMBCG cluster catalogue (green), 5 richness bins in the WHL12 case (blue), and 2 richness bins in the redMaPPer case (red). Model prediction is shown as the dotted black curve.*

Updated DR12 results

Finally, we briefly describe the results obtained on the measurement of the integrated redshift enhancement with the more recent DR12, combined with the 5.10 version of the redMaPPer catalogue (see Sec. 3.2.3). Because in this case we are not interested in a direct comparison with the results obtained from the analysis of the gravitational redshift effect, we consider the complete spectroscopic catalogue, and not only those clusters with more than 6 satellite galaxies with an spectroscopic redshift measurement. This allows us to work with a sample of 19,473 clusters, which is reduced to 13,516 clusters in the $0.10 \leqslant z \leqslant 0.40$ redshift region.

We repeat the methodology described above, but now instead of converting richness into mass, we directly consider three different richness cluster subsamples $\lambda \in [22, 30)$, $[30, 45)$, and $[45, 200)$ at redshifts below $z \leqslant 0.40$, and convert the model prediction into richness space using the mass–richness relation as we have been using it during this chapter, but now in the opposite direction. The redshift enhancement signal δ_z obtained for these three richness subsamples is shown in Fig. 4.8, together with the lensing model.

These results are a significant improvement with respect to the measurements performed with DR10 (Fig. 4.7) because of the increase in the number of clusters considered and in the number of background galaxies with measured redshifts. The redshift enhancement effect is now detected with a significance of 6.6σ for the whole sample. Also, we observe a clearer trend of higher values of δ_z for larger values of the average richness of the cluster sample considered, as expected. It should be noted, though, that all the values of δ_z fall below the model, with a deviation of $\sim 1\sigma$ for the first and third richness subsamples. This could be an indication of the level of miscentering present in the position of the CGs with respect to the deepest part of the gravitational potential well, which would be the main cause of the dilution of the redshift enhancement signal.
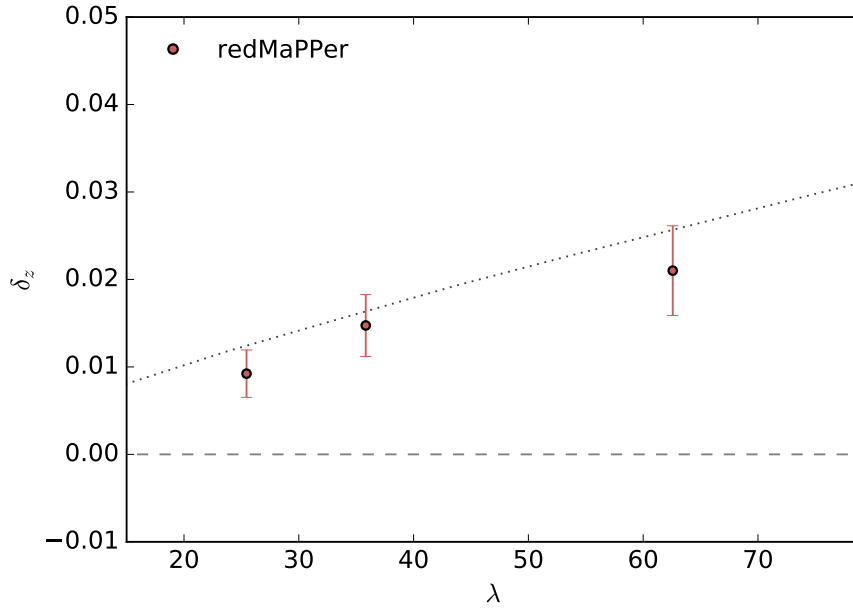
Figure 4.8: *Integrated redshift enhancement signal obtained with the more recent DR12 sample of CMASS galaxies and for three richness subsamples of the v5.10 redMaPPer catalogue, with $\lambda \in [22, 30)$, $[30, 45)$, and $[45, 200)$, in the redshift range $z_{\mathrm{clu}} \leqslant 0.40$. The model prediction (dotted line) as a function of richness is obtained through the mass–richness relation, used in this case to convert mass into richness, and not the other way around as is usually done.*

4.4 Discussion and conclusions

For the purposes of constraining cosmology, statistical work with the largest samples of clusters is required, and one may hope to obtain masses and relate the mass function obtained to cosmological parameters. Here weak lensing is often compromised by the the average quality of the observing conditions and X-ray depth is relatively shallow so deeper surveys are required together with optical follow-up to establish the cluster redshifts. The importance now of the SDSS resides on providing the photometric data and significant redshift information to establish large samples of clusters. The catalogues we have examined are so large we may pursue new, but not optimal, methods for examining masses by stacking the data. This includes the enhanced depth from magnification bias and gravitational redshifts, since the redshift accuracy is sufficient for this purpose and the calibration of the data has been established with unprecedented precision.

Gravitational redshifts are the latest and most difficult means of examining cluster mass profiles, but they also are, in principle, of great interest by directly assessing the validity of GR on large scales. Here we have examined this using the *Legacy* sample of galaxies, comprising more than 800,000 galaxy spectra.

We have produced the phase space distribution of galaxies around the BCG spectroscopic positions provided by three major cluster catalogues: GMBCG, with 20,119 clusters, WHL12, with 52,682 clusters, and redMaPPer, with 13,128 clusters. Then we have measured the internal redshift distortion Δz associated to each cluster sample as a function of cluster radius. This distortion is identified as the deviation from the BCG velocity of galaxies we associate with these clusters. We have modelled this observational signature for each cluster survey taking into account

the combination of the gravitational redshift, the transverse-Doppler, the past light cone, and the survey-dependent surface brightness effects.

The net gravitational redshift effect that we derive is consistent with the expected cluster mass–richness relation in the case of the GMBCG cluster sample, with values of Δ around $-10\,\mathrm{km\,s}^{-1}$. In the redMaPPer sample case, with a higher average cluster mass and a lower number of clusters contained in it, the agreement between model and observation is also good within the noise with a difference of at most $\sim +5\,\mathrm{km\,s}^{-1}$ on average observed above the expectation. In the WHL12 case, we observe an unexpected mildly positive signal ranging from $\sim 0\,\mathrm{km\,s}^{-1}$ to $\sim +5\,\mathrm{km\,s}^{-1}$, in complete disagreement with the model proposed for this sample.

If all our clusters were relaxed, had no substructure, and the number of spectroscopic measurements were proportional to the density of galaxies, each cluster would practically follow the stacked cluster distribution of Fig. 4.2. However, such an ideal case is not realised due to an inevitable level of substructure, and from the observational selection effects and algorithmic limitations in the definition of clusters and BCG galaxies. Even if BCG finder algorithms were perfect (in the sense of identifying the brightest most massive galaxy of each cluster), it has been shown by Skibba et al. [218] that the implicit assumption that BCGs reside at the potential minimum is subject to an significant inherent variance leading to a biased measurement of the galaxy velocity dispersion arising from a difference between the measured position of the BCG and the real position of the cluster halo center [109]. The underlying offset distribution between the dark matter projected center and the BCGs has been also studied by Zitrin et al. [271] and Johnston et al. [101], being shown in the latter that the magnification signal is qualitatively less sensitive to the miscentering effect compared to the shear signal. In principle, stacking all the velocity distributions of galaxies around BCGs into an effective distribution accounts for some of the previously mentioned effects, and enables us to measure any statistical deviation Δ from $\langle v_{\mathrm{gal}} \rangle = 0$. This is what we measured in Sec. 4.2. However, if we look again at the galaxy velocity distributions (Fig. 4.3) from which we measured Δ, we see that the velocity distributions obtained from GMBCG, WHL12 and redMaPPer catalogues are different. A further analysis of these velocity distributions shows that this difference holds for different ranges of mass. In the ideal relaxed case, these profiles should follow $\sigma_{\mathrm{obs}}^2 = \sigma_{\mathrm{gal}}^2 + \sigma_{\mathrm{BCG}}^2$, relation from which σ_{gal} is obtained after assuming a relation between the BCG motion and the velocity dispersion of satellite galaxies, $\sigma_{\mathrm{BCG}} = \gamma\,\sigma_{\mathrm{gal}}$. Wojtak et al. [264] and Zhao et al. [270] consider $\gamma \simeq 0.3$, but it is pointed by Kaiser [105] that the frequent misidentification of BCGs as central galaxies would lead to a higher value of $\gamma \sim 0.5$.

Using the appropriate mass–richness relation for each cluster sample, we analysed the dependence of the integrated internal redshift signal with mass, observing a clear correlation between the intensity of the signal Δ and the average mass of the sample, especially in the range $M_{200m} > 2 \times 10^{14}\,h^{-1}\,M_{\odot}$, where the measurements follow particularly well the model. The positive radial Δ signal in the WHL12 catalogue seems to mainly arise from lower mass clusters in the range $M_{200m} < 2 \times 10^{14}\,h^{-1}\,M_{\odot}$.

We have also measured the level of magnification bias in each cluster sample using the 850,000 galaxy spectra from DR10, almost tripling the number of galaxies used in the first measurement of this effect [52]. We detect a clear radial redshift enhancement of the background galaxies behind clusters in all three surveys with a significance of 2.8σ, 4.7σ and 3.9σ levels for GMBCG, WHL12 and redMaPPer cluster catalogues respectively.

Making use of the previously employed mass–richness relations, we have also measured the integrated signal out to $r_{\perp} = 0.4\,\mathrm{Mpc}$ for different subsamples of clusters with different average

masses. After modelling this gravitational lensing feature using projected NFW functionals for the clusters and luminosity functions based on deep spectroscopic surveys, we find a generally good agreement between theoretical predictions and observations for the three cluster catalogues, with a clear increase of the mean redshift of background sources at smaller decreasing projected radial distance from the BCG, and also an increasing redshift enhancement with increasing cluster masses. The WHL12 catalogue does not follow so well the model for the low and the high mass bins falling below the expected value with discrepancies of 2.1σ and 2.5σ, respectively.

Finally, we have shown the latest results on the integrated redshift enhancement, obtained after DR12 was made available to the public. We obtain a 6.6σ significance detection for the redMaPPer sample, and a clear relation between the richness and the amplitude of the gravitational lens magnification effect, with consistency at the 1.1σ level, a little below the model prediction. This could be produced by the intrinsic miscentering of central galaxies with respect to the center of the projected gravitational potential well.

From a comparison of our internal redshift distortion and lensing redshift enhancement measurements for three major cluster samples defined from the SDSS survey, we conclude that the WHL12 catalogue, containing the largest number of clusters, is anomalous in the sense that the net internal redshift effect is found to be uniformly positive with radius at a level of $+5\,\mathrm{km\,s^{-1}}$ instead of negative with $\sim -10\,\mathrm{km\,s^{-1}}$, as expected given the claimed richnesses of these clusters.

Examining the mass dependence of these results we find it is the clusters with $M_{200m} < 2 \times 10^{14}\,h^{-1}\,M_\odot$ that introduce the unexpected positive signal, as more massive clusters produce a net redshift of $\sim -20\,\mathrm{km\,s^{-1}}$, similar to GMBCG and redMaPPer samples. Given the much higher number of clusters claimed for the WHL12 sample compared to the other two catalogues, it could be that this positive signal arises from spurious detection of clusters or from chance projection of less massive systems. Our analysis shows that internal redshift measurements are not simply limited by the statistical precision, namely the number of clusters used, but are also sensitive to systematic effects that are not fully understood. The internal redshift and lensing magnification signals have totally different sensitivities to line-of-sight projection effects. It is very likely that a higher degree of contamination due to projection effects in this catalogue is responsible for the observed trends in both measurements, as lensing measures the sum of the projected signal.

For the redMaPPer cluster catalogue, which has the smallest sample size due to its conservative minimum richness cutoff, both measurements are shown to agree well with respective predictions albeit the large statistical uncertainties. It also exhibits the best performance in terms of the accuracy of cluster mass estimates because the mass dependence of the signal predicted by models is detected at the 1.8σ level. Our promising measurements of the internal redshift and redshift enhancement effects obtained with the redMaPPer catalogue encouraged us to choose it over other catalogues for the analyses developed in Chapters 5 and 6.

5

Clustering and Number Density Evolution of Clusters

The notorious sensitivity of cluster abundance to the growth rate of structure means that the mass density of the Universe, Ω_m, and the amplitude of the power spectrum, $\sigma_8 \propto A_s$, should be particularly accurately derived from cluster surveys ([22, 28, 42, 46, 49, 71, 76, 92, 96, 133, 162, 163, 169, 195, 248, 251], see Sec. 1.2) providing a welcomed consistency check of the current cosmological ΛCDM model. Even the presence of a few massive clusters at $z > 0.5$ has been enough to overcome the long desired $\Omega_m = 1$ consensus [22], favouring a sub-critical mean matter density for the Universe [20]. Empirically, $\Omega_m \simeq 0.2$–0.3 has long been argued by simply extrapolating galaxy mass-to-light ratios (M/L) to large scales [161] and clarified with dynamical measurements on larger scales [21, 166] and of course independently confirmed with increasingly accurate claims from CMB acoustics [179, 223].

New underway surveys to find large samples of clusters above $z \geqslant 0.5$ with lensing based masses are very exciting in this respect, so growth can be tracked as a function of cluster mass with unprecedented precision, including subtle modification by cosmological neutrinos [45, 119, 123, 258, 267], with little complication anticipated from detailed cosmological simulations that include gas physics [32]. Using clusters, the current best estimates of the $\sigma_8\,\Omega_m^{\simeq 0.5}$ combination that principally determines growth [102, 132, 195] have until now been limited to the local volumes where cosmic variance and relatively small samples means it is rather unclear how to assess differences with the CMB based $\Omega_m h^2$ combination, fixed principally by the first peak of the CMB, and σ_8, where the uncertain level of electron Thomson scattering optical depth due to reionization, τ, smooths the amplitude of CMB fluctuations. The *Planck* weighted values of these observationally interdependent parameters, σ_8, Ω_m, h, τ, are now claimed to be in significant tension with the constantly high value of H_0 derived locally from the distance ladder [190].

Undermining the use of clusters in such comparisons is the indirectness of cluster mass estimates for which empirical scaling relations have to be relied on for converting observables to mass. Cluster richness seems to provide a robust connection, as it is close to being linearly related to mass ([193, 194, 199], see Sec. 2.4), with a slope of $\mathrm{d}\log M_{200}/\mathrm{d}\log N \simeq 1.1$, and a $\simeq 20\%$ inherent scatter inferred [8] and with little evidence of evolution [9, 91, 267]. Power law scalings to convert X-ray and SZ measurements to total cluster masses are complicated by compressed gas and shocks from cluster interactions, so that the selection function and its evolution is challenging [6, 11, 144, 147, 212, 231]. Lensing based scaling relations are now feasible for limited samples but for which the initial X-ray or SZ selection complicates matters [196, 210].

Beyond cluster abundances, higher order moments of the density field, including the correlation function of clusters of galaxies, also relate directly to the growth of structure [42]. The clustering

of clusters is in this respect far more useful than for galaxies, where the strong dependence on Hubble-type implies a complex "astrophysical bias" ([118, 166], see Sec. 1.2.5). A major advantage of using clusters is their clear relation to the mass distribution, especially if direct lensing masses can be obtained for statistically large samples of clusters. This is unlike galaxies where ellipticals are measured to be much more spatially correlated than disk galaxies, implying as may be expected that the creation of galaxies from the underlying mass distribution is not simply related to the local density of dark matter. In the case of clusters the bias is more simply mass-density related, and is not expected to be significantly influenced by gas physics, allowing relatively clean comparisons between theory and observation. For clusters a nearly linear relation is established between the measured richness and mass with a modest scatter, so richness can be reliably transformed statistically when examining the clustering of clusters. Previous clustering work with the SDSS has been done either with relatively small local samples with an uncertain mass–richness relation, or relying on corrections for the wide smoothing by photometric redshifts [210], or on the angular clustering [24]. In this chapter we establish the first spectroscopically complete analysis of cluster statistics using the depth of the SDSS survey, beyond the local Universe.

Carefully carried out redMaPPer team work has been a big advance in identifying clusters by their red-sequence of member galaxies and deriving reliable richnesses using the SDSS survey data which has sufficient depth to detect clusters to $z \simeq 0.3$ with high completeness [200]. Currently 70% of the brightest cluster galaxies (BCG) in this clusters have redshift measurements with the SDSS DR12 release. Here we augment these BCG measurements with additional cluster member redshift measurements, by correlating redMaPPer identified red-sequence galaxies with the enlarged DR12 redshift sample from the BOSS survey, which we show here provides spectroscopic completeness to 93% overall, and $> 97\%$ for the redMaPPer richness complete redshift range $z < 0.325$.

In tandem with this observational progress, advances in the N-body simulations of ΛCDM have extended to volumes several times that of the observable Universe [13]. Large simulated volumes are necessary to accurately predict the number of massive clusters, given their rarity. The cosmological parameters chosen for these simulations follow the tradition set by Springel et al. [226] for such groundbreaking simulations, allowing consistency checks between these generations of simulations. The former consensus values adopted for these simulations [208] differ significantly from the present *Planck* weighted values of σ_8 and Ω_m that principally influence cluster predictions. The cause of this may be traced mainly to the relatively large τ estimated by WMAP [223] that raises $\sigma_8 = 0.9$, and lowers $\Omega_m = 0.25$. The amplitude of the CMB fluctuations on large scales scale as $A_s \exp[-2\,\tau]$, where A_s is the amplitude of the matter power spectrum. Hence a higher optical depth τ due to reionization implies a higher A_s and consequently a higher $\sigma_8 \propto A_s$. The *Planck* weighted values today are significantly "reversed" for these key parameters mainly because of the much lower inferred τ.

In this chapter we use an updated version of the redMaPPer cluster catalogue and the BOSS spectroscopic sample, both described in Chapter 3, to study the clustering and the abundance of clusters of galaxies, which we describe in Secs. 5.3 and 5.4, respectively. Throughout this chapter we compare our results with those obtained from the MXXL simulation, described in Sec. 5.2. Finally, we use this simulation in Sec. 5.5 to perform a likelihood analysis to obtain the cosmologically favoured mass–richness relation, and present our conclusions in Sec. 5.6.

As for the fiducial cosmological parameters needed to compute the correlation function and the number density of clusters, we adopt the Planck Collaboration et al. [179] weighted cosmological parameters $H_0 = 67.74\,\mathrm{km\,s^{-1}\,Mpc^{-1}}$ and $\Omega_m = 0.309$. At the end of this chapter we also

consider the consensus parameters set in 2003 used for the largest available simulations and that differ significantly in terms of σ_8, Ω_m and H_0.

5.1 Updated redMaPPer cluster catalogue

After the comparisons performed between different cluster catalogues in Chapter 4, we decide to focus our efforts on the clusters contained in the redMaPPer catalogue, that offered the most consistent results in terms of a cross comparison of the redshift enhancement and the gravitational redshift effects associated to clusters.

We update the publicly available 5.10 version catalogue, based on DR8 and DR9 data, using the more recent DR12 BOSS spectroscopic data, which contains the spectra of 1,339,107 galaxies. After selecting the spectra with the best quality (see Sec. 3.1.2), we cross correlate the angular position on the sky of the most probable central galaxy (CG) associated to each cluster, with the whole BOSS spectroscopic sample, and identify those objects that are closer than 0.50 arcsec, finding 3,772 matches for the most probable CGs that did not have an spectroscopic redshift measurement before. More than 99% of all the identifications are done for pairs that are closer than 0.02 arcsec, but we actually find a gap between 0.40 and 1.50 arcsec where no identification at all is made, making clear that we are safe from any possible misidentification due to close galaxy pairs. We repeat this identification process with the second, third, fourth and fifth most probable CGs in each cluster. A sizeable fraction of CGs do not have measured redshifts yet whereas one or more of the highly probably CGs often does. This fuller comparison of members with redshifts provides now for the first time a highly spectroscopically complete sample of clusters with which one can make several precise calculations described later in this chapter.

Finally, we exclude those clusters that, as can be seen in Fig. 5.1, are outside the considered DR12 BOSS area. This leaves us with a final sample of 19,473 clusters with spectroscopic redshift measurement of their most probable CG, and a total of 23,135 clusters with spectroscopic redshift measurement of one of their most likely "centrals". In comparison, in the original photometric redshift catalogue there were 24,869 clusters in the same BOSS region, meaning that we have now spectroscopic information of more than the 93% of the clusters. This number increases to $> 97\%$ for the 7,143 clusters within the redMaPPer selection limit, $z \leqslant 0.325$.

When needed, in order to have a global redshift estimate of those clusters with more than one CG with a spectroscopic measurement, we make an average of their redshifts $z_{\mathrm{CG},i}$, weighted by the centering probability $p_{\mathrm{cen},i}$ associated to each of the five potential CGs:

$$z_{\mathrm{cluster}} = \frac{\sum\limits_{i=1}^{5} z_{\mathrm{CG},i}\, p_{\mathrm{cen},i}}{\sum\limits_{i=1}^{5} p_{\mathrm{cen},i}} \tag{5.1}$$

The final redshift distribution of the clusters inside the BOSS region is shown in Fig. 5.2. Note that there is near full spectroscopic redshift completeness to the peak of the redMaPPer selection function at $z = 0.325$, and the bump feature at $z \simeq 0.25$ in the photo-z distribution, absent in the spectroscopic DR12 sample where the numbers smoothly rise with the increasing volume, as expected for a complete sample. The difference between our definition of z_{cluster}, and z_{photo}, the original photometric redshift provided by the catalogue, is shown in Fig. 5.3.
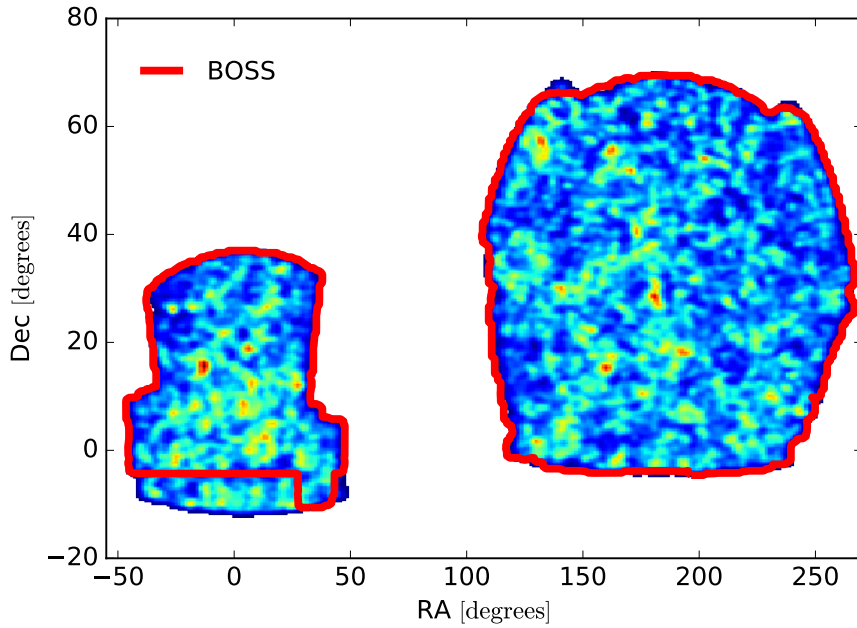
Figure 5.1: *Sky distribution of redMaPPer clusters. The region inside the red line represents the area of the sky covered by the BOSS spectroscopic survey that overlaps with the redMaPPer catalogue. We exclude clusters outside the BOSS region so that we have homogeneus high completeness within the spectroscopic cluster sample that we have constructed.*
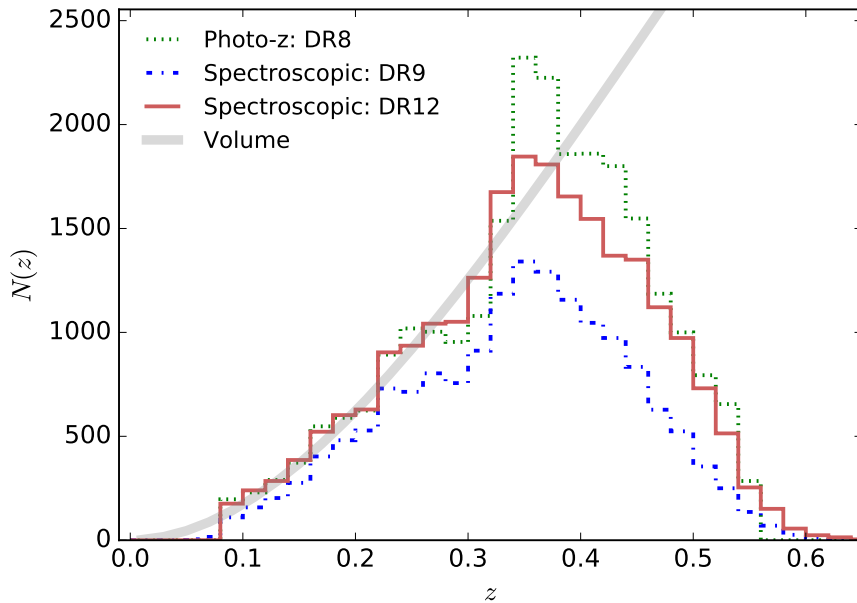

Figure 5.2: *Original photo-z (dotted green line), DR9 spectroscopic redshift (dot-dashed blue line) and updated DR12 spectroscopic redshift (solid red line) distribution of redMaPPer clusters. We plot for comparison the proportional volume in each redshift bin (grey shaded line). From the original 24,869 clusters with photometric redshift estimates, 15,936 clusters also have DR9 spectroscopic redshift information of their most likely CG, and 23,135 clusters have DR12 spectroscopic redshift measurements of at least one of their most likely CG. The clusters that fall outside the BOSS region have been excluded from these samples.*
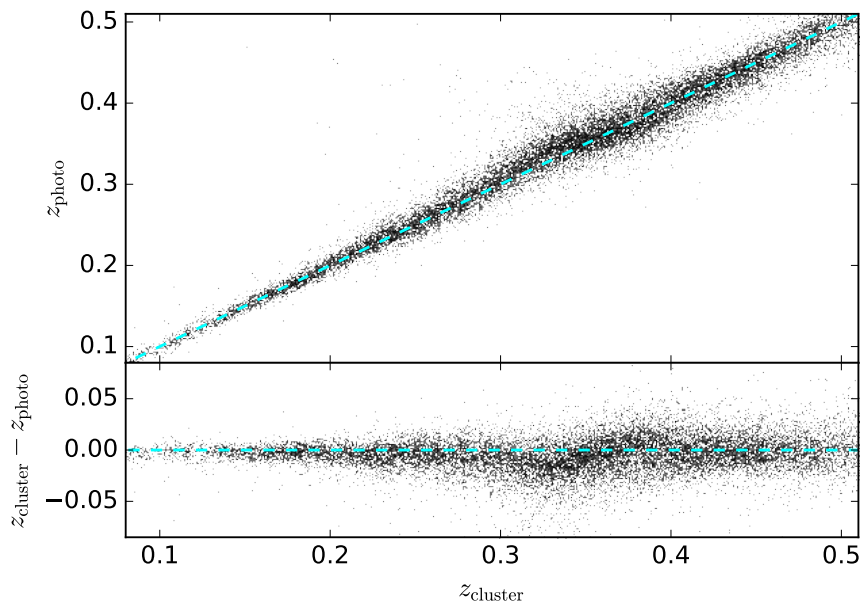
Figure 5.3: *Relation between z_{photo} and our definition of z_{cluster}, based on DR12 data and the centering probabilities $p_{\mathrm{cen},i}$ of all the CG candidates, for each of the clusters in the redMaPPer catalogue.*

5.2 MXXL simulation

The "Millennium-XXL" (MXXL, [13]) simulation is one of the largest dark matter N-body simulations performed to date. It follows the nonlinear creation and growth of dark matter structures within a cube of $3{,}000\,h^{-1}\,\mathrm{Mpc}$ on each side, which contains $6{,}720^3$ particles of mass $m_p = 8.456 \times 10^9\,M_\odot$.

Compared to its predecessor the "Millennium Simulation" (MS, [226]), the MXXL simulation volume is 200 times bigger, comprising the equivalent volume of the Universe up to $z = 0.72$, or 7 times the volume of the BOSS survey. Although the particle resolution is 7 times lower in the MXXL simulation than in the MS, it is 300 times higher than the "Hubble Volume Simulation" [73], and has ample resolution for our cluster-related purposes. Note that these large simulations deliberately share the same pre-*Planck* cosmology set by WMAP in 2003 to allow consistency checks. This is not in practice limitation for our work given the realisation by Angulo and White [12] that a simple rescaling of size and redshifts can effectively provide predictions for other cosmologies using the same simulation, within the context of ΛCDM.

This simulation was designed to provide enough statistical power as to study and interpret some of the problems related to the observation of clusters of galaxies, like the scaling between the real mass of a cluster and the associated cluster observables, i.e., richness, lensing mass, X-ray luminosity and thermal Sunyaev-Zel'dovich signal. The code employed in the simulation is a extremely memory-efficient version of `GADGET-3`, which is itself a more sophisticated and efficient version of `GADGET-2` [224], the code used for the MS.

This code is also designed to carry out halo and subhalo finding procedures during its execution with a friends-of-friends algorithm (FoF, [110]), combined with the `SUBFIND` algorithm [225], which identifies locally overdense regions within the parent haloes found by the FoF. The halo catalogues produced during this search provide information about masses, velocity dispersions,
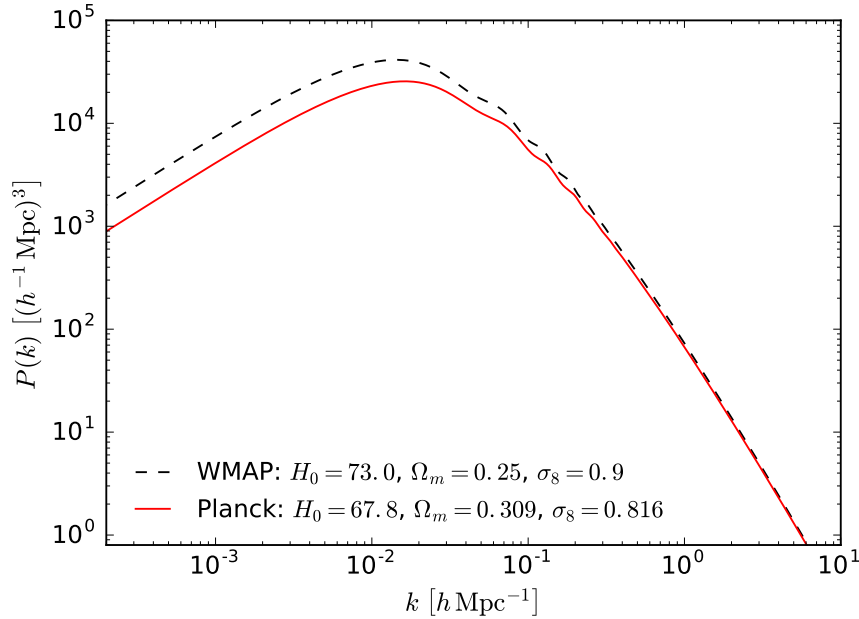
Figure 5.4: *The matter power spectrum for a WMAP (black dashed line) and a Planck (red solid line) cosmology. The former was used in the creation of the MXXL simulation, and we use the latter to update it, following the prescription given by Angulo and White [12].*

halo shapes, velocities, etc...

The original cosmology employed in the MXXL simulation is ΛCDM, with the same cosmological parameters that were employed in the MS: $\Omega_m = 0.25$, $\Omega_\Lambda = 0.75$, $\sigma_8 = 0.9$ and $H_0 = 73\,\mathrm{km\,s^{-1}\,Mpc^{-1}}$. We update this cosmology and the resulting halo catalogue using the prescription given in Angulo and White [12], with this new set of cosmological parameters taken from the combined analysis of *Planck* CMB data, BAO surveys and the JLA sample of Type Ia SNe [179]: $\Omega_m = 0.3089$, $\Omega_\Lambda = 0.6911$, $\sigma_8 = 0.8159$ and $H_0 = 67.74\,\mathrm{km\,s^{-1}\,Mpc^{-1}}$. This algorithm to update simulations relies basically on the reassignments of masses, velocities and lengths, and the rescaling of the time steps, i.e., the redshifts of the snapshots, to match the shape of the smoothed linear matter power spectra of the desired cosmology, and thus the growth of structure. The modification of the long wavelength modes relies on the Zel'dovich approximation so the difference on large scales is also taken into account. In Fig. 5.4 we show the original WMAP matter power spectrum used in the MXXL simulation, and the matter power spectrum that we obtain considering a *Planck* cosmology and that we use to update the MXXL simulation, both computed using the code `CAMB` [126]. From now on, we refer to this updated version as the MXXL simulation.

5.2.1 MXXL synthetic cluster catalogues

We now describe how to create synthetic optical cluster catalogues from the MXXL simulation, so we can compare them with the redMaPPer catalogue. We use the data coming from 5 adjacent snapshots of the MXXL simulation, corresponding to the redshifts $z = 0.027$, 0.128, 0.242, 0.393 and 0.486. In each of these snapshots, we select around 7 million dark matter haloes with masses above $M_{200c} = 10^{12}\,h^{-1}\,M_\odot$, where here M_{200c} is defined as the mass enclosed in a sphere

centered in the potential minimum of the halo, that has a mean density 200 times the critical density of the Universe.

Now, in order to build a synthetic cluster catalogue from the dark matter halo catalogue produced by the simulation, where the "true" mass, the position and peculiar velocities of the haloes are known, we need to assign a richness value and artificially place a central galaxy (CG) in each of these haloes, which is, at the end, the information provided by the redMaPPer catalogue.

Richness

First of all, we need to associate an estimate of the richness to all the haloes in the MXXL simulation. Following Sec. 2.4, we employ a mean mass–richness relation of the form:

$$\ln \left(\frac{\langle M_{200c} | \lambda \rangle}{10^{14} \, h^{-1} \, M_\odot} \right) = \ln \left(\frac{M_{200c}(\lambda_0)}{10^{14} \, h^{-1} \, M_\odot} \right) + \alpha_{M|\lambda} \ln \left(\frac{\lambda}{\lambda_0} \right) , \tag{5.2}$$

where $M_{200c}(\lambda_0)$ is a reference mass at a given value of $\lambda = \lambda_0$, and $\alpha_{M|\lambda}$ is the slope of the mass–richness relation. The fractional scatter $\sigma_{M|\lambda}$ on the halo mass at fixed richness is given by a log-normal distribution:

$$\Delta \ln \left(\frac{M_{200c}}{10^{14} \, h^{-1} \, M_\odot} \right) = \sigma_{M|\lambda} . \tag{5.3}$$

In Sec. 5.5, we find, through a likelihood analysis, the values of $\kappa_{M|\lambda}$, $\alpha_{M|\lambda}$ and $\sigma_{M|\lambda}$ that best describe the observations, where for clarity we have defined:

$$\kappa_{M|\lambda} \equiv \ln \left(\frac{M_{200c}(\lambda_0 = 60)}{10^{14} \, h^{-1} \, M_\odot} \right) , \tag{5.4}$$

and use these values in advance in Secs. 5.3 and 5.4 when comparing the results obtained from the redMaPPer catalogue with the "model" produced by the MXXL simulation. We follow the results obtained by Angulo et al. [13] and Rozo et al. [195], and consider the value of the scatter independent of the richness, and ignore any possible redshift evolution of the scatter or of the slope of the mass–richness relation. Also, because in the simulation we know the value of the true mass, rather than the value of the observable, we need to convert $\sigma_{M|\lambda}$ into $\sigma_{\lambda|M}$ inverting Eq. 5.2, so $\sigma_{M|\lambda} = \alpha_{M|\lambda} \, \sigma_{\lambda|M}$.

In Fig. 5.5 we show the distribution of the masses of the MXXL clusters as a function of one realization of the richness associated through a mass–richness relation with, e.g., a pivot mass of $\kappa_{M|\lambda} = 1.35$, a slope of $\alpha_{M|\lambda} = 1.10$, and a scatter of $\sigma_{M|\lambda} = 0.20$, in comparison to the mean mass–richness relation. The upscattering of low mass clusters into high richness regions increases with higher values of the slope or larger scatter. The snapshot number 54 of the simulation, the one considered in this figure, corresponds to $z = 0.242$, close to the mean redshift of the complete cluster sample.

Miscentering of central galaxies

Recent studies have shown that the assumption that CGs lie basically at rest in the deepest part of the potential well is not accurate. Although there is evidence of an special correlation between the mass of a cluster halo and the properties (mass, morphology, star formation rate, stellar population,
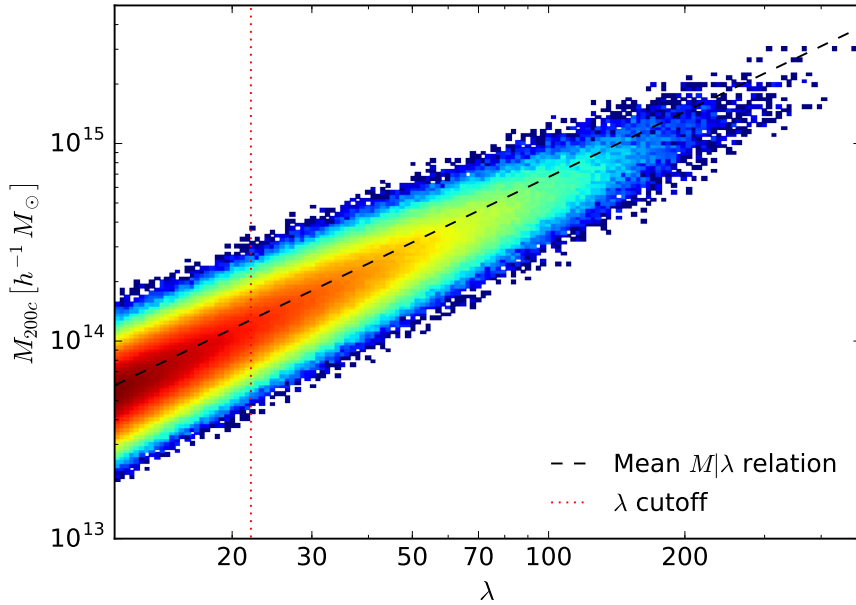
Figure 5.5: *Mass distribution as a function of richness of the MXXL dark matter haloes found in snapshot 54. As the black dashed line, the mean mass–richness relation with $\kappa_{M|\lambda} = 1.35$ and $\alpha_{M|\lambda} = 1.10$. When the scatter in the mass–richness relation is not considered, there are $\sim116,000$ clusters above the richness threshold $\lambda > 22$. If a scatter of $\sigma_{M|\lambda} = 0.20$ is introduced, we obtain the cluster distribution shown in the figure, with around $\sim128,000$ clusters now with $\lambda > 22$ due to the upscatter of low mass clusters.*

colour, etc...) of its BCG [252], we may expect a large proportion of clusters are non-relaxed dynamical systems that are still evolving, with BCGs following evolving orbits that need not be located at the time-varying minimum of the cluster potential.

Miscentering is one of the main sources of error on stacked measurements on clusters, including weak lensing mass determinations [242, 244], analyses of the power spectrum [186], gravitational redshift and redshift enhancement measurements ([52, 105], see Chapter 4), or velocity dispersion calculations [25]. That is why in the last few years many authors have tried to determine the level of miscentering statistically.

There are two reasons why this miscentering may occur: the galaxy identified as the CG not being the galaxy with the lowest specific potential energy (i.e., the one that could be considered the CG), or the real CG not being in the center of mass of the dark matter halo.

In cluster catalogues like the maxBCG [111], the GMBCG or the WHL12, the center of a cluster is identified with the position of the BCG. Although this assumption seems to improve the overall centering performance of cluster-finder algorithms [191], Skibba et al. [218] claimed that between the 25% and the 40% of cases the BCG is not the real CG, but a satellite galaxy, and von der Linden et al. [252] found in a sample of 625 clusters that in more than a half of them the BCG was not located in the center of the cluster.

Trying to quantify the level of miscentering, and using mock catalogues, Soares-Santos et al. [221] found an offset distribution that could be fitted by a 2D Gaussian with a standard deviation of $\sigma = 0.47\,h^{-1}\,\mathrm{Mpc}$, meanwhile Johnston et al. [101] found $\sigma = 0.42\,h^{-1}\,\mathrm{Mpc}$ for the BCGs that were not accurately centered, which ranged from 40% to 20% as a function of cluster richness.

In order to address this problem, the redMaPPer iterative self-training centering algorithm uses BCGs as the seeds for the centering process, but in successive calibrating iterations all the galaxies found in the cluster that are consistent with the red-sequence are considered as potential CGs, and have a centering probability assigned. When convergence is obtained, the galaxy with the highest probability of being at the center of the cluster is tagged as the CG. It should be noted that the miscentering introduced by the red-sequence prior that does not allow blue galaxies to be selected as CGs is expected to affect less than 2% of the clusters. In any case, when the cluster centers found on high resolution X-ray data were compared with the positions of the CGs found in the redMaPPer catalogue, the redMaPPer algorithm was claimed to have a centering success rate of $\approx 86\%$ [191].

To include this effect into our synthetic catalogue, we follow the results of Johnston et al. [101] and introduce a miscentering probability as a function of the halo richness. The probability p_{mc} of a CG being displaced from the center of its host halo follows: $p_{mc}(\lambda) = (2.13 + 0.046\,\lambda)^{-1}$, and such displacement is given by a 2D Gaussian of width $\sigma_{mc} = 0.42\,h^{-1}\,\mathrm{Mpc}$.

Peculiar motions of central galaxies

There are good reasons to believe that, compared to other member galaxies, CGs are a cold population of galaxies due to dynamical friction or possible central gas cooling. How much so is still a matter of discussion. Hierarchical merging of clusters means we must expect some level of dispersion periodically as CGs respond to a rapidly evolving potential and merge with each other. In any case, it is clear that their peculiar velocity cannot be ignored and in some cases is very anomalous [215] and with a small net gravitational redshift expected [38] and measured [99, 202, 264]. Puzzlingly, a significant fraction of CGs with peculiar motions are located in the peak of the X-ray emission. Given the hydrodynamical forces relevant for the cluster, it is not expected that the gas should move together with the CG during cluster encounters [144, 188].

The relation between the value of σ_{CG}, the distribution of CG motions, and σ_{gal}, the value of the dispersion associated to cluster satellite galaxies, is still quite unknown. Oegerle and Hill [154] found that from a sample of 25 clusters almost all CGs showed peculiar velocities relative to the mean velocity of the clusters studied, with $\sigma_{\mathrm{BCG}} \approx 175\,\mathrm{km\,s^{-1}}$. Coziol et al. [54], studying a much larger sample of clusters, found that CGs having peculiar motions within the cluster was a general phenomenon, with less than the 30% of them having velocities compatible with zero, and more than half of them having velocities higher than $0.3\,\sigma_{\mathrm{gal}}$, depending this value slightly on cluster richness. Skibba et al. [218], studying the miscentering of CGs, also found a relatively high value for their velocities, with $\sigma_{\mathrm{CG}} \simeq 0.5\,\sigma_{\mathrm{gal}}$, that had also little dependence with the mass of the host cluster.

In any case, to mimic this motion within clusters of our already placed mock CGs, we assign a peculiar velocity to them given by $\sigma_{\mathrm{CG}} \simeq 0.4\,\sigma_{\mathrm{vir}}$, where σ_{vir} is the virial velocity associated to the mass of the cluster. Once this peculiar motion has been added to the CGs, we move them from real-space positions $\vec{r}$ to redshift-space positions $\vec{s}$ following Eq. 1.75:

$$\vec{s} = \vec{r} + \frac{\vec{v} \cdot \vec{l}}{a\,H}\,\vec{l}, \tag{5.5}$$

where the unitary vector $\vec{l}$ is pointing to an arbitrarily chosen line-of-sight direction, and $\vec{v}$ is the final physical velocity of the CG.

5.3 Correlation function

We compute the two-point redshift-space correlation function $\xi(s, \mu)$ using the 2-dimensional Landy-Szalay estimator:

$$\xi(s, \mu) = \frac{dd(s, \mu) - 2dr(s, \mu) + rr(s, \mu)}{rr(s, \mu)}, \tag{5.6}$$

where $dd(s, \mu)$, $dr(s, \mu)$ and $rr(s, \mu)$ are the normalized number of pairs found in the data-data, data-random and random-random samples. The only difference between this equation and Eq. 1.89 is that instead of being given in terms of s_{los} and $s_\perp$, is given in terms of the absolute redshift-space distance s, and $\mu = \cos\theta$, where θ is the angle of the pair with respect to the line-of-sight (los).

We want to investigate the multipoles of the correlation function $\xi_\ell(s)$, given by Eq. 1.90. In practice, this is done weighting the dd, dr and rr pairs with the associated value of the ℓth Legendre polynomial $L_\ell(\mu)$ for the monopole ($\ell = 0$) and the quadrupole ($\ell = 2$):

$$\xi_\ell(s) = \left(\frac{2\ell + 1}{2}\right) \frac{dd_\ell(s) - 2dr_\ell(s) + rr_\ell(s)}{rr_0(s)}. \tag{5.7}$$

To optimally weight regions with different number densities, we apply FKP weighting [78] to each cluster:

$$w_P = \frac{1}{1 + n(z)P_{\mathrm{FKP}}}, \tag{5.8}$$

where $n(z)$ is the mean cluster density at redshift z, and $P_{\mathrm{FKP}} = 20{,}000\, h^3\,\mathrm{Mpc}^{-3}$.

For the data sample, i.e., redMaPPer clusters, instead of matching only the most probable CGs, we use all the five CG candidates provided by the redMaPPer catalogue for each cluster, taking their centering probabilities p to weight their contribution to the final pair count, so that $\sum_{\alpha=1}^{5} p_{i,\alpha} = 1$ for cluster i. The final data-data, data-random and random-random pair counts can be expressed as:

$$dd_\ell(s) = \frac{1}{N_d(N_d - 1)/2} \sum_{i=1}^{N_d} \sum_{j=i+1}^{N_d} \sum_{\alpha=1}^{5} \sum_{\beta=1}^{5} w_{P,i}\, w_{P,j}\, p_{i,\alpha}\, p_{j,\beta}\, L_\ell(\mu), \tag{5.9}$$

$$dr_\ell(s) = \frac{1}{N_d N_r} \sum_{i=1}^{N_d} \sum_{j=1}^{N_r} \sum_{\alpha=1}^{5} w_{P,i}\, w_{P,j}\, p_{i,\alpha}\, L_\ell(\mu), \tag{5.10}$$

$$rr_\ell(s) = \frac{1}{N_r(N_r - 1)/2} \sum_{i=1}^{N_r} \sum_{j=i+1}^{N_r} w_{P,i}\, w_{P,j}\, L_\ell(\mu), \tag{5.11}$$

where N_d is the number of clusters in the data sample, and N_r is the number of objects in the random sample, which follows the same geometry and redshift distribution of the real data sample, but is 200 times more dense.

We are also interested in the projected correlation function $\Xi(r_\perp)$, which provides information of the real-space clustering so that we do not need to worry about the complications of peculiar motions [59]. As it is obtained integrating the 2D correlation function $\xi(s_{los}, s_\perp)$ along the

line-of-sight (Eq. 1.93), we use the estimator:

$$\Xi(r_\perp) = 2 \sum_{i}^{s_{los,max}} \xi(s_{los,i},\, s_\perp)\, \Delta s_{los}\,, \tag{5.12}$$

where we bin the 2D correlation function into linearly spaced bins of constant size $\Delta s_{los} = 5\, h^{-1}\, \mathrm{Mpc}$, and select a maximum summation distance of $s_{los,max} = 30\, h^{-1}\, \mathrm{Mpc}$. $\xi(s_{los},\, s_\perp)$ is obtained from Eq. 5.6 converting s and μ in terms of s_{los} and $s_\perp$, where $s_{los} = \mu\, s$, and $s_\perp = \sqrt{s^2 - s_{los}^2}$, are the components of s parallel and perpendicular to the line-of-sight.

We use the jackknife method to compute the covariance matrices of the correlation function. For each cluster sample we randomly create 80 cluster subsamples that comprise 1/80th part of the total, and then compute 80 times the monopole, dipole and projected correlation function of the total cluster sample with one of those cluster subsamples removed. The covariance matrix C associated to this sample is then:

$$C_{ij} = \frac{N-1}{N} \sum_{k=1}^{N} \left(\langle \chi_i \rangle - \chi_i^k\right)\left(\langle \chi_j \rangle - \chi_j^k\right)\,, \tag{5.13}$$

where χ_i corresponds to either ξ_0, ξ_2 or Ξ at the ith bin, and $\langle \chi_i \rangle$ is the mean value of the $N = 80$ calculations at the ith bin.

5.3.1 Results

Redshift-space two-point correlation function

As a check of the power of both the spectroscopic sample that we have constructed and our probability-weighted estimator $\xi(s)$, we compute first the redshift-space two-point correlation function up to $s = 80\, h^{-1}\, \mathrm{Mpc}$. To do so, we use a test sample containing all the clusters in the $0.080 \leqslant z \leqslant 0.325$ redshift range, and richness $\lambda > 22$, comprising 7,143 clusters. The values obtained are shown in Fig. 5.6, where we also compare our results with previous measurements of the cluster correlation function found in the literature, namely those by Bahcall et al. [23], Estrada et al. [72] and Sereno et al. [213]. Notice in Fig. 5.6 that the correlation function rises continuously to small radius with a slope similar to previous work but with much higher precision because of the larger numbers of clusters sampled to higher redshift. The increasingly shallower slope of Sereno et al. [213] at smaller scales is due to smoothing by the relatively large proportion of photometric redshifts in their analysis of the GMBCG cluster catalogue.

Measured monopole, quadrupole, 2-dimensional, and projected correlation function

Here we first divide the redMaPPer catalogue into three different richness bins with similar numbers of clusters, $\lambda_1 \in [22, 30)$, $\lambda_2 \in [30, 45)$, and $\lambda_3 \in [45, 200)$, and then divide again each of these subsamples into two redshift regions in order to have a "low-z" and a "high-z" sample and examine any possible evolution. The redshift regions for each of these six subsamples, together with the mean redshift, mean richness and number of clusters contained, are listed in Table 5.1.

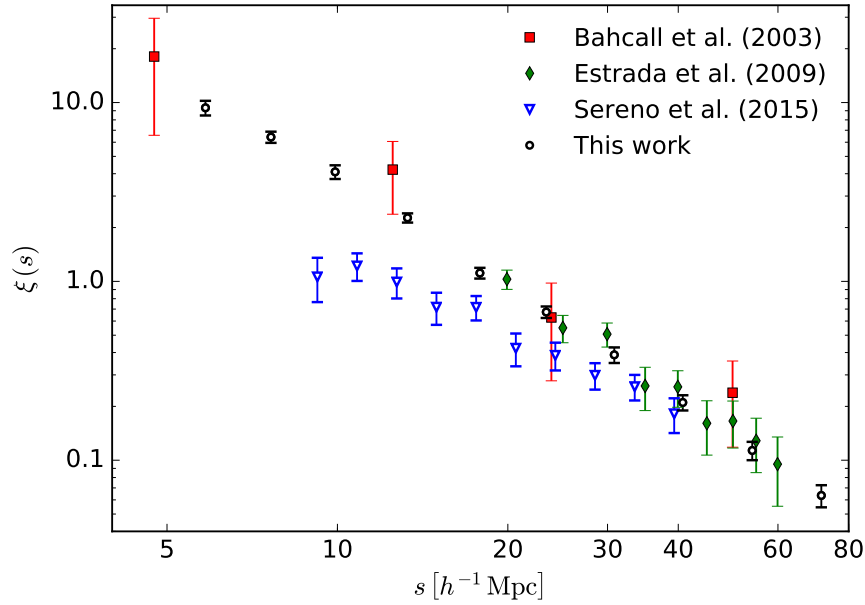We now compute the monopole $\xi_0(s)$, the quadrupole $\xi_2(s)$, the 2-dimensional $\xi(s_{los}, s_\perp)$, and

Figure 5.6: *Our measurement of the redshift space correlation function of clusters (black circles) shows the huge improvement in precision now possible with the latest SDSS release, for the spectroscopically complete sample of 7,143 redMaPPer clusters contained in the full range $0.08 \leqslant z \leqslant 0.325$, with a lower richness limit of $\lambda > 22$. For comparison, we plot previous measurements that also used SDSS cluster samples: Bahcall et al. [23] as red squares, Estrada et al. [72] as green diamonds, and Sereno et al. [213] as blue triangles.*

the projected $\Xi(r_\perp)$ correlation function following the procedure described before. We bin s into 8 logarithmic distributed bins between $5\,h^{-1}\,\mathrm{Mpc}$ and $35\,h^{-1}\,\mathrm{Mpc}$, and bin s_{los} and $s_\perp$ into linearly spaced bins of a size equal to $0.5\,h^{-1}\,\mathrm{Mpc} \times 0.5\,h^{-1}\,\mathrm{Mpc}$. The obtained values of ξ_0, ξ_2 and Ξ for the six subsamples are shown in Fig 5.7, together with the MXXL realization model that best fits the measured correlation function (see Sec. 5.5). In the same way, the redMaPPer and the MXXL 2-dimensional correlation functions are shown in Fig. 5.8.

Although the measurements of the quadrupole are too noisy to obtain any information from them, as we can see there is a clear increase in the amplitude of both the monopole and the projected correlation function for higher richness bins, in excellent agreement with the MXXL model predictions, which match very well with radius and with richness. There is no clear evidence of any evolution between the two redshift bins in any of the three richness subsamples considered, which is in good agreement with the MXXL simulation for the relatively small redshift range of the data. Some differences are apparent here in the redshift direction in Fig. 5.8 with enhancement along the line-of-sight compared to MXXL, which could be due to the higher than expected peculiar motion of the CGs used to define the observed cluster redshifts, or to some systematics associated to the way the algorithm identifies clusters that are close to each other along the line-of-sight direction.
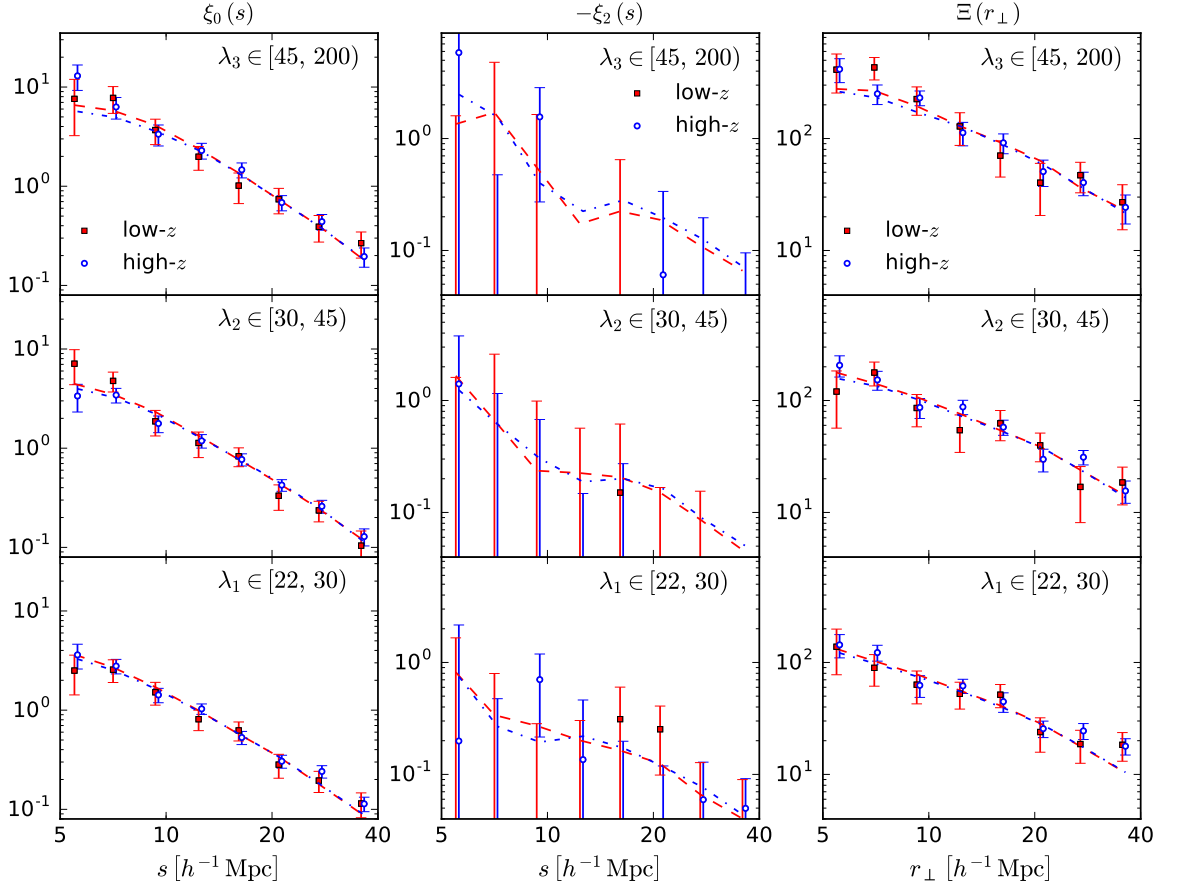
Figure 5.7: *Monopole $\xi_0(s)$ (left column), quadrupole $\xi_2(s)$ (central column) and projected correlation function $\Xi(r_\perp)$ (right column) for two redshift samples: low-z (red squares for redMaPPer and red dashed lines for the model) and high-z (blue circles for redMaPPer and blue dot-dashed lines for the model), and three richness ranges: $\lambda \in [22, 30)$ (upper panels), $[30, 45)$ (central panels), and $[45, 200)$ (lower panels). The model curve here is derived in Sec. 5.5 from our likelihood analysis based on the MXXL simulation, and the best fitting mass–richness relation.*
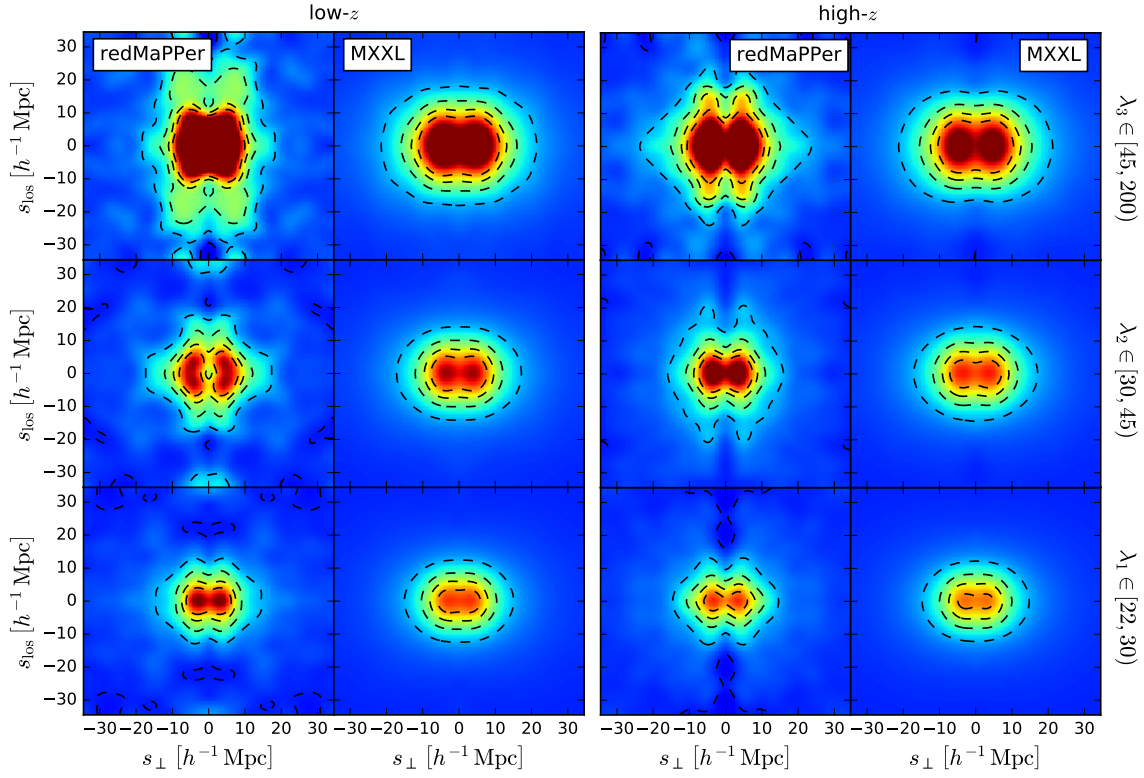
Figure 5.8: *2-dimensional correlation function $\xi(s_{los}, s_\perp)$ for two redshift samples: low-z (left panels) and high-z (right panels), and three richness bins: $\lambda \in [22, 30)$ (bottom), $[30, 45)$ (middle), and $[45, 200)$ (top). The model results derived in Sec. 5.5 from the MXXL simulation are shown for comparison. Dashed contours correspond to values $\xi(s_{los}, s_\perp) = (0.0, 1.5, 3.0, 4.5)$. For clarity, a Gaussian smoothing with a kernel of width $5\,h^{-1}\,\mathrm{Mpc}$ has been applied to the images.*

Table 5.1: *Richness range λ, redshift region z_{clu}, number of clusters N, mean richness $\langle\lambda\rangle$, and mean redshift $\langle z_{\mathrm{clu}}\rangle$ of the six redMaPPer cluster subsamples considered in the measurement of the correlation function.*

Subsample	λ	z_{clu}	N	$\langle\lambda\rangle$	$\langle z_{\mathrm{clu}}\rangle$
λ_1 low-z	$[22, 30)$	$[0.080, 0.250)$	1770	25.3	0.189
λ_1 high-z	$[22, 30)$	$[0.250, 0.400]$	4493	25.6	0.334
λ_2 low-z	$[30, 45)$	$[0.080, 0.275)$	1527	36.0	0.205
λ_2 high-z	$[30, 45)$	$[0.275, 0.425]$	4008	35.9	0.363
λ_3 low-z	$[45, 200)$	$[0.080, 0.300)$	1024	63.1	0.221
λ_3 high-z	$[45, 200)$	$[0.300, 0.450]$	2384	62.11	0.388

Table 5.2: *Values of the correlation length r_0 and the real-space correlation function slope γ obtained for the six redMaPPer cluster subsamples considered in Table 5.1.*

Subsample	$r_0\,[h^{-1}\,\mathrm{Mpc}]$	γ
λ_1 low-z	14.53 ± 1.20	2.04 ± 0.18
λ_1 high-z	15.58 ± 0.61	2.16 ± 0.11
λ_2 low-z	17.32 ± 0.90	2.26 ± 0.19
λ_2 high-z	17.74 ± 0.51	2.34 ± 0.10
λ_3 low-z	23.05 ± 1.08	2.55 ± 0.20
λ_3 high-z	22.19 ± 0.65	2.52 ± 0.13

Correlation length

In order to fit the real-space correlation function $\xi(r)$, we approximate it by a power law:

$$\xi(r) = \left(\frac{r}{r_0}\right)^{-\gamma} . \tag{5.14}$$

Considering this expression, from Eq. 1.93 we know that the projected correlation function of such a real-space correlation function should follow:

$$\Xi(r_\perp) = \sqrt{\pi}\,\frac{\Gamma\left((\gamma - 1)/2\right)}{\Gamma\left(\gamma/2\right)}\,r_0^\gamma\,r_\perp^{1-\gamma} , \tag{5.15}$$

which is the function that we fit leaving both the correlation length r_0 and the slope γ as free parameters. In this equation $\Gamma(x)$ is the usual gamma function.

The values found for both r_0 and γ for each of the six redMaPPer subsamples considered before are given in Table 5.2. The redshift and richness dependence of these results is shown in Fig. 5.9, in comparison with the MXXL model that adopts the clustering-based mass–richness relation parameters described later in Sec. 5.5. The slow increasing trend with redshift corresponds to the increasing bias at fixed mass with redshift, corresponding to rarer more biased peaks in the density field ([103], see Sec. 1.2.5).

The values of r_0 for the cluster subsamples considered agree, within the noise, with the MXXL
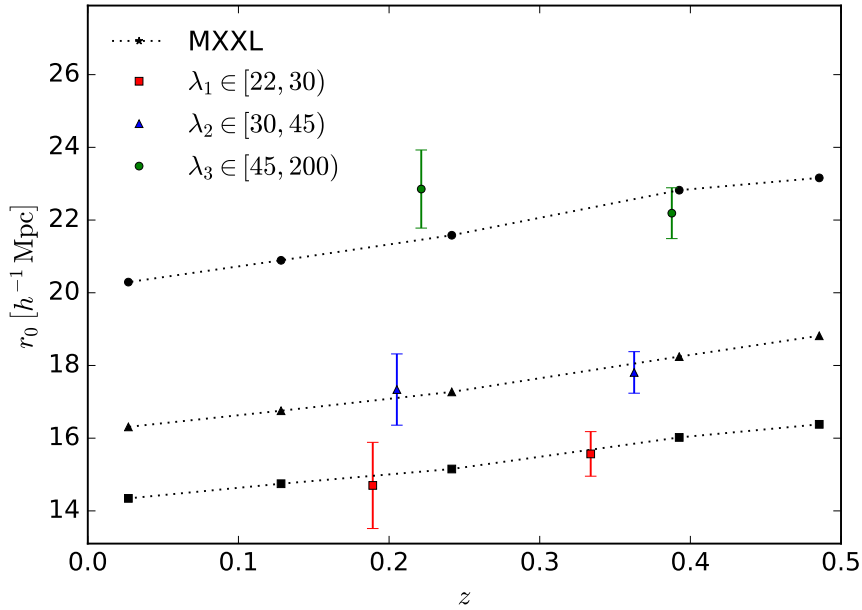
Figure 5.9: *Values of the correlation length r_0 obtained for the six cluster subsamples listed in Table 5.1 as a function of the average redshift of the sample. Within two redshift regions, three richness ranges have been considered: $\lambda \in [22, 30)$ (red squares), $[30, 45)$ (blue triangles), and $[45, 200)$ (green circles). As dotted lines, the model values that we obtain from the MXXL simulation for these three richness ranges (from bottom to top, respectively) and the snapshots available. The mass–richness relation needed to obtain the MXXL model curves is obtained in Sec. 5.5.*

simulation expected values, with the only exception of the λ_3 subsample, where the low-z subsample is slightly more than 1σ above the expected value, and the high-z is $\sim 1\sigma$ below the model. This could be an indication of the limitations of the redMaPPer algorithm above $z > 0.35$, where it may be overestimating the richness of some clusters and thus diluting the amplitude of the correlation function.

Now we make the same measurement for these three richness subsamples but considering only the more conservative redshift region $0.080 \leqslant z_{\mathrm{clu}} \leqslant 0.325$, where the upper redshift limit is defined by the careful redMaPPer analysis as the limit of their volume-complete region for clusters with richness $\lambda > 20$. The results obtained are shown in Fig. 5.10, where the relation between correlation length and richness, already noticed in Fig. 5.7 and with an obvious rising trend that is very well fitted by MXXL, reflects the enhanced bias expected for more massive clusters formed in a Gaussian random field.

From these measured values of the correlation length $r_0(\langle\lambda_1\rangle)$, $r_0(\langle\lambda_2\rangle)$ and $r_0(\langle\lambda_3\rangle)$, where $\langle\lambda_1\rangle$, $\langle\lambda_2\rangle$, and $\langle\lambda_3\rangle$ represent the average cluster richness of the three richness subsamples considered, we observe the following linear relation between the value of the richness λ and the value of the correlation length r_0:

$$r_0(\lambda) = 9.87 \pm 0.17 + (0.198 \pm 0.004)\,\lambda\,. \tag{5.16}$$

The fact that the data shows such a clear trend with richness rising at the rate that is consistent with the MXXL simulation is very clear evidence for the standard physical understanding of the
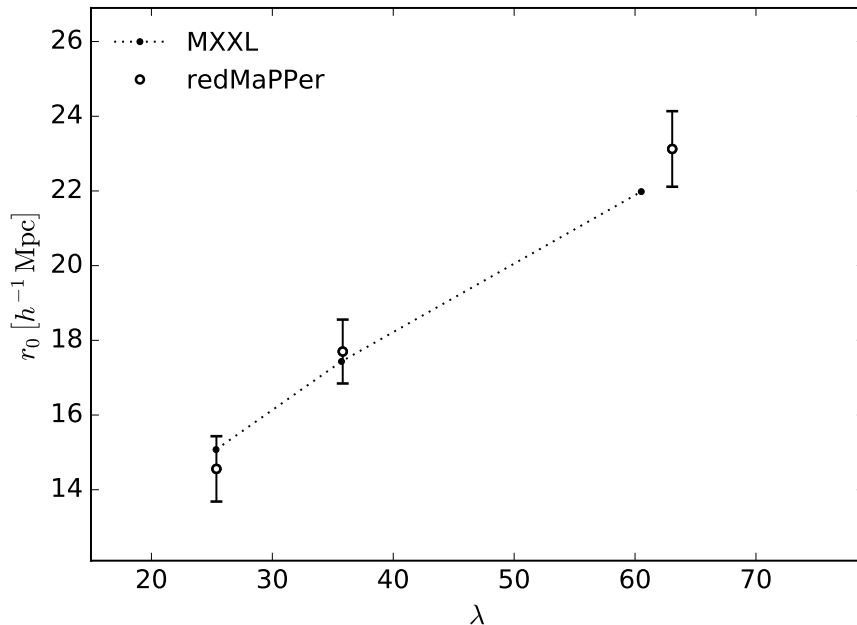
Figure 5.10: *The correlation length r_0 obtained from the projected correlation function for three redMaPPer richness subsamples, $\lambda \in [22, 30)$, $[30, 45)$, and $[45, 200)$, in the $0.080 \leqslant z_\mathrm{clu} \leqslant 0.325$ redshift range. The dotted line is the equivalent MXXL correlation length as obtained in the same richness ranges once the mass–richness relation obtained in Sec. 5.5 is applied.*

formation of structure from a Gaussian random field under gravity described in Chapter 1.

5.4 Cluster abundances

We proceed now to study the comoving density of clusters as a function of their richness and their redshift. In this section, we limit our sample to the redshift range $0.080 \leqslant z_\mathrm{clu} \leqslant 0.325$, where the authors of the redMaPPer catalogue have established volume-completeness, required in this kind of analyses. We can also see from Fig. 5.2 that this claim is supported by the way the number of clusters scale in proportion to the cosmological volume. Above $z = 0.35$, the richness calculated by the redMaPPer algorithm is increasingly limited to a diminishing proportion of relatively luminous galaxy members so that an uncertain estimate has to be made to take into account undetected galaxies below the survey magnitude limit, implying that richness estimates become more noisy above this redshift. Also, with increasing redshift Eddington bias [67] tends to increase the cluster density as a function of richness. Thus, we expect to obtain more robust results working with a cluster redshift cutoff of $z \leqslant 0.325$.

Following a similar approach to that described in Sec. 1.2.7, the number of clusters N_i that one may expect to find in the redshift range $[z_\mathrm{min}, z_\mathrm{max}]$, and within a richness range $[\lambda_i, \lambda_i + \Delta\lambda]$ is given by:

$$N_i = f_\mathrm{sky} \int_{z_\mathrm{min}}^{z_\mathrm{max}} \frac{\mathrm{d}V}{\mathrm{d}z}\, \mathrm{d}z \int_{\lambda_i}^{\lambda_i + \Delta\lambda} \frac{\mathrm{d}N(\lambda, z)}{\mathrm{d}V\,\mathrm{d}\lambda}\, \mathrm{d}\lambda \,, \tag{5.17}$$

where f_sky is the fraction of the sky covered by the survey, $\mathrm{d}V/\mathrm{d}z$ is the comoving volume per unit redshift, and $\mathrm{d}N/(\mathrm{d}V\,\mathrm{d}\lambda)$ is the theoretical cluster *richness function*.
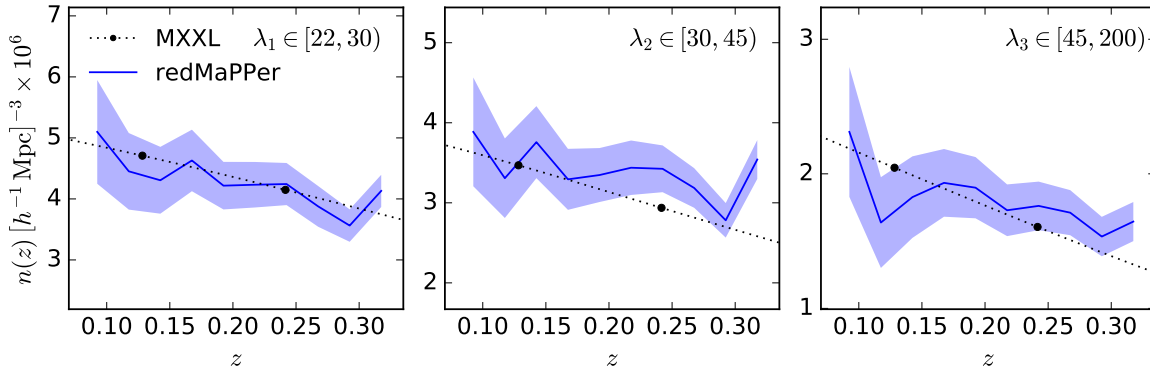
Figure 5.11: *Cluster comoving densities $n(z)$ in the $0.080 \leqslant z_{\mathrm{clu}} \leqslant 0.325$ redshift range of three richness subsamples, $\lambda \in [22, 30)$ (left), $[30, 45)$ (middle), and $[45, 200)$ (right). The shaded region represents Poisson noise and errors introduced by the uncertainty in the richness measurement of each cluster, as provided by the redMaPPer catalogue. Dotted lines represent the MXXL model density distributions in the same three richness ranges, once the optimal mass–richness relation obtained in Sec. 5.5 is used to obtain the synthetic cluster catalogue.*

5.4.1 Results

Comoving density redshift evolution

To compute cluster abundances, we average between several Monte Carlo (MC) realisations of the redMaPPer richness distribution to take into account the error on the number of clusters contained in each richness bin that the uncertainty on the richness estimate of each cluster, provided by the redMaPPer catalogue, can introduce. We take the mean values when convergence is obtained, and consider the standard deviation obtained from all these realisations an additional source of systematics, adding it in quadrature to the intrinsic Poisson noise in each bin.

The comoving density of clusters $n(z)$ found within the redshift region previously mentioned is shown in Fig. 5.11 for three richness samples, where the $\lambda_1 \in [22, 30)$, $\lambda_2 \in [30, 45)$, and $\lambda_3 \in [45, 200)$ binning has been again considered, together with the MXXL model abundances.

The agreement between the data and the simulation is within the noise in this redshift range, showing a systematic decline of about 20% in the number density of clusters between $z \sim 0.1$ and $z \sim 0.3$. This is similar to the predictions of MXXL for this redshift range, corresponding to the expected growth of massive clusters over the past $3\,\mathrm{Gyr}$ in the context of ΛCDM.

Richness function

To compute the cluster richness function we restrict the sample to those clusters in the redshift range $0.080 \leqslant z_{\mathrm{clu}} \leqslant 0.325$, and then we divide it in two redshift bins such that there is approximately equal number of objects in each redshift bin. This results in two subsamples with $0.080 \leqslant z_1 < 0.246$, and $0.246 \leqslant z_2 \leqslant 0.325$, with mean redshifts $\langle z_1 \rangle = 0.186$ and $\langle z_2 \rangle = 0.287$, respectively. We then bin each subsample into 10 log-spaced richness bins in the range $\lambda \in [22, 200]$. The results obtained are shown in Fig. 5.12. For comparison we also show the MXXL model results, obtained interpolating to the mean redshifts of the data, $z = 0.186$ and $z = 0.287$.
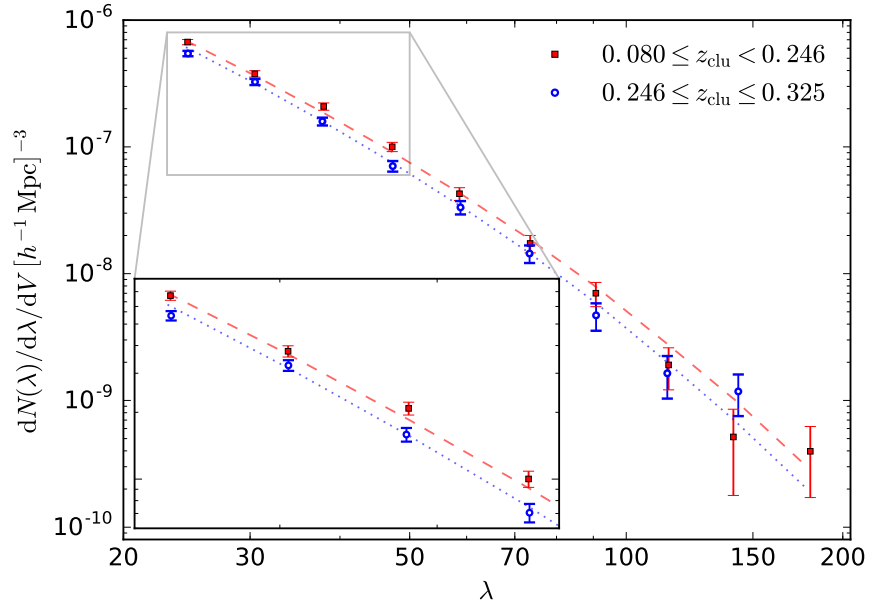
Figure 5.12: *Cluster richness function of the redMaPPer clusters in the range $\lambda \in [22,\,200]$ for two redshift subsamples: $0.080 \leqslant z_1 < 0.246$ with $\langle z_1 \rangle = 0.186$ (red squares) and $0.246 \leqslant z_2 \leqslant 0.325$ with $\langle z_2 \rangle = 0.287$ (blue circles). Error bars include both Poisson noise and errors propagated from the uncertainty on the measured richnesses. A zoomed region $\lambda \in [22, 50]$ shows the clear evolution with redshift relative to the small errors. The dashed red and dotted blue lines represent the richness functions predicted by the MXXL-based model, derived in Sec. 5.5.*

It should be noted that, as described in the following section, no evolutionary information was used at all to calibrate the mass–richness relation applied to create the MXXL synthetic cluster catalogues. Thus, the accurate agreement of the data in Fig. 5.12 with the evolution predicted by MXXL shows the degree of consistency with the predictions of ΛCDM. Note that there was no prior guarantee that this comparison would reveal the same evolutionary trend in the cluster richness function.

5.5 Likelihood analysis

We now obtain through a likelihood analysis the mass–richness relation parameter values that best describe the observations. We compare redMaPPer results with those drawn from MXXL, covering a wide range of values for a power law mass–richness relation, where, as we described in Sec. 5.2, $\kappa_{M|\lambda}$ is the pivot mass normalisation, $\alpha_{M|\lambda}$ is the slope, and the intrinsic dispersion is given by $\sigma_{M|\lambda}$. As the assignment of richness given a value of the mass is an stochastic process, we average the results generated from several realisations of the synthetic cluster catalogues produced using the MXXL simulation (as we did in Sec. 5.4 with the redMaPPer catalogue) until convergence is obtained.

For the pivot mass and for the slope we consider uniform flat priors: $\kappa_{M|\lambda} \in [1.000,\, 2.000]$, and $\alpha_{M|\lambda} \in [0.500,\, 1.600]$. For the case of the scatter, a hard cutoff $\sigma_{M|\lambda} > 0$ could bias the resulting posterior distribution, so we adopt the inverse gamma distribution prior $IG(\epsilon, \epsilon)$ for $\sigma_{M|\lambda}^2$ [10, 210, 247] with ϵ a very small number (in our case, we take $\epsilon = 10^{-3}$). We sample the

posterior distribution using a large enough 3-dimensional grid.

5.5.1 Clustering

We first derive a mass–richness relation through a likelihood analysis comparing the correlation amplitude of redMaPPer clusters with the correlation amplitude measured in the MXXL simulation.

To make a more consistent joint analysis with the values obtained from the abundances-based likelihood analysis, described later, we limit our sample to the clusters contained in the volume-complete region $0.080 \leqslant z_{\mathrm{clu}} \leqslant 0.325$.

In this case, to obtain the values for $\kappa_{M|\lambda}$, $\alpha_{M|\lambda}$ and $\sigma_{M|\lambda}$ that best describe the clustering results we rely on the projected correlation function $\Xi(r_\perp)$ of the whole sample, without any redshift nor richness binning. We follow the procedure described in Sec. 5.3 to obtain the points and the covariance matrix required for the likelihood analysis. The likelihood employed has the form:

$$\mathcal{L}(\vec{\Xi}|\vec{\theta}, C) \propto \exp\left[-\frac{1}{2}\chi^2\left(\vec{\Xi}, \vec{\theta}, C\right)\right] , \tag{5.18}$$

where $\vec{\Xi}$ is the 8-dimensional projected correlation function data vector obtained from the redMaPPer cluster sample, $\vec{\theta}$ is the mass–richness relation model vector $\vec{\theta} = (\kappa_{M|\lambda}, \alpha_{M|\lambda}, \sigma_{M|\lambda})$, C is the 8×8 covariance matrix, and

$$\chi^2\left(\vec{\Xi}, \vec{\theta}, C\right) = \left(\vec{\Xi} - \vec{\mu}(\vec{\theta})\right) C^{-1} \left(\vec{\Xi} - \vec{\mu}(\vec{\theta})\right)^T , \tag{5.19}$$

with $\vec{\mu}(\vec{\theta})$ the projected correlation function vector measured from the synthetic cluster catalogues produced from the MXXL simulation when the mass–richness with $\vec{\theta}$ is considered, as described in Sec. 5.2.

The projected correlation function obtained is shown in Fig. 5.13, together with the MXXL realization with the mass–richness relation parameters given in Table 5.3.

Finally, we mention that these results are compatible with the ones obtained when we perform the same analysis independently in three richness ranges, the previously mentioned $\lambda_1 \in [22, 30)$, $\lambda_2 \in [30, 45)$, and $\lambda_3 \in [45, 200)$ richness bins.

5.5.2 Abundances

Repeating a similar likelihood analysis, but now comparing the richness function that describes the distribution of redMaPPer clusters and the equivalent richness function provided by the MXXL simulation, we obtain another independent mass–richness relation.

To compute the richness function from the data, we restrain our sample to those clusters contained in the volume-complete region $0.080 \leqslant z_{\mathrm{clu}} \leqslant 0.325$, without any further redshift binning, and distribute them into 10 log-spaced richness bins in the range $\lambda \in [22, 200]$ (the maximum richness in this redshift range is found near ~ 200). As the median redshift of the sample considered, which comprises 7,143 clusters, is equal to $\langle z_{\mathrm{clu}} \rangle = 0.24$, we work with the dark matter halo catalogue obtained from the MXXL simulation snapshot number 54, that corresponds to a redshift $z = 0.242$.

To obtain the best fit and the associated confidence intervals, we follow the procedure derived
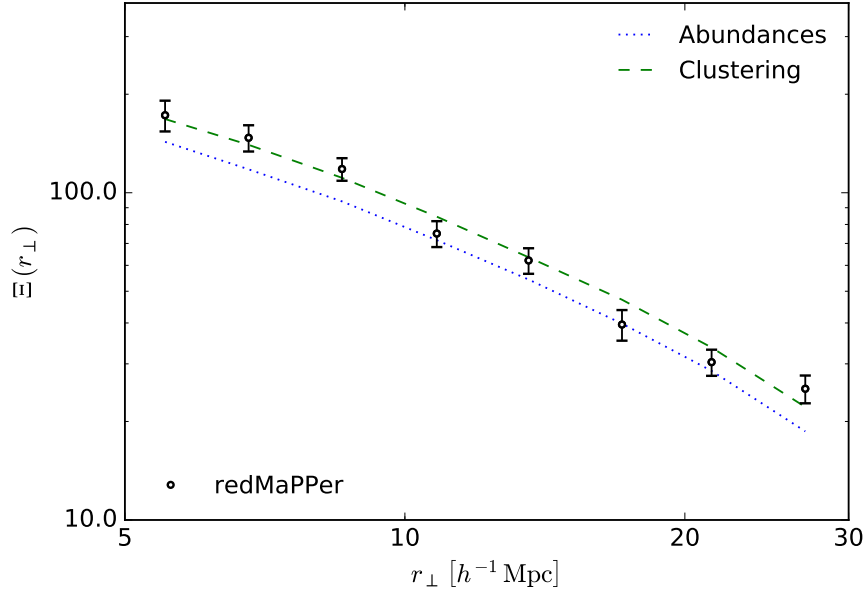
Figure 5.13: *Projected correlation function $\Xi(r_\perp)$ of the redMaPPer clusters for the full $0.080 \leqslant z_{\mathrm{clu}} \leqslant 0.325$ redshift range. The dashed green line is the expected correlation function derived from MXXL when we convert between mass and richness using the best fit mass–richness relation derived from the clustering data alone. The blue dotted line represents an independent check using the abundances-based mass–richness relation.*

by Cash [48] for Poisson statistics. To do so, we define the quantity $\mathcal{C}(\vec{n}|\vec{\theta}) = -2\ln\mathcal{L}(\vec{n}|\vec{\theta})$, where $\mathcal{L}(\vec{n}|\vec{\theta})$ is the likelihood function that depends on both the 10-dimensional data vector $\vec{n}$ and the mass–richness relation model vector $\vec{\theta} = (\kappa_{M|\lambda}, \alpha_{M|\lambda}, \sigma_{M|\lambda})$. The deviations of $\mathcal{C}$ from the minimum follow a χ^2 distribution, and in our case it is equal to:

$$\mathcal{C}(\vec{n}|\vec{\theta}) = -2\ln\mathcal{L}(\vec{n}|\vec{\theta}) = 2\left(E(\vec{\theta}) - \sum_{i=1}^{N} n_i \ln e_i(\vec{\theta})\right), \qquad (5.20)$$

where $E(\vec{\theta})$ is the total number of clusters expected in all the $N = 10$ bins, and n_i and $e_i(\vec{\theta})$ are the observed and the expected number of clusters in the bin i, respectively. To model the expected number of clusters for each value of $\vec{\theta}$, we use the MXXL synthetic cluster catalogues created applying the mass–richness relation with $\vec{\theta}$ to the original dark matter halo catalogue.

The redMaPPer distribution that we obtain from this measurement, together with the MXXL richness function obtained applying the mass–richness relation derived from this "abundance-matching" likelihood analysis and given in Table 5.3, is shown in Fig. 5.14. This measurement differs from the one described in Sec. 5.4 (Fig. 5.12) in that we are only considering one single redshift bin to improve our statistics. Note that the fit of MXXL with the data is inherently more accurate than for the correlation function, for which the link between mass and richness is less direct than for abundances as discussed below in Sec. 5.6.

Again, the results obtained through this procedure are compatible with the ones obtained when we perform the same analysis in two redshift subsets of the catalogue with equal number of clusters contained in them, like we did in Sec. 5.4, with $0.080 \leqslant z_1 < 0.246$ and $0.246 \leqslant z_2 \leqslant 0.325$.
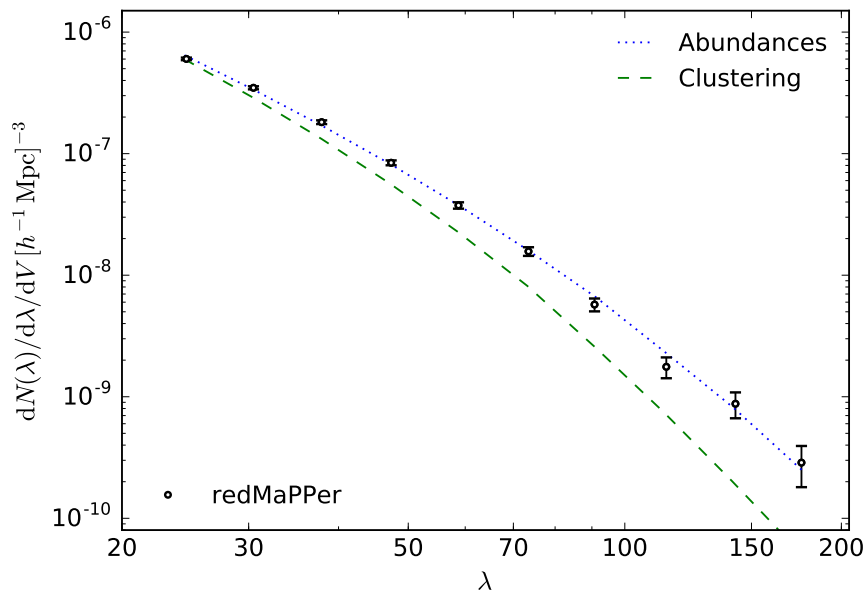
Figure 5.14: *Cluster richness function of the redMaPPer clusters for the full $0.080 \leqslant z_{\mathrm{clu}} \leqslant 0.325$ redshift range, obtained dividing the sample into 10 log-spaced richness bins in the range $\lambda \in [22, 200]$. Error bars combine Poisson errors with the errors introduced by the uncertainty on the measurement of the richness of each cluster. The dotted blue and green dashed lines correspond to the richness function of the MXXL realization with the mass–richness relation parameters obtained from the abundances analysis and the clustering analysis (Table 5.3), respectively.*

Table 5.3: *The 1σ confidence values of the marginalised posterior probabilities of the mass–richness relation parameters when the abundances, the clustering, and the combined abundances + clustering analyses are performed.*

Parameter	Abundances	Clustering	Abundances + Clustering
$\kappa_{M\|\lambda}$	1.351 ± 0.039	1.548 ± 0.205	1.341 ± 0.031
$\alpha_{M\|\lambda}$	1.127 ± 0.021	1.102 ± 0.197	1.120 ± 0.017
$\sigma_{M\|\lambda}$	0.194 ± 0.053	0.226 ± 0.089	0.164 ± 0.039

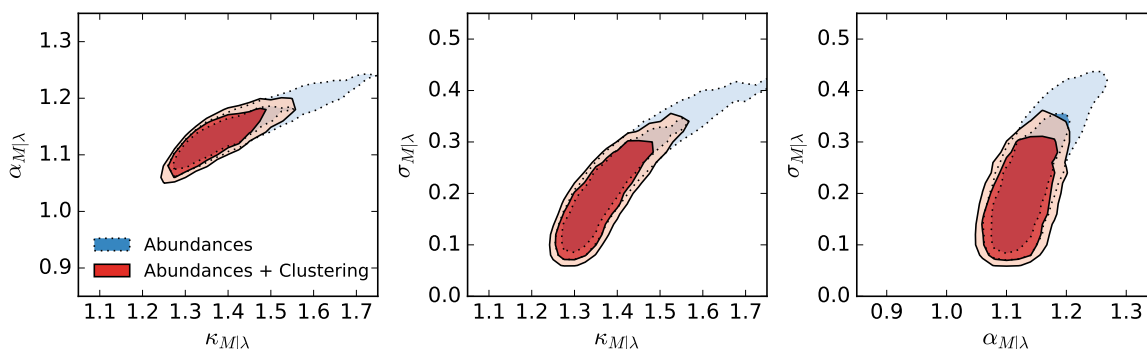**Figure 5.15:** *Constraints on the mass–richness relation parameters $\kappa_{M|\lambda}$, $\alpha_{M|\lambda}$ and $\sigma_{M|\lambda}$ at 1σ and 2σ confidence levels when the abundances (blue) and the abundances + clustering (red) analysis are performed.*

5.5.3 Results and combined analysis

The 1σ and the 2σ confidence regions of the $\kappa_{M|\lambda}$, $\alpha_{M|\lambda}$ and $\sigma_{M|\lambda}$ mass–richness relation parameters, obtained through the abundance analysis and the joint abundances + clustering analysis, are shown in Fig. 5.15, and the marginalised posterior probabilities of each parameter are given in Fig. 5.16.

To compute the center (mean) and the scale (dispersion) of the marginalised posterior distribution, we use the robust estimators described in Beers et al. [26]. The results derived from the abundances analysis, the clustering analysis, and the combined analysis are listed in Table 5.3.

From our results, it is clear that the analysis of the abundances is much powerful in means of constraining the mass–richness relation, as the range of parameters that satisfy the clustering observations is much larger in comparison.

It should be noted, though, that both measurements provide very different mass–richness relations. If we compare how the MXXL synthetic catalogues drawn from both mass–richness relations perform in terms of agreeing with the data, we find that the abundances-based mass–richness relation (i.e., the one obtained in Sec. 5.5.2) is discrepant with the correlation function observations at the 2.4σ level (Fig. 5.13). On the other hand, when we apply the clustering-based mass–richness relation (i.e., the one obtained in Sec. 5.5.1) to the MXXL and measure the richness function, we find that there is a deviation of 8.1σ with respect to the best fit, making it clear that the mass–richness relation obtained alone from the clustering data is not suitable to describe the cluster abundances observed.

In any case, when we combine both analyses and perform a joint likelihood, we obtain a
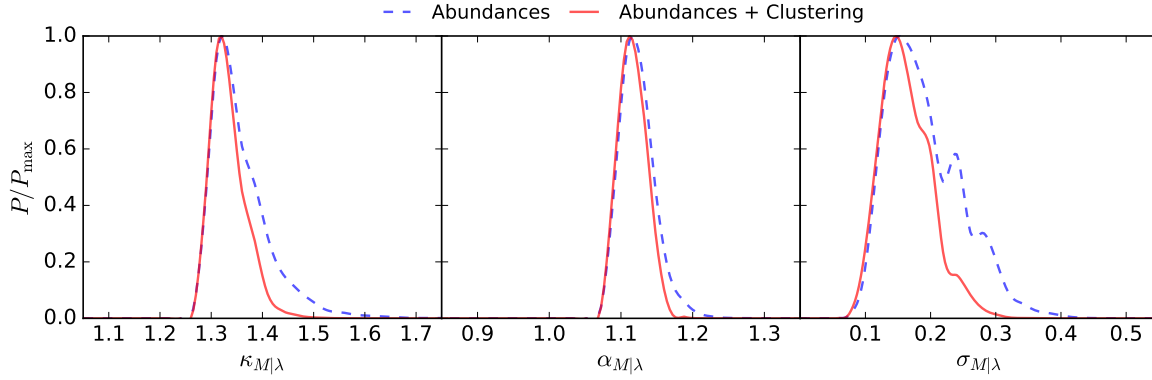
Figure 5.16: *Posterior probability distribution of the mass–richness relation parameters $\kappa_{M|\lambda}$, $\alpha_{M|\lambda}$ and $\sigma_{M|\lambda}$ marginalised over the other 2 parameters when the abundances (dashed blue) data only and the abundances + clustering (solid red) combined data are considered.*

concordance mass–richness relation that describes both measurements, with a pivot mass of:

$$\kappa_{M|\lambda} \equiv \ln\left(\frac{M_{200c}(\lambda_0 = 60)}{10^{14}\, h^{-1}\, M_\odot}\right) = 1.341 \pm 0.031\,,$$

an slope equal to:

$$\alpha_{M|\lambda} = 1.120 \pm 0.017\,,$$

and an intrinsic scatter:

$$\sigma_{M|\lambda} \equiv \Delta \ln\left(\frac{M_{200c}(\lambda)}{10^{14}\, h^{-1}\, M_\odot}\right) = 0.164 \pm 0.039\,.$$

5.6 Discussion and conclusions

From the original redMaPPer catalogue and the latest DR12 spectroscopy, we have created a sample of $\sim 23{,}000$ clusters with spectroscopic redshifts, and have studied the cluster correlation function and the cluster abundances as a function of their optical richness and redshift.

For the correlation function calculation, we have used the centering probabilities of the candidate central galaxies that the redMaPPer catalogue provides as an additional weight to obtain a clearer signal. We detect a significant increase of the amplitude of both the monopole and the projected correlation function for higher average richness subsamples, but we do not notice any redshift dependence when those richness subsamples are split into different redshift bins.

On the other hand, when we measure the cluster comoving number density on the range $0.080 \leqslant z \leqslant 0.325$, and measure the richness function for two redshift slices with mean redshifts $\langle z_1 \rangle = 0.186$ and $\langle z_2 \rangle = 0.287$, we do detect a clear continuous evolution of the abundances of clusters, which is in excellent agreement with the behaviour of the MXXL simulation.

We have compared our measurements with synthetic cluster catalogues that we have created from the MXXL simulation, one of the largest cosmological simulations available, mimicking the distribution, miscentering and peculiar velocities of central galaxies within clusters. To do so, we have assumed the usual power law mass–richness relation to convert the masses of the dark

matter haloes found in the simulation into richness. Assuming a ΛCDM *Planck* cosmology, we find that the best agreement with the data is obtained for a mass–richness relation with a pivot mass $\ln[M_{200c}/(10^{14}\,h^{-1}\,M_\odot)] = 1.341 \pm 0.031$ evaluated at $\lambda = 60$, a slope $\alpha_{M|\lambda} = 1.120 \pm 0.017$, and a scatter $\sigma_{M|\lambda} = 0.164 \pm 0.039$.

The MXXL fits to the data are remarkably good in all respects as a function of richness, redshift and separation, with no clear discrepancy visible in any of these comparisons, providing very strong confirmation of the detailed viability of the ΛCDM model. However, we do notice that the amplitude of the correlation function is slightly higher than expected when only the abundances are used to constrain the mass–richness relation, with a deviation of $\simeq 2.5\sigma$. The clustering measurements are described by a large range of mass–richness relation parameters, many of them agreeing with the abundance analysis, but the inherent precision is lower for defining the mass–richness relation via clustering. This possible tension between the abundance defined mass–richness relation and the amplitude of the observed correlation function has motivated us to make the same consistency check with the former MXXL and Millennium Simulation WMAP consensus values of σ_8, Ω_m and H_0 because they were, until recently, significantly different from the most recent *Planck* weighted values and these parameters are the most important for predicting the abundances of clusters and their correlation function. With these former values we find a completely acceptable consistency between the correlation function and the abundances. In Fig. 5.17 we show the clustering predictions for both cosmologies when the mass–richness relation is obtained independently from abundance-matching techniques. This may prove very interesting because of the increased support for $H_0 = 73\,\mathrm{km\,s^{-1}}$ from the independent local distance ladder measurements [190] that adds support to previous claims for this value at somewhat lower significance [80] and from independent lensing time delay estimates of H_0 [36].

Deeper, higher resolution, wide-field imaging surveys should finally provide the long hoped statistically large sample of "mass selected" clusters to greater depth, in particular the Subaru/HSC [143, 233], J-PAS Northern Sky [27] and DES [58] surveys now underway. Broad-band surveys like HSC will require careful avoidance of foreground/member dilution of the background lensing signal that is feasible by excluding degenerate colour space [40, 137, 138, 240], with the fullest wavelength coverage to maximise the numbers of galaxies redder than the cluster and also dropouts. In the case of J-PAS, the many narrow bands will provide unambiguous redshifts based on resolved spectral features, allowing clusters to be identified cleanly and to relatively low mass [17]. All these surveys will provide lensing masses and redshifts for all SDSS clusters, and will go beyond in redshift, measuring unprecedentedly accurate growth as a function of cluster mass in the range $z \lesssim 1.0$ (Fig. 5.18), with the prospect of constraining the total relativistic species contribution to Ω_m, and obtaining a clearer insight into the emerging tensions between the parameters describing the standard ΛCDM model.
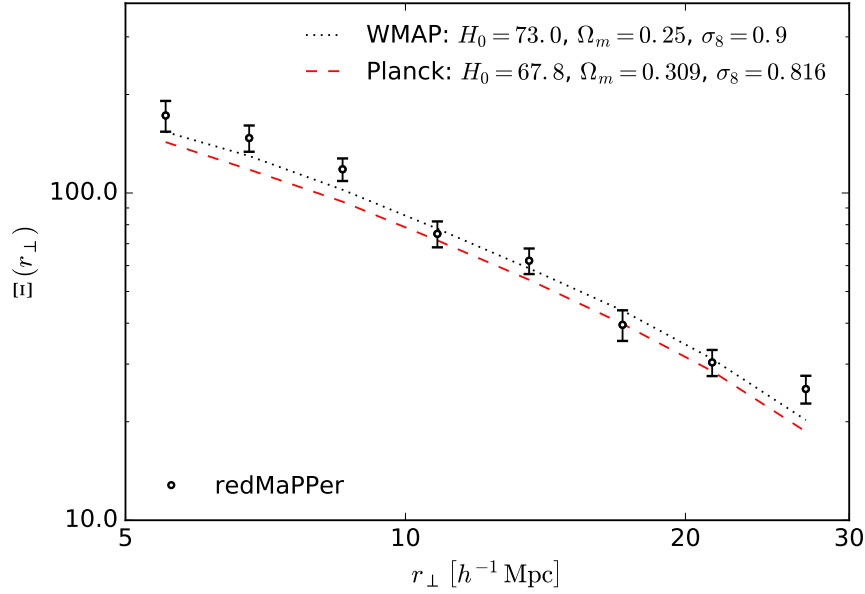
Figure 5.17: *The projected correlation function compared with those predicted by the MXXL, obtained independently in two different cosmologies through the mass–richness relations derived from the abundance-matching method: as the black dotted line, the former WMAP cosmology with $\Omega_m = 0.25$ and $\sigma_8 = 0.9$, and as the red dashed line, the Planck cosmology with $\Omega_m = 0.309$ and $\sigma_8 = 0.816$. The WMAP cosmology model agrees more with the observations than the model obtained when the Planck cosmology is considered.*
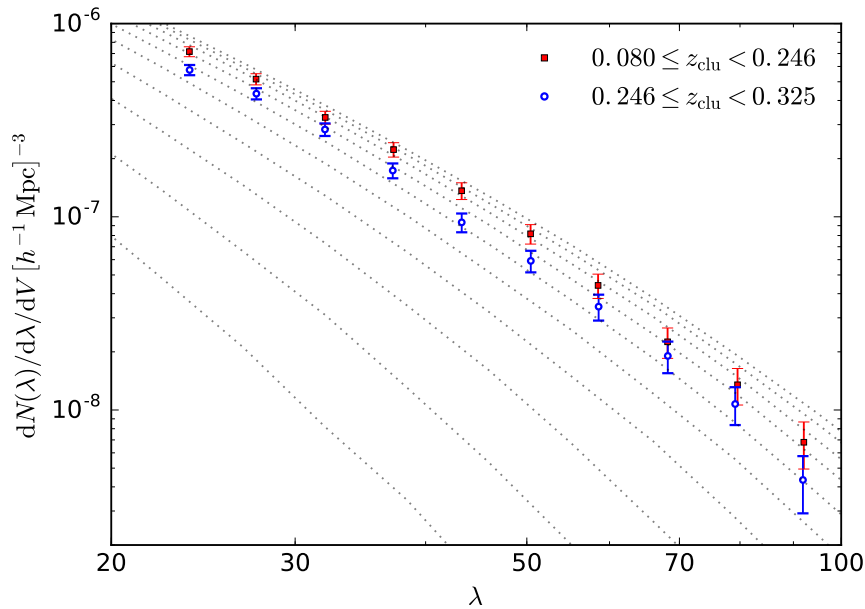
Figure 5.18: *As dotted lines, the MXXL richness function at redshifts (from top to bottom): 0.027, 0.083, 0.154, 0.242, 0.351, 0.486, 0.652, 0.857, 1.110 and 1.424. We use the joint analysis mass–richness relation (Table 5.3) to convert mass into richness. For comparison we show the cluster richness function of the redMaPPer clusters in the $22 < \lambda < 100$ range for two redshift subsamples with $\langle z_1 \rangle = 0.186$ (red squares) and $\langle z_2 \rangle = 0.287$ (blue circles), illustrating the potential of the upcoming deeper imaging surveys to evaluate the growth of structure.*

6

Planck/SDSS Cluster Mass and Gas Scaling Relations

Galaxy clusters are powerful cosmological probes that provide complementary constraints in the era of "Precision Cosmology". They contribute accurate consistency checks and unique new competitive constraints because of the well understood cosmological sensitivity of their numbers and clustering [63, 96, 98, 165, 181]. The growth of structures has led the observational evidence to support dark energy dominance today, in combination with complementary constraints [6, 19, 20, 47, 68, 117, 160]. To realize their full cosmological potential, large, homogeneous samples of clusters are now being constructed out to $z \simeq 1$ with weak lensing based masses, in particular the Subaru/HSC and JPAS surveys [27, 157].

Currently the best direct lensing masses are limited to relatively small subsamples of X-ray and Sunyaev-Zel'dovich (SZ) selected clusters, totalling ~ 100 clusters [158, 246, 272]. One of the main efforts is focused on defining scaling relations between clusters with such weak lensing masses and the more widely available X-ray, SZ and/or optical richnesses with the reasonable expectation that these relations may provide mass proxies in the absence of direct lensing masses. Such proxies have a physical basis for clusters that appear to be virialised, so that X-ray temperature and emissivity profiles can provide virial masses under hydrostatic equilibrium. Independently, the SZ distortion of the CMB spectrum relates the density and temperature of cluster gas through inverse Compton scattering, and hence naturally anticipated to scale approximately with cluster mass.

The cluster mass–richness relation, crucial in any attempt to use large number of clusters detected in the optical to constrain cosmological parameters, has been estimated in the past decade using cluster catalogues derived from the SDSS data, like the MaxBCG [112], or the already described GMBCG, WHL12, and redMaPPer cluster catalogues, both in its SDSS [200] and DES [201] versions. This relation can be estimated directly obtaining cluster masses from X-rays, weak lensing, SZ effect or velocity dispersion measurements in clusters [10, 101, 135, 139, 204, 205, 212, 217], or indirectly, using numerical simulations [13, 43] or, as we did in Chapter 5, comparing the observed abundances or clustering amplitudes with model predictions [24, 199].

The dynamical evolution and growth of galaxy clusters are driven by the dominant dark matter, but the relevant observables depend on the physical state of the baryons. Hence scaling relations between clusters observables and mass are not direct, but have been predicted to follow physically self-similar relations [103, 116] that have been tested observationally and with hydrodynamical N-body simulations. Specifically, the integrated thermal SZ effect [230], the X-ray luminosity, and the temperature are predicted to scale with the mass of the galaxy clusters as $Y \propto M^{5/3}$, $L_X \propto M^{4/3}$ and $T \propto M^{2/3}$, respectively. While simulations agree with the self-similar model [2, 57, 146, 148, 261, 262], X-ray and SZ observations have uncovered departures from self-

similarity that may be explained by complications due to cluster mergers, including shocked gas, cool gas cores, and energy injection from active galactic nuclei (AGN) [14, 15, 61, 182, 250, 251]. Differences between the observations and purely gravitationally predicted scaling relations then provide insights into the interesting physics of the intracluster medium [7, 16, 34, 51, 56, 136, 140].

In practice, samples of strong SZ-selected clusters that are also bright X-ray sources are currently being used to calibrate the SZ–mass relation [16, 172, 177, 204], but, since such clusters are often out of hydrostatic equilibrium for the reasons mentioned above, an SZ–mass scaling relation requires a correction for "hydrostatic mass bias" [150, 206, 216, 269]. This hot gas related bias can be broadened by other systematics like object selection process or by temperature inhomogeneities in X-ray measurements. Another approach to calibrate the masses of the cluster sample is to stack clusters in terms of richness and measure the SZ signal as a function of richness. This was done first by Planck Collaboration et al. [171] using the MaxBCG catalogue and stacking the *Planck* data, and more recently by Saro et al. [205] using an initial sample of 719 DES clusters with South Pole Telescope (SPT) SZ data and assuming various priors to extract the SZ signal.

In this work, we extract the *Planck* SZ signal from $\sim 8{,}000$ redMaPPer clusters identified in the SDSS, that have allowed us in Chapter 5 to define accurate clustering and density evolution measurements in the redshift range $0.100 < z < 0.325$. Here we take this well defined cluster sample and stack the *Planck* multi-frequency data over a wide range of cluster richness. We only need to assume a weak prior for the global gas fraction using X-ray measurements to simultaneously derive a more "self-sufficient" method to derive SZ pressure profiles and the corresponding mean cluster masses binned by richness. Comparing masses derived this way with those expected from weak lensing mass–richness relations found in the literature, we derive the intrinsic bias for our sample and we then derive both a debiased mass–richness and a Y_{500}–M_{500} relation describing our observational results.

This chapter is organised as follows. In Sec. 6.1 we describe the data that we use in our analysis, namely the redMaPPer cluster catalogue and *Planck* HFI maps. The basic modelling necessary to derive the gas pressure profiles and the cluster masses from the observed SZ effect is presented in Sec. 6.2, together with the mass–richness relation that we adopt. In Sec. 6.3 we process the *Planck* data to obtain SZ maps given in terms of the Compton parameter y and use them to constrain, through a joint likelihood analysis, the universal pressure profile parameters and the mean masses of the cluster subsamples considered. In Sec. 6.4 we make an estimation of the value of the bias between the weak lensing mass and the SZ derived mass, and obtain the optimal mass–richness relation able to describe our bias-corrected masses. Finally, we use all the results obtained in the previous sections to derive a Y_{500}–M_{500} relation in Sec. 6.5, and present our conclusions in Sec. 6.6.

Throughout this chapter we adopt a fiducial flat ΛCDM cosmology with a matter density $\Omega_m = 0.3$ and a Hubble parameter with a value today of $H_0 = 70\,\mathrm{km\,s^{-1}\,Mpc^{-1}}$.

6.1 Data

In this work we combine the optically selected redMaPPer cluster sample from SDSS with the all-sky temperature maps derived by the *Planck* space mission [174].

6.1.1 redMaPPer cluster catalogue

Again, we base our analysis on the large sample of clusters provided by the SDSS-based redMaPPer catalogue, described in Chapter 3.

In this chapter, we work with the latest publicly available 6.3 version [201] of the catalogue, which contains 26,111 clusters in the $0.08 < z < 0.55$ redshift region. In comparison with the previous 5.10 version, which we used in Chapter 5, this one introduces, among other things, a series of improvements to take into account the survey depth over the area of each cluster, varying the magnitude limit considered to count galaxies within them, and modifications on the initial sample of spectra that is selected to calibrate the red-sequence required for the algorithm to find clusters. However, it should be noted that these changes are focused on improving the performance of the data obtained from the DES survey [58], and should not change much the sample obtained in the previous catalogue version, as both are constructed from the same DR8 imaging data.

Following the methodology of Chapters 4 and 5, we again restrict the sample of clusters considered to those located in the volume-complete region $0.100 < z < 0.325$. In this work we do not need the accurate spectroscopic redshift estimates that the precise measurements of the gravitational redshift and the clustering required, so we use the photometric redshifts as provided by the algorithm to select those clusters we are interested in, obtaining a total of 8,030 over an area of the sky of 10,401 deg^2, shown in Fig. 5.1 of Chapter 5.

6.1.2 Planck SZ data

Although the *Planck* temperature maps have already been used to construct catalogues of SZ sources [175] and an all-sky Compton y parameter map [178], we reprocess them for our own purposes.

To obtain the Compton parameter maps required in our analysis, we use the *Planck* full mission High-Frequency Instrument maps (HFI, [176]) at 100, 143, 217, and 353 GHz. These maps are provided in HEALPix format [83], with a pixelisation of $N_{\mathrm{side}} = 2,048$, which correspond to a pixel resolution of ~ 1.7 arcmin. The *Planck* effective beams for each of the 100, 143, 217, and 353 GHz channels can be approximated by circular Gaussians with FWHM values of 9.66, 7.27, 5.01 and 4.86 arcmin, respectively. To compute the contribution of the SZ signal in the *Planck* temperature maps, we also make use of the spectral transmission information of each of these frequency channels, as given in Planck Collaboration et al. [176], and shown in Fig. 6.1.

6.2 Model

In this work we infer the shape of the gas pressure profile and the mean masses of the cluster subsamples considered from the observed values of the Compton parameter y (introduced in Sec. 2.5 of Chapter 2), obtained from stacked samples of clusters binned in richness. We now explain the necessary modelling that we perform before being able to do so.

We note that in this chapter we do not follow the $\Delta = 200$ mass definitions adopted in Chapters 4 and 5, but work instead in terms of an spherical overdensity 500 times the critical density $\rho_c(z)$ of the Universe.
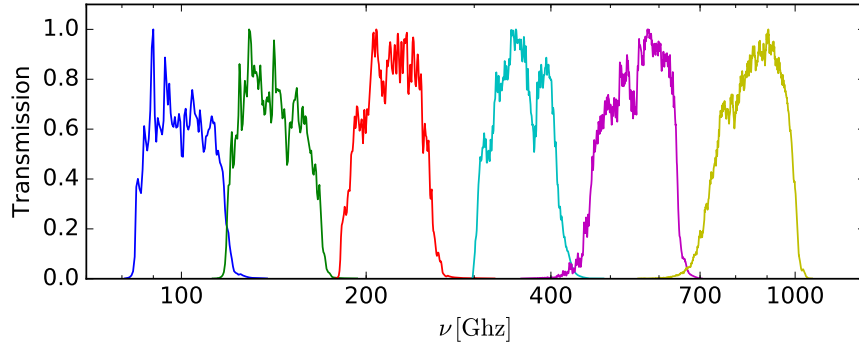
Figure 6.1: *The spectral transmission for the 6 different High-Frequency Instrument channels, with effective frequencies of 100, 143, 217, 353, 545 and 857 GHz, from left to right. Of these, in our analysis we only use information from the 100, 143, 217, and 353 GHz channels.*

Pressure profile

In this work we adopt the generalised NFW (GNFW) "universal pressure profile" proposed by Nagai et al. [150], that has a flexible double power-law form:

$$\mathbb{P}(x) = \frac{P_0}{(c_{500}\, x)^\gamma\, [1 + (c_{500}\, x)^\alpha]^{(\beta-\gamma)/\alpha}}\,, \tag{6.1}$$

where $x = r/r_{500}$ is the scaled dimensionless physical radius, and r_{500} is obtained from Eq. 2.5 for a given value of M_{500}. The physical pressure is given by:

$$P(x) = P_{500} \left(\frac{M_{500}}{3 \times 10^{14}\, h_{70}^{-1}\, M_\odot} \right)^{\alpha_p} \mathbb{P}(x)\,, \tag{6.2}$$

where:

$$P_{500} = 1.65 \times 10^{-3}\, E(z)^{8/3} \left(\frac{M_{500}}{3 \times 10^{14}\, h_{70}^{-1}\, M_\odot} \right)^{2/3} \mathrm{h}_{70}^2\, \mathrm{keV\, cm}^{-3}\,, \tag{6.3}$$

and $\alpha_p = 0.12$ accounts for the deviation from the self-similar scaling model [16].

From Eq. 6.1, it is clear that the slopes of the pressure profile are given, at different r_{500}-scaled distances, by γ for $x \ll 1/c_{500}$, α for $x \sim 1/c_{500}$, and β for $x \gg 1/c_{500}$. In our analysis and following the approach by Planck Collaboration et al. [172], we leave P_0, c_{500}, α, and β as free parameters. The low resolution of the *Planck* data does not have the power to constrain γ, so we fix it to $\gamma = 0.31$, value obtained by Arnaud et al. [16] from a sample of 33 *XMM-Newton* X-ray local clusters in the $r < r_{500}$ range.

Thermal Sunyaev-Zel'dovich effect and Compton parameter

The pressure produced by the free electrons of the intracluster medium, $P = k_B\, n_e\, T_e$, where n_e is the electron density and T_e is the temperature, is related to the Compton parameter y through:

$$y = \frac{\sigma_T}{m_e\, c^2} \int_0^\infty P(l)\, \mathrm{d}l\,, \tag{6.4}$$

equal to the optical depth times the fractional energy gain per scattering along the line-of-sight, with σ_T the Thomson cross section.

The thermal Sunyaev-Zel'dovich (SZ) distortion introduced in the CMB temperature of the *Planck* maps due to the presence of a cluster is given by:

$$\frac{\Delta T_{\mathrm{SZ}}}{T_{\mathrm{CMB}}} = g(\nu)\, y\,, \tag{6.5}$$

where the spectral distortion g is given in Eq. 2.46 in terms of the dimensionless frequency $(h\,\nu)/(k_B\,T_{\mathrm{CMB}})$. Using this formula and after properly cleaning the maps from other undesired contributions, in the following section we convert observed temperature fluctuations into values of y, integrating over the different bandpass filters (Fig. 6.1) to include the dependence of the measured amplitude of the signal with the shape of the spectral distortion g, shown in Fig. 2.5.

Assuming an spherical model for the cluster, we have from Eq. 6.4 that the Compton parameter y at a distance r from the center of the cluster is equal to:

$$y(r) = \frac{\sigma_T}{m_e\, c^2} \int_{-\infty}^{\infty} P\left(\sqrt{r'^2 + r^2}\right)\, \mathrm{d}r'\,, \tag{6.6}$$

and thus the integrated Compton parameter Y, obtained integrating y to a distance R from the center of the cluster, is given by:

$$Y(R) = \int_0^R 2\pi\, y(r)\, r\, \mathrm{d}r = \frac{\sigma_T}{m_e\, c^2} \int_0^R 2\pi\, r\, \mathrm{d}r \int_{-\infty}^{\infty} P\left(\sqrt{r'^2 + r^2}\right)\, \mathrm{d}r'\,, \tag{6.7}$$

which has units of Mpc^2. It should be noted that, as y is a projected along the line-of-sight quantity, Y is the so called "cylindrical" integrated Compton parameter Y^{cyl}, and not the "spherical" integrated Compton parameter, which would be obtained directly from the pressure profile doing:

$$Y^{\mathrm{sph}}(R) = \frac{\sigma_T}{m_e\, c^2} \int_0^R 4\pi\, P(r)\, r^2\, \mathrm{d}r\,. \tag{6.8}$$

In practice, Y^{cyl} is used when dealing with observations, as this is the quantity that can be measured from the data, and Y^{sph} is used when dealing with models. Once a pressure profile has been adopted, any measurement of $Y^{\mathrm{cyl}}(n\, r_{500})$ can be straightforwardly converted in terms of $Y^{\mathrm{cyl}}(r_{500})$, and the latter to $Y^{\mathrm{sph}}(r_{500})$. Finally, as y is dimensionless, Y can also be expressed in units of arcmin^2:

$$Y\,[\mathrm{arcmin}^2] = D_A(z)^{-2} \left(\frac{60 \times 180}{\pi}\right)^2 Y\,[\mathrm{Mpc}^2]\,. \tag{6.9}$$

From now on, we refer to $Y^{\mathrm{sph}}(r_{500})$ as Y_{500}, given in Mpc^2 units.

Gas fraction

To improve our analysis, we use established results regarding the global gas fraction f_{gas} in clusters, particularly, those by Pratt et al. [182], who derived a mass–gas fraction relation using precise hydrostatic mass measurements of 41 *Chandra* and *XMM-Newton* clusters [15, 228, 249], which is also in good agreement with the results obtained from the REXCESS sample [33]. According to their analysis, these clusters, whose masses range from $10^{13}\, M_\odot$ to $10^{15}\, M_\odot$, follow the mean

mass–gas fraction relation:

$$\ln\left(f_{\mathrm{gas},500}\, E(z)^{-3/2}\right) = (-2.37 \pm 0.03) + (0.21 \pm 0.03)\ln\left(\frac{M_{500}}{2 \times 10^{14}\, M_\odot}\right). \tag{6.10}$$

To compute the gas fraction we first need to compute the gas mass:

$$M_{\mathrm{gas},500} = \int_0^{r_{500}} \mu_e\, m_u\, n_e(r)\, 4\pi\, r^2\, \mathrm{d}r\,, \tag{6.11}$$

where $\mu_e = 1.15$ is the mean molecular weight per free electron, m_u is the atomic mass unit, and $n_e(r)$ is the electron density. Because the intra-cluster pressure is given by $P(r) = n_e(r)\, k_B\, T$, assuming an isothermal model for the cluster one can directly derive $M_{\mathrm{gas},500}$ from the adopted pressure profile (Eq. 6.2).

For the temperature, we use the mean mass–temperature relation given by Lieu et al. [128]:

$$\log_{10}\left(\frac{M_{500}\, E(z)}{h_{70}^{-1}\, M_\odot}\right) = \left(13.57^{+0.09}_{-0.09}\right) + \left(1.67^{+0.14}_{-0.10}\right)\log_{10}\left(\frac{T}{\mathrm{keV}}\right), \tag{6.12}$$

which was obtained combining weak lensing mass estimates with *Chandra* and *XMM-Newton* temperature data of 38 clusters from the XXL survey [164], 10 clusters from the COSMOS survey [108], and 48 from the Canadian Cluster Comparison Project (CCCP, [94, 131]), spanning a temperature range $T \simeq 1 - 10$ keV.

It is worth mentioning that if an isothermal model is assumed and we consider that $M_{\mathrm{gas}} \propto f_b\, M$, where M is the total cluster mass and f_b is the baryon gas fraction, from Eq. 2.49 we have that the integrated Compton parameter scales as $Y \propto f_b\, M\, T\, D_A^{-2}$. However, even clusters in hydrostatic equilibrium are not strictly isothermal, and temperatures are commonly observed to drop by a factor of 2 below a radius of $r \lesssim 100 - 200$ kpc because of strong radiative cooling, described best by a broken power law with a transition region [249]. In any case, these scales are not resolved by *Planck* and in our analysis the assumption that the temperature is constant is a good approximation for the radial scales considered in this work.

Miscentering

In the redMaPPer catalogue, for each cluster the 5 most probable central galaxies (CGs) are provided with their corresponding centering probabilities. Usually, there is one CG with a much higher probability of being the real CG than the other 4, so we consider the most probable CG to be the center of the cluster. In any case, it is now known that, because clusters are still evolving systems, CGs do not always reside at the deepest part of the DM halo potential well [252], but sometimes have high peculiar velocities, are displaced with respect to the peak of the X-ray emission [191], or are wrongly identified satellite galaxies [218].

In stacked measurements on clusters miscentering is one of the main sources of noise, and should be taken into account. When modelling the SZ signal coming from stacked samples of clusters, we introduce this effect in a similar way as we did in Chapter 5, i.e., considering the results obtained by Johnston et al. [101], who found a CG-center offset distribution that could be fitted by a Gaussian with a standard deviation of $\sigma = 0.42\, h^{-1}\, \mathrm{Mpc}$ for the CGs that were not accurately centered, something that occurs between 20% and 40% of the time as a function of

cluster richness, with a probability $p_{mc}(\lambda) = (2.13 + 0.046\,\lambda)^{-1}$.

However, it should be noted that this value of $0.42\,h^{-1}\,\mathrm{Mpc}$ is about $2\,\mathrm{arcmin}$ at $z \sim 0.2$, scale well below the resolution of the *Planck* data we work with, so we do not expect this miscentering to introduce a high level of noise in our stacked measurements of the SZ effect.

Mass bias

Usually referred to as hydrostatic equilibrium (HE) masses, in their derivation there is an implicit assumption that the pressure is purely thermal. However, we may expect a non-negligible contribution to the total pressure from bulk and turbulent gas motions related to structure formation history, magnetic fields, and AGN feedback [177, 216]. Such non-thermal contributions to the total pressure would therefore cause masses estimated using X-ray or SZ observations to be biased low with uncertain estimates ranging between 5% to 20% [149, 153, 185, 209].

We simply relate the HE mass estimates $M_{\mathrm{HE},500}$ obtained from our SZ observations to true masses M_{500} through a simple mass independent bias:

$$M_{\mathrm{HE},500} = (1 - b)\,M_{500}\,, \qquad (6.13)$$

where $(1 - b)$ is the so called mass bias factor. This term can include not only the bias coming from departures from HE, but from observational systematics or sample selection effects. We note that this bias is different from the "halo bias" described in Chapter 1, related to the distribution and clustering of astrophysical objects.

Mass–richness relation

In order to relate mass and optical richness λ in clusters, following the prescription given in Sec. 2.4 we assume a standard power law cluster mass–richness mean relation:

$$\langle M_{500}|\lambda \rangle = M_0 \left(\frac{\lambda}{\lambda_0}\right)^{\alpha_{M|\lambda}}\,, \qquad (6.14)$$

where M_0, given in terms of M_{500}, is a reference mass at a given value of $\lambda = \lambda_0$, and $\alpha_{M|\lambda}$ is the slope of the mass–richness relation. As we did in the previous chapter, we consider $\lambda_0 = 60$, and assume a log-normal fractional scatter $\sigma_{M|\lambda}$:

$$\Delta \ln \left(\frac{M_{500}}{10^{14}\,M_\odot}\right) = \sigma_{M|\lambda}\,. \qquad (6.15)$$

We choose this parametrisation over a logarithmic one, like that used in Chapter 5 (Eq. 5.2), because in this form the resulting mean relation is less affected by the uncertainty in $\sigma_{\ln M|\lambda^{\mathrm{obs}}}$.

Since it was made public, there have been multiple attempts (including our own, described in Chapter 5) to constrain in different ways the parameters of this relation using the redMaPPer cluster catalogue [24, 77, 100, 127, 139, 142, 204, 205, 217]. Although some of these works introduced a redshift dependence in the mass–richness relation, it was weakly constrained in all cases, and compatible with no redshift evolution at all. Given the small redshift range in which we work, redshift evolution is not important for our analysis and we refer our result to the mean redshift of our sample, $z = 0.245$.

6.3 Pressure profiles and mass estimation

6.3.1 Planck data processing

We first divide the redMaPPer cluster catalogue in 6 independent log-spaced richness bins, and take all those clusters that reside within the $0.100 < z < 0.325$ volume-complete redshift region. This leaves a total of 8,030 clusters, distributed in number and mean richness as shown in Table 6.2.

Then, for each cluster subsample, we produce and stack the $\nu = 100$, 143, 217 and 353 GHz 2.5 deg × 2.5 deg *Planck* maps associated to the clusters in each subsample and produce the corresponding SZ maps following a technique similar to the one used in Planck Collaboration et al. [180], based on internal linear combinations (ILC) of the four different HFI maps. In our case we do not use the 70 GHz SZ map, as we prefer to smooth all the maps to a common higher 10 arcmin resolution instead. An example of the original ΔT *Planck* stacked maps that we work with can be seen in Fig. 2.6 of Chapter 2.

Following Planck Collaboration et al. [180], we first use the $M_{353} - M_{143}$ combination to produce a "clean" M_{217} map, such that:

$$M_{217}^c = M_{217} - A\left(M_{353} - M_{143}\right) , \tag{6.16}$$

where M_ν is the *Planck* map at frequency ν, and the value of $A = 0.142$ is found to produce a $217\,\mathrm{GHz}$ map with minimal residual Galactic foreground. This M_{217}^c map contains the signal coming from the pure CMB, and from the kinetic and thermal SZ. Although thermal SZ effect is supposed to cancel at $217\,\mathrm{GHz}$, the width of the bandpass introduces a non-negible contribution coming from it. Thus, the thermal SZ signal maps at $\nu = 100\,\mathrm{GHz}$ and $\nu = 143\,\mathrm{GHz}$ that we consider to construct the final y maps, are produced from the combination:

$$\mathrm{SZ}_\nu = M_\nu - M_{217}^c - C_\nu\,M_{\mathrm{dust}} , \tag{6.17}$$

where C_ν is the value that minimises the residuals in the region not containing SZ signal, i.e., where there are no clusters, and M_{dust} is the model dust map, obtained from the map combination:

$$M_{\mathrm{dust}} = M_{353} - M_{217} . \tag{6.18}$$

In our case, we find $C_{100} = 0.015$ and $C_{143} = 0.043$.

To convert from ΔT_{SZ} to y units (Eq. 6.5), we compute the different effective spectral responses $f(\nu)$ integrating the expected SZ spectrum (Eq. 2.46) over each *Planck* bandpass, shown in Fig. 6.1. However, because the $M_{353} - M_{143}$ combination used to obtain M_{217}^c contains a certain amount of SZ signal, we need to correct for this defining an effective response $\tilde{f}(\nu)$, such that:

$$\tilde{f}(\nu) = f(\nu) - f(217)^c - C_\nu\left[f(353) - f(217)\right] , \tag{6.19}$$

where the "clean" response $f(217)^c$, that accounts for the SZ residuals found in the "clean" $217\,\mathrm{GHz}$ map, is defined as:

$$f(217)^c = f(217) - A\left[f(353) - f(143)\right] , \tag{6.20}$$
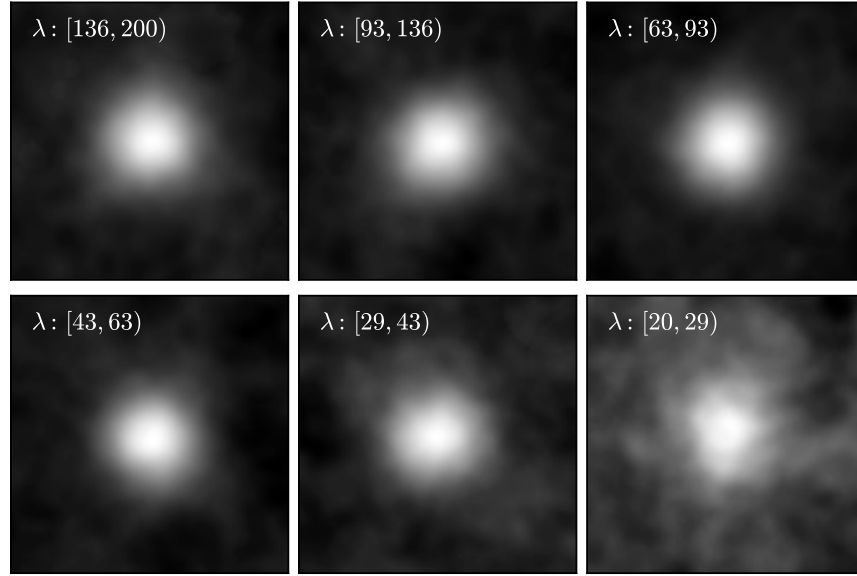
following the combination used in Eq. 6.16.

Figure 6.2: *0.75 deg $\times$ 0.75 deg stacked Compton parameter y maps in 6 richness bins (with the richness ranges indicated on each stamp), obtained through the process described in Sec. 6.3.1. These subsamples are defined in the volume-complete redshift region $0.100 < z < 0.325$. The maps have been smoothed to a common 10 arcmin resolution.*

Our final SZ maps of the cluster subsamples considered, given in terms of the Compton parameter y and shown in Fig. 6.2, are produced as a combination of the SZ_{100} and SZ_{143} maps, weighting them by the inverse of the variance of each map. This particular combination has been proposed by the *Planck* team to maximise the signal-to-noise of the SZ component whilst minimising the contamination from Galactic emission and extragalactic infrared emission within clusters [180]. From Fig. 6.2 it can be seen that the SZ effect is strongly detected in these cluster stacks over the full richness range.

6.3.2 Likelihood analysis

We now combine the data from *Planck* and the constraints imposed by the gas fractions to perform a likelihood analysis that enables us to constrain the pressure profile parameters and the mean masses of the 6 cluster subsamples. We explore the values of our 4+6 dimensional model $\vec{\phi} = (P_0, c_{500}, \alpha, \beta, M_{500,1}, ..., M_{500,6})$ through a Monte Carlo Markov Chain (MCMC) analysis.

For a given value of $r_{500}(M_{500}, z)$ we measure the Compton parameter y within a disk of radius $x = 0.35$ and in 6 annulus given by radii x_i and x_{i+1}, where the $x_i = r_i/r_{500}$ values are log-spaced between 0.35 and 3.5. This results in a y vector of 7 values. Then, to account for the background we subtract the mean value of the signal obtained from an annulus of radii x_{out} and $x_{\mathrm{out}} + x_{\mathrm{FWHM}}$, where $x_{\mathrm{out}} = 3.5$, and $x_{\mathrm{FWHM}} = \theta_{\mathrm{FWHM}} D_A(z)/r_{500}$ corresponds in x-space to the $\theta_{\mathrm{FWHM}} = 10$ arcmin FWHM effective resolution of the SZ maps. The values of r_{500} used to both model the signal and measure it from the data are obtained from M_{500} through Eq. 2.5.

The log-likelihood employed has the form:

$$\ln \mathcal{L}(\vec{\phi}) = \sum_{k=1}^{6} \ln \mathcal{L}_k(\vec{y}_k | \vec{\phi}_k) , \qquad (6.21)$$

where $\vec{\phi}_k = (P_0, c_{500}, \alpha, \beta, M_{500,k})$, $\vec{y}_k$ is the data vector obtained from the cluster subsample k, and

$$\ln \mathcal{L}_k(\vec{y}_k | \vec{\phi}_k) \propto -\frac{1}{2} \chi^2(\vec{y}_k, \vec{\phi}_k, C) , \qquad (6.22)$$

where C is the covariance matrix, and

$$\chi^2(\vec{y}_k, \vec{\phi}_k, C) = \left(\vec{y}_k - \vec{\mu}(\vec{\phi}_k) \right) C^{-1} \left(\vec{y}_k - \vec{\mu}(\vec{\phi}_k) \right)^T , \qquad (6.23)$$

with $\vec{\mu}$ the model values drawn from $\vec{\phi}_k$. To model the signal, for each $\vec{\phi}_k$ configuration we produce mock maps of the Compton parameter y as a function of redshift. Then, we mimic miscentering effects adding to the mock maps the same maps smoothed with a Gaussian of width $\sigma_{mc} = 0.42\,h^{-1}\,\mathrm{Mpc}$, and weighted by $p_{mc}(\lambda) = (2.13 + 0.046\,\lambda)^{-1}$. Finally, we produce a weighted map integrating over the redshift distribution of the subsample considered, convolve it with a $10\,\mathrm{arcmin}$ FWHM Gaussian, and perform the same measurements made in the *Planck* data maps.

It should be noted that the mock y maps that we create to fit the observed signal are generated from the pressure profile as given by Eq. 6.2 and for a given total model mass M_{500}^k. Hence, to compute $\ln \mathcal{L}^k(y^k | \phi^k)$ we do not rely on the gas mass or f_{gas}.

The covariance matrixes C are estimated from $N_R = 1{,}000$ patches randomly chosen within the redMaPPer footprint, where the same measurement described above is done. As this measurement depends on the M_{500} value proposed, the 7×7 covariance matrix is recomputed each time as:

$$C_{ij}(M_{500}) = \frac{1}{N_R - 1} \sum_{n=1}^{N_R} (y_i^n - \langle y_i \rangle)(y_j^n - \langle y_j \rangle) . \qquad (6.24)$$

As an example, the covariance matrix obtained considering a mass of $M_{500} = 5 \times 10^{14} M_\odot$ is shown in Fig. 6.3, where the 30% base level correlation is coming from the fact that in each map the same region is used to subtract the background from all the radial bins.

Finally, we consider the gas fraction constraints introducing a Gaussian prior $\sim \mathcal{N}(f_{\mathrm{gas}}, \sigma_{f_{\mathrm{gas}}})$, where f_{gas} is estimated from the results of Pratt et al. [182], as explained before. In each MCMC step we compute, following the procedure described in Sec. 6.2, the 6 gas fractions associated to a given set $\vec{\phi}$ of pressure profile parameters and masses, and then use Eq. 6.10 to model the expected gas fraction f_{gas} for each value of $M_{500,k}$, which we use for the prior. To estimate $\sigma_{f_{\mathrm{gas}}}$, we add in quadrature the errors derived from the uncertainties on both the mass–gas fraction (Eq. 6.10) and the mass–temperature (Eq. 6.12) relations, which are obtained propagating through a Monte Carlo (MC) method. Because we have decided to be as conservative as possible on the relations employed and the resulting uncertainties in this analysis are large, we notice that the contribution that this prior has in the final estimated values of the pressure profile is small, only limiting those models where the gas fraction $f_{\mathrm{gas},500}$ takes values below 0.05 or above 0.20 for masses in the $\sim 10^{14} - 10^{15}\,M_\odot$ range.

For all P_0, c_{500}, α, β, M_{500}^1, ..., M_{500}^6, we consider flat uninformative priors $\sim \mathcal{U}(\infty, -\infty)$,
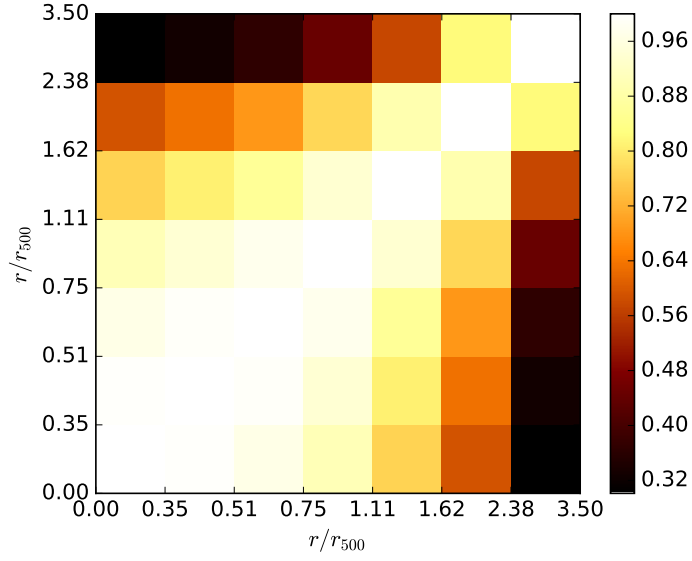
Figure 6.3: *Normalized covariance matrix used in the likelihood analysis for a mass of $M_{500} = 5 \times 10^{14} M_\odot$, corresponding to $r_{500} = 1.11\,\mathrm{Mpc}$. At the mean redshift of the sample and for the same mass, $r/r_{500} = 3.5$ corresponds to 13.5 arcmin.*

Table 6.1: *The recovered values of the GNFW universal pressure profile parameters, together with the best fit values.*

Parameter	Mean value	Best fit
P_0	6.48 ± 3.00	5.42
c_{500}	1.65 ± 0.95	1.12
α	0.87 ± 0.25	0.81
β	3.19 ± 0.66	3.47

allowing for a wide range of different model-masses configurations.

6.3.3 Results

The derived posterior probabilities of the GNFW universal pressure profile parameters P_0, c_{500}, α and β are displayed in Fig. 6.4. To compute the center (mean) and the scale (dispersion) of the marginalised posterior distributions, we use the robust estimators described in Beers et al. [26]. The values obtained with this method, together with the best fit values, are listed in Table 6.1.

The y radial profiles recovered for the cluster subsamples considered are displayed in Fig. 6.5, together with the joint best fit y profile model obtained, as shown in Table 6.1. It should be noted that the observed y radial profiles, as we are not deconvolving them in our analysis, are not necessarily self-similar due to the different relative size of the *Planck* beam with respect to r_{500} for the 6 cluster subsamples.

Finally, the mean masses recovered for the cluster subsamples are listed in Table 6.2.
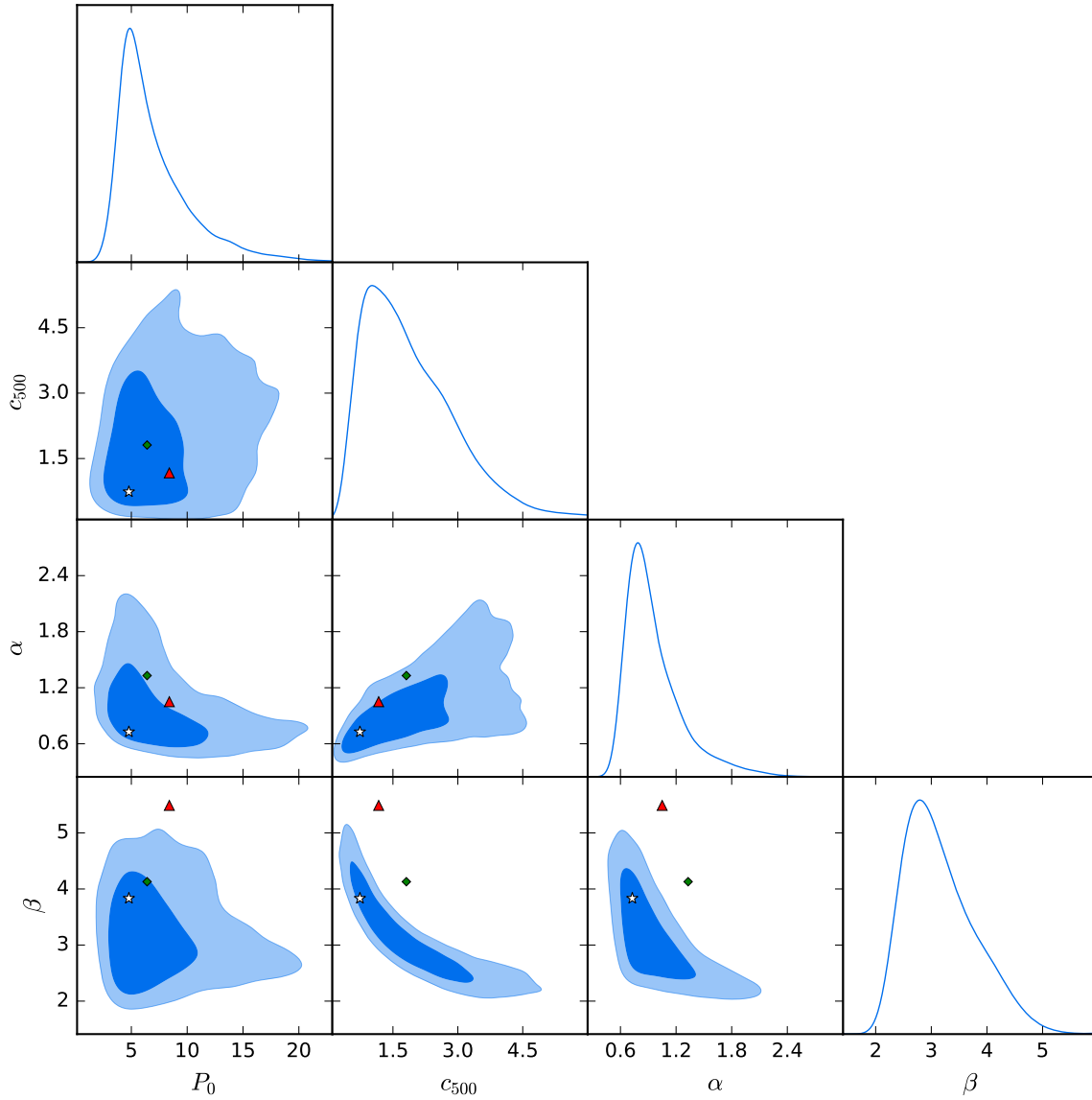
Figure 6.4: *Marginalised posterior distributions of the universal pressure profile parameters P_0, c_{500}, α and β, as obtained in our MCMC analysis. Contours represent 68% and 95% confidence levels. The best fit values, corresponding to $[P_0, c_{500}, \gamma, \alpha, \beta] = [5.42, 1.12, 0.31, 0.81, 3.47]$, are marked with a white star. The best fit obtained by Arnaud et al. [16], [8.40 $h_{70}^{-3/2}$, 1.18, 0.31, 1.05, 5.49], is marked with a red triangle, and Planck Collaboration et al. [172] best fit, [6.41, 1.81, 0.31, 1.33, 4.13], with a green diamond.*

Figure 6.5: *The values of y recovered at different scaled radii for the cluster subsets divided by richness, and ordered as in Fig. 6.2. The error bars are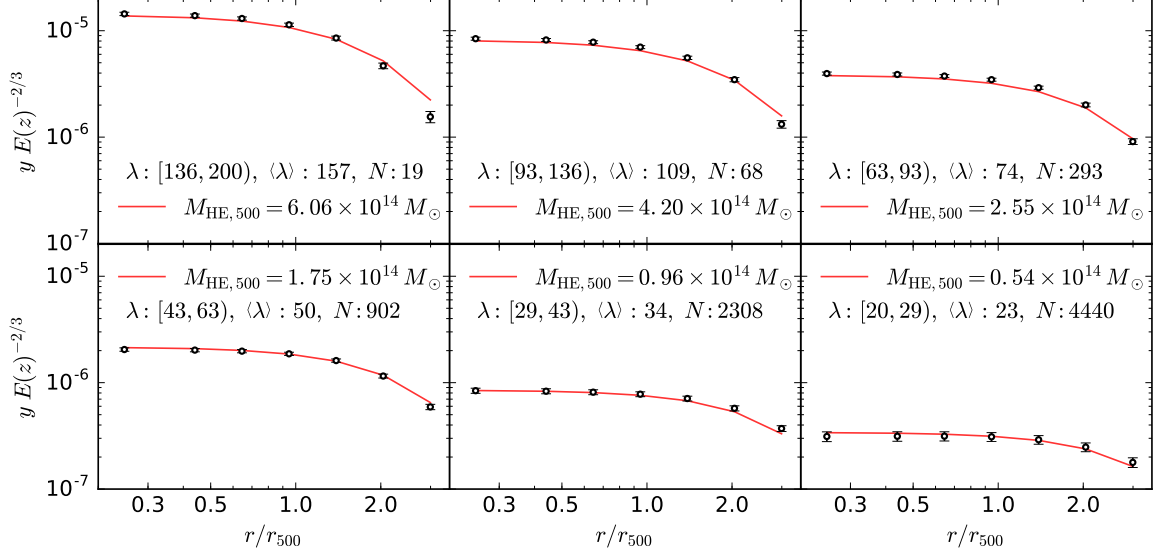 the square root of the diagonal elements of the covariance matrix. The red lines represent the prediction from the universal pressure profile with the best fit parameters, $[P_0, c_{500}, \gamma, \alpha, \beta] = [5.42, 1.12, 0.31, 0.81, 3.47]$. The best fit masses used for the model are also shown for each sample, together with the richness range, the mean richness, and the number of clusters contained in them.*

Table 6.2: *Richness range, number of clusters, mean richness and mean masses recovered from the SZ signal of the cluster subsamples studied.*

Richness range	N	$\langle \lambda \rangle$	$\langle M_{\mathrm{HE,500}} \rangle$ [$10^{14} M_\odot$]
[136, 200)	19	157.6	6.48 ± 0.66
[93, 136)	68	109.6	4.52 ± 0.42
[63, 93)	293	74.3	2.77 ± 0.25
[43, 63)	902	50.8	1.84 ± 0.18
[29, 43)	2308	34.6	1.04 ± 0.13
[20, 29)	4440	23.8	0.54 ± 0.12

Comparison with previous results

Regarding the pressure profile parameters, Arnaud et al. [16] obtained the best fit values $[P_0, c_{500}, \gamma, \alpha, \beta] = [8.403h_{70}^{-3/2}, 1.177, 0.3081, 1.0510, 5.4905]$, relying on numerical simulations for larger radii and using the *XMM-Newton* X-ray data up to $r/r_{500} \lesssim 1$ of a sample of 33 X-ray selected local ($z < 0.2$) clusters covering the $10^{14} M_\odot < M_{500} < 10^{15} M_\odot$ mass range.

More recently, deconvolving the stacked pressure profile of 62 SZ selected clusters, the Planck Collaboration et al. [172] obtained, combining *Planck* with *XMM-Newton* data, the best fit values $[6.41, 1.81, 0.31, 1.33, 4.13]$, where the Arnaud et al. [16] value of $\gamma = 0.31$ had been previously fixed, as we have done in our analysis. By comparison with pure estimates, it can be seen in Fig. 5 of Planck Collaboration et al. [172], that a large uncertainty is present in the estimation of these parameters, with a high degeneracy between them, which we attribute to the larger radial extent of our SZ profiles and the wider cluster mass coverage of our sample.

We also notice that the external slope, β, derived in this work points to shallower profiles in the outer part of the clusters. This is in agreement with the results derived in the Coma and Virgo clusters [173, 180] based on *Planck* data where the SZ signal extends to beyond the virial radius in those clusters. Like in those papers, we can reach similar distances from the virial radii and be sensitive to the external slope of clusters where the signal from neighbouring merging filaments is expected to flatten the SZ profile.

6.4 Mass bias and mass–richness relation

6.4.1 Likelihood analysis

We now obtain the value of the mass bias comparing our results with recent weak lensing mass derivations that make use of stacked subsamples of the redMaPPer cluster catalogue. We consider the results by Simet et al. ([217], S16 from now on), who, making use of SDSS data for the weak lensing mass estimates of the redMaPPer clusters in the $0.10 < z < 0.33$ redshift region, obtained one of the most precise mass–richness relations to date, and those by Melchior et al. ([139], M16 hereafter), which, using DES SV data to make stacked measurements of the weak lensing shear as a function of mean cluster richness and mean cluster redshift, measured a redshift-dependent mass–richness relation of comparable precision to that of S16. Because both of them are given in terms of M_{200m}, we consider a NFW profile [151] and the mass–concentration relation of Bhattacharya et al. [29] to convert between different mass definitions, as we have done throughout this work.

At the same time, we derive the optimal mass–richness relation able to describe our data, considering the probability distribution of the bias obtained from the comparison with S16 and M16 results. To do so, we first compare our masses with the masses estimated by S16 and M16 with a joint likelihood:

$$\ln \mathcal{L}_{\text{bias}} = \ln \mathcal{L}_{\text{S16}} + \ln \mathcal{L}_{\text{M16}}, \tag{6.25}$$

where $\mathcal{L}_{\text{S16}}$ and $\mathcal{L}_{\text{M16}}$ are computed comparing our 6 masses with the masses predicted by the S16 and the M16 mass–richness relations at the 6 cluster subsample mean richnesses, with

$\ln \mathcal{L} \propto -\chi^2/2$, and:

$$\chi^2\left[(1-b)\right] = \left(\vec{M}_{500} - \vec{M}_{500}^{\text{model}}\right) C^{-1} \left(\vec{M}_{500} - \vec{M}_{500}^{\text{model}}\right)^T , \qquad (6.26)$$

where the bias-corrected masses are computed as $M_{500} = M_{\text{HE},500}/(1-b)$, following Eq. 6.13, and the S16 and M16 M_{500}^{model} model masses are obtained evaluating the corresponding S16 or M16 mass–richness relation at the 6 cluster subsamples mean richnesses.

To obtain the resulting bias-dependent mass–richness relation, we compare these bias-corrected masses with the masses predicted by the generic mass–richness relation given by Eq. 6.14, which we compute following the steps described in Sec. 2.4 and considering a given set of free parameters $\log_{10} M_0$, $\alpha_{M|\lambda}$ and $\sigma_{M|\lambda}$, which we constrain. The global likelihood has the form:

$$\ln \mathcal{L} = \ln \mathcal{L}_{\text{bias}} + \ln \mathcal{L}_{M|\lambda} , \qquad (6.27)$$

where $\mathcal{L}_{M|\lambda}$ is computed now through another chi-square function similar to that of Eq. 6.26, but considering both the value of the bias and the values of the mass–richness relation parameters for the model masses.

Because the values of the SZ-estimated masses are correlated, this new covariance matrix C is obtained directly from the MCMC analysis performed in Sec. 6.3, and used in this new MCMC likelihood calculation. We also include the errors coming from the S16 and M16 model uncertainties, adding them in quadrature to the diagonal of the covariance matrix.

For $\log_{10} M_0$, $\alpha_{M|\lambda}$ and $(1-b)$ we assume flat uninformative priors, meanwhile for $\sigma_{M|\lambda}$ we assume the inverse gamma distribution prior $\sim IG(\epsilon, \epsilon)$, with $\epsilon = 10^{-3}$ [10].

6.4.2 Results

We notice that this analysis, based on mean masses rather than individual measurements, is not able to constrain the value of $\sigma_{M|\lambda}$. As we saw in Chapter 5, the value of the scatter, difficult to constrain in general, is usually found to be between 0.15 and 0.30. Saro et al. [204] find $\sigma_{\ln M|\lambda^{\text{obs}}} = 0.18^{+0.08}_{-0.05}$, meanwhile Rozo and Rykoff [191] and Rozo et al. [197], comparing individual redMaPPer clusters with X-ray and SZ mass estimates, find a value $\sigma_{\ln M|\lambda^{\text{obs}}} \approx 0.25 \pm 0.05$.

In any case, the posterior probability of $\log_{10} M_0$, $\alpha_{M|\lambda}$ and $(1-b)$ recovered from the MCMC is shown in Fig. 6.6. As in the previous section, we use the Beers et al. [26] estimator to obtain the values from the marginalised posterior distributions. The results are shown in Table 6.3.

Comparison with previous results

We now compare the value of the bias that we recover with those found in the literature. We also compare the associated bias-dependent mass–richness relation with those mass–richness relations used to obtain it, and with the one obtained recently by Baxter et al. [24]. We recall that our estimations of both the bias and the mass–richness relation depend on the results of S16 and M16, and should not be considered independent of them.

Comparing "observed" with "true" masses coming from several numerical simulations, Planck Collaboration et al. [177] derived a mass-dependent bias with a mean value of $(1-b) = 0.8^{+0.2}_{-0.1}$. However, a bias of the order of 40% was needed in order to reconcile *Planck* clusters counts with
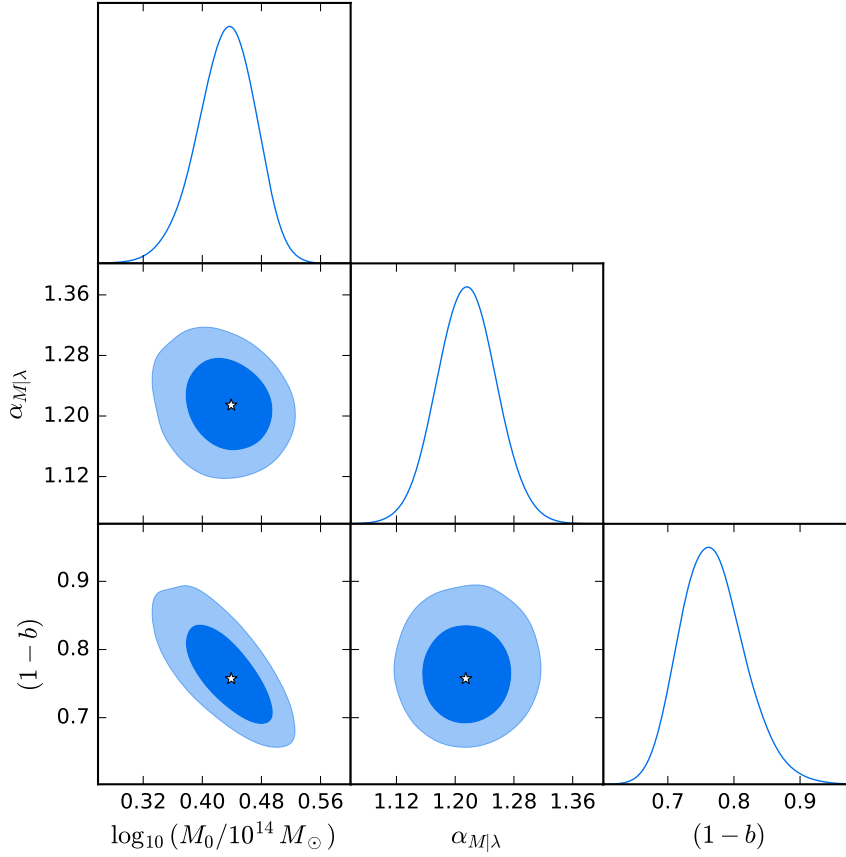
Figure 6.6: *Posterior probability distributions of the mass–richness parameters $\log_{10} M_0$ and $\alpha_{M|\lambda}$, and of the bias factor $(1-b)$. The best fit location is marked with a white star. The mass–richness relation scatter, $\sigma_{M|\lambda}$, cannot be constrained by our data and its posterior probability distribution is greatly influenced by the posterior, and thus not shown.*

Table 6.3: *The confidence values of the mass–richness relation parameters and of the bias factor $(1-b)$, together with the best fit. $\alpha_{M|\lambda}$ is the slope of the mass–richness relation, and $\log_{10} M_0$ is the pivot mass, evaluated at $\lambda_0 = 60$ and given in terms of M_{500c}. The stacking analysis performed is not able to constrain the value of $\sigma_{M|\lambda}$, which is largely determined by the prior, and thus not shown.*

Parameter	Mean value	Best fit
$\log_{10} (M_0/M_\odot)$	14.435 ± 0.040	14.446
$\alpha_{M|\lambda}$	1.22 ± 0.04	1.21
$(1-b)$	0.76 ± 0.05	0.75
$\sigma_{M|\lambda}$	-	-

CMB observations, and its value is still the focus of intense research. von der Linden et al. [254], comparing *Planck* cluster mass estimates with weak lensing masses from the Weighing the Giants (WtG) project, observed a higher bias of $(1 - b) = 0.70 \pm 0.06$. In a similar way but using 50 clusters from the Canadian Cluster Comparison Project (CCCP), Hoekstra et al. [94] found a value of $(1 - b) = 0.76 \pm 0.05 \pm 0.06$. On the other hand, Smith et al. [220] obtained a smaller mass bias of the order of the 5% from a sample of 50 clusters with X-ray and weak lensing masses in the $0.15 < z < 0.3$ redshift range, being statistical uncertainties more relevant than any bias, and claimed that the high values of the bias inferred by the WtG and CCCP samples may be dominated by clusters at $z > 0.3$. Although Sereno and Ettori [211] found a value of the bias of the order of 25% for *Planck* masses with respect to their weak lensing masses, it was claimed that this value was strongly dependent on redshift, following Smith et al. [220] results. Saro et al. [205], following an approach similar to ours but using stacked measurements of the SZ signal of 719 DES redMaPPer clusters with South Pole Telescope (SPT) data, needed a bias as high as $(1 - b) = 0.52 \pm 0.05$ to follow the model predictions when the Arnaud et al. [16] pressure profile was assumed. However, this bias was reduced to the range $(1 - b) = 0.7 - 0.9$ when only the clusters with richness $\lambda > 80$ were taken into account, or when other scaling relations were considered. More recently, and using a sample of 35 *Planck* clusters that were within the area covered by the CFHTLenS and RCSLenS photometric surveys, Sereno et al. [214] found that the *Planck* estimated masses were biased low by $\sim 27 \pm 11\%$ with respect to weak lensing masses, consistent with our findings here.

Regarding the mass–richness relation, in M16 a redshift-dependent mass–richness relation was derived with a slope of $1.12 \pm 0.20 \pm 0.06$ for a pivot mass $\log_{10}(M_{200m}/M_{\odot}) = 14.371 \pm 0.040 \pm 0.022$ at a pivot richness $\lambda = 30$ and $z = 0.5$. Evaluated at our mean redshift $z = 0.245$ and their pivot richness $\lambda = 30$, their mass–richness relation gives a mass $\log_{10}(M_{200m}/M_{\odot}) = 14.364 \pm 0.080$. Converting our masses to M_{200m}, we find at $\lambda = 30$ a value of $\log_{10}(M_{200m}/M_{\odot}) = 14.327 \pm 0.044$. In the S16 case, they obtained a mass–richness relation with a slope equal to $1.33^{+0.09}_{-0.10}$ for a pivot mass of $\log_{10}(M_{200m}/h^{-1}M_{\odot}) = 14.344 \pm 0.021 \pm 0.023$ at $\lambda = 40$. Converting to their units, we find that our mass–richness relation at their pivot richness yields a mass equal to $\log_{10}(M_{200m}/h^{-1}M_{\odot}) = 14.329 \pm 0.043$. Baxter et al. [24], using the angular clustering of redMaPPer clusters confined in two redshift bins in the $0.18 < z < 0.33$ redshift region, found a value of the slope of the mass–richness relation of 1.18 ± 0.16 and a pivot mass of $\ln(M_{200m}/M_{\odot}) = 33.66 \pm 0.18$ at $\lambda = 35$ and $z = 0.25$. In our mass–richness relation at their pivot richness, we find $\ln(M_{200m}/M_{\odot}) = 33.183 \pm 0.099$.

Our derived mass–richness relation, together with the bias-corrected masses used in this analysis and the redMaPPer-based mass–richness relations found in the literature and just mentioned, are shown in Fig. 6.7. Our estimated mass-richness relation can be seen to bracket the work of Simet et al. [217] and Melchior et al. [139], in good agreement. Whereas the Baxter et al. [24] agrees in terms of the slope of the relation, it lies significantly above the other work, including our own.

6.5 Y_{500}–M_{500} relation

We now straightforwardly derive the Y_{500}–M_{500} relation by considering the values of P_0, c_{500}, α, β and $(1 - b)$ obtained, and assuming again a value of $\gamma = 0.31$. Following the usual notation we
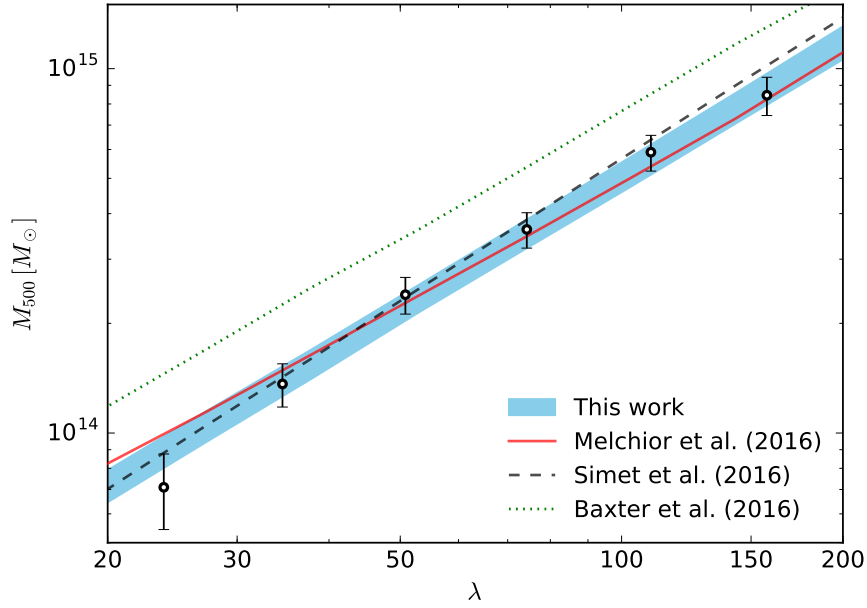
Figure 6.7: *The blue shaded region represents our 1σ confidence interval of the mean mass–richness relation with the parametrisation shown in Table 6.3, derived from the mean bias-corrected masses (black circles) of the cluster subsamples considered. The errors on the M_{500} masses include the uncertainty on the value of the bias. The Melchior et al. ([139], M16, red solid line), Simet et al. ([217], S16, black dashed line), and Baxter et al. [24] mass–richness relations (green dotted line) are also shown.*

have:

$$E^{-2/3}(z)\left[\frac{Y_{500}}{10^{-4}\,\mathrm{Mpc^2}}\right] = 10^A \left[\frac{(1-b)\,M_{500}}{6\times 10^{14} M_\odot}\right]^B, \qquad (6.28)$$

in which the redshift evolution is considered to be self-similar [103]. From the results previously obtained, we find:

$$A = -0.22 \pm 0.04\,,$$
$$B = 1.72 \pm 0.07\,.$$

The value of the slope is actually in good agreement with the expectation from self-similarity, $B \sim 5/3$. This value of the slope is within 1σ from the results of $B = 1.79 \pm 0.08$ obtained in Planck Collaboration et al. [177], with a normalisation factor of $A = 0.19 \pm 0.02$, different from our value of A but compensated by the difference in the $(1-b)$ factor. Our result is also compatible with those of Sereno et al. [212], who obtained values for the slope of 1.4 - 1.9, albeit a relatively wide range of slope, by considering samples of clusters with weak lensing mass estimates.

It should be noted that this is the mean Y_{500}–M_{500} relation, so, although small in the SZ case, a scatter $\sigma_{Y|M}$ should be considered when applying it to individual clusters, just as when converting observed richness into mass (see Sec. 2.4). In Planck Collaboration et al. [177] a value of of the scatter of $\sim 15\%$ is considered, meanwhile in Sereno et al. [212] a scatter of the the 15 - 30% order is estimated.

Finally, as a consistency check on our results, we measure $Y^{\mathrm{cyl}}(3.5\,r_{500})$ in the 6 y maps corresponding to the 6 cluster subsamples, deriving the values of r_{500} from the mean masses obtained in the MCMC analysis, listed in Table 6.2, and converting to Y_{500} using the universal
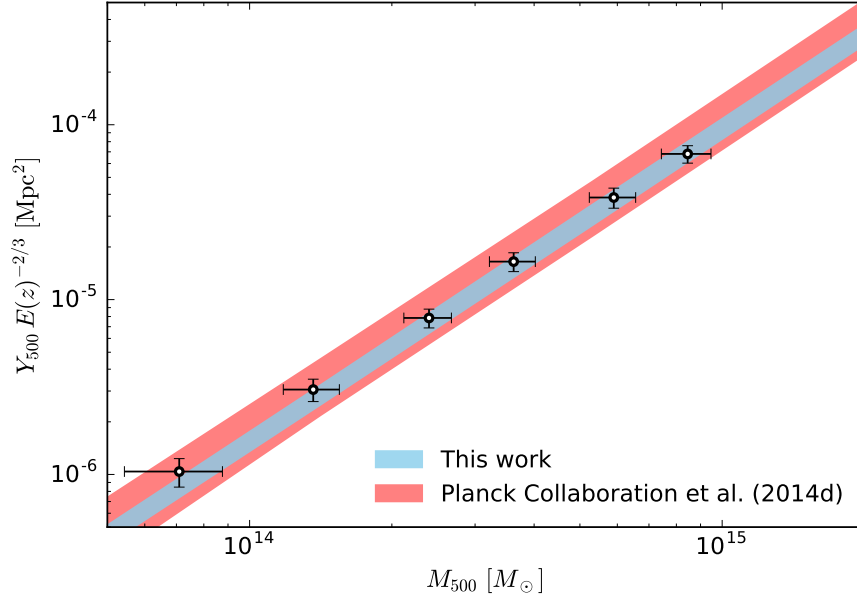
Figure 6.8: *The blue shaded region shows our 1σ confidence interval of the scaling relation between Y_{500} and M_{500}, as given by the posterior probability distribution of the pressure profile parameters P_0, c_{500}, α and β, the masses, and the bias factor. The black circles are the observed $Y^{\mathrm{cyl}}(3.5\,r_{500})$ values for the cluster subsamples, converted to Y_{500} using the pressure profile parameters of Table 6.1 and the masses of Table 6.2. The errors on the M_{500} masses include the uncertainty coming from the bias. As the red shaded region, we plot the Planck Collaboration et al. [177] Y_{500}–M_{500} relation for comparison.*

pressure profile as given by the P_0, c_{500}, α and β parametrisation of Table 6.1. We derive the errors from 1,000 random patches within the redMaPPer footprint in a similar way as we did in Sec. 6.3.2. We propagate the errors coming from the uncertainty in the pressure profile parameters, the masses and the bias factor drawing a large enough number of samples from the posterior probability distribution of the $4+6+1$ dimensional parameter space, repeating the measurements, and adding in quadrature the variance of the $Y^{\mathrm{cyl}}(3.5\,r_{500})$ values obtained.

Our mean Y_{500}–M_{500} relation and the measured values of Y_{500} are shown in Fig. 6.8, where we also plot the relation considered in Planck Collaboration et al. [177], with which good agreement is found. In comparison our work follows a tighter relation, which is attributed to the relatively large size of our cluster sample.

6.6 Discussion and conclusions

In this chapter we have presented and employed a new method to constrain simultaneously the GNFW universal pressure profile parameters and the masses of 6 different richness subsamples of clusters using stacked measurements of the SZ effect. We then estimated both a mass–richness and a Y_{500}–M_{500} relation using weak lensing mass estimates found in the literature.

Using the positions in the sky of $\sim 8,000$ redMaPPer clusters in the $0.100 < z < 0.325$ volume-complete redshift region, we have produced and stacked the *Planck* full mission SZ maps of 6 richness subsamples of clusters, and constrained the common GNFW universal pressure profile

parameters and the mean masses of each subsample through a MCMC analysis, obtaining better constraints than previous works, with $P_0 = 6.48 \pm 3.00$, $c_{500} = 1.65 \pm 0.95$, $\alpha = 0.87 \pm 0.25$ and $\beta = 3.19 \pm 0.66$ for a fixed value of $\gamma = 0.31$, and masses in the $0.7 \times 10^{14} \, M_\odot \lesssim M_{500} \lesssim 9 \times 10^{14} \, M_\odot$ range. The universal pressure profile parameters best fit is found at $[P_0, c_{500}, \gamma, \alpha, \beta] = [5.42, 1.12, 0.31, 0.81, 3.47]$. To improve the precision of our analysis, we have used as a prior the Pratt et al. [182] mass–gas fraction relation obtained from different subsets of *Chandra* and *XMM-Newton* clusters.

Then we have compared our SZ-based masses with independent weak lensing mass estimates from the mass–richness relations of Simet et al. ([217], S16) and Melchior et al. ([139], M16), finding a mean mass bias of $(1 - b) = 0.76 \pm 0.05$. This value does not depend strongly on the richness subsample considered, and is in good agreement with other independent recent estimates of the bias. Because we are working in the $0.100 < z < 0.325$ redshift region it may not be surprising that we differ with the higher redshift base estimate of Smith et al. [220], but this may be understood given their claim that this bias may be enhanced in the $z > 0.3$ region.

By correcting for our estimated bias, we have then straightforwardly derived the mass–richness relation able to describe the bias-corrected masses, finding a slope equal to $\alpha_{M|\lambda} = 1.22 \pm 0.04$ for a pivot mass $\log_{10} (M_{500c}/M_\odot) = 14.432 \pm 0.041$ evaluated at $\lambda = 60$ at the mean redshift of the sample, $z = 0.245$. The amplitude of the mass–richness relation is strongly tied to the weak lensing-based bias correction results by S16 and M16 as described above, whereas the slope of the mass-richness relation that we find is not linked because the bias correction is found to be independent of cluster mass over our observed range.

From the estimated pressure profile parameters and bias, we have then derived a mean Y_{500}–M_{500} relation $E^{-2/3}(z) \, \langle Y_{500} \rangle \propto 10^A \, \langle (1 - b) M_{500} \rangle^B$ with a normalisation factor $A = -0.22 \pm 0.04$ and a slope $B = 1.72 \pm 0.07$. When the contribution from the bias is considered, this result is within 1σ from the *Planck* mean relation in all the mass range considered, but has a tighter range because of the relatively large size of our sample.

The results obtained in this work show the potential of this method, which provides powerful tools to improve the estimation of cosmological parameters using clusters, which will be crucial in future and ongoing surveys like the J-PAS [27] or DES [58] surveys.

7

General Conclusions

The main objective of this Thesis has been to use large complete samples of clusters of galaxies, drawn from photometric catalogues constructed from Sloan Digital Sky Survey (SDSS) data, to make precise measurements of different subtle effects that emerge from their strong gravitational potential, and to obtain scaling laws that allow to relate different observable proxies to their underlying total mass. In addition to the introductory content, made of Chapters 1, 2 and 3, the main results obtained in this Thesis can be found in Chapters 4, 5 and 6.

In Chapter 4 we have examined the consistency of three cluster catalogues selected from the SDSS by measuring two independent gravity-based effects using all available spectroscopic redshifts from the SDSS Data Release 10 (DR10). These catalogues, obtained using different cluster-finder algorithms, and whose details are described in Chapter 3, are the GMBCG catalogue, with 55,424 clusters, the WHL12, with 132,684, and the redMaPPer, with 25,236. From all these clusters we have selected those that were located in the $0.1 \leqslant z \leqslant 0.4$ redshift region and had an spectroscopic measurement of their central galaxy, which is supposed to trace the deepest part of the potential well. Then, we have characterised statistically the velocity distribution of satellite galaxies and searched for deviations that could indicate the presence of the gravitational redshift effect that we have previously modelled taking into account the kinematical relativistic and flux bias corrections that need to be introduced. Considering the clusters contained in the GMBCG and redMaPPer catalogues, we have detected a signal at a level of $\sim -10\,\mathrm{km\,s^{-1}}$, compatible with the expectations, meanwhile in the WHL12 case we detect an anomalous positive signal that deviates completely from the model proposed. Splitting the cluster samples into different mass bins, we have found that the higher mass clusters of the WHL12 catalogue provide a signal that is consistent with the model proposed, meaning that the unexpected positive signal obtained from low mass clusters is probably related to bulk motions from substructure and spurious cluster detections. In the redMaPPer case we have found a clear mass-dependence of the amplitude of the signal, although it provides the smallest sample of clusters. Secondly, we have measured the redshift enhancement of flux-selected background galaxies from the BOSS survey, finding that all three catalogues generate mass-dependent levels of lensing magnification bias. Because lensing is an stacked along the line-of-sight effect, we expect catalogue contamination by projection effects to affect the measured gravitational redshift and redshift enhancement signals in a different way. We conclude from this analysis that all catalogues, specially redMaPPer, comprise a high proportion of reliable clusters, and that the GMBCG and redMaPPer cluster finder algorithms favour more relaxed clusters with a meaningful gravitational redshift signal, as anticipated by the red-sequence colour selection of the GMBCG and redMaPPer samples.

Taking into account the good results provided by the redMaPPer catalogue, in Chapter 5 we have constructed a large sample of clusters of galaxies by correlating the more recently available SDSS DR12 redshifts with the clusters identified by the redMaPPer algorithm, obtaining an spectroscopic completeness $\geqslant 97\%$ for the 7,143 clusters contained in the $z \leqslant 0.325$ region. With this volume-complete sample of clusters, and considering the probabilistic nature of the cluster-finding algorithm, we have measured the two-point redshift-space correlation function with much more precision than earlier work. Performing these measurements for different richness and redshift cluster subsamples, we have found no signs of redshift evolution and a clear increasing correlation amplitude with larger richness (rising from $r_0 = 14\,h^{-1}\,\mathrm{Mpc}$ at $\lambda \simeq 25$, to $r_0 = 22\,h^{-1}\,\mathrm{Mpc}$ at $\lambda \simeq 60$), as expected from the currently accepted large scale structure formation model where clusters reside in the rare highest peaks of a Gaussian random field. We have also measured the evolution of the number density of clusters, which we found declines by 20% over the range $0.1 < z < 0.3$. Finally, we have derived an accurate power law mass–richness relation comparing our estimated cluster richness function with the richness function constructed from the large N-body Millennium XXL (MXXL) simulation, which we have previously scaled to match a *Planck* cosmology. We have found that the observed amplitude of the correlation function at $\langle z \rangle = 0.24$ exceeds the MXXL prediction by 20% at the $\simeq 2.5\sigma$ level. Spurious, randomly located clusters cannot be blamed for this tension, as this would reduce the correlation amplitude. Much better consistency between the correlation function and the abundances is achieved when we repeat the same analysis considering pre-*Planck* values of $\sigma_8 = 0.9$, $\Omega_m = 0.25$, and $h = 0.73$.

Finally, in Chapter 6 and working again with the SDSS redMaPPer cluster catalogue, we have defined a sample of over 8,030 clusters within the volume-complete redshift region $z \leqslant 0.325$, and have then constructed Sunyaev-Zel'dovich (SZ) effect maps by stacking *Planck* data over the full range of richness considered. Making use of a Bayesian MCMC analysis and dividing the sample into richness bins, we have solved simultaneously for the mean cluster mass in each bin together with the corresponding radial pressure profile parameters. These profiles are well detected over a much wider range of cluster mass and radius than previous work, showing a clear trend towards larger break radius with increasing cluster mass. Our SZ-based masses fall $\sim 24\%$ below the predictions of mass–richness relations based on weak lensing data and found in the literature, consistent with other work that has uncovered a similar "mass bias". Relying on these weak lensing relations we have corrected for this bias, and then have found through another MCMC analysis the optimal mass–richness relation able to describe these debiased masses. Finally, we have derived a tight Y_{500}–M_{500} relation over a wide range of cluster mass, with a power law slope equal to 1.72 ± 0.07 that agrees well with the independent slope obtained by the *Planck* team with an SZ-selected cluster sample, but extends to lower masses with higher precision.

Bibliography

[1] G. O. Abell. The Distribution of Rich Clusters of Galaxies. *ApJS*, 3:211, May 1958.

[2] N. Aghanim, A. C. da Silva, and N. J. Nunes. Cluster scaling relations from cosmological hydrodynamic simulations in a dark-energy dominated universe. *A&A*, 496:637–644, Mar. 2009.

[3] C. P. Ahn, R. Alexandroff, C. Allende Prieto, F. Anders, S. F. Anderson, T. Anderton, B. H. Andrews, É. Aubourg, S. Bailey, F. A. Bastien, and et al. The Tenth Data Release of the Sloan Digital Sky Survey: First Spectroscopic Data from the SDSS-III Apache Point Observatory Galactic Evolution Experiment. *ApJS*, 211:17, Apr. 2014.

[4] S. Alam, F. D. Albareti, C. Allende Prieto, F. Anders, S. F. Anderson, T. Anderton, B. H. Andrews, E. Armengaud, É. Aubourg, S. Bailey, and et al. The Eleventh and Twelfth Data Releases of the Sloan Digital Sky Survey: Final Data from SDSS-III. *ApJS*, 219:12, July 2015.

[5] S. W. Allen, R. W. Schmidt, H. Ebeling, A. C. Fabian, and L. van Speybroeck. Constraints on dark energy from Chandra observations of the largest relaxed galaxy clusters. *MNRAS*, 353:457–467, Sept. 2004.

[6] S. W. Allen, A. E. Evrard, and A. B. Mantz. Cosmological Parameters from Observations of Galaxy Clusters. *ARA&A*, 49:409–470, Sept. 2011.

[7] K. Andersson, B. A. Benson, P. A. R. Ade, K. A. Aird, B. Armstrong, M. Bautz, L. E. Bleem, M. Brodwin, J. E. Carlstrom, C. L. Chang, T. M. Crawford, A. T. Crites, T. de Haan, S. Desai, M. A. Dobbs, J. P. Dudley, R. J. Foley, W. R. Forman, G. Garmire, E. M. George, M. D. Gladders, N. W. Halverson, F. W. High, G. P. Holder, W. L. Holzapfel, J. D. Hrubes, C. Jones, M. Joy, R. Keisler, L. Knox, A. T. Lee, E. M. Leitch, M. Lueker, D. P. Marrone, J. J. McMahon, J. Mehl, S. S. Meyer, J. J. Mohr, T. E. Montroy, S. S. Murray, S. Padin, T. Plagge, C. Pryke, C. L. Reichardt, A. Rest, J. Ruel, J. E. Ruhl, K. K. Schaffer, L. Shaw, E. Shirokoff, J. Song, H. G. Spieler, B. Stalder, Z. Staniszewski, A. A. Stark, C. W. Stubbs, K. Vanderlinde, J. D. Vieira, A. Vikhlinin, R. Williamson, Y. Yang, O. Zahn, and A. Zenteno. X-Ray Properties of the First Sunyaev-Zel'dovich Effect Selected Galaxy Cluster Sample from the South Pole Telescope. *ApJ*, 738:48, Sept. 2011.

[8] S. Andreon. Richness-based masses of rich and famous galaxy clusters. *A&A*, 587:A158, Mar. 2016.

[9] S. Andreon and P. Congdon. The insignificant evolution of the richness-mass relation of galaxy clusters. *A&A*, 568:A23, Aug. 2014.

[10] S. Andreon and M. A. Hurn. The scaling relation between richness and mass of galaxy clusters: a Bayesian approach. *MNRAS*, 404:1922–1937, June 2010.

[11] S. Andreon, A. L. Serra, A. Moretti, and G. Trinchieri. The amazing diversity in the hot gas content of an X-ray unbiased massive galaxy clusters sample. *A&A*, 585:A147, Jan. 2016.

[12] R. E. Angulo and S. D. M. White. One simulation to fit them all - changing the background parameters of a cosmological N-body simulation. *MNRAS*, 405:143–154, June 2010.

[13] R. E. Angulo, V. Springel, S. D. M. White, A. Jenkins, C. M. Baugh, and C. S. Frenk. Scaling relations for galaxy clusters in the Millennium-XXL simulation. *MNRAS*, 426:2046–2062, Nov. 2012.

[14] M. Arnaud, E. Pointecouteau, and G. W. Pratt. The structural and scaling properties of nearby galaxy clusters. II. The M-T relation. *A&A*, 441:893–903, Oct. 2005.

[15] M. Arnaud, E. Pointecouteau, and G. W. Pratt. Calibration of the galaxy cluster M{500}-Y{X} relation with XMM-Newton. *A&A*, 474:L37–L40, Nov. 2007.

[16] M. Arnaud, G. W. Pratt, R. Piffaretti, H. Böhringer, J. H. Croston, and E. Pointecouteau. The universal galaxy cluster pressure profile from a representative sample of nearby systems (REXCESS) and the Y_{SZ} - M_{500} relation. *A&A*, 517:A92, July 2010.

[17] B. Ascaso, N. Benítez, R. Dupke, E. Cypriano, G. Lima-Neto, C. López-Sanjuan, J. Varela, J. S. Alcaniz, T. Broadhurst, A. J. Cenarro, N. C. Devi, L. A. Díaz-García, C. A. C. Fernandes, C. Hernández-Monteagudo, S. Mei, C. Mendes de Oliveira, A. Molino, I. Oteo, W. Schoenell, L. Sodré, K. Viironen, and A. Marín-Franch. An accurate cluster selection function for the J-PAS narrow-band wide-field survey. *MNRAS*, 456:4291–4304, Mar. 2016.

[18] N. A. Bahcall. Clusters of galaxies. *ARA&A*, 15:505–540, 1977.

[19] N. A. Bahcall. Clusters and cosmology. *Phys. Rep.*, 333:233–244, Aug. 2000.

[20] N. A. Bahcall and X. Fan. The Most Massive Distant Clusters: Determining Ω and σ_8. *ApJ*, 504:1–6, Sept. 1998.

[21] N. A. Bahcall, L. M. Lubin, and V. Dorman. Where is the Dark Matter? *ApJ*, 447:L81, July 1995.

[22] N. A. Bahcall, X. Fan, and R. Cen. Constraining Ω with Cluster Evolution. *ApJ*, 485:L53–L56, Aug. 1997.

[23] N. A. Bahcall, F. Dong, L. Hao, P. Bode, J. Annis, J. E. Gunn, and D. P. Schneider. The Richness-dependent Cluster Correlation Function: Early Sloan Digital Sky Survey Data. *ApJ*, 599:814–819, Dec. 2003.

[24] E. J. Baxter, E. Rozo, B. Jain, E. Rykoff, and R. H. Wechsler. Constraining the Mass-Richness Relationship of redMaPPer Clusters with Angular Clustering. *MNRAS*, Aug. 2016.

[25] M. R. Becker, T. A. McKay, B. Koester, R. H. Wechsler, E. Rozo, A. Evrard, D. Johnston, E. Sheldon, J. Annis, E. Lau, R. Nichol, and C. Miller. The Mean and Scatter of the Velocity Dispersion-Optical Richness Relation for maxBCG Galaxy Clusters. *ApJ*, 669:905–928, Nov. 2007.

[26] T. C. Beers, K. Flynn, and K. Gebhardt. Measures of location and scale for velocities in clusters of galaxies - A robust approach. *AJ*, 100:32–46, July 1990.

[27] N. Benitez, R. Dupke, M. Moles, L. Sodre, J. Cenarro, A. Marin-Franch, K. Taylor, D. Cristobal, A. Fernandez-Soto, C. Mendes de Oliveira, J. Cepa-Nogue, L. R. Abramo, J. S. Alcaniz, R. Overzier, C. Hernandez-Monteagudo, E. J. Alfaro, A. Kanaan, J. M. Carvano, R. R. R. Reis, E. Martinez Gonzalez, B. Ascaso, F. Ballesteros, H. S. Xavier, J. Varela, A. Ederoclite, H. Vazquez Ramio, T. Broadhurst, E. Cypriano, R. Angulo, J. M. Diego, A. Zandivarez, E. Diaz, P. Melchior, K. Umetsu, P. F. Spinelli, A. Zitrin, D. Coe, G. Yepes, P. Vielva, V. Sahni, A. Marcos-Caballero, F. Shu Kitaura, A. L. Maroto, M. Masip, S. Tsujikawa, S. Carneiro, J. Gonzalez Nuevo, G. C. Carvalho, M. J. Reboucas, J. C. Carvalho, E. Abdalla, A. Bernui, C. Pigozzo, E. G. M. Ferreira, N. Chandrachani Devi, C. A. P. Bengaly, Jr., M. Campista, A. Amorim, N. V. Asari, A. Bongiovanni, S. Bonoli, G. Bruzual, N. Cardiel, A. Cava, R. Cid Fernandes, P. Coelho, A. Cortesi, R. G. Delgado, L. Diaz Garcia, J. M. R. Espinosa, E. Galliano, J. I. Gonzalez-Serrano, J. Falcon-Barroso, J. Fritz, C. Fernandes, J. Gorgas, C. Hoyos, Y. Jimenez-Teja, J. A. Lopez-Aguerri, C. Lopez-San Juan, A. Mateus, A. Molino, P. Novais, A. OMill, I. Oteo, P. G. Perez-Gonzalez, B. Poggianti, R. Proctor, E. Ricciardelli, P. Sanchez-Blazquez, T. Storchi-Bergmann, E. Telles, W. Schoennell, N. Trujillo, A. Vazdekis, K. Viironen, S. Daflon, T. Aparicio-Villegas, D. Rocha, T. Ribeiro, M. Borges, S. L. Martins, W. Marcolino, D. Martinez-Delgado, M. A. Perez-Torres, B. B. Siffert, M. O. Calvao, M. Sako, R. Kessler, A. Alvarez-Candal, M. De Pra, F. Roig, D. Lazzaro, J. Gorosabel, R. Lopes de Oliveira, G. B. Lima-Neto, J. Irwin, J. F. Liu, E. Alvarez, I. Balmes, S. Chueca, M. V. Costa-Duarte, A. A. da Costa, M. L. L. Dantas, A. Y. Diaz, J. Fabregat, F. Ferrari, B. Gavela, S. G. Gracia, N. Gruel, J. L. L. Gutierrez, R. Guzman, J. D. Hernandez-Fernandez, D. Herranz, L. Hurtado-Gil, F. Jablonsky, R. Laporte, L. L. Le Tiran, J. Licandro, M. Lima, E. Martin, V. Martinez, J. J. C. Montero, P. Penteado, C. B. Pereira, V. Peris, V. Quilis, M. Sanchez-Portal, A. C. Soja, E. Solano, J. Torra, and L. Valdivielso. J-PAS: The Javalambre-Physics of the Accelerated Universe Astrophysical Survey. *ArXiv e-prints: 1403.5237*, Mar. 2014.

[28] B. A. Benson, T. de Haan, J. P. Dudley, C. L. Reichardt, K. A. Aird, K. Andersson, R. Armstrong, M. L. N. Ashby, M. Bautz, M. Bayliss, G. Bazin, L. E. Bleem, M. Brodwin, J. E. Carlstrom, C. L. Chang, H. M. Cho, A. Clocchiatti, T. M. Crawford, A. T. Crites, S. Desai, M. A. Dobbs, R. J. Foley, W. R. Forman, E. M. George, M. D. Gladders, A. H. Gonzalez, N. W. Halverson, N. Harrington, F. W. High, G. P. Holder, W. L. Holzapfel, S. Hoover, J. D. Hrubes, C. Jones, M. Joy, R. Keisler, L. Knox, A. T. Lee, E. M. Leitch, J. Liu, M. Lueker, D. Luong-Van, A. Mantz, D. P. Marrone, M. McDonald, J. J. McMahon, J. Mehl, S. S. Meyer, L. Mocanu, J. J. Mohr, T. E. Montroy, S. S. Murray, T. Natoli, S. Padin, T. Plagge, C. Pryke, A. Rest, J. Ruel, J. E. Ruhl, B. R. Saliwanchik, A. Saro, J. T. Sayre, K. K. Schaffer, L. Shaw, E. Shirokoff, J. Song, H. G. Spieler, B. Stalder, Z. Staniszewski, A. A. Stark, K. Story, C. W. Stubbs, R. Suhada, A. van Engelen, K. Vanderlinde, J. D. Vieira, A. Vikhlinin, R. Williamson, O. Zahn, and A. Zenteno. Cosmological Constraints from Sunyaev-Zel'dovich-selected Clusters with X-Ray Observations in the First 178 $\deg^2$ of the South Pole Telescope Survey. *ApJ*, 763:147, Feb. 2013.

[29] S. Bhattacharya, S. Habib, K. Heitmann, and A. Vikhlinin. Dark Matter Halo Profiles of Massive Clusters: Theory versus Observations. *ApJ*, 766:32, Mar. 2013.

[30] M. Birkinshaw. The Sunyaev-Zel'dovich effect. *Phys. Rep.*, 310:97–195, Mar. 1999.

[31] M. R. Blanton, D. W. Hogg, N. A. Bahcall, J. Brinkmann, M. Britton, A. J. Connolly, I. Csabai, M. Fukugita, J. Loveday, A. Meiksin, J. A. Munn, R. C. Nichol, S. Okamura, T. Quinn, D. P. Schneider, K. Shimasaku, M. A. Strauss, M. Tegmark, M. S. Vogeley, and D. H. Weinberg. The Galaxy Luminosity Function and Luminosity Density at Redshift z = 0.1. *ApJ*, 592:819–838, Aug. 2003.

[32] S. Bocquet, A. Saro, K. Dolag, and J. J. Mohr. Halo mass function: baryon impact, fitting formulae, and implications for cluster cosmology. *MNRAS*, 456:2361–2373, Mar. 2016.

[33] H. Böhringer, P. Schuecker, G. W. Pratt, M. Arnaud, T. J. Ponman, J. H. Croston, S. Borgani, R. G. Bower, U. G. Briel, C. A. Collins, M. Donahue, W. R. Forman, A. Finoguenov, M. J. Geller, L. Guzzo, J. P. Henry, R. Kneissl, J. J. Mohr, K. Matsushita, C. R. Mullis, T. Ohashi, K. Pedersen, D. Pierini, H. Quintana, S. Raychaudhury, T. H. Reiprich, A. K. Romer, P. Rosati, K. Sabirli, R. F. Temple, P. T. P. Viana, A. Vikhlinin, G. M. Voit, and Y.-Y. Zhang. The representative XMM-Newton cluster structure survey (REXCESS) of an X-ray luminosity selected galaxy cluster sample. *A&A*, 469:363–377, July 2007.

[34] M. Bonamente, M. Joy, S. J. LaRoque, J. E. Carlstrom, D. Nagai, and D. P. Marrone. Scaling Relations from Sunyaev-Zel'dovich Effect and Chandra X-Ray Measurements of High-Redshift Galaxy Clusters. *ApJ*, 675:106-114, Mar. 2008.

[35] C. Bonvin, L. Hui, and E. Gaztañaga. Asymmetric galaxy correlation functions. *Phys. Rev. D*, 89(8):083535, Apr. 2014.

[36] V. Bonvin, F. Courbin, S. H. Suyu, P. J. Marshall, C. E. Rusu, D. Sluse, M. Tewes, K. C. Wong, T. Collett, C. D. Fassnacht, T. Treu, M. W. Auger, S. Hilbert, L. V. E. Koopmans, G. Meylan, N. Rumbaugh, A. Sonnenfeld, and C. Spiniello. H0LiCOW V. New COSMOGRAIL time delays of HE0435-1223: H_0 to 3.8% precision from strong lensing in a flat ΛCDM model. *ArXiv e-prints: 1607.01790*, July 2016.

[37] M. Boylan-Kolchin, V. Springel, S. D. M. White, A. Jenkins, and G. Lemson. Resolving cosmic structure formation with the Millennium-II Simulation. *MNRAS*, 398:1150–1164, Sept. 2009.

[38] T. Broadhurst and E. Scannapieco. Detecting the Gravitational Redshift of Cluster Gas. *ApJ*, 533:L93–L97, Apr. 2000.

[39] T. Broadhurst, N. Benítez, D. Coe, K. Sharon, K. Zekser, R. White, H. Ford, R. Bouwens, J. Blakeslee, M. Clampin, N. Cross, M. Franx, B. Frye, G. Hartig, G. Illingworth, L. Infante, F. Menanteau, G. Meurer, M. Postman, D. R. Ardila, F. Bartko, R. A. Brown, C. J. Burrows, E. S. Cheng, P. D. Feldman, D. A. Golimowski, T. Goto, C. Gronwall, D. Herranz, B. Holden, N. Homeier, J. E. Krist, M. P. Lesser, A. R. Martel, G. K. Miley, P. Rosati, M. Sirianni, W. B. Sparks, S. Steindling, H. D. Tran, Z. I. Tsvetanov, and W. Zheng. Strong-Lensing Analysis of A1689 from Deep Advanced Camera Images. *ApJ*, 621:53–88, Mar. 2005.

[40] T. Broadhurst, N. Benítez, D. Coe, K. Sharon, K. Zekser, R. White, H. Ford, R. Bouwens, J. Blakeslee, M. Clampin, N. Cross, M. Franx, B. Frye, G. Hartig, G. Illingworth, L. Infante, F. Menanteau, G. Meurer, M. Postman, D. R. Ardila, F. Bartko, R. A. Brown, C. J. Burrows, E. S. Cheng, P. D. Feldman, D. A. Golimowski, T. Goto, C. Gronwall, D. Herranz, B. Holden, N. Homeier, J. E. Krist, M. P. Lesser, A. R. Martel, G. K. Miley, P. Rosati, M. Sirianni,

W. B. Sparks, S. Steindling, H. D. Tran, Z. I. Tsvetanov, and W. Zheng. Strong-Lensing Analysis of A1689 from Deep Advanced Camera Images. *ApJ*, 621:53–88, Mar. 2005.

[41] T. J. Broadhurst, A. N. Taylor, and J. A. Peacock. Mapping cluster mass distributions via gravitational lensing of background galaxies. *ApJ*, 438:49–61, Jan. 1995.

[42] M. Brodwin, A. H. Gonzalez, L. A. Moustakas, P. R. Eisenhardt, S. A. Stanford, D. Stern, and M. J. I. Brown. Galaxy Cluster Correlation Function to z~1.5 in the IRAC Shallow Cluster Survey. *ApJ*, 671:L93–L96, Dec. 2007.

[43] J. Campa, J. Estrada, and B. Flaugher. Measuring the Scatter of the Mass–Richness Relation in Galaxy Clusters in Photometric Imaging Surveys by Means of Their Correlation Function. *ApJ*, 836:9, Feb. 2017.

[44] A. Cappi. Gravitational redshift in galaxy clusters. *A&A*, 301:6, Sept. 1995.

[45] C. Carbone, C. Fedeli, L. Moscardini, and A. Cimatti. Measuring the neutrino mass from future wide galaxy cluster catalogues. *JCAP*, 3:023, Mar. 2012.

[46] R. G. Carlberg, S. L. Morris, H. K. C. Yee, and E. Ellingson. Redshift Evolution of Galaxy Cluster Densities. *ApJ*, 479:L19–L22, Apr. 1997.

[47] S. M. Carroll, W. H. Press, and E. L. Turner. The cosmological constant. *ARA&A*, 30: 499–542, 1992.

[48] W. Cash. Parameter estimation in astronomy through application of the likelihood ratio. *ApJ*, 228:939–947, Mar. 1979.

[49] N. Clerc, T. Sadibekova, M. Pierre, F. Pacaud, J.-P. Le Fèvre, C. Adami, B. Altieri, and I. Valtchanov. The cosmological analysis of X-ray cluster surveys - II. Application of the CR-HR method to the XMM archive. *MNRAS*, 423:3561–3583, July 2012.

[50] M. Colless, B. A. Peterson, C. Jackson, J. A. Peacock, S. Cole, P. Norberg, I. K. Baldry, C. M. Baugh, J. Bland-Hawthorn, T. Bridges, R. Cannon, C. Collins, W. Couch, N. Cross, G. Dalton, R. De Propris, S. P. Driver, G. Efstathiou, R. S. Ellis, C. S. Frenk, K. Glazebrook, O. Lahav, I. Lewis, S. Lumsden, S. Maddox, D. Madgwick, W. Sutherland, and K. Taylor. The 2dF Galaxy Redshift Survey: Final Data Release. *ArXiv Astrophysics e-prints*, June 2003.

[51] B. Comis, M. de Petris, A. Conte, L. Lamagna, and S. de Gregori. X-ray calibration of Sunyaev-Zel'dovich scaling relations with the ACCEPT catalogue of galaxy clusters observed by Chandra. *MNRAS*, 418:1089–1101, Dec. 2011.

[52] J. Coupon, T. Broadhurst, and K. Umetsu. Cluster Lensing Profiles Derived from a Redshift Enhancement of Magnified BOSS-survey Galaxies. *ApJ*, 772:65, July 2013.

[53] G. Covone, M. Sereno, M. Kilbinger, and V. F. Cardone. Measurement of the Halo Bias from Stacked Shear Profiles of Galaxy Clusters. *ApJ*, 784:L25, Apr. 2014.

[54] R. Coziol, H. Andernach, C. A. Caretta, K. A. Alamo-Martínez, and E. Tago. The Dynamical State of Brightest Cluster Galaxies and The Formation of Clusters. *AJ*, 137:4795, June 2009.

[55] R. A. C. Croft. Gravitational redshifts from large-scale structure. *MNRAS*, 434:3008–3017, Oct. 2013.

[56] N. G. Czakon, J. Sayers, A. Mantz, S. R. Golwala, T. P. Downes, P. M. Koch, K.-Y. Lin, S. M. Molnar, L. A. Moustakas, T. Mroczkowski, E. Pierpaoli, J. A. Shitanishi, S. Siegel, and K. Umetsu. Galaxy Cluster Scaling Relations between Bolocam Sunyaev-Zel'dovich Effect and Chandra X-Ray Measurements. *ApJ*, 806:18, June 2015.

[57] A. C. da Silva, S. T. Kay, A. R. Liddle, and P. A. Thomas. Hydrodynamical simulations of the Sunyaev-Zel'dovich effect: cluster scaling relations and X-ray properties. *MNRAS*, 348: 1401–1408, Mar. 2004.

[58] Dark Energy Survey Collaboration, T. Abbott, F. B. Abdalla, J. Aleksić, S. Allam, A. Amara, D. Bacon, E. Balbinot, M. Banerji, K. Bechtol, A. Benoit-Lévy, G. M. Bernstein, E. Bertin, J. Blazek, C. Bonnett, S. Bridle, D. Brooks, R. J. Brunner, E. Buckley-Geer, D. L. Burke, G. B. Caminha, D. Capozzi, J. Carlsen, A. Carnero-Rosell, M. Carollo, M. Carrasco-Kind, J. Carretero, F. J. Castander, L. Clerkin, T. Collett, C. Conselice, M. Crocce, C. E. Cunha, C. B. D'Andrea, L. N. da Costa, T. M. Davis, S. Desai, H. T. Diehl, J. P. Dietrich, S. Dodelson, P. Doel, A. Drlica-Wagner, J. Estrada, J. Etherington, A. E. Evrard, J. Fabbri, D. A. Finley, B. Flaugher, R. J. Foley, P. Fosalba, J. Frieman, J. García-Bellido, E. Gaztanaga, D. W. Gerdes, T. Giannantonio, D. A. Goldstein, D. Gruen, R. A. Gruendl, P. Guarnieri, G. Gutierrez, W. Hartley, K. Honscheid, B. Jain, D. J. James, T. Jeltema, S. Jouvel, R. Kessler, A. King, D. Kirk, R. Kron, K. Kuehn, N. Kuropatkin, O. Lahav, T. S. Li, M. Lima, H. Lin, M. A. G. Maia, M. Makler, M. Manera, C. Maraston, J. L. Marshall, P. Martini, R. G. McMahon, P. Melchior, A. Merson, C. J. Miller, R. Miquel, J. J. Mohr, X. Morice-Atkinson, K. Naidoo, E. Neilsen, R. C. Nichol, B. Nord, R. Ogando, F. Ostrovski, A. Palmese, A. Papadopoulos, H. V. Peiris, J. Peoples, W. J. Percival, A. A. Plazas, S. L. Reed, A. Refregier, A. K. Romer, A. Roodman, A. Ross, E. Rozo, E. S. Rykoff, I. Sadeh, M. Sako, C. Sánchez, E. Sanchez, B. Santiago, V. Scarpine, M. Schubnell, I. Sevilla-Noarbe, E. Sheldon, M. Smith, R. C. Smith, M. Soares-Santos, F. Sobreira, M. Soumagnac, E. Suchyta, M. Sullivan, M. Swanson, G. Tarle, J. Thaler, D. Thomas, R. C. Thomas, D. Tucker, J. D. Vieira, V. Vikram, A. R. Walker, R. H. Wechsler, J. Weller, W. Wester, L. Whiteway, H. Wilcox, B. Yanny, Y. Zhang, and J. Zuntz. The Dark Energy Survey: more than dark energy - an overview. *MNRAS*, 460:1270–1299, Aug. 2016.

[59] M. Davis and P. J. E. Peebles. A survey of galaxy redshifts. V - The two-point position and velocity correlations. *ApJ*, 267:465–482, Apr. 1983.

[60] K. S. Dawson, D. J. Schlegel, C. P. Ahn, S. F. Anderson, É. Aubourg, S. Bailey, R. H. Barkhouser, J. E. Bautista, A. Beifiori, A. A. Berlind, V. Bhardwaj, D. Bizyaev, C. H. Blake, M. R. Blanton, M. Blomqvist, A. S. Bolton, A. Borde, J. Bovy, W. N. Brandt, H. Brewington, J. Brinkmann, P. J. Brown, J. R. Brownstein, K. Bundy, N. G. Busca, W. Carithers, A. R. Carnero, M. A. Carr, Y. Chen, J. Comparat, N. Connolly, F. Cope, R. A. C. Croft, A. J. Cuesta, L. N. da Costa, J. R. A. Davenport, T. Delubac, R. de Putter, S. Dhital, A. Ealet, G. L. Ebelke, D. J. Eisenstein, S. Escoffier, X. Fan, N. Filiz Ak, H. Finley, A. Font-Ribera, R. Génova-Santos, J. E. Gunn, H. Guo, D. Haggard, P. B. Hall, J.-C. Hamilton, B. Harris, D. W. Harris, S. Ho, D. W. Hogg, D. Holder, K. Honscheid, J. Huehnerhoff, B. Jordan, W. P. Jordan, G. Kauffmann, E. A. Kazin, D. Kirkby, M. A. Klaene, J.-P. Kneib, J.-M. Le Goff, K.-G. Lee, D. C. Long, C. P. Loomis, B. Lundgren, R. H. Lupton, M. A. G. Maia,

M. Makler, E. Malanushenko, V. Malanushenko, R. Mandelbaum, M. Manera, C. Maraston, D. Margala, K. L. Masters, C. K. McBride, P. McDonald, I. D. McGreer, R. G. McMahon, O. Mena, J. Miralda-Escudé, A. D. Montero-Dorta, F. Montesano, D. Muna, A. D. Myers, T. Naugle, R. C. Nichol, P. Noterdaeme, S. E. Nuza, M. D. Olmstead, A. Oravetz, D. J. Oravetz, R. Owen, N. Padmanabhan, N. Palanque-Delabrouille, K. Pan, J. K. Parejko, I. Pâris, W. J. Percival, I. Pérez-Fournon, I. Pérez-Ràfols, P. Petitjean, R. Pfaffenberger, J. Pforr, M. M. Pieri, F. Prada, A. M. Price-Whelan, M. J. Raddick, R. Rebolo, J. Rich, G. T. Richards, C. M. Rockosi, N. A. Roe, A. J. Ross, N. P. Ross, G. Rossi, J. A. Rubiño-Martin, L. Samushia, A. G. Sánchez, C. Sayres, S. J. Schmidt, D. P. Schneider, C. G. Scóccola, H.-J. Seo, A. Shelden, E. Sheldon, Y. Shen, Y. Shu, A. Slosar, S. A. Smee, S. A. Snedden, F. Stauffer, O. Steele, M. A. Strauss, A. Streblyanska, N. Suzuki, M. E. C. Swanson, T. Tal, M. Tanaka, D. Thomas, J. L. Tinker, R. Tojeiro, C. A. Tremonti, M. Vargas Magaña, L. Verde, M. Viel, D. A. Wake, M. Watson, B. A. Weaver, D. H. Weinberg, B. J. Weiner, A. A. West, M. White, W. M. Wood-Vasey, C. Yeche, I. Zehavi, G.-B. Zhao, and Z. Zheng. The Baryon Oscillation Spectroscopic Survey of SDSS-III. *AJ*, 145:10, Jan. 2013.

[61] I. De Martino and F. Atrio-Barandela. SZ/X-ray scaling relations using X-ray data and Planck Nominal maps. *MNRAS*, 461:3222–3232, Sept. 2016.

[62] A. Diaferio. Mass estimation in the outer regions of galaxy clusters. *MNRAS*, 309:610–622, Nov. 1999.

[63] S. Dodelson and S. Park. Nonlocal gravity and structure in the Universe. *Phys. Rev. D*, 90 (4):043535, Aug. 2014.

[64] M. J. d. L. Domínguez Romero, D. García Lambas, and H. Muriel. An improved method for the identification of galaxy systems: measuring the gravitational redshift by dark matter haloes. *MNRAS*, 427:L6–L10, Nov. 2012.

[65] F. Dong, E. Pierpaoli, J. E. Gunn, and R. H. Wechsler. Optical Cluster Finding with an Adaptive Matched-Filter Technique: Algorithm and Comparison with Simulations. *ApJ*, 676: 868-879, Apr. 2008.

[66] F. W. Dyson, A. S. Eddington, and C. Davidson. A Determination of the Deflection of Light by the Sun's Gravitational Field, from Observations Made at the Total Eclipse of May 29, 1919. *Philosophical Transactions of the Royal Society of London Series A*, 220:291–333, 1920.

[67] A. S. Eddington. On a formula for correcting statistics for the effects of a known error of observation. *MNRAS*, 73:359–360, Mar. 1913.

[68] G. Efstathiou, W. J. Sutherland, and S. J. Maddox. The cosmological constant and cold dark matter. *Nature*, 348:705–707, Dec. 1990.

[69] D. J. Eisenstein, J. Annis, J. E. Gunn, A. S. Szalay, A. J. Connolly, R. C. Nichol, N. A. Bahcall, M. Bernardi, S. Burles, F. J. Castander, M. Fukugita, D. W. Hogg, Ž. Ivezić, G. R. Knapp, R. H. Lupton, V. Narayanan, M. Postman, D. E. Reichart, M. Richmond, D. P. Schneider, D. J. Schlegel, M. A. Strauss, M. SubbaRao, D. L. Tucker, D. Vanden Berk, M. S. Vogeley, D. H. Weinberg, and B. Yanny. Spectroscopic Target Selection for the Sloan Digital Sky Survey: The Luminous Red Galaxy Sample. *AJ*, 122:2267–2280, Nov. 2001.

[70] D. J. Eisenstein, D. H. Weinberg, E. Agol, H. Aihara, C. Allende Prieto, S. F. Anderson, J. A. Arns, É. Aubourg, S. Bailey, E. Balbinot, and et al. SDSS-III: Massive Spectroscopic Surveys of the Distant Universe, the Milky Way, and Extra-Solar Planetary Systems. *AJ*, 142:72, Sept. 2011.

[71] V. R. Eke, S. Cole, and C. S. Frenk. Cluster evolution as a diagnostic for Omega. *MNRAS*, 282, Sept. 1996.

[72] J. Estrada, E. Sefusatti, and J. A. Frieman. The Correlation Function of Optically Selected Galaxy Clusters in the Sloan Digital Sky Survey. *ApJ*, 692:265–282, Feb. 2009.

[73] A. E. Evrard, T. J. MacFarland, H. M. P. Couchman, J. M. Colberg, N. Yoshida, S. D. M. White, A. Jenkins, C. S. Frenk, F. R. Pearce, J. A. Peacock, and P. A. Thomas. Galaxy Clusters in Hubble Volume Simulations: Cosmological Constraints from Sky Survey Populations. *ApJ*, 573:7–36, July 2002.

[74] A. E. Evrard, J. Bialek, M. Busha, M. White, S. Habib, K. Heitmann, M. Warren, E. Rasia, G. Tormen, L. Moscardini, C. Power, A. R. Jenkins, L. Gao, C. S. Frenk, V. Springel, S. D. M. White, and J. Diemand. Virial Scaling of Massive Dark Matter Halos: Why Clusters Prefer a High Normalization Cosmology. *ApJ*, 672:122-137, Jan. 2008.

[75] S. M. Faber, C. N. A. Willmer, C. Wolf, D. C. Koo, B. J. Weiner, J. A. Newman, M. Im, A. L. Coil, C. Conroy, M. C. Cooper, M. Davis, D. P. Finkbeiner, B. F. Gerke, K. Gebhardt, E. J. Groth, P. Guhathakurta, J. Harker, N. Kaiser, S. Kassin, M. Kleinheinrich, N. P. Konidaris, R. G. Kron, L. Lin, G. Luppino, D. S. Madgwick, K. Meisenheimer, K. G. Noeske, A. C. Phillips, V. L. Sarajedini, R. P. Schiavon, L. Simard, A. S. Szalay, N. P. Vogt, and R. Yan. Galaxy Luminosity Functions to z~1 from DEEP2 and COMBO-17: Implications for Red Galaxy Formation. *ApJ*, 665:265–294, Aug. 2007.

[76] X. Fan, N. A. Bahcall, and R. Cen. Determining the Amplitude of Mass Fluctuations in the Universe. *ApJ*, 490:L123–L126, Dec. 1997.

[77] A. Farahi, A. E. Evrard, E. Rozo, E. S. Rykoff, and R. H. Wechsler. Galaxy cluster mass estimation from stacked spectroscopic analysis. *MNRAS*, 460:3900–3912, Aug. 2016.

[78] H. A. Feldman, N. Kaiser, and J. A. Peacock. Power-spectrum analysis of three-dimensional redshift surveys. *ApJ*, 426:23–37, May 1994.

[79] J. Ford, H. Hildebrandt, L. Van Waerbeke, A. Leauthaud, P. Capak, A. Finoguenov, M. Tanaka, M. R. George, and J. Rhodes. Magnification by Galaxy Group Dark Matter Halos. *ApJ*, 754:143, Aug. 2012.

[80] W. L. Freedman, B. F. Madore, B. K. Gibson, L. Ferrarese, D. D. Kelson, S. Sakai, J. R. Mould, R. C. Kennicutt, Jr., H. C. Ford, J. A. Graham, J. P. Huchra, S. M. G. Hughes, G. D. Illingworth, L. M. Macri, and P. B. Stetson. Final Results from the Hubble Space Telescope Key Project to Measure the Hubble Constant. *ApJ*, 553:47–72, May 2001.

[81] M. Fukugita, T. Ichikawa, J. E. Gunn, M. Doi, K. Shimasaku, and D. P. Schneider. The Sloan Digital Sky Survey Photometric System. *AJ*, 111:1748, Apr. 1996.

[82] M. Girardi, S. Borgani, G. Giuricin, F. Mardirossian, and M. Mezzetti. Optical Luminosities and Mass-to-Light Ratios of Nearby Galaxy Clusters. *ApJ*, 530:62–79, Feb. 2000.

[83] K. M. Górski, E. Hivon, A. J. Banday, B. D. Wandelt, F. K. Hansen, M. Reinecke, and M. Bartelmann. HEALPix: A Framework for High-Resolution Discretization and Fast Analysis of Data Distributed on the Sphere. *ApJ*, 622:759–771, Apr. 2005.

[84] M. B. Gronke, C. Llinares, and D. F. Mota. Gravitational redshift profiles in the f(R) and symmetron models. *A&A*, 562:A9, Feb. 2014.

[85] J. E. Gunn, W. A. Siegmund, E. J. Mannery, R. E. Owen, C. L. Hull, R. F. Leger, L. N. Carey, G. R. Knapp, D. G. York, W. N. Boroski, S. M. Kent, R. H. Lupton, C. M. Rockosi, M. L. Evans, P. Waddell, J. E. Anderson, J. Annis, J. C. Barentine, L. M. Bartoszek, S. Bastian, S. B. Bracker, H. J. Brewington, C. I. Briegel, J. Brinkmann, Y. J. Brown, M. A. Carr, P. C. Czarapata, C. C. Drennan, T. Dombeck, G. R. Federwitz, B. A. Gillespie, C. Gonzales, S. U. Hansen, M. Harvanek, J. Hayes, W. Jordan, E. Kinney, M. Klaene, S. J. Kleinman, R. G. Kron, J. Kresinski, G. Lee, S. Limmongkol, C. W. Lindenmeyer, D. C. Long, C. L. Loomis, P. M. McGehee, P. M. Mantsch, E. H. Neilsen, Jr., R. M. Neswold, P. R. Newman, A. Nitta, J. Peoples, Jr., J. R. Pier, P. S. Prieto, A. Prosapio, C. Rivetta, D. P. Schneider, S. Snedden, and S.-i. Wang. The 2.5 m Telescope of the Sloan Digital Sky Survey. *AJ*, 131: 2332–2359, Apr. 2006.

[86] A. J. S. Hamilton. Measuring Omega and the real correlation function from the redshift correlation function. *ApJ*, 385:L5–L8, Jan. 1992.

[87] A. J. S. Hamilton. Toward Better Ways to Measure the Galaxy Correlation Function. *ApJ*, 417:19, Nov. 1993.

[88] S. M. Hansen, E. S. Sheldon, R. H. Wechsler, and B. P. Koester. The Galaxy Content of SDSS Clusters and Groups. *ApJ*, 699:1333–1353, July 2009.

[89] J. Hao, T. A. McKay, B. P. Koester, E. S. Rykoff, E. Rozo, J. Annis, R. H. Wechsler, A. Evrard, S. R. Siegel, M. Becker, M. Busha, D. Gerdes, D. E. Johnston, and E. Sheldon. A GMBCG Galaxy Cluster Catalog of 55,424 Rich Clusters from SDSS DR7. *ApJS*, 191: 254–274, Dec. 2010.

[90] I. Harrison and P. Coles. Testing cosmology with extreme galaxy clusters. *MNRAS*, 421: L19–L23, Mar. 2012.

[91] C. Hennig, J. J. Mohr, A. Zenteno, S. Desai, J. P. Dietrich, S. Bocquet, V. Strazzullo, A. Saro, T. M. C. Abbott, F. B. Abdalla, M. Bayliss, A. Benoit-Levy, R. A. Bernstein, E. Bertin, D. Brooks, R. Capasso, D. Capozzi, A. Carnero, M. Carrasco Kind, J. Carretero, I. Chiu, C. B. D'Andrea, L. N. daCosta, H. T. Diehl, P. Doel, T. F. Eifler, A. E. Evrard, A. Fausti-Neto, P. Fosalba, J. Frieman, C. Gangkofner, A. Gonzalez, D. Gruen, R. A. Gruendl, N. Gupta, G. Gutierrez, K. Honscheid, J. Hlavacek-Larrondo, D. J. James, K. Kuehn, N. Kuropatkin, O. Lahav, M. March, J. L. Marshall, P. Martini, M. McDonald, P. Melchior, C. J. Miller, R. Miquel, E. Neilsen, B. Nord, R. Ogando, A. A. Plazas, C. Reichardt, A. K. Romer, E. Rozo, E. S. Rykoff, E. Sanchez, B. Santiago, M. Schubnell, I. Sevilla-Noarbe, R. C. Smith, M. Soares-Santos, F. Sobreira, B. Stalder, S. A. Stanford, E. Suchyta, M. E. C. Swanson, G. Tarle, D. Thomas, V. Vikram, A. R. Walker, and Y. Zhang. Galaxy Populations in Massive Galaxy Clusters to z=1.1: Color Distribution, Concentration, Halo Occupation Number and Red Sequence Fraction. *ArXiv e-prints: 1604.00988*, Apr. 2016.

[92] J. P. Henry. A Measurement of the Density Parameter Derived from the Evolution of Cluster X-Ray Temperatures. *ApJ*, 489:L1–L5, Nov. 1997.

[93] H. Hildebrandt, L. van Waerbeke, D. Scott, M. Béthermin, J. Bock, D. Clements, A. Conley, A. Cooray, J. S. Dunlop, S. Eales, T. Erben, D. Farrah, A. Franceschini, J. Glenn, M. Halpern, S. Heinis, R. J. Ivison, G. Marsden, S. J. Oliver, M. J. Page, I. Pérez-Fournon, A. J. Smith, M. Rowan-Robinson, I. Valtchanov, R. F. J. van der Burg, J. D. Vieira, M. Viero, and L. Wang. Inferring the mass of submillimetre galaxies by exploiting their gravitational magnification of background galaxies. *MNRAS*, 429:3230–3237, Mar. 2013.

[94] H. Hoekstra, R. Herbonnet, A. Muzzin, A. Babul, A. Mahdavi, M. Viola, and M. Cacciato. The Canadian Cluster Comparison Project: detailed study of systematics and updated weak lensing masses. *MNRAS*, 449:685–714, May 2015.

[95] W. Hu and A. V. Kravtsov. Sample Variance Considerations for Cluster Surveys. *ApJ*, 584: 702–715, Feb. 2003.

[96] D. Huterer, D. Kirkby, R. Bean, A. Connolly, K. Dawson, S. Dodelson, A. Evrard, B. Jain, M. Jarvis, E. Linder, R. Mandelbaum, M. May, A. Raccanelli, B. Reid, E. Rozo, F. Schmidt, N. Sehgal, A. Slosar, A. van Engelen, H.-Y. Wu, and G. Zhao. Growth of cosmic structure: Probing dark energy beyond expansion. *Astroparticle Physics*, 63:23–41, Mar. 2015.

[97] O. Ilbert, L. Tresse, E. Zucca, S. Bardelli, S. Arnouts, G. Zamorani, L. Pozzetti, D. Bottini, B. Garilli, V. Le Brun, O. Le Fèvre, D. Maccagni, J.-P. Picat, R. Scaramella, M. Scodeggio, G. Vettolani, A. Zanichelli, C. Adami, M. Arnaboldi, M. Bolzonella, A. Cappi, S. Charlot, T. Contini, S. Foucaud, P. Franzetti, I. Gavignaud, L. Guzzo, A. Iovino, H. J. McCracken, B. Marano, C. Marinoni, G. Mathez, A. Mazure, B. Meneux, R. Merighi, S. Paltani, R. Pello, A. Pollo, M. Radovich, M. Bondi, A. Bongiorno, G. Busarello, P. Ciliegi, F. Lamareille, Y. Mellier, P. Merluzzi, V. Ripepi, and D. Rizzo. The VIMOS-VLT deep survey. Evolution of the galaxy luminosity function up to z = 2 in first epoch data. *A&A*, 439:863–876, Sept. 2005.

[98] B. Jain, A. Joyce, R. Thompson, A. Upadhye, J. Battat, P. Brax, A.-C. Davis, C. de Rham, S. Dodelson, A. Erickcek, G. Gabadadze, W. Hu, L. Hui, D. Huterer, M. Kamionkowski, J. Khoury, K. Koyama, B. Li, E. Linder, F. Schmidt, R. Scoccimarro, G. Starkman, C. Stubbs, M. Takada, A. Tolley, M. Trodden, J.-P. Uzan, V. Vikram, A. Weltman, M. Wyman, D. Zaritsky, and G. Zhao. Novel Probes of Gravity and Dark Energy. *ArXiv e-prints: 1309.5389*, Sept. 2013.

[99] P. Jimeno, T. Broadhurst, J. Coupon, K. Umetsu, and R. Lazkoz. Comparing gravitational redshifts of SDSS galaxy clusters with the magnified redshift enhancement of background BOSS galaxies. *MNRAS*, 448:1999–2012, Apr. 2015.

[100] P. Jimeno, T. Broadhurst, R. Lazkoz, R. Angulo, J.-M. Diego, K. Umetsu, and M.-c. Chu. Precise clustering and density evolution of redMaPPer galaxy clusters versus MXXL simulation. *MNRAS*, 466:2658–2674, Apr. 2017.

[101] D. E. Johnston, E. S. Sheldon, R. H. Wechsler, E. Rozo, B. P. Koester, J. A. Frieman, T. A. McKay, A. E. Evrard, M. R. Becker, and J. Annis. Cross-correlation Weak Lensing of SDSS galaxy Clusters II: Cluster Density Profiles and the Mass–Richness Relation. *ArXiv e-prints: 0709.1159*, Sept. 2007.

[102] N. Kaiser. On the spatial correlations of Abell clusters. *ApJ*, 284:L9–L12, Sept. 1984.

[103] N. Kaiser. Evolution and clustering of rich clusters. *MNRAS*, 222:323–345, Sept. 1986.

[104] N. Kaiser. Clustering in real space and in redshift space. *MNRAS*, 227:1–21, July 1987.

[105] N. Kaiser. Measuring gravitational redshifts in galaxy clusters. *MNRAS*, 435:1278–1286, Oct. 2013.

[106] N. Kaiser and G. Squires. Mapping the dark matter with weak gravitational lensing. *ApJ*, 404:441–450, Feb. 1993.

[107] N. Kaiser, G. Squires, and T. Broadhurst. A Method for Weak Lensing Observations. *ApJ*, 449:460, Aug. 1995.

[108] K. Kettula, A. Finoguenov, R. Massey, J. Rhodes, H. Hoekstra, J. E. Taylor, P. F. Spinelli, M. Tanaka, O. Ilbert, P. Capak, H. J. McCracken, and A. Koekemoer. Weak Lensing Calibrated M-T Scaling Relation of Galaxy Groups in the COSMOS Field^{sstarf}. *ApJ*, 778: 74, Nov. 2013.

[109] Y.-R. Kim and R. A. C. Croft. Gravitational Redshifts in Simulated Galaxy Clusters. *ApJ*, 607:164–174, May 2004.

[110] A. Knebe, S. R. Knollmann, S. I. Muldrew, F. R. Pearce, M. A. Aragon-Calvo, Y. Ascasibar, P. S. Behroozi, D. Ceverino, S. Colombi, J. Diemand, K. Dolag, B. L. Falck, P. Fasel, J. Gardner, S. Gottlöber, C.-H. Hsu, F. Iannuzzi, A. Klypin, Z. Lukić, M. Maciejewski, C. McBride, M. C. Neyrinck, S. Planelles, D. Potter, V. Quilis, Y. Rasera, J. I. Read, P. M. Ricker, F. Roy, V. Springel, J. Stadel, G. Stinson, P. M. Sutter, V. Turchaninov, D. Tweed, G. Yepes, and M. Zemp. Haloes gone MAD: The Halo-Finder Comparison Project. *MNRAS*, 415:2293–2318, Aug. 2011.

[111] B. P. Koester, T. A. McKay, J. Annis, R. H. Wechsler, A. Evrard, L. Bleem, M. Becker, D. Johnston, E. Sheldon, R. Nichol, C. Miller, R. Scranton, N. Bahcall, J. Barentine, H. Brewington, J. Brinkmann, M. Harvanek, S. Kleinman, J. Krzesinski, D. Long, A. Nitta, D. P. Schneider, S. Sneddin, W. Voges, and D. York. A MaxBCG Catalog of 13,823 Galaxy Clusters from the Sloan Digital Sky Survey. *ApJ*, 660:239–255, May 2007.

[112] B. P. Koester, T. A. McKay, J. Annis, R. H. Wechsler, A. Evrard, L. Bleem, M. Becker, D. Johnston, E. Sheldon, R. Nichol, C. Miller, R. Scranton, N. Bahcall, J. Barentine, H. Brewington, J. Brinkmann, M. Harvanek, S. Kleinman, J. Krzesinski, D. Long, A. Nitta, D. P. Schneider, S. Sneddin, W. Voges, and D. York. A MaxBCG Catalog of 13,823 Galaxy Clusters from the Sloan Digital Sky Survey. *ApJ*, 660:239–255, May 2007.

[113] B. P. Koester, T. A. McKay, J. Annis, R. H. Wechsler, A. E. Evrard, E. Rozo, L. Bleem, E. S. Sheldon, and D. Johnston. MaxBCG: A Red-Sequence Galaxy Cluster Finder. *ApJ*, 660:221–238, May 2007.

[114] E. Komatsu, K. M. Smith, J. Dunkley, C. L. Bennett, B. Gold, G. Hinshaw, N. Jarosik, D. Larson, M. R. Nolta, L. Page, D. N. Spergel, M. Halpern, R. S. Hill, A. Kogut, M. Limon, S. S. Meyer, N. Odegard, G. S. Tucker, J. L. Weiland, E. Wollack, and E. L. Wright. Seven-year Wilkinson Microwave Anisotropy Probe (WMAP) Observations: Cosmological Interpretation. *ApJS*, 192:18, Feb. 2011.

[115] M. Kowalski, D. Rubin, G. Aldering, R. J. Agostinho, A. Amadon, R. Amanullah, C. Balland, K. Barbary, G. Blanc, P. J. Challis, A. Conley, N. V. Connolly, R. Covarrubias, K. S. Dawson, S. E. Deustua, R. Ellis, S. Fabbro, V. Fadeyev, X. Fan, B. Farris, G. Folatelli, B. L. Frye, G. Garavini, E. L. Gates, L. Germany, G. Goldhaber, B. Goldman, A. Goobar, D. E. Groom, J. Haissinski, D. Hardin, I. Hook, S. Kent, A. G. Kim, R. A. Knop, C. Lidman, E. V. Linder, J. Mendez, J. Meyers, G. J. Miller, M. Moniez, A. M. Mourão, H. Newberg, S. Nobili, P. E. Nugent, R. Pain, O. Perdereau, S. Perlmutter, M. M. Phillips, V. Prasad, R. Quimby, N. Regnault, J. Rich, E. P. Rubenstein, P. Ruiz-Lapuente, F. D. Santos, B. E. Schaefer, R. A. Schommer, R. C. Smith, A. M. Soderberg, A. L. Spadafora, L.-G. Strolger, M. Strovink, N. B. Suntzeff, N. Suzuki, R. C. Thomas, N. A. Walton, L. Wang, W. M. Wood-Vasey, and J. L. Yun. Improved Cosmological Constraints from New, Old, and Combined Supernova Data Sets. *ApJ*, 686:749-778, Oct. 2008.

[116] A. V. Kravtsov and S. Borgani. Formation of Galaxy Clusters. *ARA&A*, 50:353–409, Sept. 2012.

[117] O. Lahav, P. B. Lilje, J. R. Primack, and M. J. Rees. Dynamical effects of the cosmological constant. *MNRAS*, 251:128–136, July 1991.

[118] O. Lahav, S. L. Bridle, W. J. Percival, J. A. Peacock, G. Efstathiou, C. M. Baugh, J. Bland-Hawthorn, T. Bridges, R. Cannon, S. Cole, M. Colless, C. Collins, W. Couch, G. Dalton, R. de Propris, S. P. Driver, R. S. Ellis, C. S. Frenk, K. Glazebrook, C. Jackson, I. Lewis, S. Lumsden, S. Maddox, D. S. Madgwick, S. Moody, P. Norberg, B. A. Peterson, W. Sutherland, and K. Taylor. The 2dF Galaxy Redshift Survey: the amplitudes of fluctuations in the 2dFGRS and the CMB, and implications for galaxy biasing. *MNRAS*, 333:961–968, July 2002.

[119] O. Lahav, A. Kiakotou, F. B. Abdalla, and C. Blake. Forecasting neutrino masses from galaxy clustering in the Dark Energy Survey combined with the Planck measurements. *MNRAS*, 405:168–176, June 2010.

[120] T. Y. Lam, F. Schmidt, T. Nishimichi, and M. Takada. Modeling the phase-space distribution around massive halos. *Phys. Rev. D*, 88(2):023012, July 2013.

[121] S. D. Landy and A. S. Szalay. Bias and variance of angular correlation functions. *ApJ*, 412: 64–71, July 1993.

[122] O. Le Fèvre, G. Vettolani, B. Garilli, L. Tresse, D. Bottini, V. Le Brun, D. Maccagni, J. P. Picat, R. Scaramella, M. Scodeggio, A. Zanichelli, C. Adami, M. Arnaboldi, S. Arnouts, S. Bardelli, M. Bolzonella, A. Cappi, S. Charlot, P. Ciliegi, T. Contini, S. Foucaud, P. Franzetti, I. Gavignaud, L. Guzzo, O. Ilbert, A. Iovino, H. J. McCracken, B. Marano, C. Marinoni, G. Mathez, A. Mazure, B. Meneux, R. Merighi, S. Paltani, R. Pellò, A. Pollo, L. Pozzetti, M. Radovich, G. Zamorani, E. Zucca, M. Bondi, A. Bongiorno, G. Busarello, F. Lamareille, Y. Mellier, P. Merluzzi, V. Ripepi, and D. Rizzo. The VIMOS VLT deep survey. First epoch VVDS-deep survey: 11 564 spectra with $17.5 \leq$ IAB ≤ 24, and the redshift distribution over $0 \leq z \leq 5$. *A&A*, 439:845–862, Sept. 2005.

[123] B. Leistedt, H. V. Peiris, and L. Verde. No New Cosmological Concordance with Massive Sterile Neutrinos. *Physical Review Letters*, 113(4):041301, July 2014.

[124] D. Lemze, R. Barkana, T. J. Broadhurst, and Y. Rephaeli. Mass and gas profiles in A1689: joint X-ray and lensing analysis. *MNRAS*, 386:1092–1106, May 2008.

[125] A. Lewis and S. Bridle. Cosmological parameters from CMB and other data: A Monte Carlo approach. *Phys. Rev. D*, 66(10):103511, Nov. 2002.

[126] A. Lewis, A. Challinor, and A. Lasenby. Efficient Computation of Cosmic Microwave Background Anisotropies in Closed Friedmann-Robertson-Walker Models. *ApJ*, 538:473–476, Aug. 2000.

[127] R. Li, H. Shan, J.-P. Kneib, H. Mo, E. Rozo, A. Leauthaud, J. Moustakas, L. Xie, T. Erben, L. Van Waerbeke, M. Makler, E. Rykoff, and B. Moraes. Measuring subhalo mass in redMaPPer clusters with CFHT Stripe 82 Survey. *MNRAS*, 458:2573–2583, May 2016.

[128] M. Lieu, G. P. Smith, P. A. Giles, F. Ziparo, B. J. Maughan, J. Démoclès, F. Pacaud, M. Pierre, C. Adami, Y. M. Bahé, N. Clerc, L. Chiappetti, D. Eckert, S. Ettori, S. Lavoie, J. P. Le Fevre, I. G. McCarthy, M. Kilbinger, T. J. Ponman, T. Sadibekova, and J. P. Willis. The XXL Survey . IV. Mass-temperature relation of the bright cluster sample. *A&A*, 592: A4, June 2016.

[129] M. Lima and W. Hu. Self-calibration of cluster dark energy studies: Observable-mass distribution. *Phys. Rev. D*, 72(4):043006, Aug. 2005.

[130] R. Lynds and V. Petrosian. Luminous arcs in clusters of galaxies. *ApJ*, 336:1–8, Jan. 1989.

[131] A. Mahdavi, H. Hoekstra, A. Babul, C. Bildfell, T. Jeltema, and J. P. Henry. Joint Analysis of Cluster Observations. II. Chandra/XMM-Newton X-Ray and Weak Lensing Scaling Relations for a Sample of 50 Rich Clusters of Galaxies. *ApJ*, 767:116, Apr. 2013.

[132] R. Mandelbaum, A. Slosar, T. Baldauf, U. Seljak, C. M. Hirata, R. Nakajima, R. Reyes, and R. E. Smith. Cosmological parameter constraints from galaxy-galaxy lensing and galaxy clustering with the SDSS DR7. *MNRAS*, 432:1544–1575, June 2013.

[133] A. Mantz, S. W. Allen, D. Rapetti, and H. Ebeling. The observed growth of massive galaxy clusters - I. Statistical methods and cosmological constraints. *MNRAS*, 406:1759–1772, Aug. 2010.

[134] A. B. Mantz, S. W. Allen, R. G. Morris, D. A. Rapetti, D. E. Applegate, P. L. Kelly, A. von der Linden, and R. W. Schmidt. Cosmology and astrophysics from relaxed galaxy clusters - II. Cosmological constraints. *MNRAS*, 440:2077–2098, May 2014.

[135] A. B. Mantz, S. W. Allen, R. G. Morris, A. von der Linden, D. E. Applegate, P. L. Kelly, D. L. Burke, D. Donovan, and H. Ebeling. Weighing the giants- V. Galaxy cluster scaling relations. *MNRAS*, 463:3582–3603, Dec. 2016.

[136] D. P. Marrone, G. P. Smith, J. Richard, M. Joy, M. Bonamente, N. Hasler, V. Hamilton-Morris, J.-P. Kneib, T. Culverhouse, J. E. Carlstrom, C. Greer, D. Hawkins, R. Hennessy, J. W. Lamb, E. M. Leitch, M. Loh, A. Miller, T. Mroczkowski, S. Muchovej, C. Pryke, M. K. Sharp, and D. Woody. LoCuSS: A Comparison of Sunyaev-Zel'dovich Effect and Gravitational-Lensing Measurements of Galaxy Clusters. *ApJ*, 701:L114–L118, Aug. 2009.

[137] E. Medezinski, T. Broadhurst, K. Umetsu, D. Coe, N. Benítez, H. Ford, Y. Rephaeli, N. Arimoto, and X. Kong. Using Weak-Lensing Dilution to Improve Measurements of the Luminous and Dark Matter in A1689. *ApJ*, 663:717–733, July 2007.

[138] E. Medezinski, T. Broadhurst, K. Umetsu, M. Oguri, Y. Rephaeli, and N. Benítez. Detailed cluster mass and light profiles of A1703, A370 and RXJ1347-11 from deep Subaru imaging. *MNRAS*, 405:257–273, June 2010.

[139] P. Melchior, D. Gruen, T. McClintock, T. N. Varga, E. Sheldon, E. Rozo, A. Amara, M. R. Becker, B. A. Benson, A. Bermeo, S. L. Bridle, J. Clampitt, J. P. Dietrich, W. G. Hartley, D. Hollowood, B. Jain, M. Jarvis, T. Jeltema, T. Kacprzak, N. MacCrann, E. S. Rykoff, A. Saro, E. Suchyta, M. A. Troxel, J. Zuntz, C. Bonnett, A. A. Plazas, T. M. C. Abbott, F. B. Abdalla, J. Annis, A. Benoit-Lévy, G. M. Bernstein, E. Bertin, D. Brooks, E. Buckley-Geer, A. Carnero Rosell, M. Carrasco Kind, J. Carretero, C. E. Cunha, C. B. D'Andrea, L. N. da Costa, S. Desai, T. F. Eifler, B. Flaugher, P. Fosalba, J. García-Bellido, E. Gaztanaga, D. W. Gerdes, R. A. Gruendl, J. Gschwend, G. Gutierrez, K. Honscheid, D. J. James, D. Kirk, E. Krause, K. Kuehn, N. Kuropatkin, O. Lahav, M. Lima, M. A. G. Maia, M. March, P. Martini, F. Menanteau, C. J. Miller, R. Miquel, J. J. Mohr, R. C. Nichol, R. Ogando, A. K. Romer, E. Sanchez, V. Scarpine, I. Sevilla-Noarbe, R. C. Smith, M. Soares-Santos, F. Sobreira, M. E. C. Swanson, G. Tarle, D. Thomas, A. R. Walker, J. Weller, and Y. Zhang. Weak-lensing mass calibration of redMaPPer galaxy clusters in Dark Energy Survey Science Verification data. *ArXiv e-prints: 1610.06890*, Oct. 2016.

[140] J.-B. Melin, J. G. Bartlett, J. Delabrouille, M. Arnaud, R. Piffaretti, and G. W. Pratt. The galaxy cluster Y_{SZ} - L_X and Y_{SZ} - M relations from the WMAP 5-yr data. *A&A*, 525: A139, Jan. 2011.

[141] J. Merten, M. Meneghetti, M. Postman, K. Umetsu, A. Zitrin, E. Medezinski, M. Nonino, A. Koekemoer, P. Melchior, D. Gruen, L. A. Moustakas, M. Bartelmann, O. Host, M. Donahue, D. Coe, A. Molino, S. Jouvel, A. Monna, S. Seitz, N. Czakon, D. Lemze, J. Sayers, I. Balestra, P. Rosati, N. Benítez, A. Biviano, R. Bouwens, L. Bradley, T. Broadhurst, M. Carrasco, H. Ford, C. Grillo, L. Infante, D. Kelson, O. Lahav, R. Massey, J. Moustakas, E. Rasia, J. Rhodes, J. Vega, and W. Zheng. CLASH: The Concentration-Mass Relation of Galaxy Clusters. *ApJ*, 806:4, June 2015.

[142] H. Miyatake, S. More, M. Takada, D. N. Spergel, R. Mandelbaum, E. S. Rykoff, and E. Rozo. Evidence of Halo Assembly Bias in Massive Clusters. *Physical Review Letters*, 116 (4):041301, Jan. 2016.

[143] S. Miyazaki, M. Oguri, T. Hamana, M. Tanaka, L. Miller, Y. Utsumi, Y. Komiyama, H. Furusawa, J. Sakurai, S. Kawanomoto, F. Nakata, F. Uraguchi, M. Koike, D. Tomono, R. Lupton, J. E. Gunn, H. Karoji, H. Aihara, H. Murayama, and M. Takada. Properties of Weak Lensing Clusters Detected on Hyper Suprime-Cam's 2.3 deg^2 field. *ApJ*, 807:22, July 2015.

[144] S. M. Molnar and T. Broadhurst. A Hydrodynamical Solution for the "Twin-tailed" Colliding Galaxy Cluster "El Gordo". *ApJ*, 800:37, Feb. 2015.

[145] A. D. Montero-Dorta and F. Prada. The SDSS DR6 luminosity functions of galaxies. *MNRAS*, 399:1106–1118, Nov. 2009.

[146] P. M. Motl, E. J. Hallman, J. O. Burns, and M. L. Norman. The Integrated Sunyaev-Zeldovich Effect as a Superior Method for Measuring the Mass of Clusters of Galaxies. *ApJ*, 623:L63–L66, Apr. 2005.

[147] T. Mroczkowski, S. Dicker, J. Sayers, E. D. Reese, B. Mason, N. Czakon, C. Romero, A. Young, M. Devlin, S. Golwala, P. Korngut, C. Sarazin, J. Bock, P. M. Koch, K.-Y. Lin, S. M. Molnar, E. Pierpaoli, K. Umetsu, and M. Zemcov. A Multi-wavelength Study of the Sunyaev-Zel'dovich Effect in the Triple-merger Cluster MACS J0717.5+3745 with MUSTANG and Bolocam. *ApJ*, 761:47, Dec. 2012.

[148] D. Nagai. The Impact of Galaxy Formation on the Sunyaev-Zel'dovich Effect of Galaxy Clusters. *ApJ*, 650:538–549, Oct. 2006.

[149] D. Nagai, A. V. Kravtsov, and A. Vikhlinin. Effects of Galaxy Formation on Thermodynamics of the Intracluster Medium. *ApJ*, 668:1–14, Oct. 2007.

[150] D. Nagai, A. Vikhlinin, and A. V. Kravtsov. Testing X-Ray Measurements of Galaxy Clusters with Cosmological Simulations. *ApJ*, 655:98–108, Jan. 2007.

[151] J. F. Navarro, C. S. Frenk, and S. D. M. White. The Structure of Cold Dark Matter Halos. *ApJ*, 462:563, May 1996.

[152] J. F. Navarro, C. S. Frenk, and S. D. M. White. A Universal Density Profile from Hierarchical Clustering. *ApJ*, 490:493–508, Dec. 1997.

[153] K. Nelson, E. T. Lau, and D. Nagai. Hydrodynamic Simulation of Non-thermal Pressure Profiles of Galaxy Clusters. *ApJ*, 792:25, Sept. 2014.

[154] W. R. Oegerle and J. M. Hill. Dynamics of cD Clusters of Galaxies. IV. Conclusion of a Survey of 25 Abell Clusters. *AJ*, 122:2858–2873, Dec. 2001.

[155] M. Oguri. A cluster finding algorithm based on the multiband identification of red sequence galaxies. *MNRAS*, 444:147–161, Oct. 2014.

[156] M. Oguri and T. Hamana. Detailed cluster lensing profiles at large radii and the impact on cluster weak lensing studies. *MNRAS*, 414:1851–1861, July 2011.

[157] M. Oguri, Y.-T. Lin, S.-C. Lin, A. J. Nishizawa, A. More, S. More, B.-C. Hsieh, E. Medezinski, H. Miyatake, H.-Y. Jian, L. Lin, M. Takada, N. Okabe, J. S. Speagle, J. Coupon, A. Leauthaud, R. H. Lupton, S. Miyazaki, P. A. Price, M. Tanaka, I. Chiu, Y. Komiyama, Y. Okura, M. M. Tanaka, and T. Usuda. An optically-selected cluster catalog at redshift 0.1<z<1.1 from the Hyper Suprime-Cam Subaru Strategic Program S16A data. *ArXiv e-prints: 1701.00818*, Jan. 2017.

[158] N. Okabe and G. P. Smith. LoCuSS: weak-lensing mass calibration of galaxy clusters. *MNRAS*, 461:3794–3821, Oct. 2016.

[159] N. Okabe, G. P. Smith, K. Umetsu, M. Takada, and T. Futamase. LoCuSS: The Mass Density Profile of Massive Galaxy Clusters at z = 0.2. *ApJ*, 769:L35, June 2013.

[160] J. P. Ostriker and P. J. Steinhardt. The observational case for a low-density Universe with a non-zero cosmological constant. *Nature*, 377:600–602, Oct. 1995.

[161] J. P. Ostriker, P. J. E. Peebles, and A. Yahil. The size and mass of galaxies, and the mass of the universe. *ApJ*, 193:L1–L4, Oct. 1974.

[162] J. Oukbir and A. Blanchard. X-ray clusters in open universes. *A&A*, 262:L21–L24, Sept. 1992.

[163] J. Oukbir and A. Blanchard. X-ray clusters: towards a new determination of the density parameter of the universe. *A&A*, 317:1–13, Jan. 1997.

[164] F. Pacaud, N. Clerc, P. A. Giles, C. Adami, T. Sadibekova, M. Pierre, B. J. Maughan, M. Lieu, J. P. Le Fèvre, S. Alis, B. Altieri, F. Ardila, I. Baldry, C. Benoist, M. Birkinshaw, L. Chiappetti, J. Démoclès, D. Eckert, A. E. Evrard, L. Faccioli, F. Gastaldello, L. Guennou, C. Horellou, A. Iovino, E. Koulouridis, V. Le Brun, C. Lidman, J. Liske, S. Maurogordato, F. Menanteau, M. Owers, B. Poggianti, D. Pomarède, E. Pompei, T. J. Ponman, D. Rapetti, T. H. Reiprich, G. P. Smith, R. Tuffs, P. Valageas, I. Valtchanov, J. P. Willis, and F. Ziparo. The XXL Survey. II. The bright cluster sample: catalogue and luminosity function. *A&A*, 592:A2, June 2016.

[165] Z. Pan and L. Knox. Constraints on neutrino mass from cosmic microwave background and large-scale structure. *MNRAS*, 454:3200–3206, Dec. 2015.

[166] J. A. Peacock, S. Cole, P. Norberg, C. M. Baugh, J. Bland-Hawthorn, T. Bridges, R. D. Cannon, M. Colless, C. Collins, W. Couch, G. Dalton, K. Deeley, R. De Propris, S. P. Driver, G. Efstathiou, R. S. Ellis, C. S. Frenk, K. Glazebrook, C. Jackson, O. Lahav, I. Lewis, S. Lumsden, S. Maddox, W. J. Percival, B. A. Peterson, I. Price, W. Sutherland, and K. Taylor. A measurement of the cosmological mass density from clustering in the 2dF Galaxy Redshift Survey. *Nature*, 410:169–173, Mar. 2001.

[167] P. J. E. Peebles. *The large-scale structure of the universe*. 1980.

[168] P. J. E. Peebles and M. G. Hauser. Statistical Analysis of Catalogs of Extragalactic Objects. III. The Shane-Wirtanen and Zwicky Catalogs. *ApJS*, 28:19, Nov. 1974.

[169] P. J. E. Peebles, R. A. Daly, and R. Juszkiewicz. Masses of rich clusters of galaxies as a test of the biased cold dark matter theory. *ApJ*, 347:563–574, Dec. 1989.

[170] S. Perlmutter, G. Aldering, G. Goldhaber, R. A. Knop, P. Nugent, P. G. Castro, S. Deustua, S. Fabbro, A. Goobar, D. E. Groom, I. M. Hook, A. G. Kim, M. Y. Kim, J. C. Lee, N. J. Nunes, R. Pain, C. R. Pennypacker, R. Quimby, C. Lidman, R. S. Ellis, M. Irwin, R. G. McMahon, P. Ruiz-Lapuente, N. Walton, B. Schaefer, B. J. Boyle, A. V. Filippenko, T. Matheson, A. S. Fruchter, N. Panagia, H. J. M. Newberg, W. J. Couch, and T. S. C. Project. Measurements of Ω and Λ from 42 High-Redshift Supernovae. *ApJ*, 517:565–586, June 1999.

[171] Planck Collaboration, N. Aghanim, M. Arnaud, M. Ashdown, J. Aumont, C. Baccigalupi, A. Balbi, A. J. Banday, R. B. Barreiro, M. Bartelmann, and et al. Planck early results. XII. Cluster Sunyaev-Zeldovich optical scaling relations. *A&A*, 536:A12, Dec. 2011.

[172] Planck Collaboration, P. A. R. Ade, N. Aghanim, M. Arnaud, M. Ashdown, F. Atrio-Barandela, J. Aumont, C. Baccigalupi, A. Balbi, A. J. Banday, and et al. Planck intermediate results. V. Pressure profiles of galaxy clusters from the Sunyaev-Zeldovich effect. *A&A*, 550:A131, Feb. 2013.

[173] Planck Collaboration, P. A. R. Ade, N. Aghanim, M. Arnaud, M. Ashdown, F. Atrio-Barandela, J. Aumont, C. Baccigalupi, A. Balbi, A. J. Banday, and et al. Planck intermediate results. X. Physics of the hot gas in the Coma cluster. *A&A*, 554:A140, June 2013.

[174] Planck Collaboration, P. A. R. Ade, N. Aghanim, M. I. R. Alves, C. Armitage-Caplan, M. Arnaud, M. Ashdown, F. Atrio-Barandela, J. Aumont, H. Aussel, and et al. Planck 2013 results. I. Overview of products and scientific results. *A&A*, 571:A1, Nov. 2014.

[175] Planck Collaboration, P. A. R. Ade, N. Aghanim, C. Armitage-Caplan, M. Arnaud, M. Ashdown, F. Atrio-Barandela, J. Aumont, H. Aussel, C. Baccigalupi, and et al. Planck 2013 results. XXIX. The Planck catalogue of Sunyaev-Zeldovich sources. *A&A*, 571:A29, Nov. 2014.

[176] Planck Collaboration, P. A. R. Ade, N. Aghanim, C. Armitage-Caplan, M. Arnaud, M. Ashdown, F. Atrio-Barandela, J. Aumont, C. Baccigalupi, A. J. Banday, and et al. Planck 2013 results. IX. HFI spectral response. *A&A*, 571:A9, Nov. 2014.

[177] Planck Collaboration, P. A. R. Ade, N. Aghanim, C. Armitage-Caplan, M. Arnaud, M. Ashdown, F. Atrio-Barandela, J. Aumont, C. Baccigalupi, A. J. Banday, and et al. Planck 2013 results. XX. Cosmology from Sunyaev-Zeldovich cluster counts. *A&A*, 571:A20, Nov. 2014.

[178] Planck Collaboration, P. A. R. Ade, N. Aghanim, C. Armitage-Caplan, M. Arnaud, M. Ashdown, F. Atrio-Barandela, J. Aumont, C. Baccigalupi, A. J. Banday, and et al. Planck 2013 results. XXI. Power spectrum and high-order statistics of the Planck all-sky Compton parameter map. *A&A*, 571:A21, Nov. 2014.

[179] Planck Collaboration, P. A. R. Ade, N. Aghanim, M. Arnaud, M. Ashdown, J. Aumont, C. Baccigalupi, A. J. Banday, R. B. Barreiro, J. G. Bartlett, and et al. Planck 2015 results. XIII. Cosmological parameters. *A&A*, 594:A13, Sept. 2016.

[180] Planck Collaboration, P. A. R. Ade, N. Aghanim, M. Arnaud, M. Ashdown, J. Aumont, C. Baccigalupi, A. J. Banday, R. B. Barreiro, N. Bartolo, and et al. Planck intermediate results. XL. The Sunyaev-Zeldovich signal from the Virgo cluster. *A&A*, 596:A101, Dec. 2016.

[181] A. Pouri, S. Basilakos, and M. Plionis. Precision growth index using the clustering of cosmic structures and growth data. *JCAP*, 8:042, Aug. 2014.

[182] G. W. Pratt, J. H. Croston, M. Arnaud, and H. Böhringer. Galaxy cluster X-ray luminosity scaling relations from a representative local sample (REXCESS). *A&A*, 498:361–378, May 2009.

[183] W. H. Press and P. Schechter. Formation of Galaxies and Clusters of Galaxies by Self-Similar Gravitational Condensation. *ApJ*, 187:425–438, Feb. 1974.

[184] D. Rapetti, C. Blake, S. W. Allen, A. Mantz, D. Parkinson, and F. Beutler. A combined measurement of cosmic growth and expansion from clusters of galaxies, the CMB and galaxy clustering. *MNRAS*, 432:973–985, June 2013.

[185] E. Rasia, S. Ettori, L. Moscardini, P. Mazzotta, S. Borgani, K. Dolag, G. Tormen, L. M. Cheng, and A. Diaferio. Systematics in the X-ray cluster mass estimators. *MNRAS*, 369:2013–2024, July 2006.

[186] B. A. Reid, W. J. Percival, D. J. Eisenstein, L. Verde, D. N. Spergel, R. A. Skibba, N. A. Bahcall, T. Budavari, J. A. Frieman, M. Fukugita, J. R. Gott, J. E. Gunn, Ž. Ivezić, G. R. Knapp, R. G. Kron, R. H. Lupton, T. A. McKay, A. Meiksin, R. C. Nichol, A. C. Pope, D. J. Schlegel, D. P. Schneider, C. Stoughton, M. A. Strauss, A. S. Szalay, M. Tegmark, M. S. Vogeley, D. H. Weinberg, D. G. York, and I. Zehavi. Cosmological constraints from the clustering of the Sloan Digital Sky Survey DR7 luminous red galaxies. *MNRAS*, 404: 60–85, May 2010.

[187] Y. Rephaeli. Comptonization Of The Cosmic Microwave Background: The Sunyaev-Zeldovich Effect. *ARA&A*, 33:541–580, 1995.

[188] P. M. Ricker and C. L. Sarazin. Off-Axis Cluster Mergers: Effects of a Strongly Peaked Dark Matter Profile. *ApJ*, 561:621–644, Nov. 2001.

[189] A. G. Riess, A. V. Filippenko, P. Challis, A. Clocchiatti, A. Diercks, P. M. Garnavich, R. L. Gilliland, C. J. Hogan, S. Jha, R. P. Kirshner, B. Leibundgut, M. M. Phillips, D. Reiss, B. P. Schmidt, R. A. Schommer, R. C. Smith, J. Spyromilio, C. Stubbs, N. B. Suntzeff, and J. Tonry. Observational Evidence from Supernovae for an Accelerating Universe and a Cosmological Constant. *AJ*, 116:1009–1038, Sept. 1998.

[190] A. G. Riess, L. M. Macri, S. L. Hoffmann, D. Scolnic, S. Casertano, A. V. Filippenko, B. E. Tucker, M. J. Reid, D. O. Jones, J. M. Silverman, R. Chornock, P. Challis, W. Yuan, P. J. Brown, and R. J. Foley. A 2.4% Determination of the Local Value of the Hubble Constant. *ApJ*, 826:56, July 2016.

[191] E. Rozo and E. S. Rykoff. redMaPPer II: X-Ray and SZ Performance Benchmarks for the SDSS Catalog. *ApJ*, 783:80, Mar. 2014.

[192] E. Rozo, R. H. Wechsler, B. P. Koester, T. A. McKay, A. E. Evrard, D. Johnston, E. S. Sheldon, J. Annis, and J. A. Frieman. Cosmological Constraints from SDSS maxBCG Cluster Abundances. *ArXiv Astrophysics e-prints*, Mar. 2007.

[193] E. Rozo, E. S. Rykoff, A. Evrard, M. Becker, T. McKay, R. H. Wechsler, B. P. Koester, J. Hao, S. Hansen, E. Sheldon, D. Johnston, J. Annis, and J. Frieman. Constraining the Scatter in the Mass-richness Relation of maxBCG Clusters with Weak Lensing and X-ray Data. *ApJ*, 699:768–781, July 2009.

[194] E. Rozo, E. S. Rykoff, B. P. Koester, T. McKay, J. Hao, A. Evrard, R. H. Wechsler, S. Hansen, E. Sheldon, D. Johnston, M. Becker, J. Annis, L. Bleem, and R. Scranton. Improvement of the Richness Estimates of maxBCG Clusters. *ApJ*, 703:601–613, Sept. 2009.

[195] E. Rozo, R. H. Wechsler, E. S. Rykoff, J. T. Annis, M. R. Becker, A. E. Evrard, J. A. Frieman, S. M. Hansen, J. Hao, D. E. Johnston, B. P. Koester, T. A. McKay, E. S. Sheldon, and D. H. Weinberg. Cosmological Constraints from the Sloan Digital Sky Survey maxBCG Cluster Catalog. *ApJ*, 708:645–660, Jan. 2010.

[196] E. Rozo, J. G. Bartlett, A. E. Evrard, and E. S. Rykoff. Closing the loop: a self-consistent model of optical, X-ray and Sunyaev-Zel'dovich scaling relations for clusters of Galaxies. *MNRAS*, 438:78–96, Feb. 2014.

[197] E. Rozo, E. S. Rykoff, J. G. Bartlett, and J.-B. Melin. redMaPPer - III. A detailed comparison of the Planck 2013 and SDSS DR8 redMaPPer cluster catalogues. *MNRAS*, 450:592–605, June 2015.

[198] E. Rozo, E. S. Rykoff, M. Becker, R. M. Reddick, and R. H. Wechsler. redMaPPer - IV. Photometric membership identification of red cluster galaxies with 1 per cent precision. *MNRAS*, 453:38–52, Oct. 2015.

[199] E. S. Rykoff, B. P. Koester, E. Rozo, J. Annis, A. E. Evrard, S. M. Hansen, J. Hao, D. E. Johnston, T. A. McKay, and R. H. Wechsler. Robust Optical Richness Estimation with Reduced Scatter. *ApJ*, 746:178, Feb. 2012.

[200] E. S. Rykoff, E. Rozo, M. T. Busha, C. E. Cunha, A. Finoguenov, A. Evrard, J. Hao, B. P. Koester, A. Leauthaud, B. Nord, M. Pierre, R. Reddick, T. Sadibekova, E. S. Sheldon, and R. H. Wechsler. redMaPPer. I. Algorithm and SDSS DR8 Catalog. *ApJ*, 785:104, Apr. 2014.

[201] E. S. Rykoff, E. Rozo, D. Hollowood, A. Bermeo-Hernandez, T. Jeltema, J. Mayers, A. K. Romer, P. Rooney, A. Saro, C. Vergara Cervantes, R. H. Wechsler, H. Wilcox, T. M. C. Abbott, F. B. Abdalla, S. Allam, J. Annis, A. Benoit-Lévy, G. M. Bernstein, E. Bertin, D. Brooks, D. L. Burke, D. Capozzi, A. Carnero Rosell, M. Carrasco Kind, F. J. Castander, M. Childress, C. A. Collins, C. E. Cunha, C. B. D'Andrea, L. N. da Costa, T. M. Davis, S. Desai, H. T. Diehl, J. P. Dietrich, P. Doel, A. E. Evrard, D. A. Finley, B. Flaugher, P. Fosalba, J. Frieman, K. Glazebrook, D. A. Goldstein, D. Gruen, R. A. Gruendl, G. Gutierrez, M. Hilton, K. Honscheid, B. Hoyle, D. J. James, S. T. Kay, K. Kuehn, N. Kuropatkin, O. Lahav, G. F. Lewis, C. Lidman, M. Lima, M. A. G. Maia, R. G. Mann, J. L. Marshall, P. Martini, P. Melchior, C. J. Miller, R. Miquel, J. J. Mohr, R. C. Nichol, B. Nord, R. Ogando, A. A. Plazas, K. Reil, M. Sahlén, E. Sanchez, B. Santiago, V. Scarpine, M. Schubnell, I. Sevilla-Noarbe, R. C. Smith, M. Soares-Santos, F. Sobreira, J. P. Stott, E. Suchyta, M. E. C. Swanson, G. Tarle, D. Thomas, D. Tucker, S. Uddin, P. T. P. Viana, V. Vikram, A. R. Walker, Y. Zhang, and DES Collaboration. The RedMaPPer Galaxy Cluster Catalog From DES Science Verification Data. *ApJS*, 224:1, May 2016.

[202] I. Sadeh, L. L. Feng, and O. Lahav. Gravitational Redshift of Galaxies in Clusters from the Sloan Digital Sky Survey and the Baryon Oscillation Spectroscopic Survey. *Physical Review Letters*, 114(7):071103, Feb. 2015.

[203] T. Sadibekova, M. Pierre, N. Clerc, L. Faccioli, R. Gastaud, J.-P. Le Fevre, E. Rozo, and E. Rykoff. The X-CLASS-redMaPPer galaxy cluster comparison. I. Identification procedures. *A&A*, 571:A87, Nov. 2014.

[204] A. Saro, S. Bocquet, E. Rozo, B. A. Benson, J. Mohr, E. S. Rykoff, M. Soares-Santos, L. Bleem, S. Dodelson, P. Melchior, F. Sobreira, V. Upadhyay, J. Weller, T. Abbott, F. B. Abdalla, S. Allam, R. Armstrong, M. Banerji, A. H. Bauer, M. Bayliss, A. Benoit-Lévy, G. M. Bernstein, E. Bertin, M. Brodwin, D. Brooks, E. Buckley-Geer, D. L. Burke, J. E. Carlstrom, R. Capasso, D. Capozzi, A. Carnero Rosell, M. Carrasco Kind, I. Chiu, R. Covarrubias, T. M. Crawford, M. Crocce, C. B. D'Andrea, L. N. da Costa, D. L. DePoy, S. Desai, T. de Haan, H. T. Diehl, J. P. Dietrich, P. Doel, C. E. Cunha, T. F. Eifler, A. E. Evrard, A. Fausti Neto, E. Fernandez, B. Flaugher, P. Fosalba, J. Frieman, C. Gangkofner, E. Gaztanaga, D. Gerdes, D. Gruen, R. A. Gruendl, N. Gupta, C. Hennig, W. L. Holzapfel, K. Honscheid, B. Jain, D. James, K. Kuehn, N. Kuropatkin, O. Lahav, T. S. Li, H. Lin, M. A. G. Maia, M. March,

J. L. Marshall, P. Martini, M. McDonald, C. J. Miller, R. Miquel, B. Nord, R. Ogando, A. A. Plazas, C. L. Reichardt, A. K. Romer, A. Roodman, M. Sako, E. Sanchez, M. Schubnell, I. Sevilla, R. C. Smith, B. Stalder, A. A. Stark, V. Strazzullo, E. Suchyta, M. E. C. Swanson, G. Tarle, J. Thaler, D. Thomas, D. Tucker, V. Vikram, A. von der Linden, A. R. Walker, R. H. Wechsler, W. Wester, A. Zenteno, and K. E. Ziegler. Constraints on the richness-mass relation and the optical-SZE positional offset distribution for SZE-selected clusters. *MNRAS*, 454:2305–2319, Dec. 2015.

[205] A. Saro, S. Bocquet, J. Mohr, E. Rozo, B. A. Benson, S. Dodelson, E. S. Rykoff, L. Bleem, T. M. C. Abbott, F. B. Abdalla, S. Allen, J. Annis, A. Benoit-Levy, D. Brooks, D. L. Burke, R. Capasso, A. Carnero Rosell, M. Carrasco Kind, J. Carretero, I. Chiu, T. M. Crawford, C. E. Cunha, C. B. D'Andrea, L. N. da Costa, S. Desai, J. P. Dietrich, A. E. Evrard, A. Fausti Neto, B. Flaugher, P. Fosalba, J. Frieman, C. Gangkofner, E. Gaztanaga, D. W. Gerdes, T. Giannantonio, S. Grandis, D. Gruen, R. A. Gruendl, N. Gupta, G. Gutierrez, W. L. Holzapfel, D. J. James, K. Kuehn, N. Kuropatkin, M. Lima, J. L. Marshall, M. McDonald, P. Melchior, F. Menanteau, R. Miquel, R. Ogando, A. A. Plazas, D. Rapetti, C. L. Reichardt, K. Reil, A. K. Romer, E. Sanchez, V. Scarpine, M. Schubnell, I. Sevilla-Noarbe, R. C. Smith, M. Soares-Santos, B. Soergel, V. Strazzullo, E. Suchyta, M. E. C. Swanson, G. Tarle, D. Thomas, V. Vikram, A. R. Walker, and A. Zenteno. Optical-SZE Scaling Relations for DES Optically Selected Clusters within the SPT-SZ Survey. *ArXiv e-prints: 1605.08770*, May 2016.

[206] J. Sayers, S. R. Golwala, A. B. Mantz, J. Merten, S. M. Molnar, M. Naka, G. Pailet, E. Pierpaoli, S. R. Siegel, and B. Wolman. A Comparison and Joint Analysis of Sunyaev-Zel'dovich Effect Measurements from Planck and Bolocam for a Set of 47 Massive Galaxy Clusters. *ApJ*, 832:26, Nov. 2016.

[207] P. Schechter. An analytic expression for the luminosity function for galaxies. *ApJ*, 203:297–306, Jan. 1976.

[208] U. Seljak, A. Makarov, P. McDonald, S. F. Anderson, N. A. Bahcall, J. Brinkmann, S. Burles, R. Cen, M. Doi, J. E. Gunn, Ž. Ivezić, S. Kent, J. Loveday, R. H. Lupton, J. A. Munn, R. C. Nichol, J. P. Ostriker, D. J. Schlegel, D. P. Schneider, M. Tegmark, D. E. Berk, D. H. Weinberg, and D. G. York. Cosmological parameter analysis including SDSS Lyα forest and galaxy bias: Constraints on the primordial spectrum of fluctuations, neutrino mass, and dark energy. *Phys. Rev. D*, 71(10):103515, May 2005.

[209] F. Sembolini, G. Yepes, M. De Petris, S. Gottlöber, L. Lamagna, and B. Comis. The MUSIC of galaxy clusters - I. Baryon properties and scaling relations of the thermal Sunyaev-Zel'dovich effect. *MNRAS*, 429:323–343, Feb. 2013.

[210] M. Sereno and S. Ettori. Comparing masses in literature (CoMaLit) - I. Bias and scatter in weak lensing and X-ray mass estimates of clusters. *MNRAS*, 450:3633–3648, July 2015.

[211] M. Sereno and S. Ettori. CoMaLit-V. Mass forecasting with proxies. Method and application to weak lensing calibrated samples. *ArXiv e-prints: 1603.06581*, Mar. 2016.

[212] M. Sereno, S. Ettori, and L. Moscardini. CoMaLit - II. The scaling relation between mass and Sunyaev-Zel'dovich signal for Planck selected galaxy clusters. *MNRAS*, 450:3649–3664, July 2015.

[213] M. Sereno, A. Veropalumbo, F. Marulli, G. Covone, L. Moscardini, and A. Cimatti. New constraints on σ_8 from a joint analysis of stacked gravitational lensing and clustering of galaxy clusters. *MNRAS*, 449:4147–4161, June 2015.

[214] M. Sereno, G. Covone, L. Izzo, S. Ettori, J. Coupon, and M. Lieu. PSZ2LenS. Weak lensing analysis of the Planck clusters in the CFHTLenS and in the RCSLenS. *ArXiv e-prints: 1703.06886*, Mar. 2017.

[215] R. M. Sharples, R. S. Ellis, and P. M. Gray. The structure and dynamics of Abell 2670. I - M/L ratio and orbital anisotropy. *MNRAS*, 231:479–508, Mar. 1988.

[216] X. Shi and E. Komatsu. Analytical model for non-thermal pressure in galaxy clusters. *MNRAS*, 442:521–532, July 2014.

[217] M. Simet, T. McClintock, R. Mandelbaum, E. Rozo, E. Rykoff, E. Sheldon, and R. H. Wechsler. Weak Lensing Measurement of the Mass–Richness Relation of SDSS redMaPPer Clusters. *ArXiv e-prints: 1603.06953*, Mar. 2016.

[218] R. A. Skibba, F. C. van den Bosch, X. Yang, S. More, H. Mo, and F. Fontanot. Are brightest halo galaxies central galaxies? *MNRAS*, 410:417–431, Jan. 2011.

[219] S. A. Smee, J. E. Gunn, A. Uomoto, N. Roe, D. Schlegel, C. M. Rockosi, M. A. Carr, F. Leger, K. S. Dawson, M. D. Olmstead, J. Brinkmann, R. Owen, R. H. Barkhouser, K. Honscheid, P. Harding, D. Long, R. H. Lupton, C. Loomis, L. Anderson, J. Annis, M. Bernardi, V. Bhardwaj, D. Bizyaev, A. S. Bolton, H. Brewington, J. W. Briggs, S. Burles, J. G. Burns, F. J. Castander, A. Connolly, J. R. A. Davenport, G. Ebelke, H. Epps, P. D. Feldman, S. D. Friedman, J. Frieman, T. Heckman, C. L. Hull, G. R. Knapp, D. M. Lawrence, J. Loveday, E. J. Mannery, E. Malanushenko, V. Malanushenko, A. J. Merrelli, D. Muna, P. R. Newman, R. C. Nichol, D. Oravetz, K. Pan, A. C. Pope, P. G. Ricketts, A. Shelden, D. Sandford, W. Siegmund, A. Simmons, D. S. Smith, S. Snedden, D. P. Schneider, M. SubbaRao, C. Tremonti, P. Waddell, and D. G. York. The Multi-object, Fiber-fed Spectrographs for the Sloan Digital Sky Survey and the Baryon Oscillation Spectroscopic Survey. *AJ*, 146:32, Aug. 2013.

[220] G. P. Smith, P. Mazzotta, N. Okabe, F. Ziparo, S. L. Mulroy, A. Babul, A. Finoguenov, I. G. McCarthy, M. Lieu, Y. M. Bahé, H. Bourdin, A. E. Evrard, T. Futamase, C. P. Haines, M. Jauzac, D. P. Marrone, R. Martino, P. E. May, J. E. Taylor, and K. Umetsu. LoCuSS: Testing hydrostatic equilibrium in galaxy clusters. *MNRAS*, 456:L74–L78, Feb. 2016.

[221] M. Soares-Santos, R. R. de Carvalho, J. Annis, R. R. Gal, F. La Barbera, P. A. A. Lopes, R. H. Wechsler, M. T. Busha, and B. F. Gerke. The Voronoi Tessellation Cluster Finder in 2+1 Dimensions. *ApJ*, 727:45, Jan. 2011.

[222] G. Soucail, B. Fort, Y. Mellier, and J. P. Picat. A blue ring-like structure, in the center of the A 370 cluster of galaxies. *A&A*, 172:L14–L16, Jan. 1987.

[223] D. N. Spergel, L. Verde, H. V. Peiris, E. Komatsu, M. R. Nolta, C. L. Bennett, M. Halpern, G. Hinshaw, N. Jarosik, A. Kogut, M. Limon, S. S. Meyer, L. Page, G. S. Tucker, J. L. Weiland, E. Wollack, and E. L. Wright. First-Year Wilkinson Microwave Anisotropy Probe (WMAP) Observations: Determination of Cosmological Parameters. *ApJS*, 148:175–194, Sept. 2003.

[224] V. Springel. The cosmological simulation code GADGET-2. *MNRAS*, 364:1105–1134, Dec. 2005.

[225] V. Springel, N. Yoshida, and S. D. M. White. GADGET: a code for collisionless and gasdynamical cosmological simulations. *New Astronomy*, 6:79–117, Apr. 2001.

[226] V. Springel, S. D. M. White, A. Jenkins, C. S. Frenk, N. Yoshida, L. Gao, J. Navarro, R. Thacker, D. Croton, J. Helly, J. A. Peacock, S. Cole, P. Thomas, H. Couchman, A. Evrard, J. Colberg, and F. Pearce. Simulations of the formation, evolution and clustering of galaxies and quasars. *Nature*, 435:629–636, June 2005.

[227] M. A. Strauss, D. H. Weinberg, R. H. Lupton, V. K. Narayanan, J. Annis, M. Bernardi, M. Blanton, S. Burles, A. J. Connolly, J. Dalcanton, M. Doi, D. Eisenstein, J. A. Frieman, M. Fukugita, J. E. Gunn, Ž. Ivezić, S. Kent, R. S. J. Kim, G. R. Knapp, R. G. Kron, J. A. Munn, H. J. Newberg, R. C. Nichol, S. Okamura, T. R. Quinn, M. W. Richmond, D. J. Schlegel, K. Shimasaku, M. SubbaRao, A. S. Szalay, D. Vanden Berk, M. S. Vogeley, B. Yanny, N. Yasuda, D. G. York, and I. Zehavi. Spectroscopic Target Selection in the Sloan Digital Sky Survey: The Main Galaxy Sample. *AJ*, 124:1810–1824, Sept. 2002.

[228] M. Sun, G. M. Voit, M. Donahue, C. Jones, W. Forman, and A. Vikhlinin. Chandra Studies of the X-Ray Gas Properties of Galaxy Groups. *ApJ*, 693:1142–1172, Mar. 2009.

[229] R. A. Sunyaev and I. B. Zel'dovich. Microwave background radiation as a probe of the contemporary structure and history of the universe. *ARA&A*, 18:537–560, 1980.

[230] R. A. Sunyaev and Y. B. Zeldovich. The Observations of Relic Radiation as a Test of the Nature of X-Ray Radiation from the Clusters of Galaxies. *Comments on Astrophysics and Space Physics*, 4:173, Nov. 1972.

[231] Y. Suto, K. Yamamoto, T. Kitayama, and Y. P. Jing. Two-Point Correlation Functions of X-Ray-Selected Clusters of Galaxies: Theoretical Predictions for Flux-Limited Surveys. *ApJ*, 534:551–558, May 2000.

[232] T. Szabo, E. Pierpaoli, F. Dong, A. Pipino, and J. Gunn. An Optical Catalog of Galaxy Clusters Obtained from an Adaptive Matched Filter Finder Applied to Sloan Digital Sky Survey Data Release 6. *ApJ*, 736:21, July 2011.

[233] M. Takada. Subaru Hyper Suprime-Cam Project. In N. Kawai and S. Nagataki, editors, *American Institute of Physics Conference Series*, volume 1279 of *American Institute of Physics Conference Series*, pages 120–127, Oct. 2010. doi: 10.1063/1.3509247.

[234] A. N. Taylor, S. Dye, T. J. Broadhurst, N. Benítez, and E. van Kampen. Gravitational Lens Magnification and the Mass of Abell 1689. *ApJ*, 501:539–553, July 1998.

[235] M. Tegmark and M. Zaldarriaga. Separating the early universe from the late universe: Cosmological parameter estimation beyond the black box. *Phys. Rev. D*, 66(10):103508, Nov. 2002.

[236] E. Tempel, A. Tamm, M. Gramann, T. Tuvikene, L. J. Liivamägi, I. Suhhonenko, R. Kipper, M. Einasto, and E. Saar. Flux- and volume-limited groups/clusters for the SDSS galaxies: catalogues and mass estimation. *A&A*, 566:A1, June 2014.

[237] J. Tinker, A. V. Kravtsov, A. Klypin, K. Abazajian, M. Warren, G. Yepes, S. Gottlöber, and D. E. Holz. Toward a Halo Mass Function for Precision Cosmology: The Limits of Universality. *ApJ*, 688:709-728, Dec. 2008.

[238] J. L. Tinker, E. S. Sheldon, R. H. Wechsler, M. R. Becker, E. Rozo, Y. Zu, D. H. Weinberg, I. Zehavi, M. R. Blanton, M. T. Busha, and B. P. Koester. Cosmological Constraints from Galaxy Clustering and the Mass-to-number Ratio of Galaxy Clusters. *ApJ*, 745:16, Jan. 2012.

[239] K. Umetsu. Model-free Multi-probe Lensing Reconstruction of Cluster Mass Profiles. *ApJ*, 769:13, May 2013.

[240] K. Umetsu and T. Broadhurst. Combining Lens Distortion and Depletion to Map the Mass Distribution of A1689. *ApJ*, 684:177-203, Sept. 2008.

[241] K. Umetsu, E. Medezinski, T. Broadhurst, A. Zitrin, N. Okabe, B.-C. Hsieh, and S. M. Molnar. The Mass Structure of the Galaxy Cluster Cl0024+1654 from a Full Lensing Analysis of Joint Subaru and ACS/NIC3 Observations. *ApJ*, 714:1470–1496, May 2010.

[242] K. Umetsu, T. Broadhurst, A. Zitrin, E. Medezinski, D. Coe, and M. Postman. A Precise Cluster Mass Profile Averaged from the Highest-quality Lensing Data. *ApJ*, 738:41, Sept. 2011.

[243] K. Umetsu, T. Broadhurst, A. Zitrin, E. Medezinski, and L.-Y. Hsu. Cluster Mass Profiles from a Bayesian Analysis of Weak-lensing Distortion and Magnification Measurements: Applications to Subaru Data. *ApJ*, 729:127, Mar. 2011.

[244] K. Umetsu, T. Broadhurst, A. Zitrin, E. Medezinski, and L.-Y. Hsu. Cluster Mass Profiles from a Bayesian Analysis of Weak-lensing Distortion and Magnification Measurements: Applications to Subaru Data. *ApJ*, 729:127, Mar. 2011.

[245] K. Umetsu, E. Medezinski, M. Nonino, J. Merten, A. Zitrin, A. Molino, C. Grillo, M. Carrasco, M. Donahue, A. Mahdavi, D. Coe, M. Postman, A. Koekemoer, N. Czakon, J. Sayers, T. Mroczkowski, S. Golwala, P. M. Koch, K.-Y. Lin, S. M. Molnar, P. Rosati, I. Balestra, A. Mercurio, M. Scodeggio, A. Biviano, T. Anguita, L. Infante, G. Seidel, I. Sendra, S. Jouvel, O. Host, D. Lemze, T. Broadhurst, M. Meneghetti, L. Moustakas, M. Bartelmann, N. Benítez, R. Bouwens, L. Bradley, H. Ford, Y. Jiménez-Teja, D. Kelson, O. Lahav, P. Melchior, J. Moustakas, S. Ogaz, S. Seitz, and W. Zheng. CLASH: Mass Distribution in and around MACS J1206.2-0847 from a Full Cluster Lensing Analysis. *ApJ*, 755:56, Aug. 2012.

[246] K. Umetsu, E. Medezinski, M. Nonino, J. Merten, M. Postman, M. Meneghetti, M. Donahue, N. Czakon, A. Molino, S. Seitz, D. Gruen, D. Lemze, I. Balestra, N. Benítez, A. Biviano, T. Broadhurst, H. Ford, C. Grillo, A. Koekemoer, P. Melchior, A. Mercurio, J. Moustakas, P. Rosati, and A. Zitrin. CLASH: Weak-lensing Shear-and-magnification Analysis of 20 Galaxy Clusters. *ApJ*, 795:163, Nov. 2014.

[247] K. Umetsu, A. Zitrin, D. Gruen, J. Merten, M. Donahue, and M. Postman. CLASH: Joint Analysis of Strong-lensing, Weak-lensing Shear, and Magnification Data for 20 Galaxy Clusters. *ApJ*, 821:116, Apr. 2016.

[248] P. T. P. Viana and A. R. Liddle. The cluster abundance in flat and open cosmologies. *MNRAS*, 281:323, July 1996.

[249] A. Vikhlinin, A. Kravtsov, W. Forman, C. Jones, M. Markevitch, S. S. Murray, and L. Van Speybroeck. Chandra Sample of Nearby Relaxed Galaxy Clusters: Mass, Gas Fraction, and Mass-Temperature Relation. *ApJ*, 640:691–709, Apr. 2006.

[250] A. Vikhlinin, R. A. Burenin, H. Ebeling, W. R. Forman, A. Hornstrup, C. Jones, A. V. Kravtsov, S. S. Murray, D. Nagai, H. Quintana, and A. Voevodkin. Chandra Cluster Cosmology Project. II. Samples and X-Ray Data Reduction. *ApJ*, 692:1033–1059, Feb. 2009.

[251] G. M. Voit. Tracing cosmic evolution with clusters of galaxies. *Reviews of Modern Physics*, 77:207–258, Apr. 2005.

[252] A. von der Linden, P. N. Best, G. Kauffmann, and S. D. M. White. How special are brightest group and cluster galaxies? *MNRAS*, 379:867–893, Aug. 2007.

[253] A. von der Linden, M. T. Allen, D. E. Applegate, P. L. Kelly, S. W. Allen, H. Ebeling, P. R. Burchat, D. L. Burke, D. Donovan, R. G. Morris, R. Blandford, T. Erben, and A. Mantz. Weighing the Giants - I. Weak-lensing masses for 51 massive galaxy clusters: project overview, data analysis methods and cluster images. *MNRAS*, 439:2–27, Mar. 2014.

[254] A. von der Linden, A. Mantz, S. W. Allen, D. E. Applegate, P. L. Kelly, R. G. Morris, A. Wright, M. T. Allen, P. R. Burchat, D. L. Burke, D. Donovan, and H. Ebeling. Robust weak-lensing mass calibration of Planck galaxy clusters. *MNRAS*, 443:1973–1978, Sept. 2014.

[255] J.-C. Waizmann, S. Ettori, and L. Moscardini. On a novel approach using massive clusters at high redshifts as cosmological probe. *MNRAS*, 418:456–466, Nov. 2011.

[256] D. Walsh, R. F. Carswell, and R. J. Weymann. 0957 + 561 A, B - Twin quasistellar objects or gravitational lens. *Nature*, 279:381–384, May 1979.

[257] W. A. Watson, I. T. Iliev, J. M. Diego, S. Gottlöber, A. Knebe, E. Martínez-González, and G. Yepes. Statistics of extreme objects in the Juropa Hubble Volume simulation. *MNRAS*, 437:3776–3786, Feb. 2014.

[258] D. H. Weinberg, M. J. Mortonson, D. J. Eisenstein, C. Hirata, A. G. Riess, and E. Rozo. Observational probes of cosmic acceleration. *Phys. Rep.*, 530:87–255, Sept. 2013.

[259] Z. L. Wen, J. L. Han, and F. S. Liu. Galaxy Clusters Identified from the SDSS DR6 and Their Properties. *ApJS*, 183:197–213, Aug. 2009.

[260] Z. L. Wen, J. L. Han, and F. S. Liu. A Catalog of 132,684 Clusters of Galaxies Identified from Sloan Digital Sky Survey III. *ApJS*, 199:34, Apr. 2012.

[261] M. White, L. Hernquist, and V. Springel. Simulating the Sunyaev-Zeldovich Effect(s): Including Radiative Cooling and Energy Injection by Galactic Winds. *ApJ*, 579:16–22, Nov. 2002.

[262] D. R. Wik, C. L. Sarazin, P. M. Ricker, and S. W. Randall. The Impact of Galaxy Cluster Mergers on Cosmological Parameter Estimation from Surveys of the Sunyaev-Zel'dovich Effect. *ApJ*, 680:17-31, June 2008.

[263] R. Wojtak, E. L. Łokas, G. A. Mamon, S. Gottlöber, F. Prada, and M. Moles. Interloper treatment in dynamical modelling of galaxy clusters. *A&A*, 466:437–449, May 2007.

[264] R. Wojtak, S. H. Hansen, and J. Hjorth. Gravitational redshift of galaxies in clusters as predicted by general relativity. *Nature*, 477:567–569, Sept. 2011.

[265] C. O. Wright and T. G. Brainerd. Gravitational Lensing by NFW Halos. *ApJ*, 534:34–40, May 2000.

[266] D. G. York, J. Adelman, J. E. Anderson, Jr., S. F. Anderson, J. Annis, N. A. Bahcall, J. A. Bakken, R. Barkhouser, S. Bastian, E. Berman, W. N. Boroski, S. Bracker, C. Briegel, J. W. Briggs, J. Brinkmann, R. Brunner, S. Burles, L. Carey, M. A. Carr, F. J. Castander, B. Chen, P. L. Colestock, A. J. Connolly, J. H. Crocker, I. Csabai, P. C. Czarapata, J. E. Davis, M. Doi, T. Dombeck, D. Eisenstein, N. Ellman, B. R. Elms, M. L. Evans, X. Fan, G. R. Federwitz, L. Fiscelli, S. Friedman, J. A. Frieman, M. Fukugita, B. Gillespie, J. E. Gunn, V. K. Gurbani, E. de Haas, M. Haldeman, F. H. Harris, J. Hayes, T. M. Heckman, G. S. Hennessy, R. B. Hindsley, S. Holm, D. J. Holmgren, C.-h. Huang, C. Hull, D. Husby, S.-I. Ichikawa, T. Ichikawa, Ž. Ivezić, S. Kent, R. S. J. Kim, E. Kinney, M. Klaene, A. N. Kleinman, S. Kleinman, G. R. Knapp, J. Korienek, R. G. Kron, P. Z. Kunszt, D. Q. Lamb, B. Lee, R. F. Leger, S. Limmongkol, C. Lindenmeyer, D. C. Long, C. Loomis, J. Loveday, R. Lucinio, R. H. Lupton, B. MacKinnon, E. J. Mannery, P. M. Mantsch, B. Margon, P. McGehee, T. A. McKay, A. Meiksin, A. Merelli, D. G. Monet, J. A. Munn, V. K. Narayanan, T. Nash, E. Neilsen, R. Neswold, H. J. Newberg, R. C. Nichol, T. Nicinski, M. Nonino, N. Okada, S. Okamura, J. P. Ostriker, R. Owen, A. G. Pauls, J. Peoples, R. L. Peterson, D. Petravick, J. R. Pier, A. Pope, R. Pordes, A. Prosapio, R. Rechenmacher, T. R. Quinn, G. T. Richards, M. W. Richmond, C. H. Rivetta, C. M. Rockosi, K. Ruthmansdorfer, D. Sandford, D. J. Schlegel, D. P. Schneider, M. Sekiguchi, G. Sergey, K. Shimasaku, W. A. Siegmund, S. Smee, J. A. Smith, S. Snedden, R. Stone, C. Stoughton, M. A. Strauss, C. Stubbs, M. SubbaRao, A. S. Szalay, I. Szapudi, G. P. Szokoly, A. R. Thakar, C. Tremonti, D. L. Tucker, A. Uomoto, D. Vanden Berk, M. S. Vogeley, P. Waddell, S.-i. Wang, M. Watanabe, D. H. Weinberg, B. Yanny, N. Yasuda, and SDSS Collaboration. The Sloan Digital Sky Survey: Technical Summary. *AJ*, 120:1579–1587, Sept. 2000.

[267] J. D. Younger, N. A. Bahcall, and P. Bode. Evolution of the Cluster Mass and Correlation Functions in a ΛCDM Cosmology. *ApJ*, 622:1–6, Mar. 2005.

[268] Y. B. Zel'dovich. Gravitational instability: An approximate theory for large density perturbations. *A&A*, 5:84–89, Mar. 1970.

[269] Y.-Y. Zhang, N. Okabe, A. Finoguenov, G. P. Smith, R. Piffaretti, R. Valdarnini, A. Babul, A. E. Evrard, P. Mazzotta, A. J. R. Sanderson, and D. P. Marrone. LoCuSS: A Comparison of Cluster Mass Measurements from XMM-Newton and Subaru–Testing Deviation from Hydrostatic Equilibrium and Non-thermal Pressure Support. *ApJ*, 711:1033–1043, Mar. 2010.

[270] H. Zhao, J. A. Peacock, and B. Li. Testing gravity theories via transverse Doppler and gravitational redshifts in galaxy clusters. *Phys. Rev. D*, 88(4):043013, Aug. 2013.

[271] A. Zitrin, M. Bartelmann, K. Umetsu, M. Oguri, and T. Broadhurst. Miscentring in galaxy clusters: dark matter to brightest cluster galaxy offsets in 10 000 Sloan Digital Sky Survey clusters. *MNRAS*, 426:2944–2956, Nov. 2012.

[272] A. Zitrin, A. Fabris, J. Merten, P. Melchior, M. Meneghetti, A. Koekemoer, D. Coe, M. Maturi, M. Bartelmann, M. Postman, K. Umetsu, G. Seidel, I. Sendra, T. Broadhurst, I. Balestra, A. Biviano, C. Grillo, A. Mercurio, M. Nonino, P. Rosati, L. Bradley, M. Carrasco, M. Donahue, H. Ford, B. L. Frye, and J. Moustakas. Hubble Space Telescope Combined Strong and Weak Lensing Analysis of the CLASH Sample: Mass and Magnification Models and Systematic Uncertainties. *ApJ*, 801:44, Mar. 2015.

[273] Y. Zu and D. H. Weinberg. The redshift-space cluster-galaxy cross-correlation function - I. Modelling galaxy infall on to Millennium simulation clusters and SDSS groups. *MNRAS*, 431:3319–3337, June 2013.

[274] F. Zwicky, E. Herzog, and P. Wild. *Catalogue of galaxies and of clusters of galaxies*. 1968.